Understanding Ionic Liquid Properties for Carbohydrate Dissolution

Stephen Mark Green

School of Physics and Astronomy

University of Leeds

A thesis submitted for the degree of

Doctor of Philosophy

June 2017

The candidate confirms that the work submitted is his/her/their own and that appropriate credit has been given where reference has been made to the work of others.

This thesis is dedicated to the memory of my Grandfather

Because he always wanted a 'Dr Green' in the family.

Acknowledgements

Firstly, I would like to thank my supervisor at the University of Leeds, Dr. Mike Ries, for all your support, guidance and countless interesting discussions, both scientific and otherwise! I would like to thank Prof. Tatiana Budtova at CEMEF for all her assistance, collaboration and tireless proofreading. I would also like to thank Dr. Jamie Moffat at Innovia Films, for all your guidance. I would like to thank the EPSRC and Innovia Films, for funding this project.

My thanks to Dr. Robin Damion, and Glenn Jones of Bruker UK Limited, for vital assistance and training on NMR. Huge thanks go to our group experimental officer, Dr. Dan Baker, for sharing your laboratory knowledge and pain, and also for your consistent out-of-hours work, assisting me in the safe disposal of many toxic chemicals at the pub on Friday nights. My thanks to all the staff and researchers at both CEMEF and Innovia Films, for lending me your expertise. Special thanks to Kalila Cook and Natasha Goran, who assisted in collecting vital data as part of their BSc projects.

I'd also like to thank everyone in the SMP office for all the support, distraction and motivation. Thanks to Shajeth, Ethan, Sophie, Edgar, Devesh, Outi, Helen, Guanghui, Pete and Winke, for everything! Special mention to Ben, for joining me in my late night insanity and crazed ranting. My thanks to all my friends outside the university for making my downtime fantastic. My particular thanks to the Smalley brothers for the constant stream of gigs and to Emma, James, Graeme, Matt, Luke, Chloë and Flora for looking after me too. Congratulations to Lee, for your wonderful wedding, here's to many more days like that!

Finally, I'd like to thank my family for all your support throughout the last 26 years. Thanks to my sister, Sarah, for feeding and looking after me at the height of thesis-writing. Thanks to my brother, Rob, for mostly staying out of the way! And most of all, thanks to my parents for all your encouragement. Thank you for always being there, whether I needed you or not. I would not be where I am without all your support. And most of all, thank you for bringing the family dog Dora, to visit me in Leeds!

Abstract

The study of ionic liquids (ILs) is one of the fastest growing research fields today, both in academic and industrial spheres. One important use of ILs is in dissolving and processing biological resources, particularly cellulose. There is huge interest in understanding the properties of cellulose-dissolving ILs and how different IL features affect the dissolution environment.

The work presented in this thesis is an experimental study into two classes of cellulose-dissolving ILs. Two distinct investigations are undertaken on pure ILs, first with imidazolium-carboxylate ILs and then with 1,5-diazabicyclo[4.3.0]non-5-enium (DBN) carboxylate ILs. A third investigation is then presented, examining solutions of glucose, cellobiose and cellulose in the imidazolium-based IL, 1-ethyl-3-methylimidazolium octanoate ([C_2MIM][Oct]). Several NMR techniques are used, along with rheological, conductivity and density data. A novel modelling approach is formulated and then applied to the pure IL series', where simple systems of ion pairs and charged aggregates are considered, in order to accurately model several key experimental features.

Four pure imidazolium-based ILs are studied with varying-length carboxylate anions. Microscopic properties, such as NMR data, are compared to macroscopic properties, such as viscosity. Stokes-Einstein-Debye theories are applied to the different datasets, providing an insight into the microscopic structuring in the different ILs. Nernst-Einstein theory and the Walden rule are also examined for these ILs. Inconsistencies between different datasets and theoretical expectations are addressed and several simple models are applied, in order

to account for these inconsistencies. An ion pairing model, a charged aggregate model and a combination of both models are tested, indicating that this approach is reasonably successful in describing the imidazolium-based ILs and suggesting a small amount of ion aggregation is present.

In a similar study, eight pure DBN-carboxylate ILs are studied, with systematically varying anion sizes between formate and octanoate. Experimental data are presented, indicating a complex dependence on anion chain length. Comparisons of micro- and macroscopic properties are shown, comparing and contrasting the effects of changing anion chain length and changing the cation. The three models of ion aggregation are successfully applied to the six room-temperature DBN-based ILs, indicating a higher degree of aggregation and ion pairing, as compared to the imidazolium-based ILs.

Finally, $[C_2MIM][Oct]$ is investigated as a solvent for the carbohydrates glucose, cellobiose and cellulose. NMR and rheological data are presented and compared for carbohydrate solutions. Different NMR datasets are studied in-depth, including diffusion, relaxation and chemical shift. The carbohydrate-concentration dependence of each dataset is examined and compared to literature data for the same solutions in $[C_2MIM][Ac]$. The relative time and length scales of the NMR techniques were found to affect how the solutions respond to increasing carbohydrate concentration and changing between glucose, cellobiose and cellulose.

This thesis forms part of a project funded by the EPSRC CASE award with Innovia Films, aiming to better understand the process of cellulose dissolution in ILs. The results and techniques described here can aid in understanding the properties of these ILs, both for cellulose dissolution and other IL applications.

Abbreviations

AGU	Anhydroglucose unit
BPP	Bloembergen, Purcell and Pound
C_2MIM	1-ethyl-3-methylimidazolium
C_nMIM	1-alkyl-3-methylimidazolium
IL	Ionic liquid
NMR	Nuclear magnetic resonance
PFG	Pulsed-field gradient
PIL	Protic ionic liquid
RF	Radio-frequency
SE	Stokes-Einstein
[Form]	Formate
[Ac]	Acetate
[Pr]	Propionate
[But]	Butyrate
[Pent]	Pentanoate
[Hex]	Hexanoate
[Hept]	Heptanoate
[Oct]	Octanoate
[Ddc]	Dodecanoate

Nomenclature

α	Associated fraction of hydroxyl groups
δ	Chemical shift or gradient pulse length (Section 2.1.2 only)
τ	Dynamical correlation time
n	Size of charged aggregate
N	Number of hydroxyl groups per AGU
P	Fraction of neutral ion pairs
R	Molar gas constant or ratio of charged entities to neutral entities (Section 2.3 only)
r_h	Hydrodynamic radius
r_{H-H}	System-average interproton distance
Λ_{imp}	Molar conductivity from impedance measurements
Λ_{NMR}	Molar conductivity from PFG NMR data

Contents

List of Figures

Chapter 1

Introduction

1.1 Cellulose

Cellulose is a carbohydrate polymer formed from a linear chain of $\beta(1-4)$-linked glucose units, as shown in Figure 1.1. Cellulose is the principal component of plant cell walls, making it the most abundant biopolymer on Earth, with more than one trillion tons produced every year [1]. Unsurprisingly, this means cellulose is very attractive as a sustainable resource for a wide range of applications, across a whole spectrum of scientific industries. One significant hindrance in many of these applications is the difficulty in processing cellulose, due to its relative insolubility in common industrial solvents.

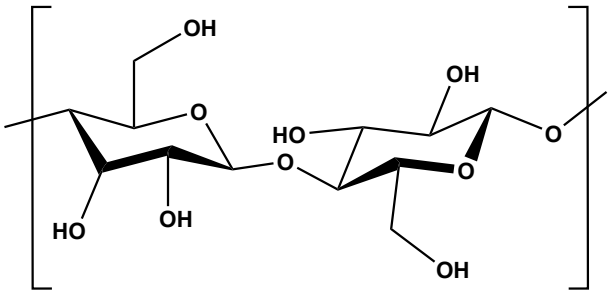

Figure 1.1: The molecular structure of the biopolymer cellulose. The conformational repeat unit is shown, which consists of two glucose monomers.

1.1.1 A Brief History of Cellulose

Cellulose is a major constituent of wood, along with lignin and various hemicelluloses. Therefore, it is arguable that cellulose was a key component of the first man-made chemical reaction in the wood-fires of prehistoric humans; utilising cellulose has been a driving factor in the development of all human society. Over thousands of years, cellulose use has been refined beyond simply setting fire to it. For example, cellulose is also the major constituent of papyrus, used as a writing material by the ancient Egyptians as early as 3000BC [2]. Mass production of pulped paper in more modern times has allowed the recording, storage and dissemination of scientific and cultural knowledge on a vast scale.

The first scientific studies on cellulose were by Anselme Payen in 1838 [3]. Payen isolated cellulose from lignocellulosic plant material and determined its chemical formula. Chemical modification of cellulose followed, first as cellulose nitrate, then as cellulose acetate and cellulose xanthate [1]. These modified celluloses were soluble in appropriate industrial solvents, allowing the spinning of rayon fibres and casting of cellophane films [4]. Like natural cotton fibres before them (up to 99% cellulose), synthetic rayon fibres are used extensively in the production of clothes and textiles [5]. Cellulose nitrate films were used as the stock for 'film' in the photography and movie industries, before being replaced by cellulose acetate 'safety film'; yet more examples of the cultural and societal benefits gained from utilising cellulose effectively.

In 1920, Hermann Staudinger determined the chemical structure of cellulose as part of his groundbreaking work on polymers [6], which provided the foundations of the disciplines of macromolecular chemistry and polymer science. Staudinger determined that cellulose was formed of chemically bonded, repeating glucose units, as shown in Figure 1.1. Each glucose unit bonds to two others, giving a linear-chain polymer with a high number of hydroxyl groups (three per monomer unit). These hydroxyl groups readily form hydrogen bonds, giving rise to many of the properties of cellulose, including its high tensile strength and its insolubility in most solvents.

Since the first industrial-scale applications, commercial cellulose processing has changed remarkably little in over a century. At the beginning of the 21st

century, the majority of cellulose was used to make paper by pulping processes, and textiles such as rayon fibres using the viscose process [1]. The processing techniques have been refined over the years but the chemical mechanisms remain the same. A notable exception to this is the Lyocell process, introduced in the 1970s, where N-methylmorpholine-N-oxide (NMMO) monohydrate is used as a direct solvent for cellulose and has supplemented the viscose process in the global production of rayon fibres.

Despite the chemistry remaining unchanged, the global and political climate is very different in recent years, as compared to the dawn of industrial cellulose processing. This has brought in new pressures on commercial ventures from environmental groups and policymakers; first, a demand on reducing the output and use of polluting chemicals, such as the carbon disulphide used by the viscose process, then more recently, a drive towards the tenets of green chemistry [7] and producing sustainable materials from cellulose.

As the most abundant natural polymer, cellulose is clearly a desirable target for a range of sustainable materials and technologies. Nature has designed cellulose to fit a number of useful criteria, including possessing a high energy density, being biodegradable, biocompatible, resistant to natural wear and tear, strong and renewable on a massive scale. This grants it great potential for replacing fossil fuel-based chemicals as sources of fuels, plastics and feedstock chemicals for the chemical industry. Unfortunately, many of the beneficial features of cellulose also hinder its use in large-scale processing, for example, cellulose will thermally degrade before it forms a melt and is resistant to common (and cheap) solvents. However, any truly sustainable future will most likely hinge on the renewal and exploitation of lignocellulosic materials on a global scale.

1.1.2 Cellulose Solvents

Many useful processing options for cellulose require chemical modification and the most efficient way to effect these modifications is in the dissolved state. However, this requires new and more cost-effective solvents to overcome the natural recalcitrance of cellulose.

The hydroxyl groups in cellulose readily form H-bonds, both to other hydroxyl groups on the same polymer chain (intrachain) and to other nearby polymer chains (interchain). Intrachain H-bonds provide rigidity and strength to the polymer chain. Large bundles of individual chains arrange into flat sheets, held together by interchain H-bonds. These sheets stack into an extended crystalline structure, where the polymer chains are aligned lengthways and are held together by a combination of intersheet H-bonding and hydrophobic van der Waals (vdW) bonding. Extended networks of cellulose sheets are known as microfibrils and are found in native cellulose [1, 8–10].

Cellulose microfibrils can take one of four crystal structures, depending on how they are processed [1]. Naturally occurring cellulose takes the crystal structure cellulose I; this structure is further divided into two forms, I_α and I_β, defined by the symmetry of the respective unit cells [9]. Native cellulose typically contains a mixture of both I_α and I_β, with the relative populations depending on the source of the cellulose. Treatment with sodium hydroxide or dissolution/regeneration from a solvent gives the more thermodynamically-stable cellulose II.

The crystal structures of native cellulose lead to the formation of the aforementioned sheets and fibrils, where the mixture of hydrophilic and hydrophobic bonding gives two distinct surfaces [11, 12]. This is a significant reason for the insolubility of cellulose in water: while water molecules can form strong H-bonds with cellulose hydroxyl groups, the nearby hydrophobic surfaces require the water molecules to form long-range structures around each sheet/fibril. The entropic penalty for this water structuring is higher than the enthalpic gain from additional cellulose-water bonding (hydrophobic effect). Presence of both hydrophilic H-bonds and hydrophobic vdW forces suggest any cellulose solvent must be able to break both types of bonding. This 'amphiphilic' nature of cellulose, and therefore hypothetical cellulose solvents, is the subject of a renewed debate in recent years [11, 13, 14].

As mentioned previously, there are a number of established methods for dissolving cellulose. Derivatising solvents are the most common, for example, cellulose acetate is soluble in acetone and is formed from cellulose, acetic acid and acetic anhydride. The most prevalent use of derivatising solvents is the viscose process; cellulose is reacted with sodium hydroxide and then carbon disulphide

to produce cellulose xanthate. The cellulose xanthate is dissolved in sodium hydroxide solution and then cellulose is recovered by precipitation through sulfuric acid. A more recent derivatising process involves reacting alkali cellulose with urea to form cellulose carbamate, which is then precipitated in a similar fashion to the viscose process [1].

Direct solvents are more desirable due to their relative simplicity. However, the nature of cellulose means these direct solvents are often more exotic and therefore more expensive or difficult to use. The first direct solvent was cuprammonium hydroxide, known as Schweizer's reagent. Other solvents include the aforementioned NMMO (Lyocell process), lithium chloride in dimethylacetamide [1], and aqueous sodium hydroxide in a narrow concentration range (7-9%) [15]. One of the more recent entries in the field of cellulose are ionic liquids (ILs), which will be discussed in detail in the following sections.

1.2 Ionic Liquids

1.2.1 An Introduction to ILs

An ionic liquid (IL) is simply a salt in the liquid phase, hence the alternative name of 'molten salts'. The standard definition of an IL includes the requirement of a melting point below 100 °C, though this is somewhat arbitrary [16]. Room-temperature ionic liquids (RTILs) are sometimes distinguished as a separate class, describing ILs with a melting point below 25 °C. Typical ILs consist of a single cation and anion. Both cation and anion are interchangeable within a large set of potential ions, giving roughly one million possible combinations [17]. In fact, mixing multiple ions in different ratios gives ILs with distinct properties, meaning the number of possible ILs becomes infinite [18, 19]. This flexibility affords a high degree of fine-tuning to ILs, allowing them to be tailored to specific applications and conditions. Figure 1.2 shows just a small selection of ions commonly used in ILs.

In Figure 1.2, each of the four cations can be paired with each of the four anions, giving 16 combinations. Many of the ions also contain aliphatic carbon side-chains; these side-chains can be varied in length to give yet more distinct

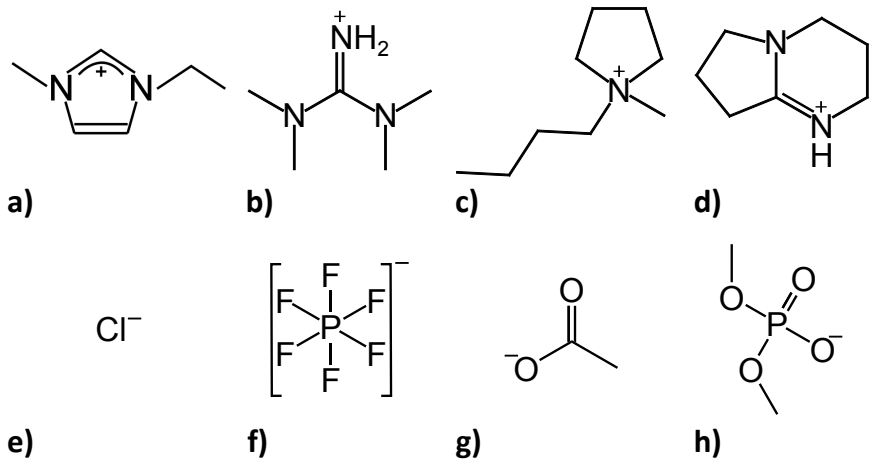

Figure 1.2: A series of commonly used cations (**a**-**d**) and anions (**e**-**h**). The cations are: **a)** 1-ethyl-3-methylimidazolium ($[C_2MIM]^+$), **b)** 1,1,3,3-tetramethylguanidium, **c)** N-butyl-N-methylpyrrolidium and **d)** 1,5-diazabicyclo[4.3.0]non-5-enium ($[DBNH]^+$). The anions are: **e)** chloride, **f)** hexafluorophosphate, **g)** acetate ($[Ac]^-$) and **h)** dimethylphosphate.

ions and potential cation-anion combinations. There are many systematic studies across many fields, investigating how IL properties change while varying the functionality of the cation [20], the anion [21–23] or simply varying the side-chain length [24]. There are also publications dedicated to IL databasing [25] and the National Institute of Standards and Technology (NIST) has hosted a dedicated, online IL database since 2006 (ILThermo).

The key difference between an ionic liquid and an ionic solid is the lack of an extended crystalline structure in the former. However, this does not mean ILs are completely disordered on a molecular level. In ILs, the strong ionic interactions try to bring ions together into a solid structure but steric factors frustrate the crystallisation, keeping the system in a liquid state [17]. This means both the size and shape of ions is important in determining the melting point of ionic systems; bulky, asymmetric ions are generally the most effective at depressing the melting point [17, 26]. While highly-ordered structures may be suppressed, the strong interionic forces in ILs often give rise to nano-, micro- and even meso-scale ordering and phase segregation, as evidenced by both simulation [27, 28] and experimental work [29, 30].

1.2.2 Common IL Properties

IL have many desirable properties, with the desirability depending mainly on the application. Some of the more useful properties common in ILs are low volatility, low flammability, recyclability, high electrical conductivity and good solvating power for a wide range of solutes. Many of these properties match well with the principles of green chemistry [7], leading to ILs being widely regarded as 'green solvents'. Unfortunately, there are also a number of significant drawbacks and difficulties in utilising most ILs. Pure ILs tend to exhibit high viscosities, inhibiting conductivity and mass transfer.

The complexity of many ILs means they are expensive to produce, with multiple synthesis steps. This complexity often means ILs have fairly high toxicity too [31, 32]. Low volatility in ILs is useful during an industrial process but it means low pressures and higher temperatures are required to distil, purify and recycle many ILs [33]. The presence of microscopic order in ILs means they are sensitive to impurities that can disrupt this structuring; for example, halide impurities can increase IL viscosity and water impurities will have the opposite effect [34]. When working with ILs, one of the most important considerations is the water content and the potential for atmospheric moisture absorption. Even small weight percentages of water (1 - 5%) can have drastic effects on the IL viscosity [21, 34–36] and therefore transport properties like diffusion [35, 37] and conductivity. The melting point and any microscopic structuring in an IL is also significantly reduced by the addition of water, indeed, any ionic solid can become a 'room-temperature ionic liquid' with a high enough water content.

1.2.3 A Few Applications of ILs

The first academic report on ILs was by Paul Walden in 1914 [38], however, the field remained relatively unexplored for decades. Momentum began to pick up in the 1960s, where extensive research began into using ILs as battery electrolytes [39]. At the turn of 21st century, the advent of green chemistry and environmental awareness brought a renewed enthusiasm for ILs as 'green solvents' in both academia and industry. In recent years, a huge number of new applications have emerged from the academic realm. Applications as diverse as

biofuels extraction [40], CO_2 capture [41], liquid crystal materials [42] and a range of biomedical processes [43–45]. There are even a number of large-scale industrial applications, such as the BASIL and Difasol processes at the production and pilot scales (see reference [17] for further details).

Another important application of ILs is for the dissolution of lignocellulosic biomass. In particular, the dissolution of cellulose in ILs will form a significant focus of the work presented here. The field of ILs as cellulose solvents will be explored in the following section.

1.3 ILs as Solvents for Cellulose

1.3.1 Discovery and Development of ILs as Cellulose Solvents

The first report of using ILs for cellulose dissolution was also the first patent involving ILs, filed in 1934 by Charles Graenacher [46]. The reported process was conducted at $110 - 120$ °C, high enough to risk significant degradation of the cellulose and not in keeping with the modern definition of 'ionic liquid', however, it is remarkable that this potentially revolutionary finding was overlooked for so long. It took nearly 70 years for an IL-cellulose renaissance, beginning with the paper by Swatloski et al. in 2002 [47] and a patent [48]. The paper by Swatloski et al. studied a series of imidazolium-based ILs as solvents for several different grades of cellulose, finding 1-butyl-3-methylimidazolium chloride ($[C_4MIM][Cl]$) to be the most effective.

Arriving in the early years of the IL resurgence, IL-cellulose research experienced swift growth after the initial work of Swatloski et al. Research groups around the world sprang up, investigating every facet of cellulose isolation, dissolution and regeneration; Figure 1.3 illustrates this rapid expansion in terms of publications and citations. Initial studies used imidazolium-based cations [47, 49–52] and more recent studies have expanded to other aprotic nitrogen-containing cations, both cyclic and aliphatic [53–55], as well as protic cations based on superbases [56–58]. For the anion, halides were used first [47, 49–51], followed by

carboxylates [52, 54, 57–61], dialkylphosphates [62] and many other formulations, often including sulphides and fluorinated ions [53, 63].

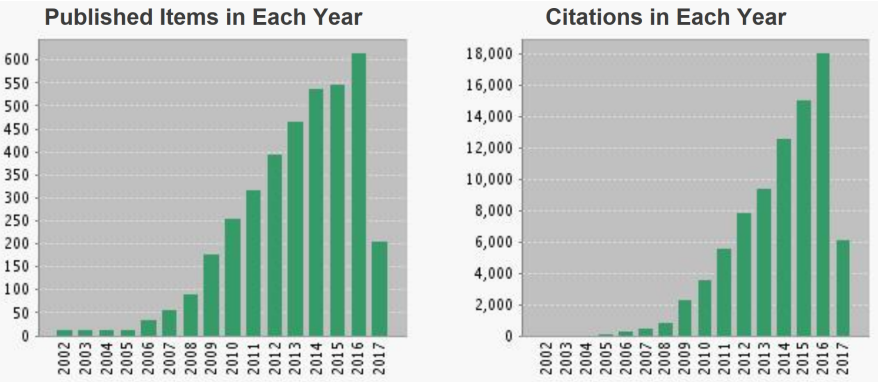

Figure 1.3: Plots showing the number of publications and citations in the field of ionic liquids and cellulose, year-by-year. Obtained from a search of "ionic liquids and cellulose" on Web of Science in May 2017 [64].

Unsurprisingly, changing the IL even slightly can have a dramatic effect on its ability to dissolve cellulose. It is equally unsurprising that the dissolution process, particularly the rate of dissolution, depends significantly on the properties of the cellulose. The degree of polymerisation (DP) of the cellulose is important, as is the crystallinity to an extent. Celluloses of all kinds have been trialled in ILs, including microcrystalline cellulose (DP≈150) [52, 60, 61], industrial-grade dissolving pulp (DP$= 1000 - 2000$) [47, 57] and high-molecular-weight bacterial cellulose (DP$= 4000 - 10000$) [60, 65]. ILs have been used for processing full lignocellulosic material, for example, by directly dissolving wood chips [66–68]. There are also a multitude of computational studies of cellulose dissolution, see references [69–74] for a few examples.

The diversity in the IL-cellulose field is vast and rapidly growing, both in terms of materials and techniques. There have been thousands of papers published in the last 15 years, requiring a correspondingly large number of reviews. In fact, for the general field of ILs there were close to 2000 review articles, as of 2016 [75]. See references [63, 76–78] for just a small selection of reviews focused on cellulose dissolution in ILs.

1.3.2 Kinetic and Thermodynamic Factors Affecting Cellulose Dissolution

As discussed previously, an effective cellulose solvent needs to break the extensive bonding structure of cellulose and then form strong solvent-solute bonds. The ions in ILs are well-suited to forming strong bonds. Typically, H-bonding between the IL anion and hydroxyl groups on cellulose are the dominant mechanism in the solvated state [47, 51, 59, 69]. Most ILs are also amphiphilic, making them compatible with the multiple environments along a cellulose chain [13, 14].

The formation of anion-cellulose bonds is energetically favourable but there are a number of barriers that may need to be overcome first. The strong cellulose-cellulose interactions need to be broken but ion-ion interactions in the IL, such as the structuring detailed in Section 1.2.1, also need to be broken; these two factors can combine to give a large energy barrier to dissolution. There is some evidence that a decrease in entropy in the solvated state can also provide a significant barrier [79]. In polymer dissolution, kinetic factors will also play an important part in controlling the reaction rate. Many pure ILs exhibit high viscosities already and dissolving cellulose will greatly increase the solution viscosity. The viscosity can quickly become high enough to inhibit solvent diffusion into regions of undissolved cellulose, effectively reducing the dissolution rate to zero.

Heating and stirring an IL-cellulose system will decrease the viscosity and increase solvent contact, as such, most studies are conducted at temperatures between 60 and 120 °C in order to speed up dissolution. However, many studies also report substantial temperature dependence in the maximum solubility of cellulose, with higher temperature giving higher solubilities [47, 54, 80, 81]. This would suggest that dissolution is an endothermic process. However, calorimetric data have shown that dissolution of cellulose in several ILs is exothermic [82, 83]. Rheological studies of IL-cellulose solutions have also shown that the solvent thermodynamic quality is reduced as temperature increases [60, 84]. There are also concerns about the degradation of dissolved cellulose at higher temperatures [85, 86]. In short, there is a complex interplay of factors to consider in any dissolution study or application.

An important practical consideration is the presence of impurities in the IL solvent, particularly water. In cellulose-solvating ILs, water is an anti-solvent and will cause coagulation of the dissolved cellulose. Therefore, it follows that residual water will hinder the solvation of cellulose in ILs [47, 54, 87, 88]. Additionally, cellulose itself is hygroscopic and will retain an amount of adsorbed water, even after vacuum drying. Wherever possible, water content should be monitored throughout the dissolution process. Although, very small amounts of water will decrease the IL viscosity, increasing the dissolution rate of cellulose but decreasing the maximum solubility.

1.3.3 Applications of ILs as Solvents for Cellulose

An obvious application for an effective cellulose-dissolving IL would be to replace traditional processes, such as the polluting viscose process, or the energy-intensive Lyocell process. This has been achieved on the laboratory scale by the Sixta and Kilpeläinen groups in their "Ioncell-F" process for spinning cellulose fibres via IL solutions [89–94]. A number of other uses for ILs as cellulose solutions have been demonstrated, including producing cellulose nanocrystals [95, 96], nanowhiskers [97], all-cellulose composite materials [98–100] and cellulose aerogels [101].

In the field of bio-based materials, IL use has not been limited to cellulose. ILs have been used as solvents for other polysaccharides, including cellulose acetate [102], xylan [103, 104], starch [105–108], pectin [109] and animal-derived compounds like chitin and chitosan [110–113]. As mentioned previously, ILs have also been used for processing lignocellulosic biomass. The different solubilities of the different polysaccharide components in ILs allows fractionation of the components, showing potential for a 'biorefinery' [66–68, 114, 115].

Over the last 15 years, ILs have demonstrated great potential as cellulose solvents, as well as for processing a range of natural materials. There are many promising applications emerging from academia and commercial interest in these applications is building across the chemical industries. However, there are still many challenges and barriers, hindering the large-scale implementation of IL-based processes. The behaviour and properties of the ILs themselves is a key

factor in many of these challenges. Fundamental knowledge of the microscopic structure in ILs is required for a complete understanding of their properties. This provides a foundation for understanding the microscopic interactions of cellulose dissolved in ILs, which in turn, leads to an improved understanding of the entire dissolution process.

1.4 Thesis Overview

This thesis presents an experimental study into cellulose-dissolving ionic liquids, first investigating a range of pure ILs and then examining carbohydrate solutions in one IL. Experimental methods consist principally of nuclear magnetic resonance (NMR) techniques, in conjunction with rheology, conductivity and density measurements. The ILs studied are based on the imidazolium and 1,5-diazabicyclo[4.3.0]non-5-enium (DBN) cations, paired with carboxylate anions of varying lengths. A simple mathematical model is introduced, based on Stokes-Einstein and Nernst-Einstein theories, to combine micro- and macroscopic approaches and reconcile certain discrepancies between datasets. Carbohydrate solutions consist of glucose, cellobiose and cellulose dissolved in 1-ethyl-3-methylimidazolium octanoate ([C_2MIM][Oct]), as a comparison to previous work on similar solutions in 1-ethyl-3-methylimidazolium acetate ([C_2MIM][Ac]). The aim of these studies is to provide a greater understanding of IL microscopic structure, how it relates to the properties of these ILs and their effectiveness as cellulose solvents.

Chapter 2 starts with an introduction to the main experimental techniques and basic theory used in subsequent chapters. This is followed by the mathematical derivation of a novel theory, used to model ion pairing and aggregation in pure IL data. Chapters 3, 4 and 5 are results-based chapters, each consisting of a focused literature review, experimental data and an in-depth analysis of that data.

Chapter 3 studies a series of four imidazolium-based ILs using NMR, rheology and conductivity measurements. The ion pairing and aggregation models are then applied to all four IL datasets, in order to test the ability of this modelling approach to describe experimental data. Chapter 4 takes a similar approach with a series of eight DBN-based ILs. NMR, rheology and conductivity measurements

are presented, followed by application of the ion pairing and aggregation models to the six room-temperature ILs in the series. Chapter 5 uses $[C_2MIM][Oct]$ to dissolve glucose, cellobiose and cellulose. NMR and rheological data are presented, followed by an in-depth examination of the NMR data, comparing and contrasting the properties of $[C_2MIM][Oct]$ solutions to published work on the equivalent $[C_2MIM][Ac]$ solutions.

This thesis attempts to improve the understanding of fundamental IL structure in cellulose-dissolving ILs and apply this understanding to solutions of cellulose in ILs. The techniques described here relate experimental data to IL properties and can assist in designing future IL systems and processes.

Chapter 2

Methods and Theory

2.1 Methods

Several different experimental techniques will be used in the investigations presented here, in order to provide a variety of physical and chemical perspectives. Nuclear magnetic resonance (NMR), rheology and conductivity measurements will form the majority of experimental data and the basis of further discussions. This chapter will detail the experimental techniques and methods used, then present established theoretical background to the experimental results. Following that, a novel approach for modelling ionic pairing and aggregation will be detailed.

NMR is a highly versatile technique, which can be used to probe a variety of chemical information across a range of time and length scales. NMR is commonly used for chemical characterisation but can also be used to measure diffusion properties and molecular relaxation dynamics.

A traditional NMR setup is, in essence, a system comprised of two components: a strong external field along one axis and a probing radio-frequency (RF) pulse acting along a perpendicular axis. By varying the length and sequence of RF pulses, a significant range of information can be obtained, including chemical structures and time-dependent dynamical properties via relaxometry measurements. Adding inhomogeneous magnetic field gradients to the basic NMR setup introduces additional avenues for experimentation, by introducing spatial resolution along the axes of the field gradients. In fact, this principle forms the basis

of Magnetic Resonance Imaging (MRI). Field gradients also allow the investigation of properties that require both temporal and spatial resolution, such as molecular diffusion. The NMR techniques referred to above will be introduced practically here, a full theoretical treatment of these techniques can be found in many textbooks; see references [116–118] for just a few examples.

Rheological techniques provide a broad range of investigations into the macroscopic flow properties of fluids and soft matter, which can in turn, provide insight into the microscopic properties. The rheological experiments presented here will be limited to the measurement of steady-state viscosity as a function of shear rate, in order to obtain flow curves for each sample. Appropriate flow curves show the rheological character of a liquid or solution, *e.g.* Newtonian, shear-thinning etc. Flow curves also allow the calculation of the Newtonian, or 'zero-shear', viscosity. All of the values of viscosity, η, used in experimental results and theoretical considerations, refer to the Newtonian viscosity here: η is a macroscopic property, describing a fluid's resistance to motion. This can be directly related to other transport properties, such as diffusion, and these relationships will be discussed extensively in subsequent sections.

Electrical conductivity, σ, describes how effective a material is at conducting an electrical current. Dielectric spectroscopy can be used to examine many electrical properties of a substance. Here, it will be used to give a relatively direct measure of the conductivity via impedance measurements. σ depends principally on the density and mobility of charge carriers, such as ions; this mobility is directly related to both microscopic diffusion and viscosity, as subsequent sections will explore.

The details of experimental equipment and generic methodology used in Chapters 3, 4 and 5 are given below. Each chapter also contains additional specific detail, related to the differences in materials and techniques between chapters.

2.1.1 Controlling Sample Water Content

ILs are usually hygroscopic: even some ILs referred to as 'hydrophobic' exhibit noticeable moisture uptake over a period of hours at ambient conditions and humidity [34]. Therefore, it is important to keep ILs in a controlled atmosphere

and minimise exposure to external humidity; atmospheric exposure should be limited wherever possible during storage, sample preparation and measurement.

An MBraun Labmaster 130 glove box was used to prevent water contamination in IL samples. A dry nitrogen atmosphere was maintained in the glove box, with a dew point between -40 and -70 °C. All ILs used for NMR, conductivity and density measurements were stored in this dry nitrogen atmosphere with no exposure to atmospheric humidity. Water content in pure ILs was measured by Karl-Fischer titration on a Metrohm 899 Coulometer, and monitored *in situ* during NMR experiments. It was found to conform to the specification of $< 0.5\%$ by weight in all experiments [61]. If storage in a glove box was not possible, pure ILs and IL solutions were sealed tightly and stored in a desiccator.

2.1.2 NMR Methods

Diffusion measurements, 'high-field' relaxometry, chemical shift measurements and ^{1}H spectra were all obtained on a Bruker Avance II 400 MHz spectrometer with a Diff50 diffusion probe and a ^{1}H coil. Gradient strengths of up to 20 Tm^{-1} were obtainable and the gradient field strength was calibrated by measuring the self-diffusion coefficient of water at 20 °C. Temperature was controlled to an accuracy of ±0.1 °C, using a heating element and a dry airflow. Samples were allowed to equilibrate for a minimum of 10 minutes before measurement.

Samples for these high-field measurements were prepared in a glove box and sealed before removal, as detailed above. The recommendations of Annat et al. were followed [119], including keeping the sample height short (below 1 cm) to minimise convection currents. In addition to this, the water-cooling system for the gradient coils was maintained at 15 °C below the measurement temperature, in order to minimise convection currents from temperature gradients across the sample.

Diffusion coefficients, D, were measured using a pulsed-field gradient (PFG) technique, with a stimulated echo pulse sequence and bipolar gradients [119]. Gradient strength was varied stepwise and D was obtained by fitting the Stejskal-Tanner equation [120]. Gradient pulse lengths, δ, were between 1 and 4 ms

and diffusion times, Δ, were between 10 and 100 ms. Recycle delay times were maintained at $> 5T_1$, where T_1 is the spin-lattice relaxation time.

'Low-field' relaxometry was carried out on a 20 MHz Maran Benchtop NMR spectrometer. Temperature was controlled with a heating element and dry airflow at 30 °C and above. Temperatures of 20 °C and below were reached using a cryogenic nitrogen flow. In both cases, temperatures were maintained to an accuracy of ±0.2 °C. For the pure imidazolium-based ILs (Chapter 3), low-field samples were prepared using larger amounts of IL, then freeze-dried with liquid nitrogen and permanently sealed under vacuum. In chapters 4 and 5, the same samples were used for both high-field and low-field measurements.

Identical pulse sequences were used for relaxometry at 400 MHz and 20 MHz. The longitudinal relaxation time, T_1, was measured using a standard inversion-recovery pulse sequence, where the delay times were varied stepwise. The transverse (or spin-spin) relaxation time, T_2, was measured using a Carr-Purcell-Meiboom-Gill (CPMG) pulse sequence [121, 122], where the number of echoes in the pulse train or the time between echoes were varied to obtain an exponential signal decay. In both sequences, recycle delay times were $> 5T_1$.

2.1.3 Viscosity Methods

Imidazolium-based ILs

Steady-state viscosity was measured in Chapters 3 and 5 at CEMEF (Center for Material Forming of MINES ParisTech, France), using a stress-controlled Bohlin Gemini rheometer, equipped with a cone-plate geometry (4 ° - 40 mm) and a Peltier temperature control system. To prevent water uptake from the air, a thin film of low-viscosity silicon oil was used to cover the edges of the measuring cell [84].

Viscosity-shear rate flow curves were obtained for the pure ILs and IL-carbohydrate solutions. In all cases, these curves exhibited a Newtonian plateau for at least two decades of shear rate. The mean values of Newtonian viscosity were taken from these plateaus with a standard deviation of less than 10%. For high viscosity solutions, the shear rate range was chosen carefully to prevent fluid ejection during measurement.

DBN-based ILs

Steady-state viscosity was measured in Chapter 4 in Leeds (UK), using a Rheometrics Dynamic Stress Rheometer equipped with a plate-plate geometry (15 mm diameter, gap size ≈ 0.7 mm). Temperature was controlled using an external water bath to an accuracy of ±0.5 °C. As with the method detailed above, a thin film of low-viscosity silicon oil was used to cover the edges of the measuring cell. All viscosity-shear rate flow curves exhibited a Newtonian plateau for at least two decades and mean values of Newtonian viscosity were taken from these plateaus with a standard deviation of less than 10%.

2.1.4 Conductivity Methods

Broadband dielectric spectroscopy was performed using a Novocontrol Alpha-A dielectric analyser. The ILs were loaded into a cylindrical, enclosed liquid measurement cell of height 6.75 mm and diameter 18.0 mm. ILs were stored under a dry nitrogen atmosphere until use and care was taken to minimise exposure to the open atmosphere during cell loading. Temperature was controlled by a heating element and a flow of cryogenic nitrogen as part of a Novocontrol Quatro cooling system, to an accuracy of ±0.1 °C. Impedance was measured across a frequency range of 0.01 - 10^6 Hz and converted into conductivity.

2.1.5 Density Methods

Density was measured using an oscillating U-tube Anton Paar DMA 4100M density meter. Samples were kept under a dry nitrogen atmosphere before use and atmospheric exposure was kept to a minimum when loading into the density meter. Density values were measured across a full temperature range of 20 °C to 80 °C and then the temperature was reduced to 20 °C again to compensate for any change in density due to moisture absorption. For all ILs, moisture absorption was found to be negligible during the timescale of the experiment, as density was found to be the same for both 20 °C measurements within experimental error.

2.2 Theory

2.2.1 NMR Theory

Consider a system containing many nuclear magnetic spins, such as ^{1}H nuclei: if there is no external magnetic field the direction of the nuclear spins will average out to give a net magnetic moment of zero. If an external magnetic field is applied in the z-direction, defined as B_z, a proportion of the spins will align with the field to give a net magnetic moment, $\mathbf{M}$. Introducing a perturbation in the form of an RF pulse, at the Larmor frequency and perpendicular to the z-axis, will cause $\mathbf{M}$ to precess about the pulse. A "90°" pulse will rotate the direction of the net moment into the xy-plane, where it will precess about B_z. This is the basic NMR experiment, where the rotating xy-component of the net magnetic moment induces a current in a measurement coil.

While precessing, the xy-component of $\mathbf{M}$ will decay due to two processes. Firstly, $\mathbf{M}$ is in it's lowest energy configuration when aligned to the external field B_z. Therefore, it will relax towards this low energy state; this is longitudinal, or T_1, relaxation. Secondly, the individual elements of $\mathbf{M}$ can precess at slightly different speeds due to spin-spin interactions across the system. This decoherence will reduce the measured xy-component in a process known as transverse, or T_2, relaxation.

The work of Bloembergen, Purcell and Pound (BPP) presented a theory relating T_1 and T_2 to the temperature-dependent dynamical correlation time, τ [123]. Based on this, for an NMR system of spin-1/2 particles (*e.g.* ^{1}H nuclei) at a Larmor freqency ω, the relaxation times can be written as follows [124],

$$\frac{1}{T_1} = 2A\left(\frac{\tau}{1+\omega^2\tau^2} + \frac{4\tau}{1+4\omega^2\tau^2}\right) \tag{2.1}$$

$$\frac{1}{T_2} = A\left(3\tau + \frac{5\tau}{1+\omega^2\tau^2} + \frac{2\tau}{1+4\omega^2\tau^2}\right) \tag{2.2}$$

where T_1 is the spin-lattice relaxation time, T_2 is the spin-spin relaxation time

and A is a system-dependent quantity defined as follows,

$$A = \frac{3}{20}\gamma^4\hbar^2\left(\frac{\mu_0}{4\pi}\right)^2 r_{H-H}^{-6} \tag{2.3}$$

where γ is the gyromagnetic ratio for protons, $\hbar$ is the reduced Planck constant, μ_0 is the permeability of free space and r_{H-H} is the distance between any two interacting protons, averaged across the entire system.

The correlation times, and therefore T_1 and T_2, are strongly dependent on the temperature. According to BPP theory, when T_1 is plotted as a function of temperature, there will be two distinct regimes, separated by a turning point. In the high-temperature regime, known as 'liquid-like', T_1 is equal to T_2 and both increase as temperature increases. In the low-temperature regime, known as 'solid-like', T_1 increases as temperature decreases, whereas T_2 diverges and decreases as temperature decreases. The T_1 minimum between these two regions is often referred to as the 'transitional' regime and occurs at the point where $\omega\tau = 0.62$.

2.2.2 Stokes-Einstein-Debye-Nernst Theory

The classical work of Stokes related the rotational motion of a sphere to the viscosity of the surrounding medium. Einstein built upon this work and used it to describe the Brownian motion of diffusing particles in a viscous medium. The result was the Stokes-Einstein equation, which can be used to relate the microscopic diffusion of a particle (molecule, ion etc.) to the macroscopic viscosity as follows,

$$D_i = \frac{k_B T}{6f\pi\eta r_{h,i}} \tag{2.4}$$

where D_i is the self-diffusion coefficient of component i, f is a correction term [125–128], η is the bulk (Newtonian) viscosity of the system and $r_{h,i}$ is the hydrodynamic radius of component i.

In classical Brownian motion, the diffusing sphere is assumed to be large relative to the particles of the diffusing medium and f is equal to 1. However, if the diffusing particle is small or similarly sized to the surrounding diffusing molecules, then f can be lower than 1 (see for example, reference [129]). This

is obviously the case for self-diffusion in a molecular liquid. Theoretical studies have confirmed the validity of the Stokes-Einstein in these types of systems too [130]. The deviation of f from unity can also occur if the particle is non-spherical, particle aggregation occurs or there are strong intermolecular interactions, such as hydrogen bonding [125, 127, 128]. All four of these criteria are found to some extent in ILs. Köddermann et al. investigated 1-ethyl-3-methylimidazolium bis(trifluoromethylsulfonyl)imide using molecular dynamics simulations [131]. They showed that this IL did not follow Stokes-Einstein behaviour when a value of $f = 1$ was used. This was attributed to regions in the molecule or aggregate where the structural relaxation time varied significantly from the system average, known as dynamical heterogeneities. The values of f were found to be between 2/3 and 0.9. This is similar to the findings of McLaughlin, who showed that for a variety of molecular liquids, a pre-factor of 4 instead of 6 should be used in the Stokes-Einstein equation, equivalent here to setting f to 2/3 in Equation 2.4 [129]. For both the anion and cation in $[C_2MIM][Ac]$, Hall et al. found $f = 0.71$ and 0.58, respectively [35]. Tokuda et al. also investigated the value of the prefactor for a range of imidazolium-based ILs [22]. It was found that the prefactor f spanned from 0.55 to 0.83, with the average value of the prefactor found to be 0.65. Based on all these results a value of $f = 2/3$ will be used in the following chapters, equivalent to the prefactor of 6 being replaced by 4 in the Stokes-Einstein equation.

The hydrodynamic radius can be calculated from the diffusion coefficient and viscosity, using the Stokes-Einstein equation above. However, if one wants to estimate the diffusion coefficient solely from the viscosity, or vice versa, a value of r_h is needed. An expression based on the volume occupied by one mole of component i was derived in a number of publications to give the following [126, 129],

$$r_{h,i} \approx \frac{1}{2}\left(\frac{V_{m,i}}{N_A}\right)^{\frac{1}{3}} = \frac{1}{2}\left(\frac{M_i}{\rho N_A}\right)^{\frac{1}{3}} \tag{2.5}$$

where $V_{m,i}$ is the molar volume of component i, M_i is the molar mass of component i and ρ is the bulk density. This equation only gives an approximate value for $r_{h,i}$ but it was found to agree well with experimental data for a range of liquids [126].

The Stokes-Einstein equation (Equation 2.4) can be extended to consider the rotational correlation time of a diffusing particle in a viscous medium, according to the work of Debye. The Stokes-Einstein-Debye equation describes this relation [35, 132],

$$\tau_r = \frac{4}{3}\pi r_h^3 \frac{\eta}{k_B T} \tag{2.6}$$

where τ_r is the correlation time for molecular rotation.

The Stokes-Einstein-Debye equation can now be utilised to directly compare the viscosity of the system to the NMR relaxation constants, under certain conditions. Considering BPP theory (Equations 2.1 and 2.2) in the high-temperature limit ($\omega\tau \ll 1$) gives the following,

$$\frac{1}{T_1} = \frac{1}{T_2} = 10A\tau \tag{2.7}$$

where A is defined as in Equation 2.3. Assuming that the dominant relaxation mechanism is molecular rotation ($\tau = \tau_r$), allows Equations 2.6 and 2.7 to be combined; this gives an expression relating T_1 and T_2 to the viscosity as follows,

$$T_1 = T_2 = \frac{3k_B}{40\pi A r_h^3} \frac{T}{\eta} \tag{2.8}$$

The conductivity, σ, describes the ability of a material or solution to conduct electrical current. A related quantity is the molar conductivity, Λ, which describes the inherent conductivity of the charge carrying elements. In an electrolytic solution, Λ gives detail on how effective the ions are at conducting, regardless of how diluted they are in the solution. The molar conductivity is defined as follows [133],

$$\Lambda = \frac{\sigma}{c} \tag{2.9}$$

where σ is the conductivity and c is the molar concentration. Section 2.1.4 described the method used here for conducting σ from impedance measurements. The molar conductivity calculated from these σ values will be referred to as Λ_{imp}.

The Nernst-Einstein equation links the processes of self-diffusion and conduction. For an ionic system of two charge carriers, one positive and one negative,

the molar conductivity can be calculated as follows [134],

$$\Lambda = \frac{N_A e^2}{k_B T}(v_+ z_+^2 D_{pos} + v_- z_-^2 D_{neg}) \tag{2.10}$$

where e is the electronic charge, D_{pos} and D_{neg} are diffusion coefficients of the positive and negative charge carriers respectively, and z_+ and z_- are the valences of the positive and negative charge carriers. v_+ and v_- are the number of charge carriers per formula unit of electrolyte for the positive and negative charge carriers respectively (also known as the stoichiometric numbers), that is, the formula for dissociation of an ionic salt dissolved in a non-conducting solvent is written as follows,

$$[pos]_{v_+}[neg]_{v_-} + m[solv] \rightleftharpoons v_+[pos]^{z_+} + v_-[neg]^{z_-} + m[solv] \tag{2.11}$$

where m is the number of solvent molecules per formula unit, and $[pos]$, $[neg]$ and $[solv]$ are the formulae for the positive charge carrier, negative charge carrier and solvent, respectively. In general, if $z_+ = z_-$, then $v_+ = v_-$.

There are a number of assumptions made in the ideal case described by the Nernst-Einstein equation. The two ions are assumed to be in an infinitely dilute electrolytic solution and are therefore non-interacting. Additionally, the diffusing ions and the conducting ions must be identical and both processes must proceed via the same mechanism [134, 135]. The closer the system is to this idealised case, the more accurate the Nernst-Einstein equation should be at calculating Λ. Here, diffusion coefficients will be calculated using PFG NMR measurements. Therefore, the molar conductivity calculated from these D values will be referred to as Λ_{NMR}.

If the molar conductivity can be related to the diffusion coefficient, it must be possible to relate Λ and the viscosity. This relation is known as the Walden rule, which simply states that the molar conductivity is inversely proportional to the viscosity [39, 135, 136],

$$\Lambda\eta = constant \tag{2.12}$$

Using the appropriate units, an ideal solution of single, isolated charges (aqueous KCl is used most commonly) will give a value of $\Lambda\eta = 1$. Based on this, a plot

of Λ as a function of $1/\eta$ in appropriate units, known as a Walden plot [39, 136], should give a straight line of gradient = 1 for this ideal solution. For real solutions or ILs, any deviation from this ideal case will lead to a deviation from the straight line. Appendix C contains several of the key equations from this section, for quick reference.

2.3 Aggregate Modelling

2.3.1 Isolated Ions Model

The simplest picture of an ionic liquid is that of two isolated ions, one positive and one negative, as shown in Figure 2.1. They diffuse independently and conduct in opposite directions under an electric field. In this picture the diffusion coefficients, viscosity and conductivity are all related in a fairly straightforward manner, as in a molecular liquid or a dilute electrolytic solution. The diffusion coefficients can be related to the viscosity using the Stokes-Einstein equation (Equation 2.4), to the conductivity using the Nernst-Einstein equation (Equation 2.10) and the conductivity and viscosity can be related using the Walden rule (Equation 2.12).

Figure 2.1: A representation of the isolated ions model, showing a single, charged cation and a single charged anion.

At this point it is useful to clarify the notation that will be used in this section. The subscript '+' refers to a single, isolated cation (*e.g.* D_+ and M_+) and the subscript '-' refers to a single isolated anion (*e.g.* D_- and M_-). Additional subscripts will be introduced and detailed in subsequent sections to represent different entities. A distinction will be drawn between the 'true' diffusion coefficients of the single isolated ions, D_+ and D_-, and the diffusion coefficients directly obtained from PFG NMR measurements, D_{cat} and D_{an}. In the simple case of single isolated ions, the two sets of diffusion coefficients will be identical, that is, $D_{cat} = D_+$ and $D_{an} = D_-$. When discussing molar mass, M_+ and M_-

refer to the masses of single isolated ions; M_{IL} will be used to refer to the molar mass of a single IL formula unit *i.e.* one cation and one anion.

A final definition to clarify is that of the molar conductivity, Λ. The molar conductivity calculated from NMR measurements and the Nernst-Einstein equation was introduced in the previous section and defined as Λ_{NMR}. Dielectric spectroscopy can be used to obtain the conductivity, σ, more directly from complex impedance measurements. This can be converted into the molar conductivity, termed Λ_{imp} here. Assuming all ions are involved in the conduction process, the molar conductivity for pure ILs can be calculated by treating them as 100% concentrated electrolyte solutions as follows,

$$\Lambda_{imp} = \frac{\sigma}{c} = \frac{\sigma M_{IL}}{\rho} \tag{2.13}$$

where σ is conductivity from impedance measurements, c is the molar concentration, M_{IL} is the IL molar mass and ρ is the density of the IL.

Using the simple model of single isolated ions leads to a number of testable predictions. Equations 2.4 and 2.5 can be combined to relate diffusion and molar mass. Therefore, assuming the Stokes-Einstein equation holds, the ratio of the experimentally measured anion diffusion coefficient to cation diffusion coefficient can be expressed as follows,

$$\frac{D_{an}}{D_{cat}} = \left(\frac{M_+}{M_-}\right)^{\frac{1}{3}} \tag{2.14}$$

where M_+ and M_- are the molar masses of a single isolated cation and anion, respectively.

The Nernst-Einstein equation (Equation 2.10) can be simplified for the case of single isolated ions in a pure IL. The charge carriers are simply the single cation and anion. Both ions are singly charged, so $z_+ = z_- = 1$; there are also equal numbers of both ions directly participating in the conduction process, so $v_+ = v_- = 1$. Additionally, the experimentally measured diffusion values are identical to the ion diffusions, so $D_{cat} = D_+$ and $D_{an} = D_-$. This gives the

following for the molar conductivity from NMR measurements,

$$\Lambda_{NMR} = \frac{N_A e^2}{k_B T}(D_{cat} + D_{an}) \tag{2.15}$$

If this model is an accurate description of the IL system, Λ_{NMR} should be equal to Λ_{imp}.

The theory presented above is correct for a model of single isolated ions. However, there is significant experimental and theoretical evidence that this is not the case in the ILs studied here, which will be presented and discussed in later chapters. The following sections will explore several different simple models to represent the formation of ion pairs and charged aggregates.

2.3.2 Pair Model

Ionic liquids are distinct from ionic salts due to their relative lack of persistent ionic bonding and long-range crystal structure. However, it is not difficult to imagine a certain degree of ion pairing, where the anion and cation diffuse as a neutral bonded pair. This effect has been shown in the gas phase of ILs using distillation [33, 137, 138] and used to explain lower than expected conductivity in many ILs [139, 140].

The simplest representation of an IL system containing ion pairs consists of an equal number of single charged cations and anions, alongside a number of neutral, bonded ion pairs. The fraction of ions existing in neutral pairs is defined here as P, meaning there will be a fraction of $1 - P$ cations and $1 - P$ anions existing as isolated charged ions; a fraction of $P = 1$ means all the ions in the system exist as neutral pairs. This model is represented pictorially in Figure 2.2.

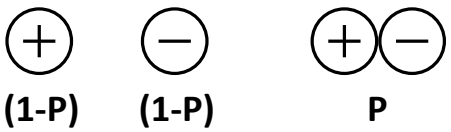

Figure 2.2: A simple representation of the ion pairing model, showing single charged ions and an ion pair. The relevant mole fractions are given below each configuration.

The presence of neutral ion pairs would decrease the conductivity of the IL system by reducing the number of charge carriers. The measured diffusion coefficients would also be affected, due to the presence of a larger diffusing entity. In the case of NMR-measured diffusion coefficients and assuming the fast exchange limit, the isolated ions and the ion pairs will be indistinguishable and measured D_{cat} and D_{an} will be averages across the whole system. This assumption has been repeated for ion pairing and aggregation in several publications [22, 139–141]. The measured coefficients will be a weighted average of the diffusion coefficients for the isolated ions and the diffusion coefficient of the ion pairs, D_p, which can be written as follows,

$$D_{an} = PD_p + (1 - P)D_- \tag{2.16}$$

$$D_{cat} = PD_p + (1 - P)D_+ \tag{2.17}$$

note that D_- and D_+ are now components of the measured diffusion coefficients and can not be measured directly, in contrast to the isolated ions model.

The effects of ion pairs on the ratio of D_{an} and D_{cat} can now be described. Using Equations 2.4 and 2.5, D values can be related to molar masses. Therefore, the diffusion coefficient ratio can be written as follows,

$$\frac{D_{an}}{D_{cat}} = \frac{PM_p^{-\frac{1}{3}} + (1 - P)M_-^{-\frac{1}{3}}}{PM_p^{-\frac{1}{3}} + (1 - P)M_+^{-\frac{1}{3}}} \tag{2.18}$$

where M_p is the molar mass of an ion pair, exactly equal to M_{IL} introduced earlier. It is worth evaluating the equations for D as P changes; a value of $P = 0$ (no pairs) recovers the relations for the case of isolated ions, and in the limit of only ion pairs ($P = 1$), $D_{an} = D_{cat} = D_p$ and therefore $D_{an}/D_{cat} = 1$. This is consistent with the expected phenomenological picture, where all the ions are diffusing in pairs at the same average rate of D_p.

The Nernst-Einstein can be evaluated for the pair model by considering Equations 2.10 and 2.11. Neutral ion pairs will not participate in conduction, effectively acting as an electrolytic solvent for the charged single ions (charge carriers) and 'diluting' the solution. Therefore, the stoichiometric numbers will become $v_+ = v_- = 1 - P$. Rearranging Equations 2.16 and 2.17 for D_+ and D_- gives a

factor of $(1-P)^{-1}$ in the Nernst-Einstein equation, cancelling with the factor of $1-P$ from the stoichiometric numbers, leaving the following,

$$\Lambda_{NMR} = \frac{N_A e^2}{k_B T}(D_{cat} + D_{an} - 2PD_p) \tag{2.19}$$

Once again, this expression can be evaluated for the two limiting cases of $P = 0$ and $P = 1$. No ion pairs ($P = 0$) gives Equation 2.15 from the isolated ions model. If $P = 1$, D_{an} and D_{cat} both become D_p and Λ_{NMR} becomes zero, as expected from a system comprised entirely of non-conducting ion pairs.

The 'dilution' of conducting ions by neutral pairs must also be accounted for in the calculation of Λ_{imp}. This can be done simply by reducing the molar concentration of ions by a factor of $1-P$, giving $c = \rho(1-P)/M_{IL}$. Substituting this into Equation 2.9 gives

$$\Lambda_{imp} = \frac{\sigma M_{IL}}{\rho(1-P)} \tag{2.20}$$

It is clear that Λ_{imp} behaves as expected in the limiting cases, with Equation 2.13 recovered for $P = 0$ and $\Lambda_{imp} = 0$ for $P = 1$. Equations 2.19 and 2.20 can be compared as a measure of how effectively this pair model approximates any given IL at any given value of P.

As a sidenote, it is worth mentioning potential calculation of D_p for Equations 2.18 and 2.19. Assuming fast exchange, single ions and ion pairs are indistinguishable in NMR measurements, meaning D_p can not be measured directly. Therefore, D_p must be estimated using the Stokes-Einstein equation (Equation 2.4) and Equation 2.5.

2.3.3 Charged Aggregate Model

Anion-rich Triplet Model

As well as ion pairs, some publications have proposed the formation of larger, charged aggregates [142–144]. A basic formation of charged aggregates is one consisting of a single, charged cation and a charged triplet containing two anions and one cation, such as those proposed by Hou et al. [145]. The formation of

these anion-rich triplets will have an effect on diffusion and conductivity in the system, in a similar manner to the ion pairs presented in the previous section.

The simplest model of these anion-rich triplets contains only single cations and triplets, that is, all the anions exist only as part of a triplet. This picture is shown in Figure 2.3.

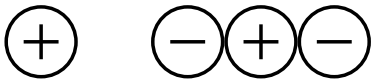

Figure 2.3: A representation of the ion triplet model, showing a single charged cation and an anion-rich triplet.

The measured diffusion coefficients will be averaged across the system, assuming single cations and cations in triplets are indistinguishable by NMR. D_{an} will simply be the diffusion coefficient of the triplet, whereas, D_{cat} will contain equally weighted components from single cations and the triplet. This can be written mathematically as

$$D_{an} = D_{tr} \tag{2.21}$$

$$D_{cat} = \frac{1}{2}D_{tr} + \frac{1}{2}D_{+} \tag{2.22}$$

where D_{tr} is the diffusion coefficient of the anion-rich triplet.

For the Nernst-Einstein equation (Equation 2.10), the charge carriers are now the single cation and the triplet, so $D_{pos} = D_{+}$ and $D_{neg} = D_{tr}$. The valences and stoichiometries are all equal to 1, as it is effectively only the size of the charge carriers that has changed, not the charge or relative concentrations. Therefore by rearranging Equations 2.21 and 2.22, the Nernst-Einstein equation for this triplet model can be written as,

$$\Lambda_{NMR} = \frac{N_A e^2}{k_B T}(2D_{cat}) \tag{2.23}$$

Note that D_{tr} has cancelled out in the evaluation of $D_{pos} + D_{neg}$ for this system.

In order to calculate Λ_{imp} the concentration, and therefore mass, of the charge-carrying 'pairs' needs to be considered. This mass will be termed the 'effective mass', or M_{eff}, here. As discussed above, the charge carriers are the single cation and the triplet, therefore, the mass of the charge-carrying pair is given

by $M_{eff} = 2M_+ + 2M_- = 2M_{IL}$. The molar conductivity is then given by the following,

$$\Lambda_{imp} = \frac{\sigma M_{eff}}{\rho} = \frac{2\sigma M_{IL}}{\rho} \tag{2.24}$$

Variable-size Charged Aggregates

The findings of Hou et al. suggested charged triplets in their system [145], however, they also considered the possibility of larger charged aggregates. This proposition was in agreement with a number of other publications that found experimental evidence for larger aggregates [20, 22, 143, 144, 146, 147]. The triplet model can be generalised and expanded to consider these larger aggregates. This more general charged aggregate model will be presented below.

A simplistic picture of only two charged entities will be used, as with the triplet model; the only positive charge carrier is the single cation and the only negative charge carrier is the charged, anion-rich aggregate. The parameter n will be used to represent the size of the aggregate, where n is the number of anions in the aggregate and $n-1$ gives the number of cations in the aggregate. This is shown pictorially in Figure 2.4.

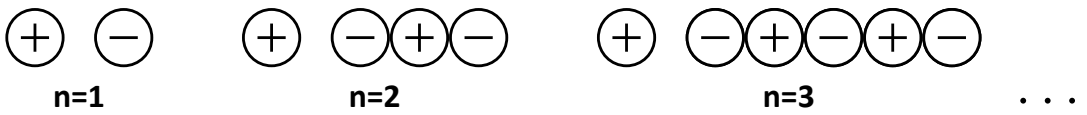

Figure 2.4: A representation of the charged aggregate model, showing different configurations of a single charged cation and a variable-size anion-rich aggregate. n defines the number of anions in the negatively-charged aggregate.

The measured diffusion coefficients can be related to the diffusion coefficients of the two charge carriers by considering weighted averages of the cation and anion. All anions will exist only in the aggregate, whereas the cations will exist as both a single cation and as part of the aggregate, depending on the size, n, of the aggregate. This can be written as follows,

$$D_{an} = D_{agg} \tag{2.25}$$

$$D_{cat} = \frac{n-1}{n} D_{agg} + \frac{1}{n} D_{+} \tag{2.26}$$

where D_{agg} is the diffusion coefficient of the anion-rich charged aggregate of size n. Equations 2.25 and 2.26 can then be rearranged to obtain the sum of the charge carriers in terms of the experimentally measure diffusion coefficients as follows,

$$D_{pos} + D_{neg} = D_{agg} + D_{+} = nD_{cat} - (n-2)D_{an} \tag{2.27}$$

This expression can then be substituted into the Nernst-Einstein equation (Equation 2.10) to give the following,

$$\Lambda_{NMR} = \frac{N_A e^2}{k_B T}(nD_{cat} - (n-2)D_{an}) \tag{2.28}$$

As with the triplet model, the valences and stoichiometries are all equal to 1. Equations 2.25, 2.26 and 2.28 can all be validated at this stage: setting n to 2 recovers the equivalent equations for the triplet model and setting n to 1 gives the isolated ions model.

The ratio of equations 2.25 and 2.26 gives the diffusion coefficient ratio in terms of D_{agg} and D_{+}. Using Equations 2.4 and 2.5 then gives the diffusion coefficient ratio in terms of molar masses as follows,

$$\frac{D_{an}}{D_{cat}} = \frac{nM_{agg}^{-\frac{1}{3}}}{M_{+}^{-\frac{1}{3}} + (n-1)M_{agg}^{-\frac{1}{3}}} \tag{2.29}$$

where M_{agg} is the molar mass of the charged aggregate, which can be calculated by $M_{agg} = nM_{-} + (n-1)M_{+}$.

The effective mass for this system is simply $M_{agg} + M_{+} = nM_{IL}$, that is, there are n cations and n anions in one conducting 'pair'. Using this to calculate Λ_{imp} gives the following,

$$\Lambda_{imp} = \frac{\sigma M_{eff}}{\rho} = \frac{n\sigma M_{IL}}{\rho} \tag{2.30}$$

It is clear here that $n = 2$ gives the triplet model and $n = 1$ gives the isolated ions model.

2.3.4 Combined Model

The two models presented in the previous sections, ion pair and charged aggregate, simulate the effects of ionic association using different entities but similar methods. Therefore, it is possible to combine the two models and simulate the formation of both neutral pairs and charged aggregates simultaneously.

This new, combined model consists of a single charged cation, an anion-rich charged aggregate and a neutral cation-anion pair. For simplicity, the negative charge carriers will be restricted to a single size of aggregate, defined by n, and the neutral entities will be restricted to pairs. For mathematical ease, the system will be parametrised differently to previous models but will remain directly relatable to the pair model and charged aggregate model. The system will be described in terms of the number of each species, where s describes the number of single cations, necessarily equal to the number of charged aggregates, and m describes the number of ion pairs. This picture is shown in Figure 2.5.

Figure 2.5: A representation of the combined model of ion pairs and charged aggregates, showing the different configurations of a single charged cation, a variable-size anion-rich aggregate and a neutral ion pair. n defines the number of anions in the negatively-charged aggregate, s is the number of single cations or charged aggregates in the system and m is the number of neutral ion pairs in the system.

A new parameter, R, will be defined to describe the ratio of charged entities to neutral entities, where $R = m/s$. For comparison, the fraction of pairs, P, can be related to m, s and R as follows,

$$P = \frac{m}{ns + m} = \frac{R}{n + R} \tag{2.31}$$

The derivations in this section will use R and n for mathematical clarity but it is possible to convert any equation into a function of P and n only.

By using the numbers of each species, it is possible to derive weighted sums for all cations and anions in the system. The number (s) and size (n) of the charged aggregates must be considered, as well as the number of pairs (m) and single cations (s); these sums can be converted into weighted fractions by dividing by the total number of cations or anions in the system. These fractions can then give expressions for the measured diffusion coefficients as follows,

$$D_{an} = \frac{nsD_{agg} + mD_p}{ns + m} \tag{2.32}$$

$$D_{cat} = \frac{sD_+ + s(n-1)D_{agg} + mD_p}{s + s(n-1) + m} \tag{2.33}$$

Dividing Equations 2.32 and 2.33 by s/s returns expressions that depend only on R and n,

$$D_{an} = \frac{nD_{agg} + RD_p}{n + R} \tag{2.34}$$

$$D_{cat} = \frac{D_+ + (n-1)D_{agg} + RD_p}{n + R} \tag{2.35}$$

Taking the ratio of Equations 2.34 and 2.35 and then converting diffusion coefficients into molar masses using Equations 2.4 and 2.5 gives the following expression for the diffusion coefficient ratio,

$$\frac{D_{an}}{D_{cat}} = \frac{nM_{agg}^{-\frac{1}{3}} + RM_p^{-\frac{1}{3}}}{M_+^{-\frac{1}{3}} + (n-1)M_{agg}^{-\frac{1}{3}} + RM_p^{-\frac{1}{3}}} \tag{2.36}$$

This provides the first of three measurable quantities that allow the model to be tested for different values of n and R.

Equation 2.34 can be rearranged in terms of D_{agg} and Equation 2.35 can be rearranged in terms of D_+ to give the following,

$$D_{agg} = \frac{(n+R)D_{an} - RD_p}{n} \tag{2.37}$$

$$D_+ = (n+R)D_{cat} - (n-1)D_{agg} - RD_p \tag{2.38}$$

Taking the sum of D_+ and D_{agg} and substituting Equations 2.38 and 2.37

gives the following,

$$\begin{aligned} D_{pos} + D_{neg} &= D_+ + D_{agg} \\ &= (n+R)D_{cat} - (n-2)D_{agg} - RD_p \\ &= (n+R)\left(D_{cat} + \left(\frac{2}{n} - 1\right)D_{an} - \frac{2RD_p}{n(n+R)}\right) \end{aligned} \tag{2.39}$$

The presence of pairs means the charge carriers will be 'diluted' by the neutral pairs, affecting v_+ and v_-. The valences still remain equal to 1. Therefore, the stoichiometric numbers will be equal for both charge carriers ($v_+ = v_-$) and can be calculated by considering either charge carrier and finding the fractional number of charge carriers. For the positive charge carrier,

$$v_+ = \frac{s}{s+m} = \frac{1}{1+R} \tag{2.40}$$

as before, the initial equation was divided by s/s to obtain an expression in terms of R.

Taking Equations 2.39 and 2.40 and substituting them into the Nernst-Einstein equation (Equation 2.10) gives the following,

$$\Lambda_{NMR} = \frac{N_A e^2 (n+R)}{k_B T (1+R)} \left(D_{cat} + \left(\frac{2}{n} - 1\right)D_{an} - \frac{2RD_p}{n(n+R)}\right) \tag{2.41}$$

note that D_p must be estimated from the molar mass of the ion pair, as detailed in the ion pair model section.

The numbers s and m are defined for a cation-aggregate-pair system of arbitrary size. The total molar mass of this system, defined as M_{tot} here, is the mass of one mole of: s single cations, s charged aggregates (of size n) and m ion pairs, and can be calculated as follows,

$$\begin{aligned} M_{tot} &= sM_+ + s\left(nM_- + (n-1)M_+\right) + mM_p \\ &= sn(M_- + M_+) + mM_p \\ &= M_{IL}(sn+m) \end{aligned} \tag{2.42}$$

where M_p and M_{IL} are used interchangeably. In order to find M_{eff}, the arbitrarily-sized system of molar mass M_{tot} must be rescaled for a system of one positive

charge carrier and one negative charge carrier. This is done by dividing Equation 2.42 by s to give the following,

$$M_{eff} = M_{IL}(n + R) \tag{2.43}$$

The molar conductivity from impedance can now be calculated using Equation 2.43,

$$\Lambda_{imp} = \frac{\sigma M_{eff}}{\rho} = \frac{(n + R)\sigma M_{IL}}{\rho} \tag{2.44}$$

Equations 2.32 through 2.44 can be evaluated for several limiting cases: *i*) the isolated ions model can be recovered by setting $n = 1$ and $R = 0$, *ii*) the ion pair model can be recovered by setting $n = 1$ and using Equation 2.31, *iii*) the charged aggregate model can be recovered by setting $R = 0$, *iv*) the expected results are obtained in the limiting cases of all ions pairing or aggregating (R and n become infinitely large).

In case *iv*), as n tends towards infinity, D_{an} and D_{cat} will tend towards the same value of D_{agg}; as R tends towards infinity, D_{an} and D_{cat} will tend towards the same value of D_p; as either n or R tends towards infinity, σ will tend towards zero. As a consequence, D_{an}/D_{cat} should tend towards 1 and Λ should tend towards zero. This behaviour is accurately modelled by the equations presented above, indicating this combined model is theoretically consistent with the previous models. Appendix C contains the key equations for each model, as a quick reference.

2.3.5 Motivation

The primary motivation for the models presented above is to address a number of discrepancies between experimental data and theoretical expectations, in a number of ILs. By varying P and n, the effects of pairing and aggregation can be simulated. Specifically, there are three criteria that can be modelled and compared: *i*) a theoretical value for D_{an}/D_{cat} can be obtained, to directly compare with experimental data *ii*) values of Λ_{imp} and Λ_{NMR} can be obtained and compared to each other, as theoretically, Λ_{imp} and Λ_{NMR} should be equal *iii*) Λ_{imp}

can be compared to the viscosity using the Walden rule (Equation 2.12) for an ideal electrolytic solution.

An accurate model of ionic pairing and aggregation should provide useful information about IL structure in itself. By modelling and comparing the type and amount of aggregation in different ILs, further understanding can be gained into the similarities between different groups and classes of ILs.

Chapter 3

Investigation of the Microstructure in Imidazolium-based Ionic Liquids

3.1 Introduction

Ionic liquids can be designed and utilised for a wide range of applications, with an equally wide range of properties. However, when tailoring any IL for a specific application, an in-depth understanding of the IL structure and properties is required. Knowledge of bulk properties, such as rheology, density or conductivity, is key for large-scale use. Additionally, understanding the microscopic properties of these ILs can assist in the optimisation of any process and may be vital in more complex applications, such as catalysis or fractionation.

This chapter will investigate a series of four imidazolium-based ILs in their pure form. The modelling approaches detailing in Section 2.3 will be applied to these ILs, in order to test this new approach and gain new insight into their microscopic structure. First, a literature review will be presented, exploring imidazolium-based ILs. Next, NMR, rheology, conductivity and density data will be presented and analysed. Finally, the models will be applied to several datasets for all four ILs. The effectiveness of the models will be assessed and notable findings will be discussed in the context of literature studies.

3.1.1 Imidazolium-carboxylate Ionic Liquids

In carbohydrate dissolution, a commonly used class of ILs are those based on the imidazolium cation, combined with a wide range of different anions [47]. The imidazolium cation consists of an aromatic ring with one or more aliphatic side-groups. 1-alkyl-3-methylimidazolium ($[C_nMIM]^+$) is most commonly used, where n is the number of carbon atoms in the side-chain and can be varied relatively easily. These cations are paired with a variety of anions including halides [47], $[BF_4]^-$ or $[PF_6]^-$ [47], dimethylphosphates and carboxylates [52, 62] as just a few examples. Aliphatic carboxylate anions have found widespread use, particularly for the dissolution of cellulose [59–62, 101, 148, 149] and other biomolecules [111, 112, 150]. The length of the carbon chain in these anions can also be varied. This means that ILs formed from $[C_nMIM]^+$ cations and carboxylate anions have two different carbon chains that can be varied in length, allowing the hydrophobicity of each ion to be fine-tuned. This will affect how the ions interact in the bulk IL, as well as potentially changing interactions with a solute or co-solvent.

3.1.2 Effects of Modifying Side-chain Lengths

For the most part, previous studies on pure ILs have focused on systematically changing the side-chain length on the cation, most commonly with the aforementioned imidazolium cations [24, 47, 151, 152]. Huddleston et al. conducted a systematic study of ILs containing $[C_nMIM]^+$ cations and a range of anions, in order to assess the impact of changing the cation chain length [21]. Comparisons were made for alkyl side-chain lengths between methyl ($n = 1$) to octyl ($n = 8$). It was found that, for the same anion, increasing the chain length increased the viscosity uniformly, decreased the melting point and decreased the density. They also measured the water miscibility as the cation side-chain length was increased, as a measure of hydrophobicity; it was found that as the chain length increased, the water miscibility decreased. Fendt et al. measured viscosity for a series of $[C_nMIM]$ chloride ILs, finding a similar trend as Huddleston et al. where the viscosity increased uniformly as n increased [153].

In comparison, there have been relatively few investigations of any kind on the influence of the anion chain length. A number of papers have focused on changing the size and structure of carboxylate anions in the context of cellulose dissolution [52, 56, 58, 154]. The Kilpeläinen group investigated a range of ILs with protic cations and various carboxylate anions, first for distillation potential [56] and then for viscosity and other physicochemical properties [58]. It was found that, for all studied cations, the propionate anion gave an IL with a lower viscosity than that of the equivalent acetate-based IL. Xu et al. investigated a range of carboxylate-anion chain lengths in ILs containing the $[C_4MIM]^+$ cation [155]. They found that $[C_4MIM]$ propionate was the most effective at dissolving cellulose.

3.1.3 Microscopic Structure of Imidazolium-carboxylate Ionic Liquids

It is well known that ILs form pairs, clusters and even larger microstructures in the bulk liquid [20, 22, 24, 27–29, 139, 143]. These phemonena have been attributed to various unexpected properties of ILs, such as high viscosity [27], anomalous diffusion [145] and lower than expected conductivity [139].

Simulations by Canongia Lopes and Pádua showed the formation of non-polar domains in $[C_nMIM]$-based ILs for $n \geq 4$ [27]. It was found that the longer the side-chain, the larger the size of the non-polar domains, with the highest values of $n = 12$ tending towards microphase separation between polar head groups and hydrophobic side-chains in the bulk IL. Wang and Voth used a coarse-graining computational method to investigate $[C_nMIM][NO_3]$ ILs and how the cation side-chain length affects the microscopic structuring [28, 156]. They found that for ILs with $n \geq 3$, the hydrophobic tail groups aggregated to form distinct domains, subject to the positioning of the charged head groups by Coulomb interactions with anions. These simulated hydrophobic domains were stable, even up to 1200 K, and would diffuse through the medium without losing their ordering. Longer chains had more hydrophobic interactions and therefore exhibited a higher degree of ordering. Experimental work by Zhao et al. hinted at a similar picture, showing the formation of IL-micelles in aqueous solutions

[157]. [C_nMIM][Br] ILs were dissolved in D_2O at a range of concentrations. It was found that for $n \geq 6$, the ILs self-assembled into micelles with a stair-like stacking structure, where polar groups stack together, away from hydrophobic tail groups. This is in agreement with other studies on self-aggregation of aqueous, imidazolium-based ILs [158, 159].

While there is a significant evidence-base for IL aggregation from simulations, there is relatively little work on relating experimental data directly to aggregation or pairing. As well as this, the effects of changing anion size has also received relatively little attention. Understanding more about IL aggregation and how it is affected by the anion size is vital to designing these types of ILs to work in specific systems or possess specific properties.

3.1.4 Investigating Microscopic Structure and Aggregation in Imidazolium-based ILs

[C_2MIM][Ac] is a commonly used and studied IL, due to a low melting point (well below room temperature) and moderate viscosity. Therefore in this chapter, the $[C_2MIM]^+$ cation was chosen as a representative cation to use, while the anion is varied. Aliphatic carboxylates were judged to be a good class of anion, as they are relatively easy to vary in length, providing a tunable degree of both hydrophobicity and size. Odd-even cation chain length effects have been observed for various properties of imidazolium-based ILs [160–163]. Therefore a series of four even-length anions were chosen to eliminate any potential odd-even effects in this study. [C_2MIM][Ac], [C_2MIM][But], [C_2MIM][Oct] and [C_2MIM][Ddc] were chosen to give a good range of properties and will be investigated in this chapter. These four ILs are shown in Figure 3.1.

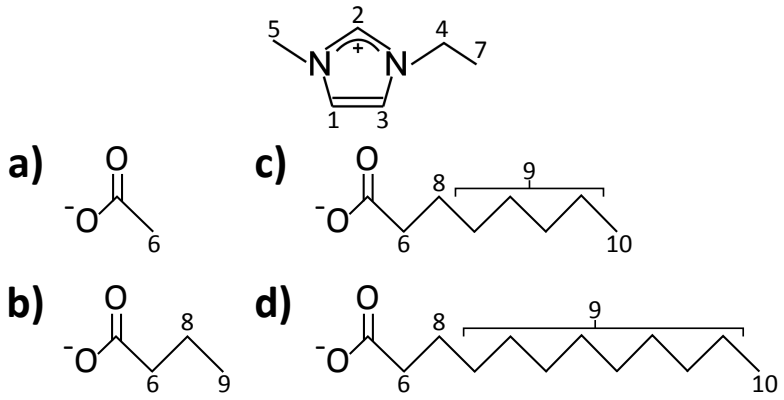

Figure 3.1: The 1-ethyl-3-methylimidazolium cation and the four carboxylate anions in the ionic liquids investigated in this study: **a)** [C_2MIM][Ac] **b)** [C_2MIM][But] **c)** [C_2MIM][Oct] and **d)** [C_2MIM][Ddc]. ^{1}H NMR resonances are labelled for each cation-anion pair.

3.2 Method

3.2.1 Materials and Sample Preparation

[C_2MIM][Ac] was obtained from Sigma Aldrich with a purity of $> 97\%$ for NMR measurements. [C_2MIM][But], [C_2MIM][Oct] and [C_2MIM][Ddc] were purchased from IoLiTec GmbH, Germany, with an advertised purity of $> 95\%$. [C_2MIM][Ac] and [C_2MIM][Oct] were used as received. However, the purchased samples of [C_2MIM][But] and [C_2MIM][Ddc] were found by NMR to contain methanol impurities of up to 8%. Therefore, [C_2MIM][But] and [C_2MIM][Ddc] samples were dried before use in a vacuum oven at 60 °C for 24 - 72 hours, until the methanol content was $< 2.5\%$ in all cases. All ILs used for NMR, conductivity and density measurements were stored in a dry nitrogen atmosphere with no exposure to atmospheric humidity.

3.2.2 NMR Method

Self-diffusion coefficients and low-field relaxation times were measured using the equipment and pulse sequences detailed in Section 2.1.2. Diffusion coefficients for

each ion were averaged over the relevant peaks for the imidazolium cation (peaks 1-5, 7) and the carboxylate anions (6, 8-10) based on the spectral assignment of each peak, as shown in Figure 3.1. ^{1}H spectra for all four ILs are shown in Appendix Figures A.1 to A.4.

3.2.3 Viscosity, Conductivity and Density Method

Viscosity, conductivity and density were measured for all four ILs according to the equipment and methods detailed in Sections 2.1.3, 2.1.4 and 2.1.5, respectively. [C_2MIM][Ac] viscosity data was obtained, with permission, from a previous publication [84].

3.3 Results

3.3.1 Diffusion

Figure 3.2 shows the temperature variation of the self-diffusion coefficients, D, of the [C_2MIM]$^+$ cation for all four ILs. In all cases, the diffusion coefficient increases as temperature increases, as expected. The data are consistent with previously reported diffusion coefficients for [C_2MIM][Ac] [35, 61, 148]. Generally, as the anion chain length, l, increases from [C_2MIM][Ac] ($l = 2$) to [C_2MIM][Ddc] ($l = 12$), the diffusion coefficient decreases. However, the D values for [C_2MIM][Ddc] appear to be similar to, or even higher, than those of [C_2MIM][Oct]; this is unexpected, based on molecular weight arguments. The reason for this discrepancy is likely the reliability of the [C_2MIM][Ddc] data. [C_2MIM][Ddc] is a very high viscosity fluid when dried of the excess methanol and high-field T_2 values were very low, around 20 ms even at 60 °C. These two factors combined to give a high degree of chemical shift broadening in the dried sample. The broadening was significant enough to give higher uncertainties in the D coefficients. As well as this, any remaining presence of methanol will increase D through a decreased viscosity, as well as disrupting any structures formed in a viscous phase and further increasing D. Therefore, it is likely that the values of D for [C_2MIM][Ddc] shown in Figure 3.2 have been overestimated.

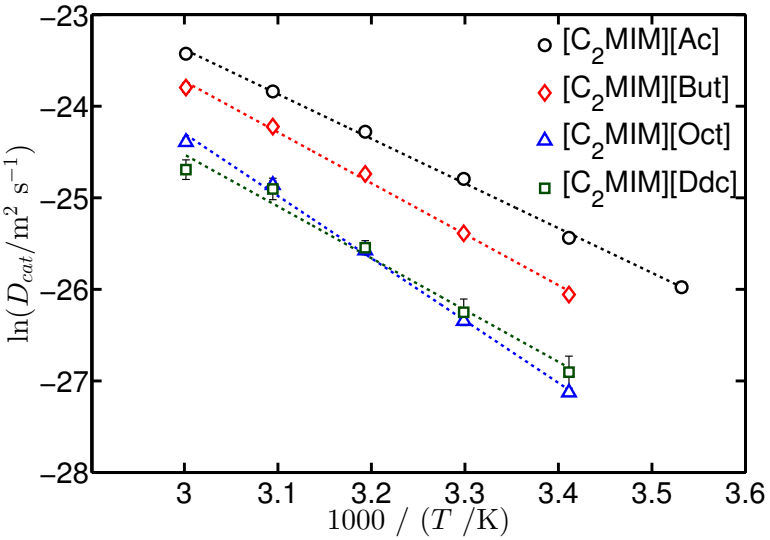

Figure 3.2: Arrhenius plot for self-diffusion coefficients of the imidazolium cation in $[C_2MIM][Ac]$, $[C_2MIM][But]$, $[C_2MIM][Oct]$ and $[C_2MIM][Ddc]$. Plots are only shown for the $[C_2MIM]^+$ cation, as plots for the carboxylate anion show very similar values. Straight lines show fits based on Equation 3.1. Error bars are approximately the size of the data points for the first three ILs.

Figure 3.3 shows the ratio of anion diffusion coefficient to cation diffusion coefficient for all four ILs, calculated partly from the data shown in Figure 3.2. All the D_{an}/D_{cat} values are below 1 and there are two slightly different temperature trends shown by the ILs (Figure 3.3c); the diffusion ratios broadly increase with increasing temperature for $[C_2MIM][Ac]$ and $[C_2MIM][But]$, but slightly decrease with increasing temperature for $[C_2MIM][Oct]$ and $[C_2MIM][Ddc]$. Figure 3.3b shows the diffusion ratio as a function of anion chain length. As expected, D_{an}/D_{cat} decreases as the anion size increases. The expected ratio is also shown in Figure 3.3b, this was calculated using molecular weights of the ILs and Equation 2.5.

In all cases, the measured D_{an}/D_{cat} is lower than the expected value, indicating that the cation is diffusing faster than expected, relative to the anion (or the anion is diffusing relatively slower than expected). It is worth noting that the term "anomalous diffusion" is often used in IL literature, referring to the case when the geometrically larger cation diffuses slower than the geometrically smaller anion, giving $D_{an}/D_{cat} < 1$ [164]. Assuming geomet-

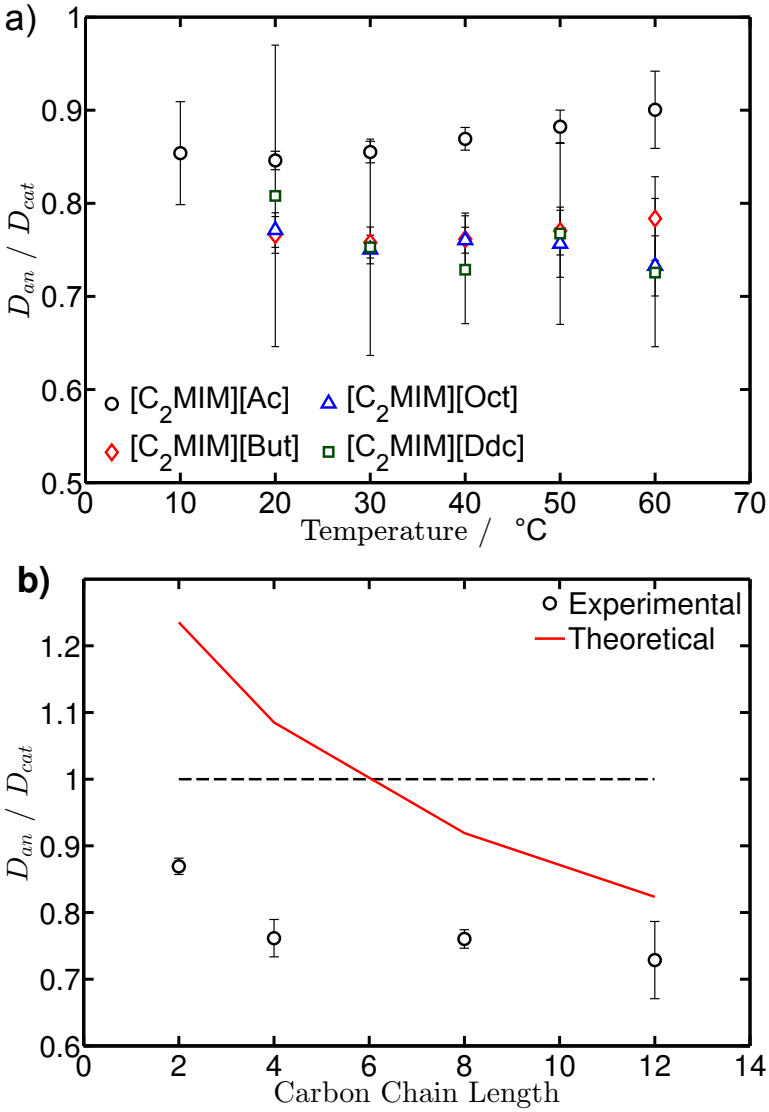

Figure 3.3: Ratio of anion diffusion coefficient to cation diffusion coefficient for the four ILs studied. **a)** Diffusion ratio as a function of temperature. **b)** Diffusion ratio as a function of chain length, n, at a temperature of 40 °C. Points show experimental values, coloured solid line shows expected diffusion ratios calculated from Equation 2.5. Dashed line shows a ratio of 1, *i.e.* when the cation and anion diffuse at the same rate.

ric size is roughly proportional to the cube root of the molecular weight, then [C_2MIM][Ac] and [C_2MIM][But] exhibit "anomalous" diffusion, whereas the diffusion in [C_2MIM][Oct] and [C_2MIM][Ddc] is technically not "anomalous", as the

expected D_{an}/D_{cat} is already below 1. However, the observed behaviour is the same for all ILs, regardless of whether it would be considered "anomalous" behaviour or not, *i.e.* D_{an}/D_{cat} data are significantly lower than expected for all four ILs (below the red line in Figure 3.3b). This behaviour has been attributed to various factors, including ion geometry, anisotropic local structuring [164] and aggregation between ions [145].

Activation energies provide important insight into transport properties. An activation energy of diffusion, $E_{a,D}$, can be calculated using the following Arrhenius-type equation,

$$\ln D = \ln D_0 - \frac{E_{a,D}}{RT} \tag{3.1}$$

where D_0 is the diffusion coefficient at infinite temperature and R is the universal gas constant. Figure 3.2 shows Arrhenius plots for diffusion data of all four ILs. All four ILs show a linear trend within the temperature range studied, therefore an Arrhenius approach is valid for these systems and a more complex VTF (Vogel-Tamman-Fulcher) fitting is not required. The activation energies obtained from the Arrhenius plots are given in Figure 3.4 for both cation and anion.

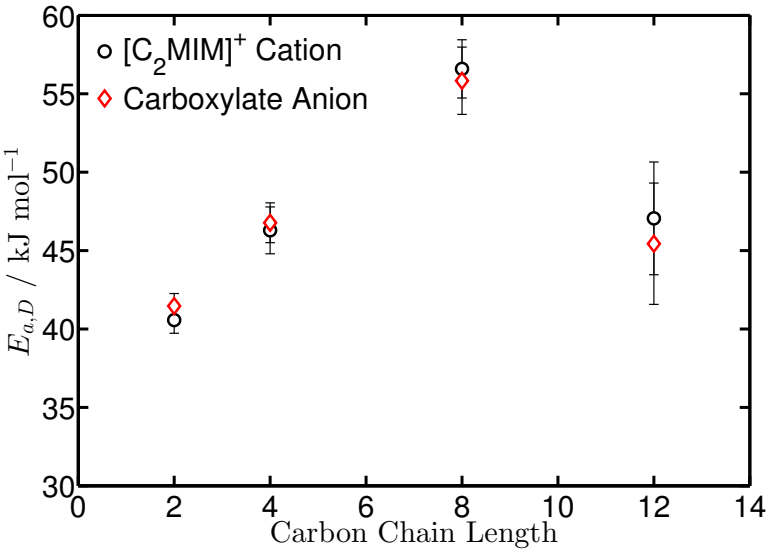

Figure 3.4: Diffusion activation energy as a function of anion chain length for $[C_2MIM][Ac]$, $[C_2MIM][But]$, $[C_2MIM][Oct]$ and $[C_2MIM][Ddc]$, calculated from the plots shown in Figure 3.2. Activation energies are given for both cation diffusion data and anion diffusion data.

For all four ILs, $E_{a,D}$ values for the cation are close, or identical, to $E_{a,D}$ for the anion, within experimental error. Unlike the D values, the activation energies do not quite follow a simple increasing/decreasing trend with anion chain length. Activation energy shows an increase from $[C_2MIM][Ac]$ to a peak at $[C_2MIM][Oct]$, then decreasing again for $[C_2MIM][Ddc]$. This is as expected for the first three ILs, as increasing size/weight will require more energy to diffuse. However, the lower-than-expected value of $E_{a,D}$ for $[C_2MIM][Ddc]$ suggests there are additional, more complex factors affecting the activation energies.

3.3.2 NMR Relaxometry

Low-field Relaxometry

Figure 3.5 shows NMR relaxation data for all four ILs, measured at 20 MHz. In all cases above about 20 °C, T_1 and T_2 both increase as temperature increases. This indicates the ILs are in the 'liquid-like' relaxation regime at these temperatures. However for low temperature data (below ≈10 °C), T_1 decreases as temperature increases, indicating the relaxation has transitioned to the 'solid-like' regime at low temperatures. Returning to the 'liquid-like' regime, T_1 is very close to T_2 for $[C_2MIM][Ac]$ and $[C_2MIM][But]$ (Figures 3.5a and 3.5b), but there is a significant difference between T_1 and T_2 for $[C_2MIM][Oct]$ and $[C_2MIM][Ddc]$ (Figures 3.5c and 3.5d), this will be discussed in more detail below.

The experimental data was fitted using BPP theory (Equations 2.1 and 2.2), where the correlation time, τ, was modelled using an Arrhenius-type equation as follows,

$$\ln\tau = \ln\tau_0 + \frac{E_{a,\tau}}{RT} \tag{3.2}$$

where τ_0 is the correlation time at infinite temperature and $E_{a,\tau}$ is the activation energy for molecular rotation. Note that $E_{a.\tau}$ is a fitting parameter here, not an experimentally-derived quantity. Fitting parameters are given in Table 3.1. The A values (Equation 2.3) correspond to inter-proton distances between 2.1 and 2.2 Å, a reasonable size for the average distance across the system. The values of τ, shown in Table 3.1 for 40 °C, are also reasonable for ionic liquid systems [59, 128, 132].

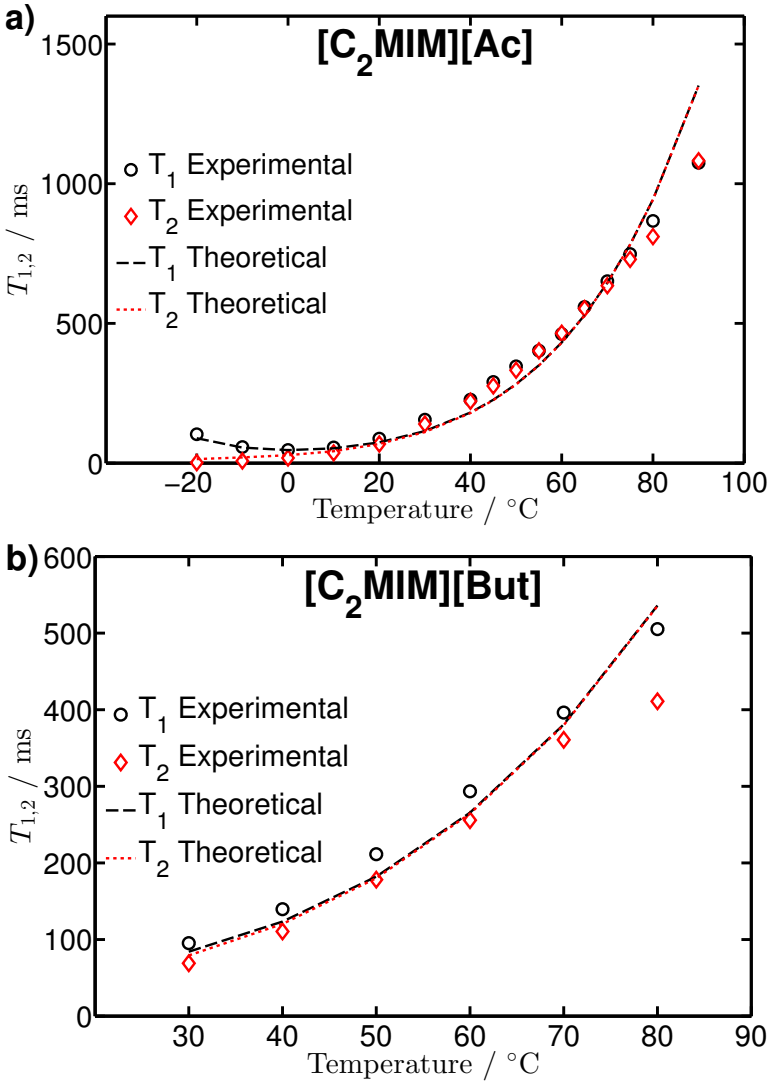
a)
[C2MIM][Ac]
T1 Experimental
T2 Experimental
T1 Theoretical
T2 Theoretical
T1,2 / ms
Temperature / °C
b)
[C2MIM][But]
T1 Experimental
T2 Experimental
T1 Theoretical
T2 Theoretical
T1,2 / ms
Temperature / °C

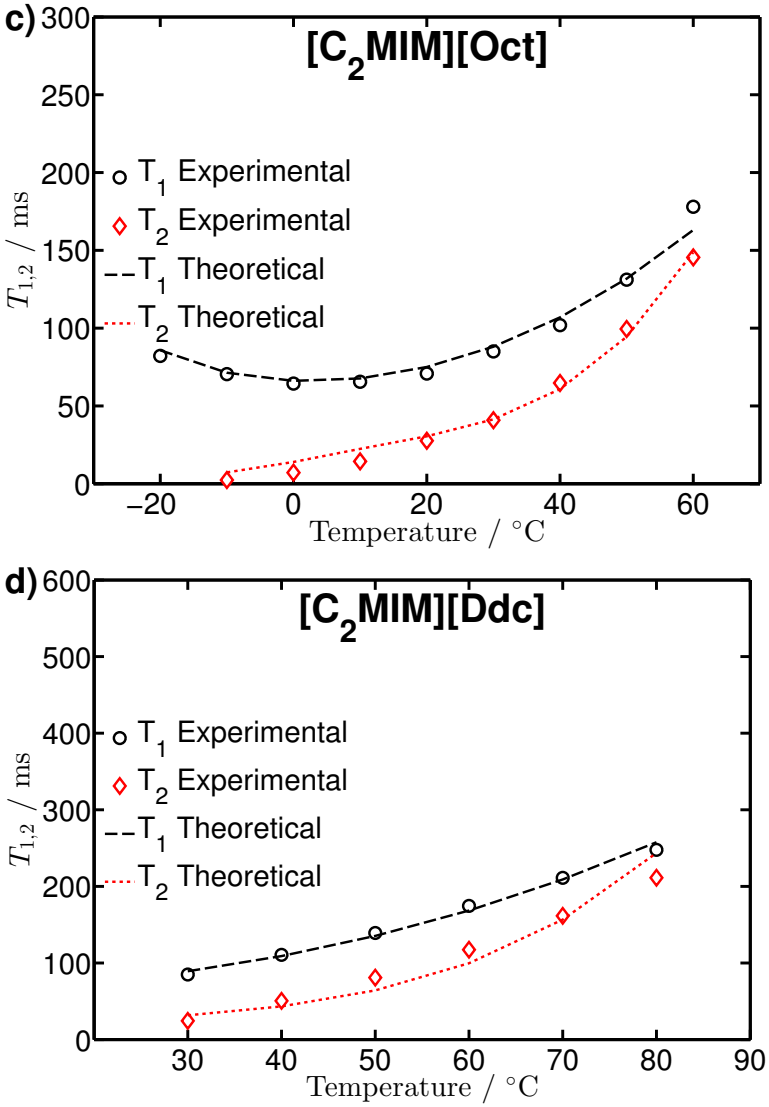

Figure 3.5: T_1 and T_2 relaxation at 20 MHz as a function of temperature for **a)** [C_2MIM][Ac], **b)** [C_2MIM][But], **c)** [C_2MIM][Oct] and **d)** [C_2MIM][Ddc]. Points show experimentally measured T_1 and T_2, dashed lines show fits obtained from Equations 2.1 and 2.2. Fitting parameters are given in Table 3.1.

	A / 10^8 s^{-2}	$E_{a,\tau}$ / kJ mol^{-1}	τ_0 / s	τ / 10^{-10} s (at 40 °C)
[C_2MIM][Ac]	9.50	38.4	2.37×10^{-16}	5.92
[C_2MIM][But]	9.49	38.4	2.37×10^{-16}	8.90
[C_2MIM][Oct] T_1	6.69	21.6	3.94×10^{-13}	15.8
[C_2MIM][Oct] T_2	6.69	43.5	1.56×10^{-16}	28.0
[C_2MIM][Ddc] T_1	6.70	22.0	3.22×10^{-13}	15.4
[C_2MIM][Ddc] T_2	6.70	45.6	1.12×10^{-16}	44.9

Table 3.1: Fitting parameters for low-field relaxation data shown in Figure 3.5, based on Equations 2.1 and 2.2. Single fits were obtainable for both T_1 and T_2 of [C_2MIM][Ac] and [C_2MIM][But], whereas, [C_2MIM][Oct] and [C_2MIM][Ddc] required separate fits for T_1 and T_2.

It can be seen from Figure 3.5 that the fits for T_1 data and T_2 data are very similar to each other in both [C_2MIM][Ac] and [C_2MIM][But], which is reflected well by the experimental data. In contrast, there is a noticeable difference between the experimental T_1 and T_2 values for both [C_2MIM][Oct] and [C_2MIM][Ddc]. In fact, T_1 and T_2 required separate fitting procedures for these two ILs. Unlike T_1, T_2 is sensitive to the frequency-independent 'zero frequency' dynamics of a system, shown in the 3τ term in Equation 2.2. This means that T_2 will be affected by slow dynamical motions, as compared to the timescale set by the $1/(20$ MHz) used here [123]. The influence of these motions will cause a discrepancy between T_1 and T_2, as shown in Figure 3.5c and 3.5d. Therefore, it is clear that there is a significant degree of slower motion in [C_2MIM][Oct] and [C_2MIM][Ddc]; this type of motion could be due to the slower gyration of the extended anion carbon chain in these two ILs. It is also consistent with larger scale aggregation and the formation of hydrophobic domains. The two different relaxation behaviours, one exhibited by [C_2MIM][Ac] and [C_2MIM][But], the other by [C_2MIM][Oct] and [C_2MIM][Ddc], will be investigated further below.

High-field Relaxometry

Figure 3.6 shows high-field T_1 data for [C_2MIM][Ac] and [C_2MIM][Oct], as a function of temperature. These two ILs were chosen to be representative of the two distinct relaxation behaviours shown by low-field T_1 measurements. Based on

BPP theory (Equations 2.1 and 2.2), the high-field data for $[C_2MIM][Ac]$ matches well with the low-field data shown in Figure 3.5; taking a representative low-field (20 MHz) τ value of 1×10^{-9} s with a new field strength of 400 MHz gives a T_1 value of 1.8 s, using Equation 2.1. This is similar in magnitude to the data presented in Figure 3.6.

There are some minor features that can be seen in the T_1 data in Figure 3.6, namely the correlation between temperature dependences of specific peaks and the dynamical mobility of the associated proton. However, the most striking feature is the difference in behaviour between $[C_2MIM][Ac]$ and $[C_2MIM][Oct]$: $[C_2MIM][Oct]$ exhibits a convergence of T_1 for all 10 resonances towards a single value at low temperatures. In contrast, $[C_2MIM][Ac]$ behaves roughly as predicted by BPP theory. This indicates that there is a single, shared T_1 value across the whole system in $[C_2MIM][Oct]$ at low temperatures. This is consistent with spin-diffusion and shared relaxation times, due to a relatively large and long-lived aggregation involving both the cation and the anion in $[C_2MIM][Oct]$ [165].

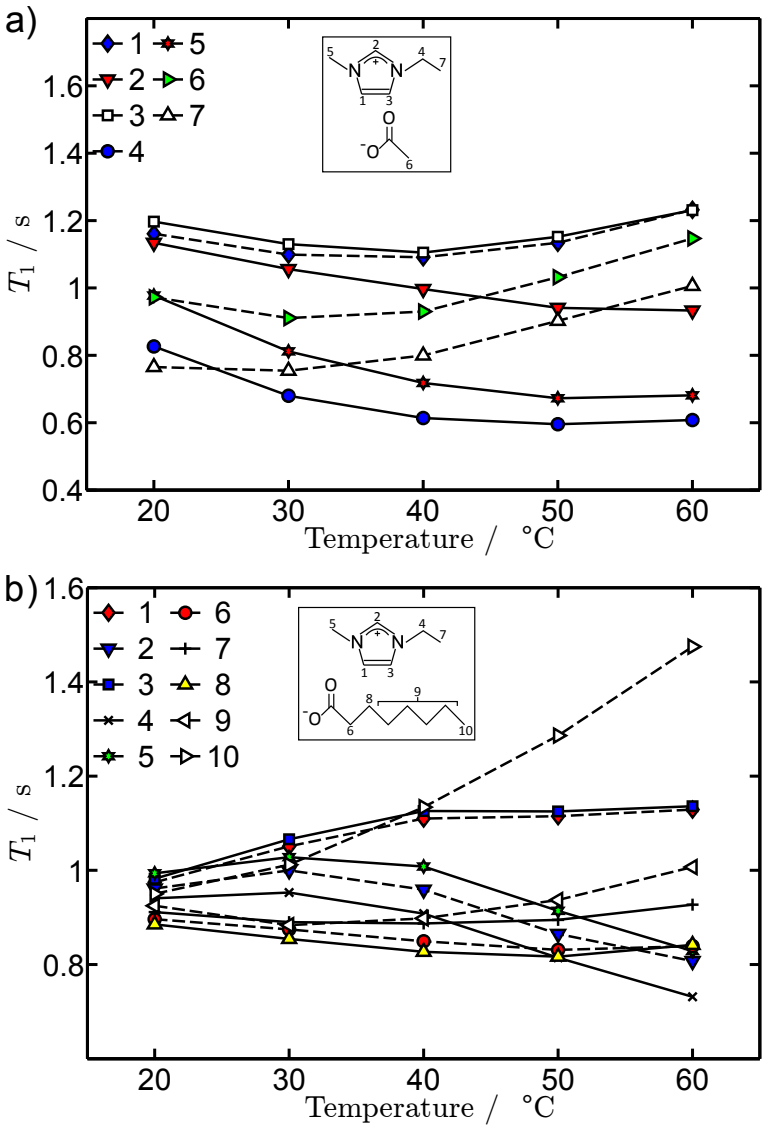

Figure 3.6: T_1 relaxation at 400 MHz as a function of temperature for **a)** [C_2MIM][Ac] and **b)** [C_2MIM][Oct]. Series number corresponds to labelling shown in Figure 3.1. Uncertainties of 5% are approximately the size of the data points and were omitted for clarity. Lines are given to guide the eye.

3.3.3 Viscosity

Figure 3.7 shows the Newtonian viscosity, η, for all four ILs as a function of temperature and chain length.

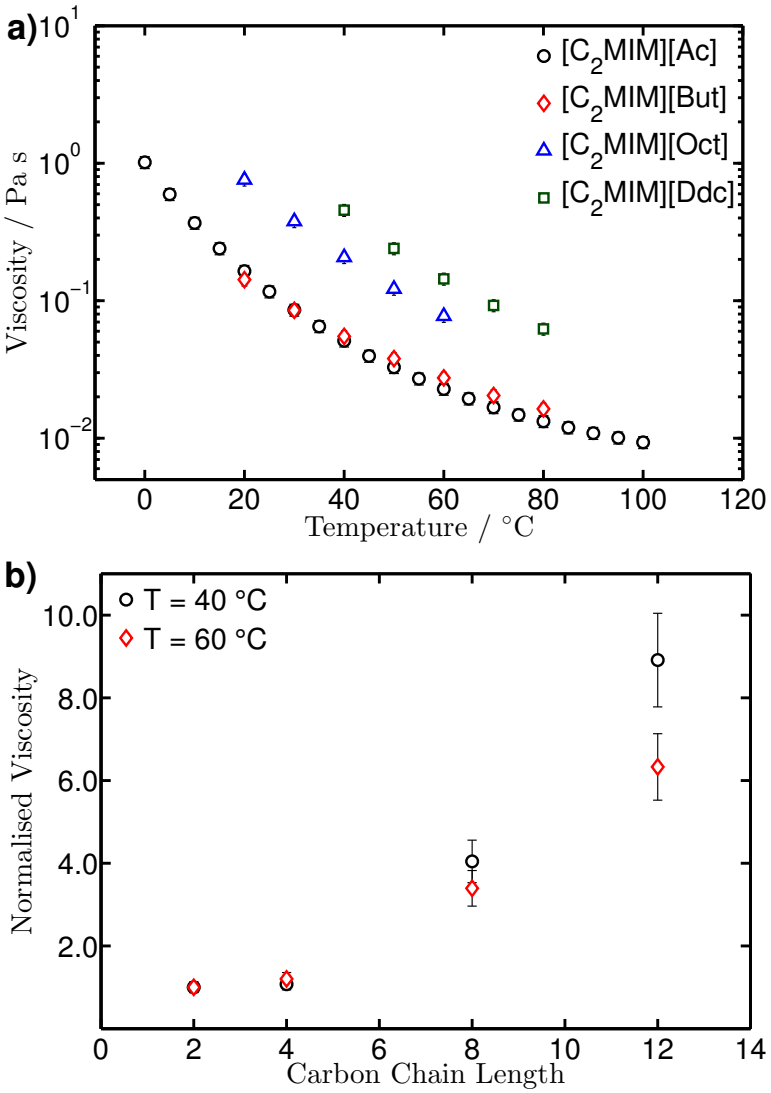

Figure 3.7: Newtonian viscosity data for $[C_2MIM][Ac]$ [84], $[C_2MIM][But]$, $[C_2MIM][Oct]$ and $[C_2MIM][Ddc]$. Plots show **a)** viscosity as a function of temperature for all four ILs and **b)** fractional viscosity as a function of anion chain length for two set temperatures, normalised to the viscosity of $[C_2MIM][Ac]$ for each temperature.

Figure 3.7a shows η to decrease as temperature increases, as expected. Data

for [C_2MIM][Ddc] begin at 40 °C due to the formation of some kind of gel-like phase below this temperature; flow curves were obtained at these temperatures but exhibited non-Newtonian behaviour through the whole shear rate range. The 'gel' phase 'melted' between 30 and 40 °C, giving a Newtonian liquid similar to the other 3 ILs. Figure 3.7b shows the ratio $\eta(l)$ / $\eta(2)$, that is, the viscosity of each IL compared to the viscosity of [C_2MIM][Ac]. It indicates that η generally increases as the anion chain length increases, in agreement with the diffusion data. However unlike with diffusion, [C_2MIM][Ac] and [C_2MIM][But] exhibit very similar viscosities at all temperatures, highlighting a discrepancy between macroscopic and microscopic behaviour in these ILs.

Viscosity is expected to increase as the molecular weight (and therefore size) of the IL increases. However, compared to [C_2MIM][Ac], the molecular weights of [C_2MIM][Oct] and [C_2MIM][Ddc] are 1.5 and 1.8 times larger respectively, whereas the viscosities are $\approx$ 4 and 7 times larger. This suggests there is something more complex occurring in the longer-chain anions, such as more elaborate aggregation and structuring. This is further supported by Figure 3.7b, which shows the effect to be more pronounced at lower temperatures; suggesting larger aggregates and domains that shrink and break up at higher temperatures.

3.3.4 Conductivity

Figure 3.8 shows the molar conductivity, Λ_{imp}, for all four ILs as a function of temperature and anion chain length. The [C_2MIM][Ac] data are consistent with previously reported data, exhibiting a similar but systematically lower conductivity than that of 90% purity [C_2MIM][Ac] [166].

Figure 3.8a shows that Λ_{imp} decreases as temperature increases, as expected. The molar conductivity also decreases with increasing anion chain length, as shown by Figure 3.8b. This is similar to the trend observed when increasing the cation chain length in imidazolium-based ILs [24].

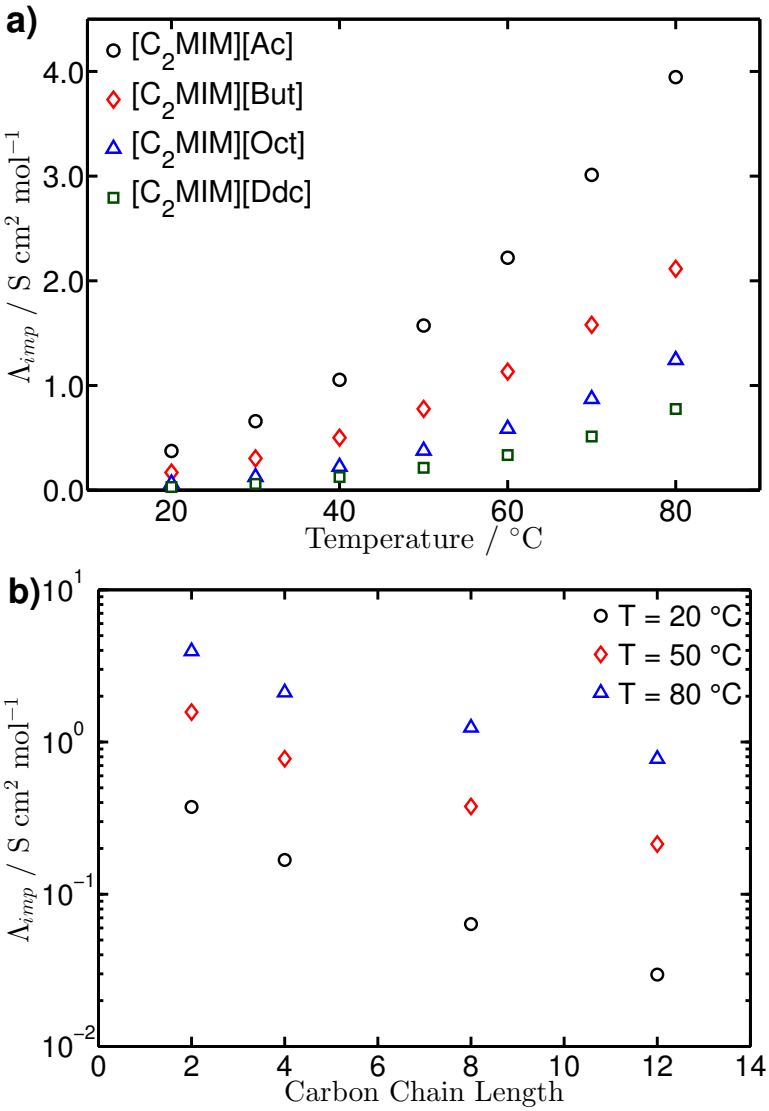

Figure 3.8: Molar conductivity data for $[C_2MIM][Ac]$, $[C_2MIM][But]$, $[C_2MIM][Oct]$ and $[C_2MIM][Ddc]$ obtained from impedance measurements. Plots show **a)** molar conductivity as a function of temperature for all four ILs and **b)** molar conductivity as a function of anion chain length for three set temperatures. Error bars of 2% are smaller than the data points.

3.3.5 Density

Density data for $[C_2MIM][Ac]$, $[C_2MIM][But]$, $[C_2MIM][Oct]$ and $[C_2MIM][Ddc]$ are shown in Figure 3.9. The density values, ρ, are consistent with previously reported values for $[C_2MIM][Ac]$ [84] and other imidazolium-based ILs [142, 151].

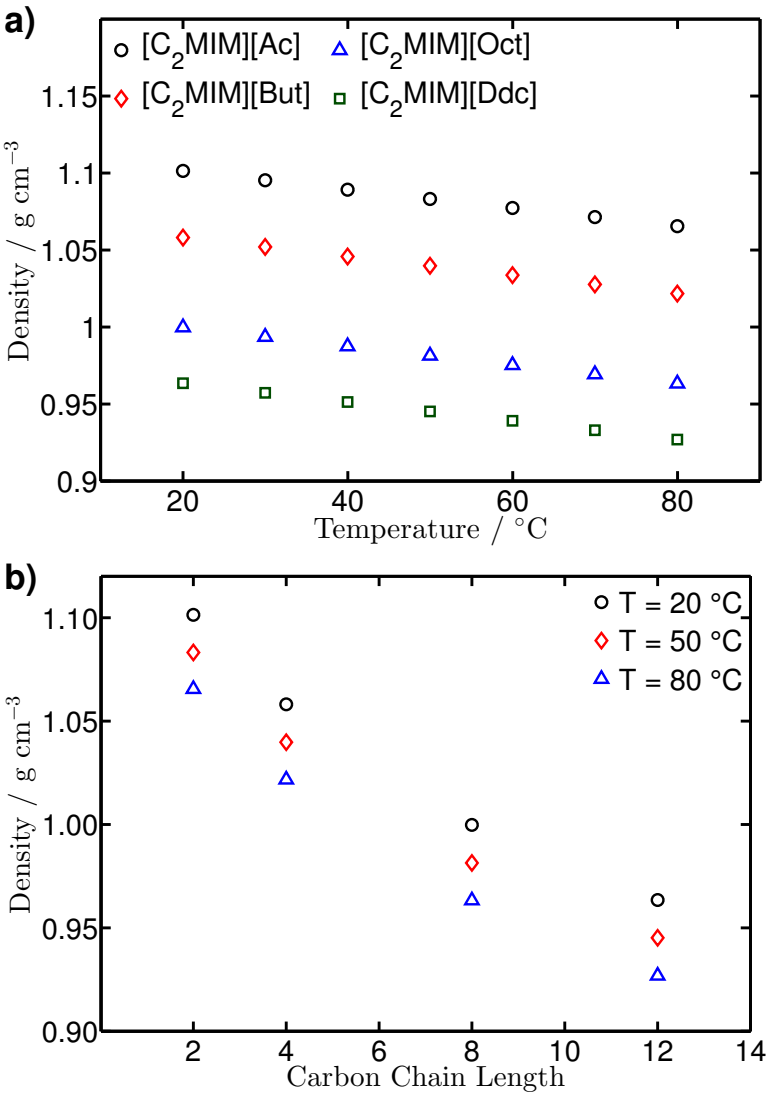

Figure 3.9: Density data for $[C_2MIM][Ac]$, $[C_2MIM][But]$, $[C_2MIM][Oct]$ and $[C_2MIM][Ddc]$. Plots show **a)** density as a function of temperature for all four ILs and **b)** density as a function of anion chain length for three set temperatures. Error bars of 2% are smaller than the data points.

Figure 3.9a shows a linear decrease in ρ as temperature decreases; it is worth noting that the gradient is identical for all four ILs, within experimental error. Figure 3.9b shows a slightly non-linear decrease in ρ as the anion chain length increases within the entire temperature range studied, consistent with similar studies of cation chain length increase in other ILs [24, 167].

Filipov et al. studied dialkylpyrrolidinium ILs with varying length of alkyl side-chains [167]. They found that the IL density could be modelled by a weighted addition of the densities of the ionic regions and the aliphatic side chains. Therefore, as side-chain length increased, the density tended towards that of a very long $CH_3(CH_2)_mCH_3$ chain. This matches well with the densities shown in Figure 3.9: density decreases from roughly the value of imidazole ($\rho \approx 1.2$ g cm^{-3}) towards that of polyethylene ($\rho \approx 0.9$ g cm^{-3}).

3.3.6 Stokes-Einstein-Debye Analysis

As discussed in Section 2.2.2, Stokes-Einstein analysis can be applied to ILs in order to gain an insight into the correlation between microscopic and macroscopic properties. With knowledge of the diffusion coefficient and viscosity, the Stokes-Einstein equation (Equation 2.4) can be rearranged to calculated the hydrodynamic radius of a molecule or ion. While there are some caveats in the application of the Stokes-Einstein equation in this way, as discussed in Section 2.2.2, the values of $r_{h,i}$ obtained can be considered as broadly accurate in magnitude.

As NMR measurements can give distinct D values for each ion [35], the Stokes-Einstein equation (Equation 2.4) was used to calculate $r_{h,i}$ for both ions, from diffusion and viscosity data. The $r_{h,i}$ values from this method will be referred to as 'Stokes-Einstein' (or 'SE') values and are shown as points in Figure 3.10. The dashed lines in Figure 3.10 show $r_{h,i}$ values calculated using density data and Equation 2.5. These will be referred to as 'density' values. The key difference between the two methods is the use of microscopic data (diffusional), compared to bulk properties (density). The discrepancy between the two datasets provides an insight into the microscopic behaviour of the systems, such as ionic packing and aggregation, as will be discussed later.

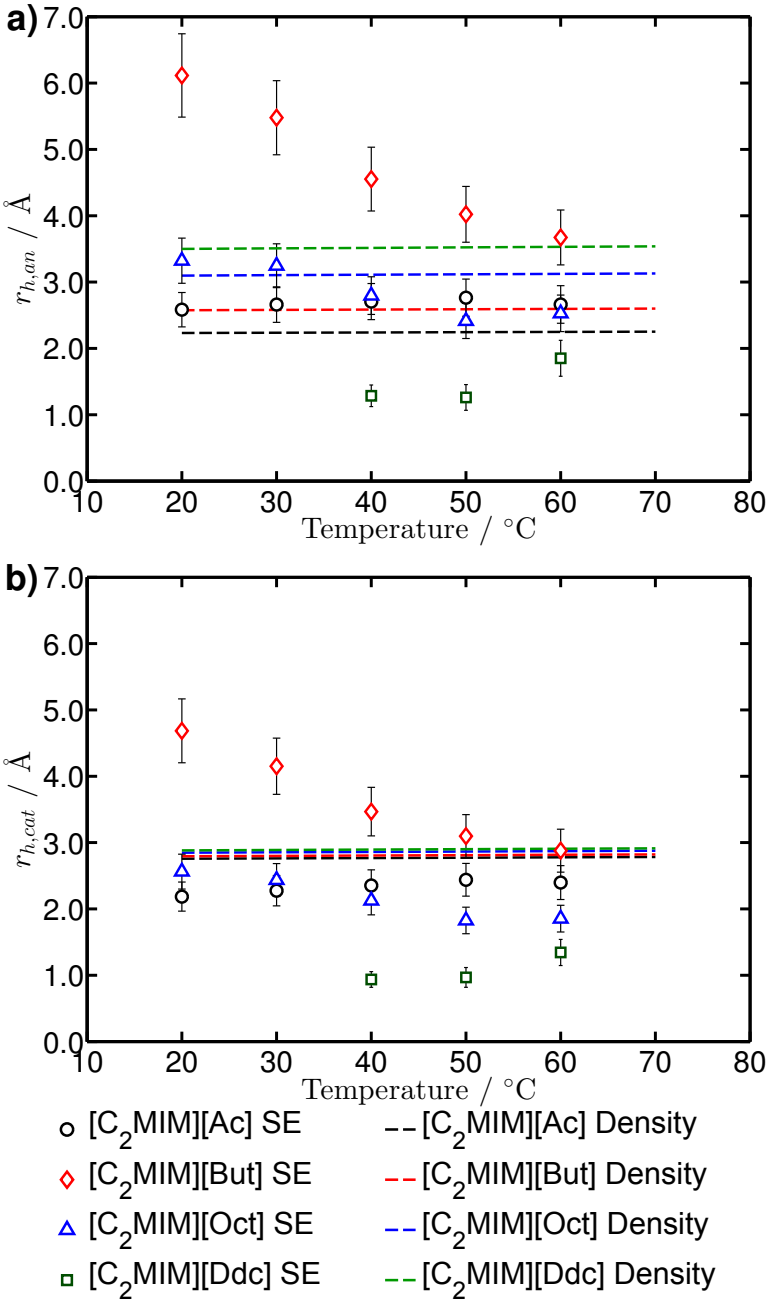

Figure 3.10: Hydrodynamic radii of **a)** the carboxylate anion and **b)** the $[C_2MIM]^+$ cation as a function of temperature for $[C_2MIM][Ac]$, $[C_2MIM][But]$, $[C_2MIM][Oct]$ and $[C_2MIM][Ddc]$. Points show radii calculated using diffusion data and the Stokes-Einstein equation (Equation 2.4). Dashed lines show radii calculated using density data and Equation 2.5.

One significant feature is the difference between cation and anion behaviours shown in Figure 3.10. For the cation, the SE values are smaller than the density values in almost all cases. Whereas, for the anion the opposite is true in the majority of data. This shows that the microscopic data is underestimating the size of the cation and overestimating the size of the anion. This is consistent with the formation of 'anion-rich' triplets, as proposed by Hou et al. [145] and will be explored further in following sections.

Following on from Stokes-Einstein analysis, Equation 2.8 can be used to compare NMR relaxation behaviour with viscosity data. The relationship between the relaxation times and viscosity are shown in Figure 3.11.

Based on Equation 2.8, a linear relationship between T_1 or T_2 and T/η would be expected, with a y intercept of zero. This trend is shown clearly by $[C_2MIM][Ac]$ and $[C_2MIM][But]$ (Figure 3.11a and 3.11b). However, there are significant deviations shown between the T_1 data of $[C_2MIM][Oct]$ and $[C_2MIM][Ddc]$ (Figure 3.11c and 3.11d), notably, neither dataset has a y-intercept of zero. This is consistent with additional low-frequency dynamics in $[C_2MIM][Oct]$ and $[C_2MIM][Ddc]$ which are not observed by T_1 measurements at these field strengths; this points to the existence of more complex and significant aggregation in $[C_2MIM][Oct]$ and $[C_2MIM][Ddc]$ than in $[C_2MIM][Ac]$ and $[C_2MIM][But]$, as discussed in Section 3.3.2. There is also likely to be a simple component of T_2 from the longer anion tails in $[C_2MIM][Oct]$ and $[C_2MIM][Ddc]$. A value for r_h can be calculated here using Equation 2.8. Values for A were used from Table 3.1. The r_h values for all four ILs fell within the range of 2-3 Å, in agreement with the data shown in Figure 3.10. It should be noted that the low-field experiments used here have insufficient chemical resolution to distinguish between the cation and the anion, therefore the r_h values reported here represent an averaged value across the cation and anion. It is still interesting that the simple approach used here predicts such reasonable ionic sizes from the NMR relaxation data.

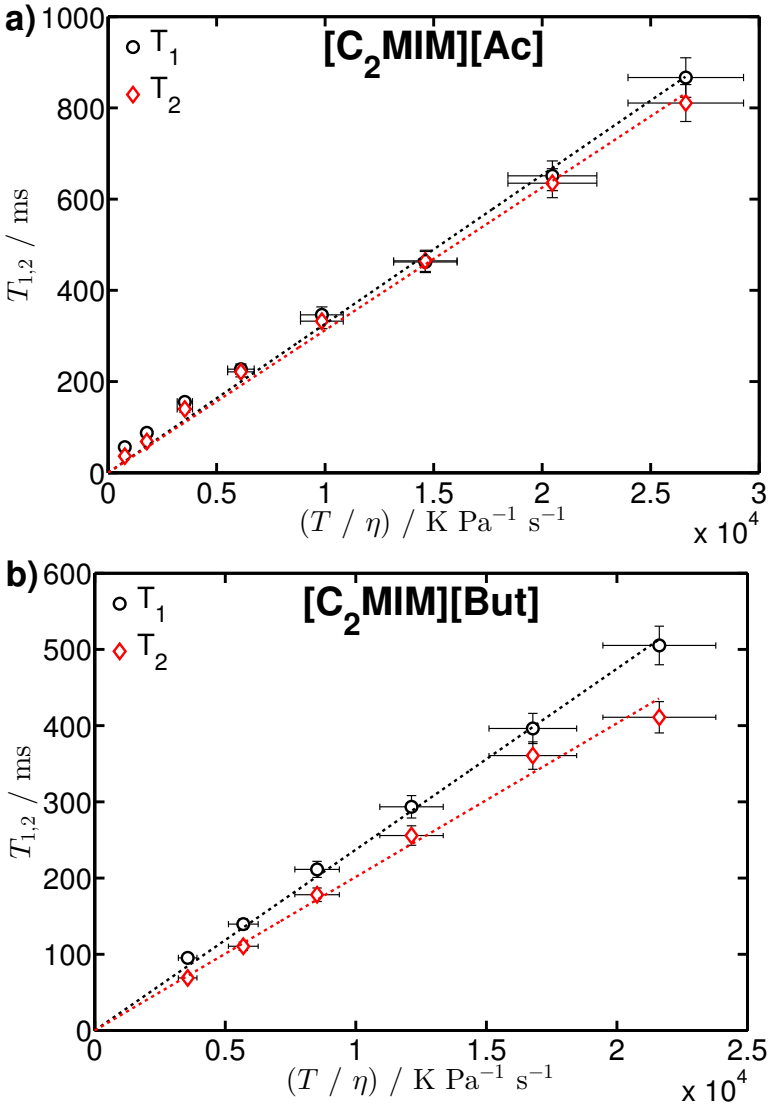
a)
[C2MIM][Ac]
T1
T2
T1,2 / ms
(T / η) / K Pa−1 s−1
x 10^4
b)
[C2MIM][But]
T1
T2
T1,2 / ms
(T / η) / K Pa−1 s−1
x 10^4

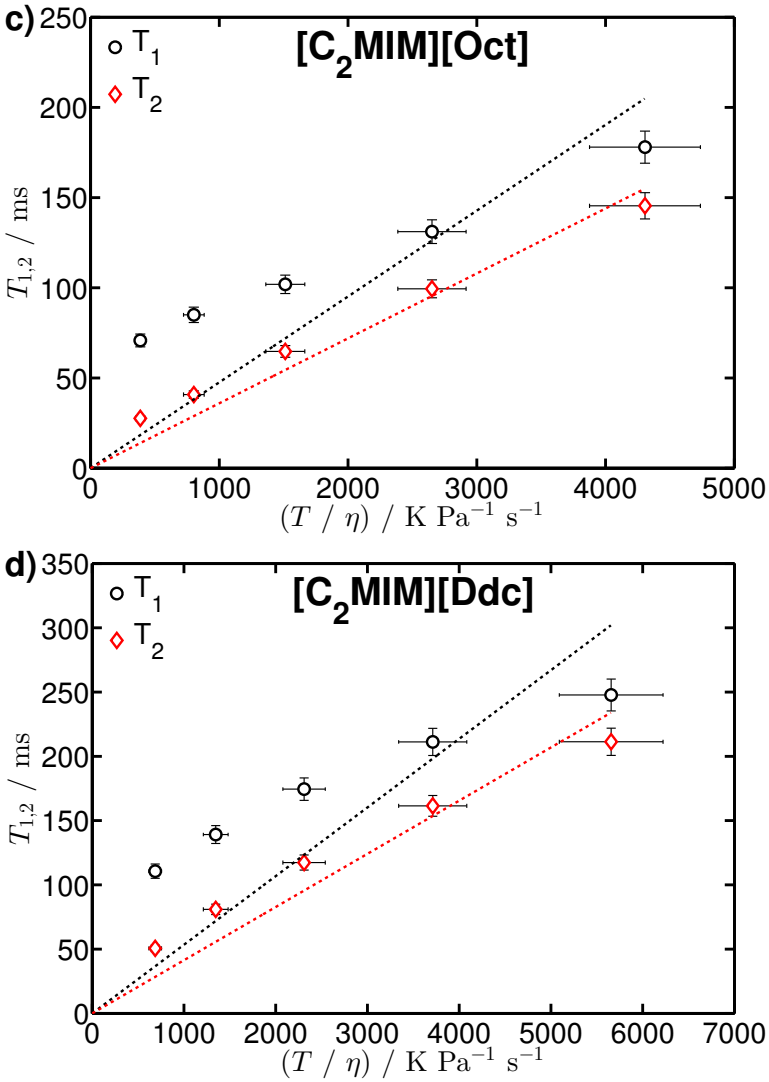

Figure 3.11: Plots showing the relationship between NMR relaxation data and the ratio of temperature and viscosity for all four ILs, based on Equation 2.8. Plots show data for **a)** [C_2MIM][Ac], **b)** [C_2MIM][But], **c)** [C_2MIM][Oct] and **d)** [C_2MIM][Ddc]. Lines show linear fits with an intercept of zero, according to Equation 2.8.

3.3.7 Nernst-Einstein Analysis

As well as relating viscosity to NMR data, it is also possible to relate conductivity and diffusion data, using the Nernst-Einstein equation (Equation 2.10). The predicted conductivity obtained in this way, referred to as Λ_{NMR} here, can be compared to the conductivity measured through impedance measurements, referred to as Λ_{imp} (Equation 2.9). Initially, this method will be applied on the assumption that the ionic liquids are simply highly-concentrated electrolytic solutions, where all the ions behave as isolated charge carriers with no correlated motion, except for the motion due to an applied electric field. If these assumptions hold, then Λ_{NMR} should be equal to Λ_{imp}, and consequently, the ratio $\Lambda_{NMR}/\Lambda_{imp}$ should be equal to 1. The inverse of this ratio is often referred to as the Haven ratio, H_r. Figure 3.12 shows the inverse-Haven ratio as a function of temperature for all four ILs.

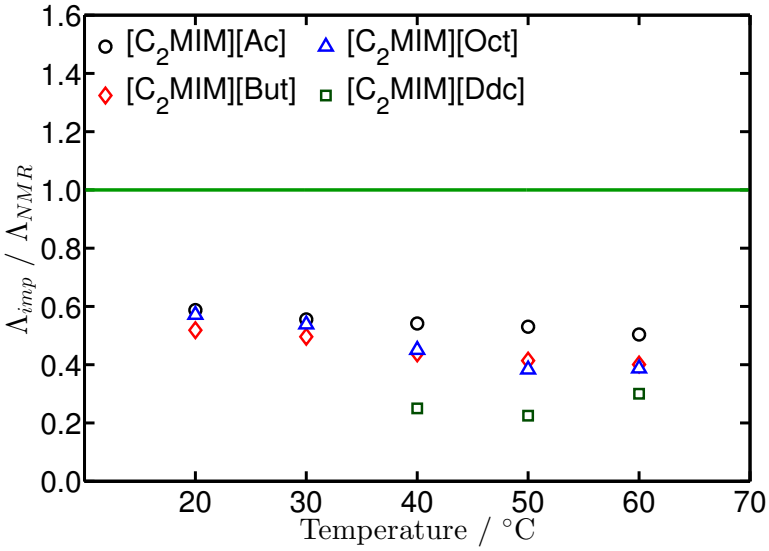

Figure 3.12: Ratio of molar conductivity calculated from impedance measurements (Equation 2.9) and molar conductivity calculated from NMR measurements of diffusion coefficients (Equation 2.10), as a function of temperature. Λ_{NMR} was calculated simply from D_{cat} and D_{an} values, partially shown in Figure 3.2. Solid line shows a ratio of 1, where the molar conductivity is the value predicted by the Nernst-Einstein equation.

It is quite clear that the conductivity ratio for all four ILs is significantly

below 1. This shows that the picture of single, isolated ions is not a valid description for these systems. The four ILs show broadly similar trends, suggesting the discrepancy in the molar conductivity values is due to a common phenomenon, backed up by literature studies on a range of other ILs. Some publications attribute this type of discrepancy principally to ion pairing in the bulk IL, leading to decreased conductivity but relatively unchanged diffusion, compared to fully dissociated ions [139]. Many publications then go a step further, attributing the lowered conductivity to the existence of larger aggregates [142–144], in particular, Hou et al. describe triplets formed of two anions and one cation [145]. Here, the concept of these anion-rich triplets will be used as a basis and will be analysed in detail in the following section.

Another important tool for understanding conducting liquids is the Walden plot [39, 136]. Equation 2.12 shows the Walden rule, which provides a simple relation between the molar conductivity and the viscosity. The Walden plot for these ILs is shown in Figure 3.13. In an ideal electrolytic solution, the ions are all isolated and non-interacting. Aqueous KCl is commonly considered an ideal electrolytic solution and will be used herein; we will term this situation the 'ideal case'. In this ideal case and with the appropriate units, Λ_{imp} will be equal to $1/\eta$, the product $\Lambda_{imp} \cdot \eta$ will equal 1 and therefore, the gradient of the Walden plot will be 1. Figure 3.13 shows this is not the case for these ILs, as they all fall below the ideal line. This type of behaviour is attributed to the same factors described above for the conductivity ratio *i.e.* ion pairing or aggregation [139].

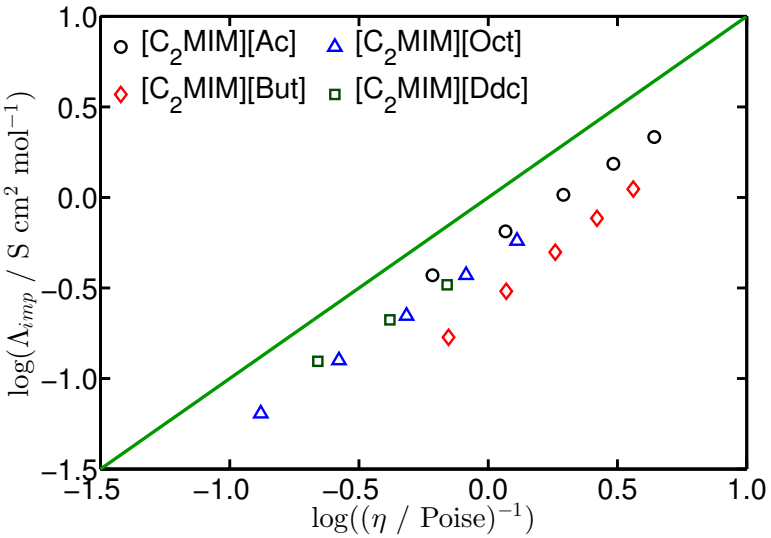

Figure 3.13: A Walden plot for $[C_2MIM][Ac]$, $[C_2MIM][But]$, $[C_2MIM][Oct]$ and $[C_2MIM][Ddc]$ at a range of temperatures. Molar conductivity is calculated using Equation 2.12, from the conductivity data shown in Figure 3.8. Solid line shows the data for an ideal electrolyte (aqueous KCl), with a gradient of 1.

3.4 Analysis and Discussion

There are some unexplained features in the physical and chemical properties of the four ILs studied here, as shown in the previous sections. In particular, there are notable discrepancies between certain macroscopic and microscopic properties. The trends shown by bulk properties, such as density and viscosity, are consistent with an increase in molecular size/mass. In contrast, microscopic data, such as diffusion and relaxometry, show some unexpected behaviour and deviate from Stokes-Einstein theory and other similar theories. There are three significant discrepancies shown in the previous sections:
i) The inverse-Haven plot (Figure 3.12) shows Λ_{imp} is too low in comparison to the measured D coefficients, *ii*) the Walden plot (Figure 3.13) shows Λ_{imp} is too low in comparison to the measured η, and *iii*) the experimental ratio of the diffusion coefficients (Figure 3.3) is lower than expected. All three of these previous plots assumed a simple situation, where both cation and anion exist as isolated ions. This picture fails to explain the observed behaviour in all three cases.

One of the potential causes of the behaviour detailed above is ionic association. This section will discuss methods for investigating this possibility through simple models of ionic pairing and aggregation. First, ionic pairing will be modelled, as the simplest possible type of ionic association. Next, the idea of anion-rich triplets proposed by Hou et al. [145] will be used as a basis for modelling systems composed purely of single cations and charged, aggregated anions. Finally, the two models will be combined and evaluated together. Appendix C contains the key equations for each model, as a quick reference.

3.4.1 Pair Model

In ILs, all oppositely charged ions will have a strong attraction to each other, as with all ionic materials. Despite this, ILs are unique in that the ions do not form fixed ionic bonds in large, regularly-ordered structures. However, it is possible that two oppositely charged ions can form an ionic bond between each other, forming a single uncharged complex. As discussed in the previous section, this is theorised to occur in imidazolium-based ILs, influencing the physical properties of the ILs.

In Section 2.3.2, a model is presented that can simulate the effects of ion pairing in ILs. The main parameter in this model is the total fraction of the ions (either anions or cations) that exist in a neutral pair, P. To reiterate, there are three important characteristic relationships that are not adequately described by a simple model of single isolated ions: *i*) the discrepancy between molar conductivity calculated by impedance measurements and the molar conductivity calculated from NMR measurements of diffusion coefficients using the Nernst-Einstein equation (Equation 2.10), *ii*) the deviation from ideality in a Walden plot, describing the relationship between the molar conductivity and viscosity, *iii*) the ratio between the diffusion coefficient of the anion and the diffusion coefficient of the cation (see Figure 3.3). These three factors will be analysed and used as a measure of accuracy for the ion pair model. While it is possible to fit each relation separately, an effective model should be able to describe all three relations simultaneously. Additionally, the freedom of the models allow accurate fitting of most individual datasets, regardless of how realist those fits may be. Therefore,

these models will be assessed against the criteria of a simultaneous fit for all three relations.

By varying P, it is possible to model the ILs as systems with a varying amount of ion pairing. This will change the calculation of three quantities: Λ_{imp}, Λ_{NMR} and D_{an}/D_{cat}. Figure 3.14 shows the molar conductivity ratio and Walden plot for a moderate degree of pairing, $P = 0.35$. This value was chosen as a compromise between the best P values for the inverse-Haven plot and the Walden plot. From a comparison of Figure 3.12 and Figure 3.14a, it is clear that the agreement between data and the ideal value of $\Lambda_{imp}/\ \Lambda_{NMR} = 1$ is improved noticeably at $P = 0.35$. Figures 3.13 and 3.14b show a similar improvement for the Walden plot at $P = 0.35$.

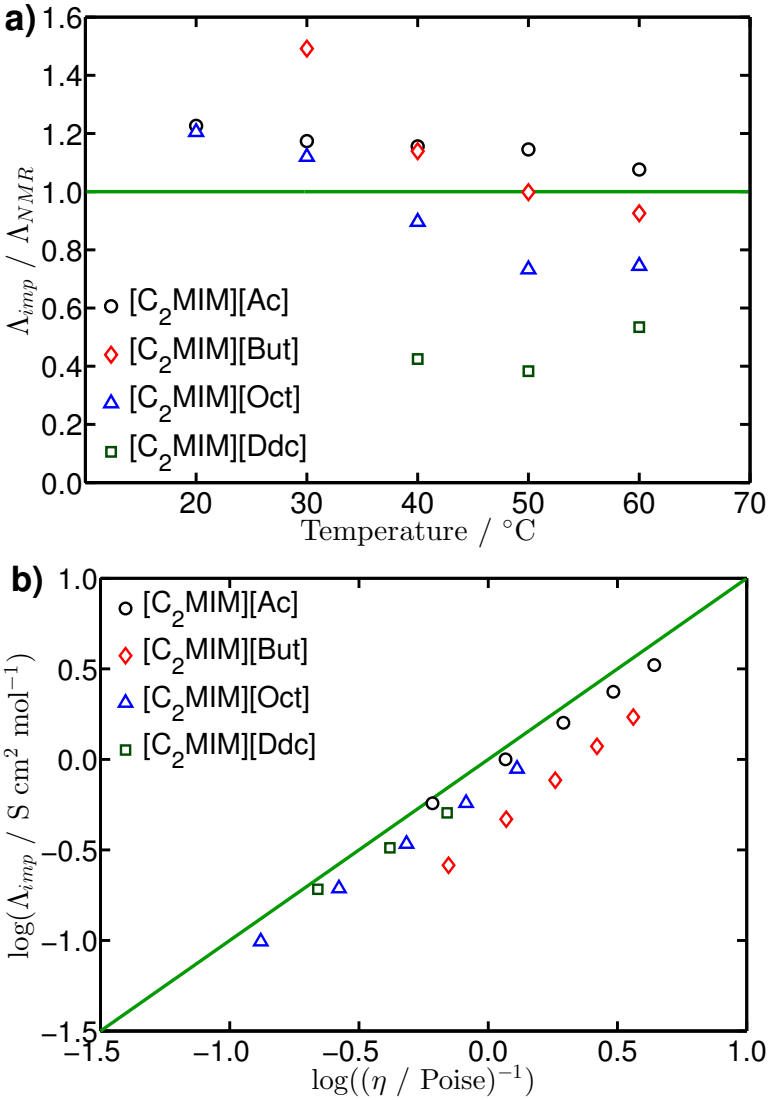

Figure 3.14: Effects of modelling ion pairs on the molar conductivity for $[C_2MIM][Ac]$, $[C_2MIM][But]$, $[C_2MIM][Oct]$ and $[C_2MIM][Ddc]$. Aggregation is limited to ion pairing (*i.e.* $n = 1$). A relatively low degree of pairing is shown ($P = 0.35$). **a)** Ratio of molar conductivities from impedance and NMR measurements, as a function of temperature. See Figure 3.12 for more detail. **b)** Walden plot for these parameters, see Figure 3.13 for details.

A more systematic approach can be taken to investigate the effects of increasing pairing on the inverse-Haven ratio and the Walden plot. Figure 3.15 shows conductivity ratio data as a function of anion chain length for a range of P values

at 40 °C. The ideal conductivity ratio of 1 is shown as a comparison. Figure 3.16 shows a similar visualisation for the Walden rule (Equation 2.12); the product of Λ_{imp} and η, as a function of anion chain length, is compared to the ideal case of $\Lambda_{imp} = 1/\eta$ at 40 °C. If the Walden rule is obeyed, then $\Lambda_{imp} \cdot \eta$ will be equal to 1, as in aqueous KCl.

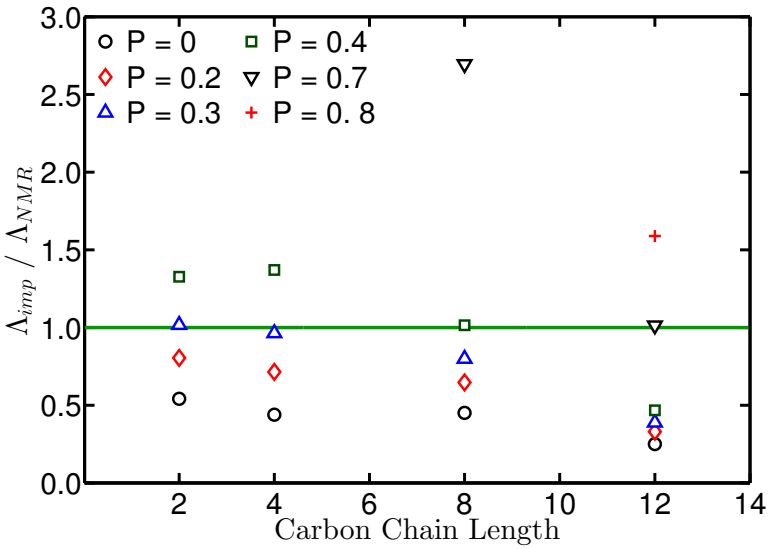

Figure 3.15: Effects of modelling ion pairs on the molar conductivity ratio for [C_2MIM][Ac], [C_2MIM][But], [C_2MIM][Oct] and [C_2MIM][Ddc] at 40 °C. Aggregation is limited to ion pairing (*i.e.* $n = 1$), while pairing fraction, P, is varied. Data from the model are shown as points and solid line shows a ratio of 1, where the molar conductivity is the value predicted by the Nernst-Einstein equation.

Figures 3.15 and 3.16 highlight the discrepancy between the isolated ions model ($P = 0$) and the ideal data for all four ILs. Increasing P leads to an increased Λ_{imp} to account for non-conducting ion pairs, this will have the initial effect of improving both the inverse-Haven ratio plot and the Walden plot. In general, increasing P improves the model up to around $P = 0.3$, after which the inverse-Haven ratio becomes too high. However, [C_2MIM][Ddc] requires a higher degree of pairing of $P = 0.7$. Unsurprisingly, while all four ILs can be individually modelled well by the ion pairing model, there is no shared optimum value for any two ILs, with optimum values of $P \approx 0.3$, 0.35, 0.4 and 0.7 for [C_2MIM][Ac], [C_2MIM][But], [C_2MIM][Oct] and [C_2MIM][Ddc], respectively. This is consis-

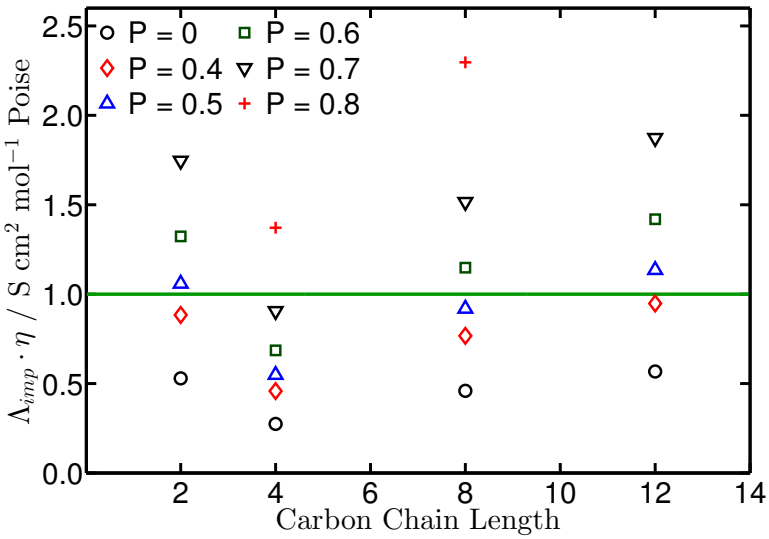

Figure 3.16: Effects of modelling ion pairs on the molar conductivity for [C_2MIM][Ac], [C_2MIM][But], [C_2MIM][Oct] and [C_2MIM][Ddc] compared to the viscosity, at 40 °C. Aggregation is limited to ion pairing (*i.e.* $n = 1$), while pairing fraction, P, is varied. The Walden rule (Equation 2.12) is used to evaluate the model, where the solid line shows the expected data for an ideal electrolyte (aqueous KCl) and data from the model are shown as points.

tent with the differences of behaviour between the ILs presented in the previous sections.

The increasing Λ_{imp} with P is also shown in Figure 3.16. Once again, increasing P improves the model at first, until Λ_{imp} overshoots the ideal case at higher values of P. However, unlike with the molar conductivity ratio, the optimum value of P is around 0.5. Additionally, [C_2MIM][Ddc] is modelled well by $P = 0.4$, whereas, [C_2MIM][But] is not modelled well until P is greater than 0.7. As with the inverse-Haven ratio, it is possible to find an optimum P value for each IL. For [C_2MIM][Ac], [C_2MIM][Oct] and [C_2MIM][Ddc] the optimum P for the Walden plot falls in the range $0.4 - 0.6$, all higher than the optimum range of $0.3 - 0.4$ for the inverse-Haven ratio.

The third condition to be satisfied by a successful model is the diffusion coefficient ratio (Figure 3.3). However even before applying the ion pairing model, it can be deduced that the pair model cannot adequately describe the "anomalous" diffusion ratios found in these ILs. As the degree of pairing increases, the

diffusion coefficients of the cation and anion will tend towards the same value. Therefore, as P tends towards 1 (when all ions exist in neutral pairs), D_{an}/D_{cat} will also tend towards 1. As D_{an}/D_{cat} is below 1 for all four ILs, it follows that data modelled this way will never agree well with experimental data, regardless of the value of P used. This can also be seen mathematically by setting P to 1 in Equation 2.18. The diffusion coefficient ratio for varying P is shown graphically in Figure 3.17, compared to experimental D_{an}/D_{cat} data at 40 °C.

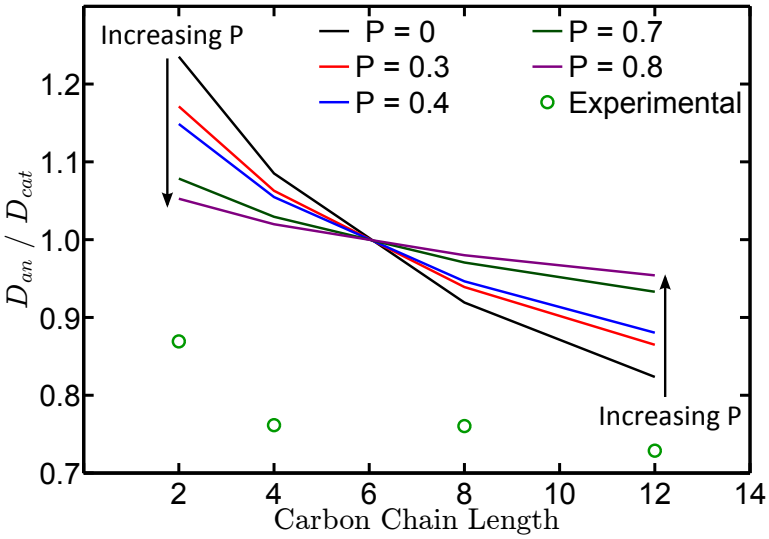

Figure 3.17: Effects of modelling ion pairs on the ratio of anion diffusion coefficient to cation diffusion coefficient for [C_2MIM][Ac], [C_2MIM][But], [C_2MIM][Oct] and [C_2MIM][Ddc] at 40 °C. Aggregation is limited to ion pairing (*i.e.* $n = 1$), while pairing fraction, P, is varied. Data from the model are shown as solid lines and experimental data from Figure 3.3 are shown as points.

Figure 3.17 shows a small improvement for [C_2MIM][Ac] and [C_2MIM][But] as P increases, as expected. However, increasing P actually brings the model further from experimental data for [C_2MIM][Oct] and [C_2MIM][Ddc]. Once again, this is as expected, as the model will tend towards $D_{an}/D_{cat}= 1$ as P increases.

It has been shown that the ion pairing model can accurately describe the inverse-Haven ratio and the Walden plot, unlike the simple isolated ions model. While it is a highly simplified model, this suggests the ILs form pairs or some kind of aggregates, removing ions from the conduction mechanism and decreasing

Λ_{imp}. However, it is not possible to model the diffusion ratio correctly with this approach. Additionally, each IL generally had a different optimum P, depending on whether the fitting was for the molar conductivity ratio or the Walden plot. Therefore, a second model will be described in the next section, attempting to improve on these shortcomings.

3.4.2 Aggregate Model

An obvious next step after a ion pairing model is a model describing ion triplets. Any ion triplet must be charged, therefore a counterion is required. In order to keep the model as simple as possible, the models presented here will always use a single (imidazolium) cation as the positive ion. Initially, the negative ion will be modelled as an anion-cation-anion triplet ('anion-rich' triplet), as suggested by Hou et al. [145] and detailed in Section 2.3.3. The reason for choosing anion-rich triplets over cation-rich triplets is the discrepancy in diffusion coefficient ratios: cation-rich triplets would lead to a decrease in D_{cat}, relative to D_{an}. This will lead to an increase in modelled D_{an}/D_{cat}, taking it further from the experimental values. As with the ion pair model, the aim of the triplet model, and then the aggregate model, is to address the discrepancies in the molar conductivity ratio, Walden plot and the diffusion ratio.

Figure 3.18 shows the inverse-Haven ratio and Walden plot for all four ILs, using the simple triplet model. Compared to the same plots using the ion pair model (Figure 3.14), it can be seen that the triplet model provides similar improvement as the pair model for these ILs. In particular, $[C_2MIM][Ac]$ is modelled near-perfectly in both the molar conductivity ratio plot (Figure 3.18a) and the Walden plot (Figure 3.18b). It is striking that even this simple approximation can model both datasets so accurately. Though the temperature dependence in the inverse-Haven ratio of $[C_2MIM][But]$ and $[C_2MIM][Oct]$ affects the fit, the triplet model improves the fit of both these ILs substantially from the isolated ions model. The Walden plot for $[C_2MIM][Oct]$ and $[C_2MIM][Ddc]$ is also greatly improved by the triplet model.

While the triplet model provides an excellent description for the properties of $[C_2MIM][Ac]$, there is room for improvement in the other three ILs. Therefore,

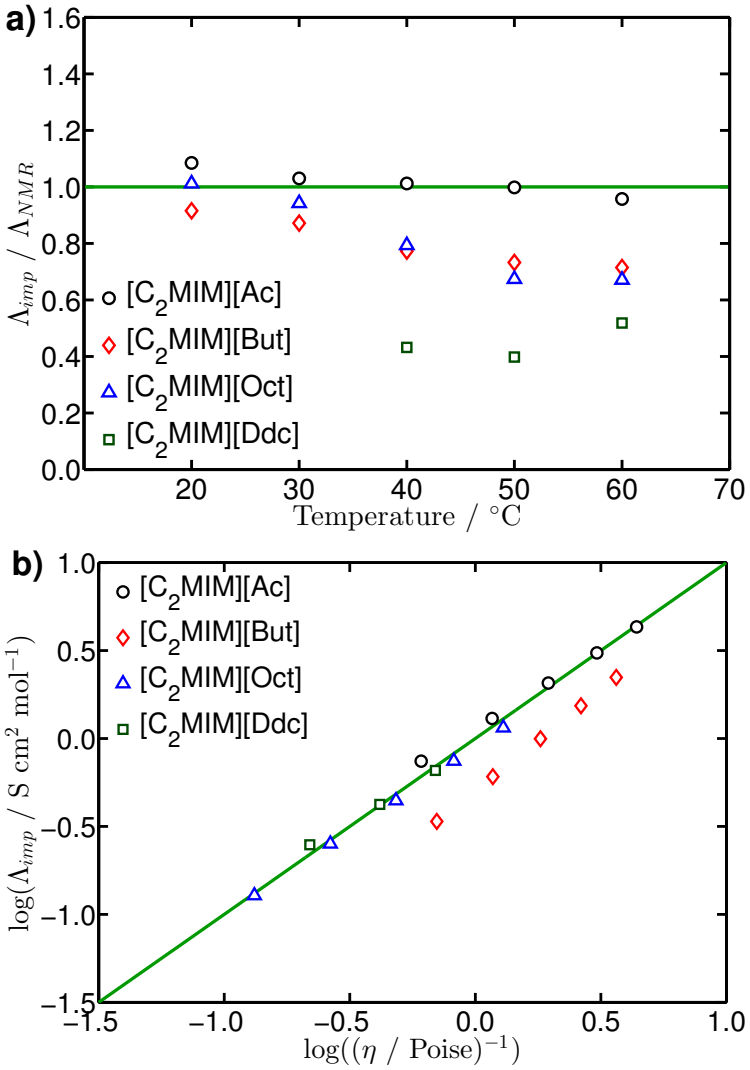

Figure 3.18: Effects of modelling ionic aggregation on the molar conductivity for $[C_2MIM][Ac]$, $[C_2MIM][But]$, $[C_2MIM][Oct]$ and $[C_2MIM][Ddc]$. Aggregation is limited to charged aggregates only (*i.e.* $P = 0$). A model with the lowest size of charged aggregates is shown ($n = 2$), corresponding to anion-rich triplets. **a)** Ratio of molar conductivities from impedance and NMR measurements, as a function of temperature. See Figure 3.12 for more detail. **b)** Walden plot for these parameters, see Figure 3.13 for details.

the model was expanded to a more general charged-aggregate model, as detailed in the second part of Section 2.3.3. As before, the positive ion remains a single cation for all modelled systems. The negative ion will now be modelled as a

singly charged aggregate consisting of n carboxylate anions and $n-1$ imidazolium cations; the triplet model is obtained by setting this n parameter to a value of 2, see Figure 2.4 for a depiction of this model. This model is a substantial oversimplification, especially at higher n, but it provides a useful insight into the effects of IL structuring.

Figures 3.19 and 3.20 show the effects of varying n at a fixed temperature (40 °C) on the inverse-Haven ratio and the Walden relation of the four ILs. Increasing n leads to an increased $\Lambda_{imp}/\Lambda_{NMR}$, with the first three ILs falling in line with the ideal value somewhere between $n = 2$ and $n = 3$. Using $n \geq 3$ results in a conductivity ratio greater than 1. Once again, [C_2MIM][Ddc] falls well below the ideal line compared to the other ILs, requiring a value of $n = 9$ to reach $\Lambda_{imp}/\Lambda_{NMR}$= 1.

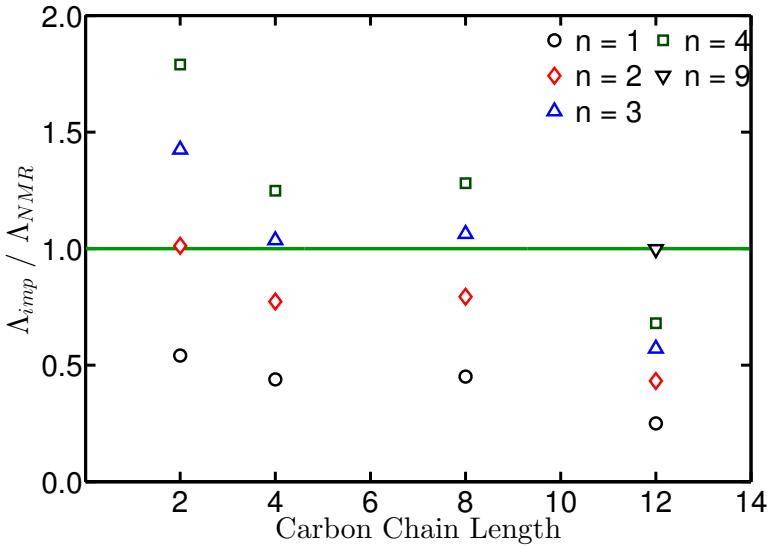

Figure 3.19: Effects of modelling ionic aggregation on the molar conductivity ratio for [C_2MIM][Ac], [C_2MIM][But], [C_2MIM][Oct] and [C_2MIM][Ddc] at 40 °C. Aggregation is limited to charged aggregates only (*i.e.* $P = 0$), while size of charged aggregates, n, is varied. Data from the model are shown as points and solid line shows a ratio of 1, where the molar conductivity is the value predicted by the Nernst-Einstein equation.

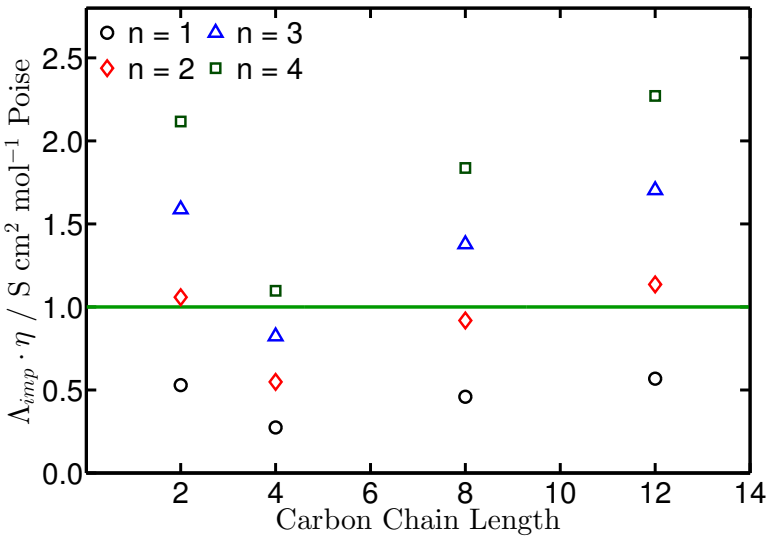

Figure 3.20: Effects of modelling ionic aggregation on the molar conductivity for $[C_2MIM][Ac]$, $[C_2MIM][But]$, $[C_2MIM][Oct]$ and $[C_2MIM][Ddc]$ compared to the viscosity, at 40 °C. Aggregation is limited to charged aggregates only (*i.e.* $P = 0$), while size of charged aggregates, n, is varied. The Walden rule (Equation 2.12) is used to evaluate the model, where the solid line shows the expected data for an ideal electrolyte (aqueous KCl) and data from the model are shown as points.

Increasing n has a similar effect on the relationship between Λ_{imp} and η, as shown in Figure 3.20; the value of Λ_{imp} increases as n increases. Interestingly, $n = 2$ gives excellent agreement with the ideal case for $[C_2MIM][Ac]$, $[C_2MIM][Oct]$ and $[C_2MIM][Ddc]$, whereas using $n > 2$ gives too large values of Λ_{imp}. $[C_2MIM][But]$ is less well-described, requiring a value between $n = 3$ and $n = 4$ to get a good agreement. This is mainly due to the lower-than-expected viscosity for $[C_2MIM][But]$. There is some consistency between fitting of the two datasets for $[C_2MIM][Ac]$ and $[C_2MIM][Oct]$, as the optimum n values are close for both the inverse-Haven ratio plot and the Walden rule plot.

As with the pair model, it is worth briefly evaluating the theory before examining the data for the diffusion coefficient ratio. Equation 2.29 shows the theoretical dependence of D_{an}/D_{cat} on n. This equation will tend towards 1 as n becomes large, just like the pair model and P. However, by definition the molar mass of the single cation is smaller than that of the aggregate *i.e.* $M_+ - M_{agg} < 0$ for all $n > 1$. It follows that $M_+^{-\frac{1}{3}} - M_{agg}^{-\frac{1}{3}} > 0$ and therefore, the denomina-

tor in Equation 2.29 will be higher than the numerator. As a consequence of this, D_{an}/D_{cat} will decrease below 1 initially as n increases. Given the values of D_{an}/D_{cat} for the four ILs (Figure 3.3), this is already likely to be an improvement on the pair model.

Figure 3.21 shows the effects of changing n on the diffusion ratio for the four ILs, compared to experimental data at 40 °C. It is clear that this model is far more effective than the pair model (Figure 3.17), as predicted. There is a very strong agreement between the model and the experimental values for all the n values shown. There is excellent agreement with experiment for [C_2MIM][Ac], [C_2MIM][Oct] and [C_2MIM][Ddc] at $n = 2$ and [C_2MIM][But] is greatly improved compared to $n = 1$. Though, there is relatively little change in the modelled D_{an}/D_{cat} for $n > 2$ compared to $n = 2$. This is in contrast to the changes shown for the inverse-Haven ratio and the Walden plot (Figures 3.19 and 3.20), where there are fairly uniform increases in Λ_{imp} as n increases. This means that D_{an}/D_{cat} is improved greatly by the existence of aggregates but it is relatively insensitive to the size of those aggregates. Due to this insensitivity, there is strong agreement between the optimum n values for diffusion ratio and optimum n values for the two other datasets.

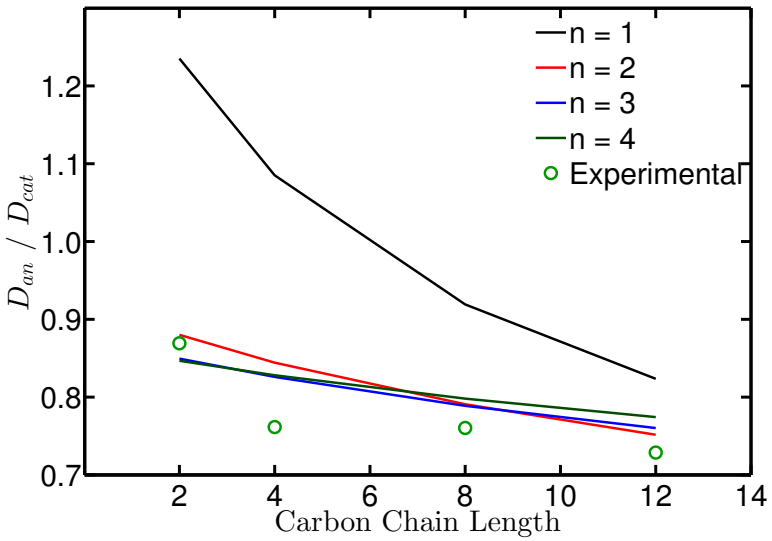

Figure 3.21: Effects of modelling ionic aggregation on the ratio of anion diffusion coefficient to cation diffusion coefficient for $[C_2MIM][Ac]$, $[C_2MIM][But]$, $[C_2MIM][Oct]$ and $[C_2MIM][Ddc]$ at 40 °C. Aggregation is limited to charged aggregates only (*i.e.* $P = 0$), while size of charged aggregates, n, is varied. Data from the model are shown as solids lines and experimental data from Figure 3.3 are shown as points.

As with the ion pairing model, the aggregate model can accurately model the inverse-Haven ratio and the Walden plot. In addition to this, the aggregate model provides an accurate description of the diffusion coefficient ratio for these ILs. This ability to provide greatly improved agreement in all three datasets shows the aggregate model is more effective than the ion pairing model. Even with the simplified picture of just two ionic configurations (cation and aggregate), the model finds good agreement for the experimental data. Of course, it is difficult to believe that the physical structure really is as simple as this model assumes. For example, it seems unlikely that larger charged aggregates would form but not smaller neutral pairs. In the next section, the aggregate model and the pair model will be combined in order to provide further insight into the structure of these ILs.

3.4.3 Combined Model

Modelling ion pairing and modelling charged, anion-rich aggregates have similar effects on two of the three datasets examined in the previous sections (the inverse-Haven ratio and the Walden plot). However while the two models are similar in effect, they are not identical and the diffusion coefficient ratio is affected very differently by each model. Therefore, a combination of the aggregate model and the ion pairing model will provide information on how these two modifications interact. In the previous section it was discussed why cation-rich triplets and aggregates were not added into the models used here. A similar argument applies to the addition of single anions into the combined model presented in this section; any increase in single anions will cause a decrease in D_{an} and a decrease in Λ_{imp}, both of which would worsen the agreement between model and experiment.

The mathematical framework of this combined model is set out in Section 2.3.4. Briefly, the parameters n and P will be used as in the two preceding sections, describing the number of anions in the anion-rich, negatively charged aggregate, and the fraction of ion pairs compared to unpaired ions (cations or aggregated anions), respectively. Note that P can be related to the ratio of paired ions to unpaired ions, R, according to Equation 2.31 (Section 2.3.4). Both parameters can be varied independently, with both co-operative and competing effects.

One key difference between the modelling in this section and the previous section will be the departure from a strict physical definition of n, that is, non-integer values of n will be allowed. This does not make sense on an individual cation-anion-pair basis, as a fractional number of ions in a single aggregate is not possible, but it is more representative of a large mixed system of single ions and aggregates of various sizes, where n is the average aggregate size. Physically, this would represent a distribution of aggregates of varying size, from single anions to much larger aggregates, with the distribution centred on an average size of n. Of course, this is merely an interpretation; all the initial approximations and simplifications are still present in this model.

In Sections 3.4.1 and 3.4.2, the modelled data were compared qualitatively to experimental or theoretically ideal values. It is also possible to make these com-

parisons quantitative, allowing a more rigorous, weighted fitting of the models to the ideal data. The method used here is a relatively simple one: the absolute difference between modelled and ideal data was calculated point-by-point, the differences were summed across all points for each dataset and these individual sums were normalised to give an equal weight to the inverse-Haven ratio, the Walden plot and the diffusion ratio datasets. These weighted sums were then added together to give a final 'universal' sum, representing the total deviation from the ideal cases; this was minimised for each IL by varying n and P. Minimisations were performed for each IL individually and Table 3.2 shows the optimised parameters obtained in each case.

Dataset Fitted	n	P
$[C_2MIM][Ac]$	1.9	0.0
$[C_2MIM][But]$	3.0	0.0
$[C_2MIM][Oct]$	2.2	0.06
$[C_2MIM][Ddc]$	2.1	0.4

Table 3.2: Optimised fitting parameters for the combined aggregate and ion pairing model. Size of charged aggregates, n, and fraction of paired ions, P, are shown for the optimised fits for each IL fitted separately. Errors are roughly 5% for $[C_2MIM][Ac]$, 10% for $[C_2MIM][But]$ and $[C_2MIM][Oct]$, and 15% for $[C_2MIM][Ddc]$.

The parameters shown in Table 3.2 were used to calculate optimal values for the conductivity ratio, Λ_{imp} in the Walden plot and D_{an}/D_{cat} for each IL. The optimised fits are shown in Figures 3.22, 3.23 and 3.24. Due to the number of data points fitted simultaneously, uncertainties for the fitted n and P values were difficult to assess. As a rough estimate, n values are accurate to ± 0.2 and P values to ± 0.1.

Figures 3.22, 3.23 and 3.24 show a very good agreement between the optimised models for each IL and the ideal or experimental values. $[C_2MIM][Ac]$ and $[C_2MIM][Oct]$ are both in excellent agreement with the ideal molar conductivity ratio (Figure 3.22) and the Walden rule (Figure 3.23). $[C_2MIM][But]$ shows very good agreement with the inverse-Haven ratio value; the Walden rule is also followed to a reasonable extent, hindered by the aforementioned discrepancy in the viscosity data. $[C_2MIM][Ddc]$ shows moderate success in accurately modelling the

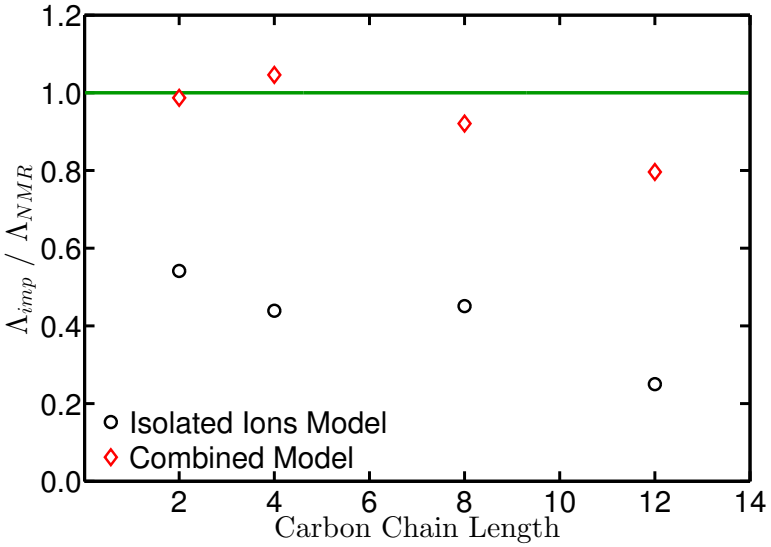

Figure 3.22: Effects of modelling ionic aggregation and ion pairing on the molar conductivity ratio for $[C_2MIM][Ac]$, $[C_2MIM][But]$, $[C_2MIM][Oct]$ and $[C_2MIM][Ddc]$ at 40 °C. Aggregation includes both charged aggregates and ion pairs *i.e.* both P and n are varied. The modelled data were obtained from the parameters shown in Table 3.2. Data from the models are shown as points and solid line shows a ratio of 1, where the molar conductivity is the value predicted by the Nernst-Einstein equation.

ideal values, as shown in Figures 3.22 and 3.23, though there is an antagonistic relationship between the two datasets: the inverse-Haven ratio is underestimated by the optimum fit, whereas, Λ_{imp} in the Walden plot is overestimated. The mathematical relationship between these two datasets mean it is impossible to reconcile this difference using this model of aggregation. This could be either due to the quality of the diffusion data for this IL or perhaps due to some additional complexity in the microscopic structuring and behaviour, not accounted for in this model.

The D_{an}/D_{cat} data for $[C_2MIM][Ac]$, $[C_2MIM][But]$ and $[C_2MIM][Oct]$ shown in Figure 3.24 are generally much-improved as a result of the model. $[C_2MIM][Ac]$ and $[C_2MIM][Oct]$ show particularly good agreement with the experimental data. Though, the optimised fit for $[C_2MIM][Ddc]$ shows less improvement in D_{an}/D_{cat}, compared to the $n = 1$, $P = 0$ case, due to the same factors discussed above.

A closer inspection of the fitting parameters shown in Table 3.2 provides

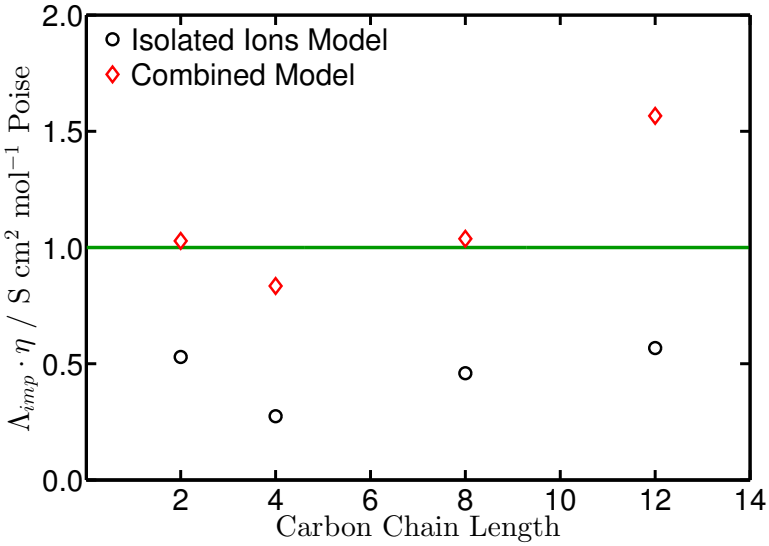

Figure 3.23: Effects of modelling ionic aggregation and ion pairing on the molar conductivity for [C_2MIM][Ac], [C_2MIM][But], [C_2MIM][Oct] and [C_2MIM][Ddc] compared to the viscosity, at 40 °C. Aggregation includes both charged aggregates and ion pairs *i.e.* both P and n are varied. The Walden rule (Equation 2.12) is used to evaluate the model, where the solid line shows the expected data for an ideal electrolyte (aqueous KCl) and data from the model are shown as points. The modelled data were obtained from the parameters shown in Table 3.2.

some insight into the nature of the IL structure. The optimum n values are all fairly low. More significantly, with the exception of [C_2MIM][Ddc], P is either exactly 0 or very close despite the use of a combined model. This suggests that the majority of the ionic aggregates are charged and that any larger charged structures ($n > 3$) are short-lived. It is also interesting that the n values for the individually fitted ILs are all fairly close to integer values, despite the freedom of the model. This could be a coincidence, or it could suggest that there are actually favoured structures (mostly triplets) that are formed in the majority of cases. The deviation of [C_2MIM][Ddc] parameters from those of the other three ILs is significant and the quality of fit is lower, but the combined model is still much more successful than the isolated ions model. The quality of the data prevents any strong inferences being drawn about the structure or behaviour of [C_2MIM][Ddc]. [C_2MIM][Ddc] aside, the combined model offers an excellent description of the other three ILs; the agreement between theory and experiment

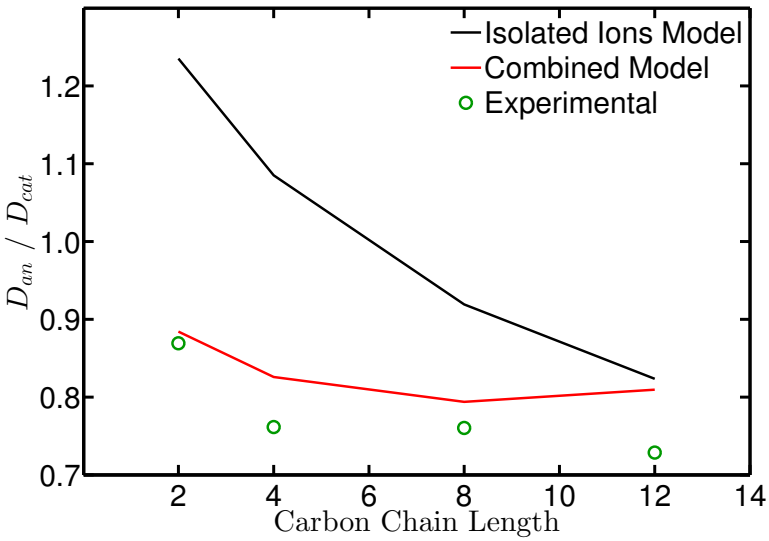

Figure 3.24: Effects of modelling ionic aggregation and ion pairing on the ratio of anion diffusion coefficient to cation diffusion coefficient for $[C_2MIM][Ac]$, $[C_2MIM][But]$, $[C_2MIM][Oct]$ and $[C_2MIM][Ddc]$ at 40 °C. Aggregation includes both charged aggregates and ion pairs *i.e.* both P and n are varied. The modelled data were obtained from the parameters shown in Table 3.2. Experimental data from Figure 3.3 are shown as points and the two different models are shown as solid lines.

is greatly improved compared to the isolated ions model, despite the simplicity of this approach.

In fact, a number of literature studies have used mass spectrometry to assess the degree of ion association in imidazolium and other similar ILs [144, 146, 147]. These studies have found that small, triplet-like aggregates were major constituents of these ILs, with peaks in population at this size. This is in excellent agreement with the results found by the combined model, adding further weight to the usefulness of this approach.

3.5 Conclusion

The physical properties of four imidazolium-based ionic liquids, $[C_2MIM][Ac]$, $[C_2MIM][But]$, $[C_2MIM][Oct]$ and $[C_2MIM][Ddc]$, were investigated using a range of techniques. Both microscopic properties and macroscopic properties were mea-

sured, compared and contrasted. These properties were then modelled using several simple representations of ionic pairing and aggregation.

The different techniques present different perspectives on the IL's structure and properties. Density and conductivity measurements show a simple change across the IL series as the anion chain length increases. Viscosity and diffusion data showed similar trends with some additional complexity, notably a lower viscosity in $[C_2MIM][But]$ than expected. NMR relaxometry showed a yet more complex picture, suggesting some differences in microscopic behaviour across the series, relating to the size and motion of the anion tail.

Molar conductivity, viscosity and diffusion data were shown to deviate from ideal Stokes-Einstein and Nernst-Einstein behaviour, based on a simple picture of single isolated ions. Therefore, three simple models were introduced to account for this discrepancy; first, only neutral ion pairs were introduced, then only charged anion-rich aggregates, and finally the two models were combined to model both structures simultaneously. The ion pair model showed good agreement with theoretical data for the molar conductivity and viscosity data, whereas the experimental ratio of ionic diffusion coefficients showed poor agreement with the model. The aggregate model showed good agreement with molar conductivity and viscosity and, unlike in the pair model, the diffusion ratio was also modelled well. The two models were combined and optimised to find the most effective description of each IL structure. The optimum systems for the majority of the ILs had a very low amount of pairing or none at all, suggesting that the charged aggregate model is more representative of the structure in these ILs. This is in agreement with experimental data in the literature [144, 146, 147].

While they contain a great degree of simplification, it is clear that these models provide a useful insight into the nature of IL structure. For example, it is highly unlikely that ions in $[C_2MIM][Ac]$ exist only as single cations and anion-cation-anion triplets. Despite this, the results presented here suggest that the ions spend the majority of the time switching between configurations that resemble this simple picture, consistent with the short-lived nature of any aggregates that form. Applying these models to different IL systems and comparing results to experimental data will provide insight into the strengths and limitations of this approach.

Chapter 4

Investigation of the Microstructure in 1,5-Diazabicyclo[4.3.0]non-5-enium-based Ionic Liquids

4.1 Introduction

The previous chapter presented a study into the properties of four imidazolium-based ILs and a novel approach to modelling these properties. This new method was successful in modelling the four ILs studied. The next step to any model is to test it on different systems. Therefore, this chapter will study the class of 1,5-diazabicyclo[4.3.0]non-5-enium (DBN) based ILs, applying a similar approach and methodology as in Chapter 3. First, a literature review for DBN-based ILs and the wider class of protic ILs will be presented. Next, a series of DBN-based ILs will be investigated experimentally. Finally, the aggregation and pairing models will be applied to the series. The performance of the models will be evaluated for the DBN-based ILs and the results will be compared to those of the imidazolium-based ILs.

4.1.1 Protic Ionic Liquids

Amongst the many classes of ionic liquids, a distinction can be drawn between aprotic ILs, such as the imidazolium-based ILs, and protic ILs. Protic ILs (PILs) are defined as liquid salts formed by proton transfer from a Brønsted acid to a Brønsted base [39, 136]. As such, they are generally very easy to synthesise, requiring only the mixing of the acid and base. One caveat of these ILs is that the synthesis reaction is actually an equilibrium reaction, potentially reducing the ionic character of system; PILs are often 'poor ionic liquids' because of this [136, 139, 140, 168]. Careful choice of the precursors can mitigate this to an extent, pushing the equilibrium far towards the ionic products.

The key difference between PILs and aprotic ILs is the highly mobile acidic proton in the former, capable of forming strong hydrogen-bonds. This gives rise to many of the unique features of PILs, including microstructure [140, 169, 170], distillation properties [33, 56, 137] and conductivities [139, 140, 168]. Though, it is worth noting that PILs are defined only by their formation, indeed, some aprotic ILs can have moderately acidic protons capable of forming H-bonding networks. The proton attached to the C2 carbon in the imidazolium cation discussed in the previous chapter (see Figure 3.1) is a good example of this [144, 171–173]. There are also structural factors, such as accessibility and orientation [170], that can affect the behaviour of an acidic proton aside from just the strength of the acidity.

As with all ILs, PILs have been shown to form aggregates and structures on the microscopic scale [27, 28]. There are some suggestions that this aggregation is different between protics and aprotics in general [147, 170, 174] but there are many similarities and other structural factors affecting different ILs. For example, Burrell et al. used NMR relaxometry to show that dialkylamine-based PILs with carboxylate anions formed structures with segregated ionic and hydrophobic domains [140]. They found that these structures were formed for cation chain lengths above four carbon atoms (butyl), though, the anion identity also had significant effects. Atkin et al. used neutron scattering to show that these types of heterogeneous microstructures were also formed in PILs with shorter cation chains, such as ethylammonium nitrate [169].

An important feature of protic ILs is their distillability, a highly desirable property for large-scale industrial application. The chemical-equilibrium state in PILs mean the more volatile precursors can boil off at lower temperatures than the ionic product, driving the equilibrium towards the precursors, which then continue to boil off [136]. Leal et al. showed that the gas phase in PIL distillation is formed of isolated, neutral acid or base molecules, in contrast to the gas phase of aprotic ILs, which were shown to contain ionic pairs and potentially even larger ion clusters [137]; this was in agreement with initial work on aprotic IL distillation by Earle et al. [33]. In 2011, a new class of distillable PILs was developed by King et al. [56], based on the tetramethylguanidium cation. Unlike aprotic ILs, these PILs were distillable at atmospheric pressure and lower temperatures, while still capable of dissolving cellulose in comparable amounts to aprotic ILs like [C_2MIM][Ac] [56, 57]. Xie et al. showed that this class of PIL could also dissolve cellulose and CO_2 [41].

4.1.2 Diazabicycloalkene-based Ionic Liquids

While tetramethylguanidium-based ILs were shown to have great potential, they possessed a number of drawbacks including relatively high melting points and high viscosities. Hauru et al. showed one key property in cellulose dissolution to be the acidity of the cation [57], as well as the basicity of the anion; using this, a number of similar protic cations were narrowed down and screened [58]. Out of this study, cations based on diazabicycloalkenes were proven to be effective, with 1,5-diazabicyclo[4.3.0]non-5-ene (DBN) and 1,8-diazabicyclo[5.4.0]undec-7-ene (DBU) cations dissolving cellulose; the significantly lower viscosity of DBN-based ILs made it the favoured PIL for applications. Despite this, many papers have studied DBU-based ILs [175, 176] and their uses, including CO_2 capture/cellulose dissolution [177] and a number of organic sythesis processes [178–180].

The low viscosity and relatively easy distillation of [DBNH][Ac] lends itself well to large scale industrial application. This led to the development of the Ioncell-F process by the Sixta and Kilpeläinen groups in 2015 [89]. The Ioncell-F process uses [DBNH][Ac] as a direct solvent for cellulose, spinning it into strong cellulosic fibres for use in textile production [89–93]. The process is even versatile

enough to find use in upcycling cardboard waste into value-added products [181]. In addition to Ioncell-F, the Ioncell-P process uses DBN-based ILs to pre-treat lignocellulosic material in preparation for the Ioncell-F process [94, 182].

4.1.3 Investigating DBN-carboxylate ILs

[DBNH][Ac] has moved beyond purely academic interest and towards novel applications in the chemical industry. However, there is still much to learn about this important class of IL. When Parviainen et al. reported on the series of PILs, it was found that ILs with this propionate anion had a lower viscosity than those with acetate anion for the DBN, DBU and imidazolium cations [58]. At first glance, this is counter-intuitive, as viscosity would simply be expected to increase with an increase in molecular weight. This was investigated for the $[C_2MIM]^+$ cation in the previous chapter but the simple synthesis of DBN-based ILs allows the anion to be changed with relative ease, allowing a more systematic approach in changing the anion chain length.

In the following chapter, a series of eight DBN-based ILs will be presented in some detail, with anion chain length, l, varying between formate ($l = 1$) and octanoate ($l = 8$). The six room temperature ILs ($l = 3 - 8$) will then be focused on; the microscopic properties of these ILs will be compared and contrasted to macroscopic properties. Finally, the simple pair, aggregate and combined models presented in previous chapters will be applied to the six room-temperature DBN-based ILs, in order to understand the differences in microscopic structure between protic and aprotic ILs. Figure 4.1 shows the $[DBNH]^+$ cation and the eight carboxylate anions used in this study.

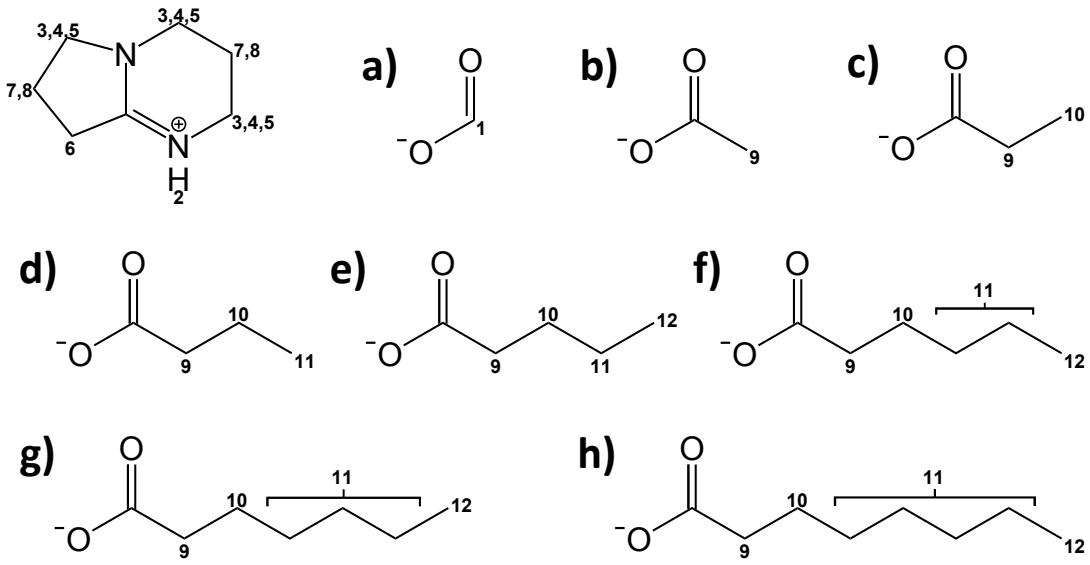

Figure 4.1: The 1,5-diazabicyclo[4.3.0]non-5-enium cation and the eight carboxylate anions in the ionic liquids investigated in this study: **a)** [DBNH][Form] **b)** [DBNH][Ac] **c)** [DBNH][Pr] and **d)** [DBNH][But] **e)** [DBNH][Pent] **f)** [DBNH][Hex] **g)** [DBNH][Hept] **h)** [DBNH][Oct]. ^{1}H NMR resonances are labelled for each cation-anion pair, multiple numbering of protons represents closely overlapping resonance peaks. The large chemical shift of the proton in the formate ion is even higher than that of the labile proton on the $[DBNH]^{+}$ cation but this resonance is not present in any of the other carboxylate anions.

4.2 Materials and Methods

4.2.1 Materials and Sample Preparation

1,5-Diazabicyclo[4.3.0]non-5-ene (DBN) was obtained from Sigma Aldrich with a purity of > 98%. Formic acid (> 95%), acetic acid (> 99.7%), propionic acid (> 99.5%), butyric acid (> 99%), pentanoic acid (> 99%), hexanoic acid (> 99.5%), heptanoic acid (> 99%) and octanoic acid (> 98%) were also obtained from Sigma Aldrich.

The precursor chemicals were stored in a glove box under a dry nitrogen atmosphere prior to use, to avoid exposure to atmospheric humidity. The $[DBNH]^{+}$ ILs were synthesised by dropwise addition of each acid to neat DBN to give the

eight ILs detailed in Figure 4.1. The acids were added sufficiently slowly to prevent any excessive exotherm from the reaction. The resulting ILs were kept in the nitrogen atmosphere until use. Water content in the ILs was measured at various points in the process and found to remain below 0.5 % in all experimental uses [61]. In contrast, when one IL was left on the benchtop exposed to the atmosphere for 4 hours, the water content reached 3%.

4.2.2 NMR Method

Self-diffusion coefficients and low-field relaxation times were measured using the equipment and pulse sequences detailed in Section 2.1.2. Diffusion coefficients were measured across a temperature range of 20 - 60 °C. The [DBNH][Form] and [DBNH][Ac] samples in NMR tubes were melted on a hot plate at ≈100 °C prior to measurement and remained supercooled liquids across the 1 - 2 hour experimental time scale, with the exception of [DBNH][Form] at 20 °C.

Diffusion coefficients were averaged over the relevant peaks for the $[DBNH]^+$ cation (peaks $3-8$) and the carboxylate anions (peaks 1 or 9 - 12) based on the spectral assignment of each peak, as shown in Figure 4.1. The labile proton on the cation (C2 position) was excluded from D calculations, as it tended to diffuse at a substantially different rate to the other cation protons. ^{1}H spectra for all eight ILs are shown in Appendix Figures A.5 to A.12.

4.2.3 Viscosity Method

Steady state viscosity was measured for six ILs using the equipment and methods detailed in Section 2.1.3. Viscosity flow curves were obtained for a temperature range of 30 - 60 °C. Viscosity was not measurable for [DBNH][Form] and [DBNH][Ac] using this experimental setup, as they both quickly crystallised in the rheometer and remained 'superheated' solids at all available temperatures. The other six ILs were liquid at room temperature. This was a contrast to Differential Scanning Calorimetry (DSC) data obtained on these ILs (see Appendix A.2) but is consistent with two separate studies on [DBNH][Ac], that showed it to have a broad melting point between 42 and 63 °C [58, 93]. The same restrictions were encountered for the conductivity and density measurements detailed below.

4.2.4 Conductivity and Density Method

Conductivity and density measurements were carried out on the six room-temperature ILs, using the equipment and methods described in Sections 2.1.4 and 2.1.5, respectively.

4.3 Results

4.3.1 Diffusion

Figure 4.2 shows the temperature dependence of the self-diffusion coefficients, D, of the $[DBNH]^+$ cation for four representative ILs. These four ILs span the full range of D values for the full set and provide some insight into the effects of changing anion size. To the best of the author's knowledge, diffusion data for these ILs is previously unreported but agrees well with similar ILs, such as the imidazolium carboxylates investigated in Chapter 3.

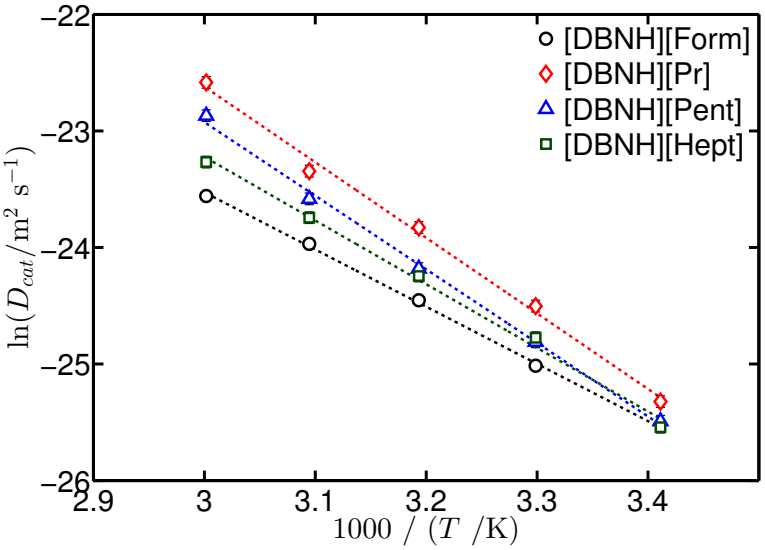

Figure 4.2: Arrhenius plot for self-diffusion coefficients of the $[DBNH]^+$ cation in four of the DBN-based ILs, chosen as a representative sample for clarity. Plots are only shown for the $[DBNH]^+$ cation, as plots for the carboxylate anions show very similar values. Straight lines show fits based on Equation 3.1. Error bars are approximately the size of the data points.

Figure 4.2 shows the diffusion coefficient to increase as temperature increases for all eight ILs, as expected. This temperature dependence is linear on the Arrhenius plot shown in Figure 4.2, suggesting Arrhenius analysis is appropriate here. The dependence of D on chain length can also be seen; D increases from [DBNH][Form] to [DBNH][Pr] but decreases again to [DBNH][Pent] and then [DBNH][Pent]. This indicates there is not a simple relationship between D and the molecular weight of the IL.

Therefore, Figure 4.3 shows the relationship between D and the anion chain length, l, of all eight ILs. The effects of anion size are much more stark here, the trend is the same for all temperatures shown but is clearest at 60 °C. D increases with l at first; there is a clear peak in the diffusion coefficient for [DBNH][Pr] ($l = 3$), before decreasing again as l increases. It is interesting to note that D is approximately the same for [DBNH][Form] and [DBNH][Oct], despite the large disparity in chain length.

It is clear from Figure 4.3 that D is not simply related to anion size/length, as might be expected. Instead, there is something more complex occurring at the microscopic scale of diffusion. It is likely that diffusion will be restricted in the supercooled liquids, due to the stronger interionic forces that cause it to freeze at room temperature. However, the same trend in D remains at 60 °C, *i.e.* D is higher for [DBNH][Pr] than [DBNH][Ac], despite this temperature being above the melting point of this [DBNH][Ac] ($\approx$ 24 °C, see Appendix A.2). However, Parviainen et al. found a melting point of 63 °C for [DBNH][Ac] [58] and Ostonen et al. found the melting point to range between 42 °C and 48 °C. Taken together, these results highlight the complex phase behaviour of these ILs. Therefore, it is possible that this complexity is affecting the D results shown in Figure 4.3.

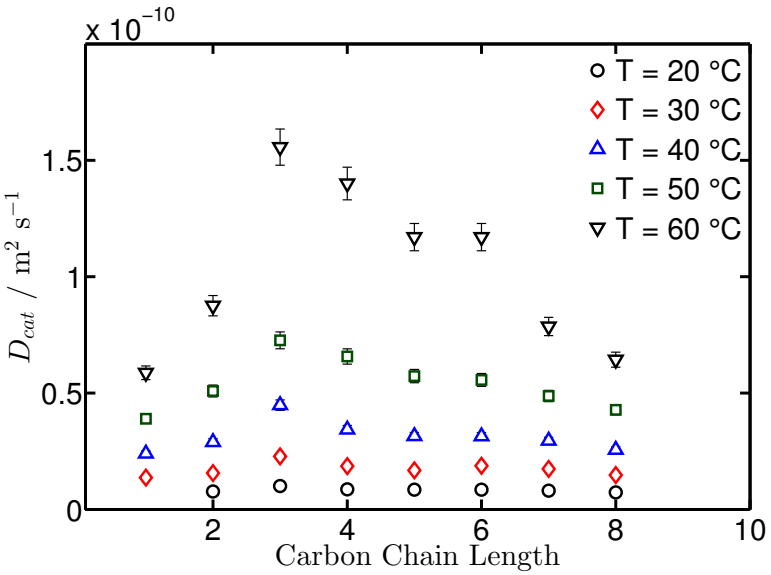

Figure 4.3: Self-diffusion coefficients of the $[DBNH]^+$ cation as a function of anion chain length for all eight of the DBN-based ILs. Plots are only shown for the $[DBNH]^+$ cation, as plots for the carboxylate anions show similar values.

Figure 4.4 shows the ratio between the anion diffusion coefficient to cation diffusion coefficient for all eight of the ILs studied. Figure 4.4a shows the diffusion ratio as a function of temperature and Figure 4.4b shows a comparison of the ratio at 40 °C as a function of anion chain length. Figure 4.4b also shows the expected value for D_{an}/D_{cat}, based purely on molecular weights of the ions (Equation 2.5).

The diffusion ratio values are all below 1, with the exception of [DBNH][Form]. This is consistent with the term "anomalous diffusion", as discussed in Section 3.3.1. D_{an}/D_{cat} also decreases as anion size increases, as expected. In general, there is very little change in D_{an}/D_{cat} with increasing temperature (Figure 4.4a). All eight ILs show a shallow, positive gradient; the ILs become slightly less "anomalous" as temperature increases. There is a slight increase in gradient towards higher l but this is relatively minor compared to experimental uncertainty.

Figure 4.4b shows the dependence of the diffusion ratio on l, that is, D_{an}/D_{cat} decreases smoothly with increasing l. All eight ILs show a markedly lower D_{an}/D_{cat} than expected. The decrease in experimental data matches well with the decrease in the expected values (based on the molecular mass). It is worth noting that the diffusion of [DBNH][Form] and [DBNH][Oct] is not strictly "anomalous"

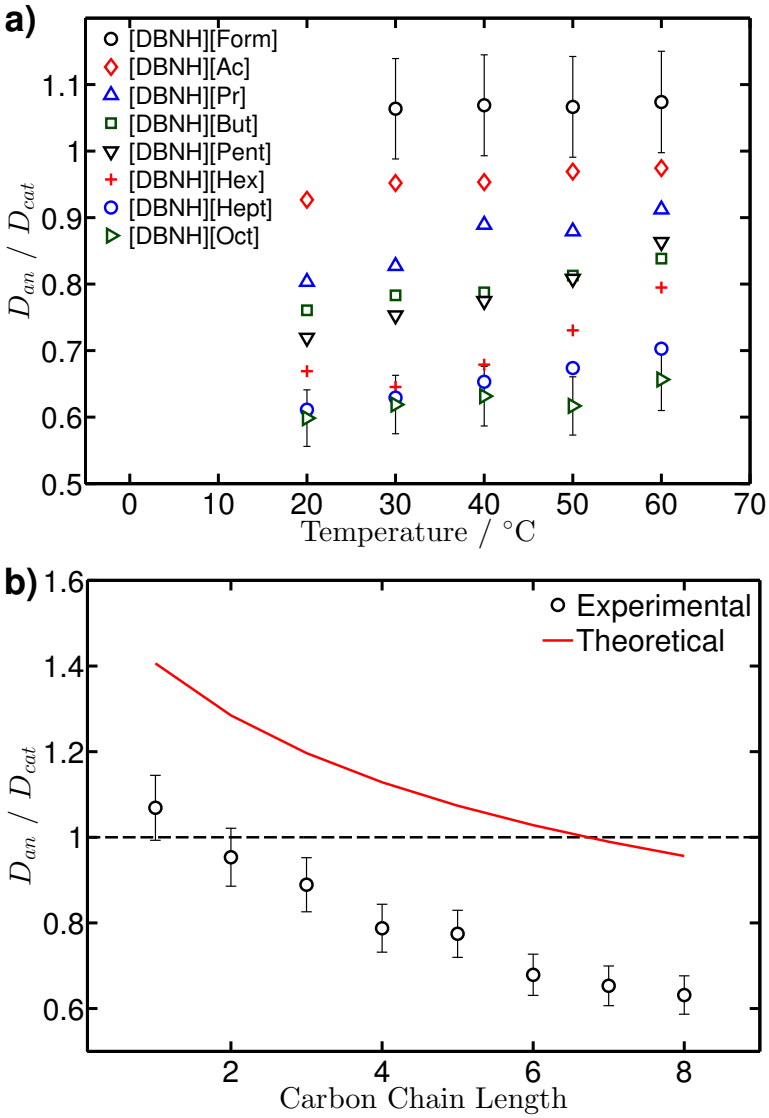

Figure 4.4: Plots showing the ratio of the anion diffusion coefficient to cation diffusion coefficient for the eight DBN-based ILs. Plots show **a)** D_{an}/D_{cat} as a function of temperature and **b)** D_{an}/D_{cat} as a function of the chain length at 40 °C. Representative error bars are shown for [DBNH][Form] and [DBNH][Oct] in **a)** and omitted in the other six ILs for clarity.

in the often used sense *i.e.* the experimental D_{an}/D_{cat} of [DBNH][Form] is above 1 and the D_{an}/D_{cat} of [DBNH][Oct] is expected to be below 1. However, it is clear from Figure 4.4b that the general trend is the same for all eight ILs, as experimental data (points) are all lower than predicted data (red line). Therefore,

it is safe to assume a common phenomenon is acting in all the ILs to give rise to this effect. Potential causes for this are differences in ion geometry, anisotropic local structuring [164] and aggregation between ions [145].

Figure 4.2 shows that $\ln(D_{cat})$ is linear with the inverse-temperature in the temperature range studied. Therefore, it is acceptable to use an Arrhenius fitting to these datasets, according to Equation 3.1, to calculate the activation energy of diffusion and the pre-exponential factor D_0. Figure 4.5 shows the activation energy and D_0 for all eight ILs as a function of anion chain length. The activation energy and pre-exponential factor are shown for both cation and anion, though both ions show very similar trends.

Once again, the activation energy (Figure 4.5a) does not simply increase with increasing anion size, as might be expected. Instead, there is an increase in $E_{a,D}$ up to a peak at $l = 4$, followed by a steady decrease. This is similar to the D values that show a peak at $l = 3$ (Figure 4.3). This means that it requires more energy to break the local bonding structure and begin diffusing for [DBNH][But] than for [DBNH][Form] or [DBNH][Oct]. This suggests there is much stronger local bonding and structuring in [DBNH][But], enough to counteract and exceed the increased $E_{a,D}$ required to diffuse the larger anions in $l > 4$. This could be due to a closer packing in the moderate chain lengths, as these chains will have some hydrophobic bonding from the carbon chains but not so much as to disrupt the hydrophilic/ionic bonding from the charged head-group of the carboxylate.

The $E_{a,D}$ peaks are roughly in line with the D values, which seems counter-intuitive *i.e.* a higher activation energy should give a lower diffusion coefficient. However, the increases in $E_{a,D}$ are counteracted by the pre-exponential factor D_0, shown in Figure 4.5b. D_0 is the diffusion coefficient at 'infinite' temperature, which gives information on the configurational degrees of freedom available to the system and therefore the configurational entropy of the system [183]. A higher D_0 suggests a more ordered system, in agreement with the factors discussed above for the moderate chain lengths.

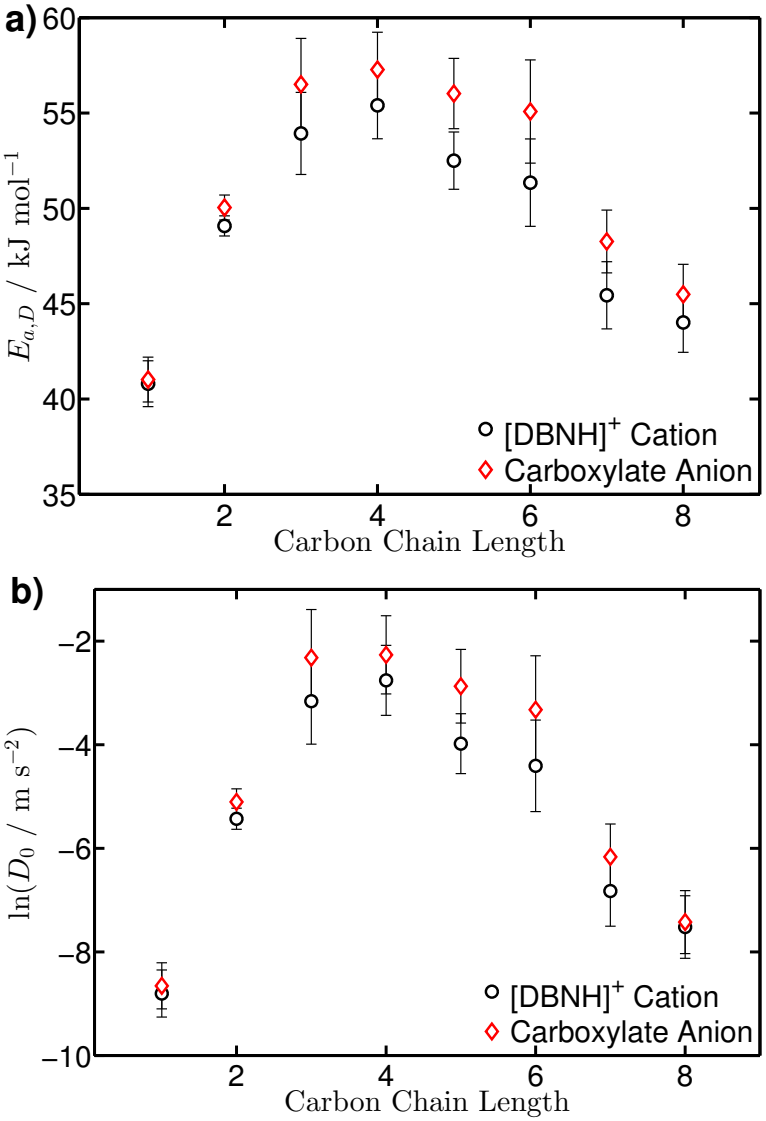

Figure 4.5: Arrhenius fitting parameters as a function of anion chain length for all eight DBN-based ILs, calculated from plots shown in Figure 4.2 and Equation 3.1. Plots show **a)** diffusion activation energy and **b)** the pre-exponential factor, lnD_0. Parameters are given for both cation and anion diffusion data.

4.3.2 Low-field NMR Relaxometry

Figure 4.6 shows the T_1 and T_2 relaxation times for all eight ILs, measured at 20 MHz. Measurements started at 90 °C and worked downwards, in order to ensure [DBNH][Form] and [DBNH][Ac] were liquid, at least at the beginning.

The data showed no discontinuities, suggesting both ILs remained supercooled liquids. T_1 and T_2 both increase with temperature increase, as predicted by BPP theory in the high-temperature regime. However, as with previously discussed results, there is no simple dependence on l. There is a peak in both T_1 and T_2 for [DBNH][Pr], followed by a gradual decrease; the same trend is shown for all temperatures, with only minor differences between T_1 and T_2. This adds further weight to the existence of microscopic structuring.

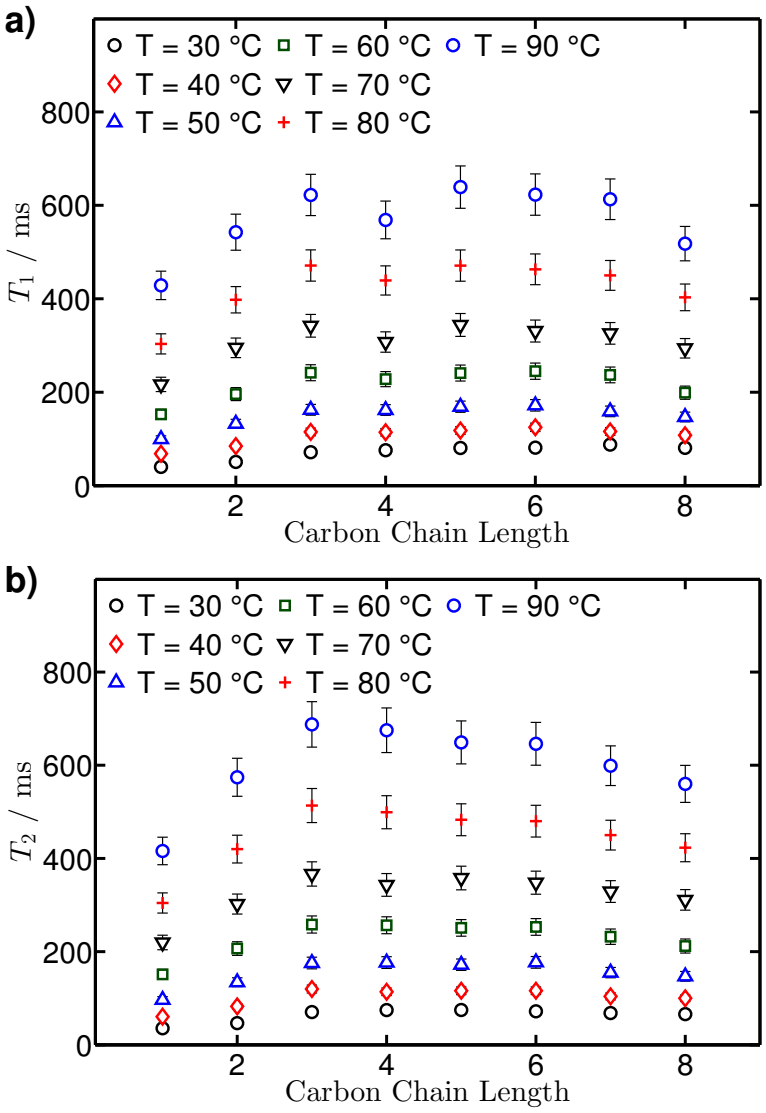

Figure 4.6: NMR relaxation data at 20 MHz as a function of anion chain length for all eight ILs from 30 °C to 90 °C. **a)** T_1 values **b)** T_2 values.

Figure 4.7 shows relaxation data plotted as a function of temperature for several ILs. [DBNH][Form] and [DBNH][Oct] were chosen to represent the minimum and maximum chain lengths and [DBNH][Pr] had the highest T_1 and T_2 values; the remaining five ILs showed very similar trends, with values falling somewhere between the three ILs plotted.

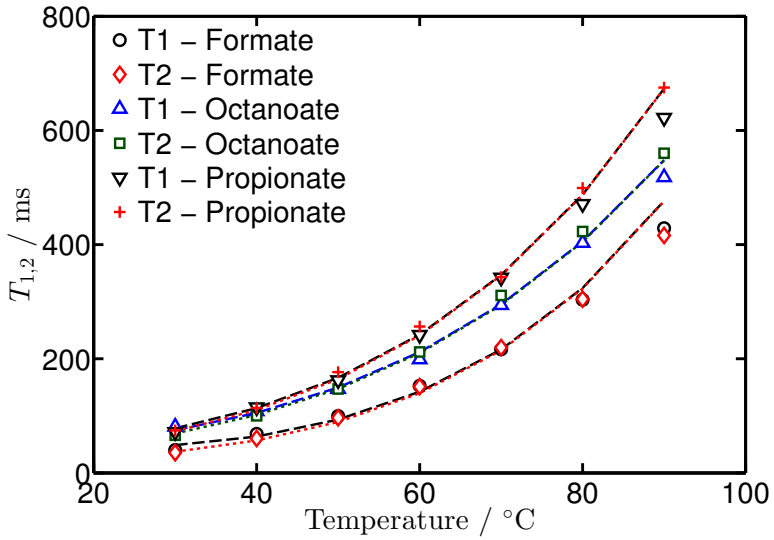

Figure 4.7: T_1 and T_2 relaxation data at 20 MHz as a function of temperature for three representative ILs: [DBNH][Form], [DBNH][Pr] and [DBNH][Oct]. Points show experimentally measured T_1 and T_2, dashed lines show fits obtained from Equations 2.1 and 2.2. Fitting parameters are given in Table 4.1.

Figure 4.7 also shows the fits obtained from BPP fitting for these ILs. The correlation time was modelled using an Arrhenius-type equation (Equation 3.2) and fitted to BPP theory (Equations 2.1 and 2.2) by varying τ_0, $E_{a,\tau}$ and A. These fitting parameters are shown in Table 4.1. T_1 and T_2 are very close in each of the eight ILs, indicating these ILs are in the high-temperature regime at the temperatures studied. This is supported by the BPP fits, which are near-identical for T_1 and T_2, even for [DBNH][Oct]. This is in contrast to the relaxation data for [C_2MIM][Oct], which shows a marked difference between T_1 and T_2, as shown in Figure 3.5c.

The fitting parameters are somewhat consistent across the eight ILs. A is similar for all the ILs, however, $E_{a,\tau}$ and τ_0 show a slight step change between

	A / 10^8 s^{-2}	$E_{a,\tau}$ / kJ mol^{-1}	τ_0 / 10^{-16} s	τ / 10^{-10} s (at 40 °C)
[DBNH][Form]	9.64	41.7	2.18	19.5
[DBNH][Ac]	9.35	40.6	2.34	13.8
[DBNH][Pr]	9.51	34.6	16.7	9.72
[DBNH][But]	9.51	32.7	33.8	9.64
[DBNH][Pent]	9.50	33.6	23.5	9.39
[DBNH][Hex]	9.50	33.1	28.1	9.32
[DBNH][Hept]	9.50	33.4	27.1	9.93
[DBNH][Oct]	9.49	32.3	43.7	10.6

Table 4.1: Fitting parameters for low-field relaxation data shown in Figure 4.6, based on Equations 2.1 and 2.2. Fits for [DBNH][Form], [DBNH][Pr] and [DBNH][Oct] are shown in Figure 4.7.

$l = 1 - 2$ and the other ILs. This is likely related to the suppression of relaxation dynamics in a supercooled or solid state in [DBNH][Form] and [DBNH][Ac]. Once again, these trends are different to those of the imidazolium ILs shown in Section 3.3.2, where there was a significant discrepancy between fitting parameters for T_1 and T_2 of [C_2MIM][Oct]. Firstly, it suggests that the slow dynamics that cause this discrepancy are not simply due to the gyrating motion of the longer anion tail, rather, it supports the hypothesis of aggregate formation involving the octanoate anion in [C_2MIM][Oct]. Additionally, it suggests the cation plays a significant role in the formation of any aggregates, as even the relatively similar [C_2MIM]$^+$ and [DBNH]$^+$ cations lead to substantially different microscopic behaviour.

4.3.3 Viscosity

Figure 4.8 shows the Newtonian viscosity, η, for the six room-temperature DBN-based ILs as a function of chain length. Viscosity decreases as temperature increases for all the ILs, as expected.

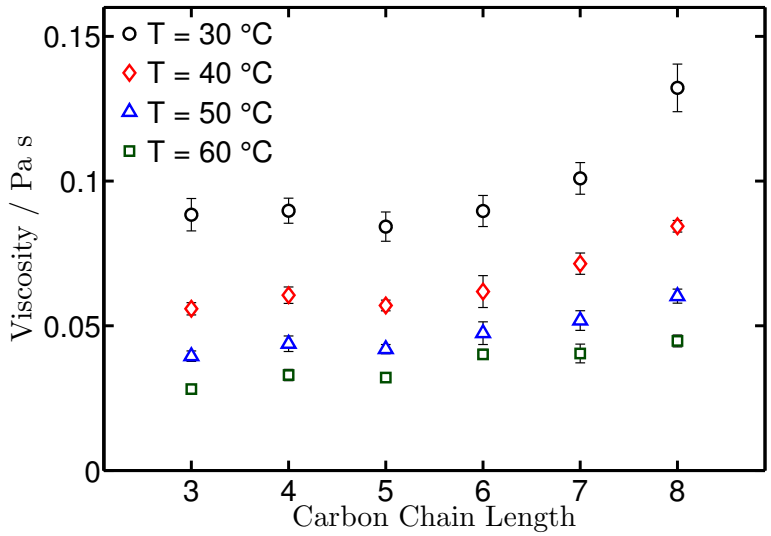

Figure 4.8: Newtonian viscosity of six DBN-based ILs as a function of anion chain length from 30 °C and 60 °C.

The η values shown in Figure 4.8 show a different trend to the diffusion data discussed previously. Instead of a clear maximum/minimum at [DBNH][Pr], there is very little change between $l = 3$ and $l = 6$, followed by a noticeable increase for [DBNH][Hept] and [DBNH][Oct]. This is in contrast to the classically expected result, where η increases uniformly as molecular size increases. Though, previous studies have shown these types of ILs to break that trend [58]. When compared to diffusion, the viscosity data indicates that there is a discrepancy between the microscopic and macroscopic behaviour of DBN-based ILs.

4.3.4 Conductivity

Figure 4.9 shows the molar conductivity from impedance measurements, Λ_{imp}, for six of the ILs. As temperature increases, Λ_{imp} increases as expected. However, the dependence of Λ_{imp} on l is less simple. Λ_{imp} shows a maximum for [DBNH][But], followed by a decrease from $l = 5$ to $l = 8$. This is similar to the peak observed in the diffusion data and will be discussed further in subsequent sections.

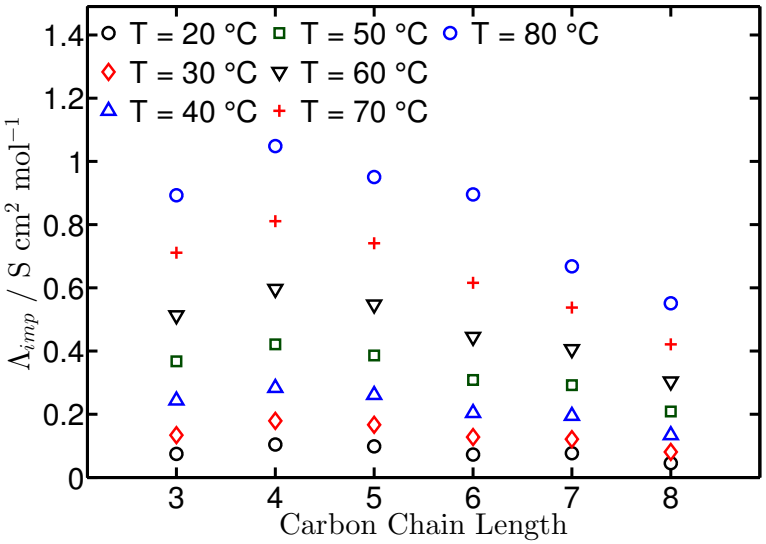

Figure 4.9: Molar conductivity of six room-temperature DBN-based ILs as a function of anion chain length, obtained from impedance measurements. Error bars of 2% are smaller than the data points.

4.3.5 Density

Figure 4.10 shows density as a function of temperature for the six DBN-based room-temperature ILs. The density data broadly behaves as expected; ρ decreases with increasing temperature and increasing chain length. The density values also fall within a similar range to other ILs, including the imidazolium-based ILs presented in the previous chapter (Section 3.3.5). The only notable feature of the density data is that of [DBNH][Pr], which shows less temperature dependence than the rest of the series. This suggests that some of the complexity observed in the microscopic data also extends to the bulk properties of these ILs.

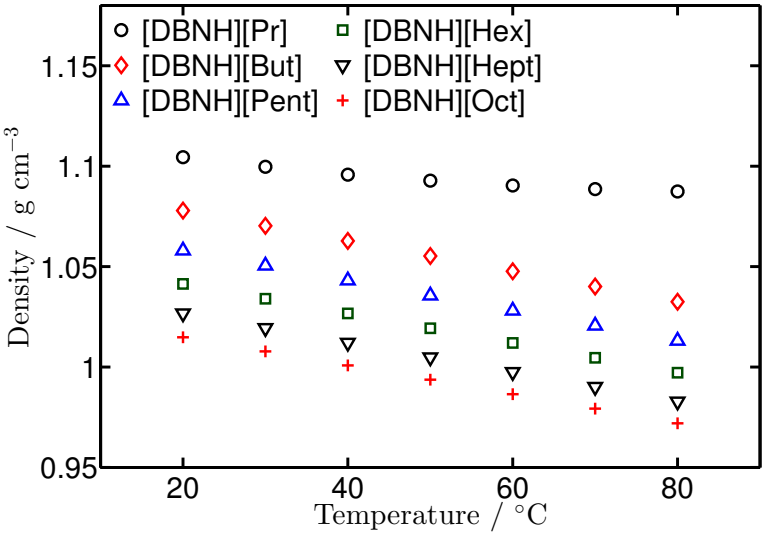

Figure 4.10: Density data for six room-temperature DBN-based ILs as a function of temperature. Error bars of 2% are smaller than the data points.

4.3.6 Stokes-Einstein-Debye Analysis

It is possible to relate the macroscopic viscosity to the microscopic diffusion coefficient using the Stokes-Einstein equation, as discussed in Sections 2.2.2 and 3.3.6. With knowledge of both η and D_i, the hydrodynamic radii can be calculated for an ion or molecule. Figure 4.11 shows the hydrodynamic radii as a function of the anion chain length for the six room-temperature DBN-based ILs (plotted as points), calculated using the Stokes-Einstein equation. Additionally, Equation

2.5 was used to calculate $r_{h,i}$ values for these ILs from the density data (plotted as lines). As before, these two datasets will be referred to as 'Stokes-Einstein' (or 'SE') values and 'density' values, see Section 3.3.6 for more detail.

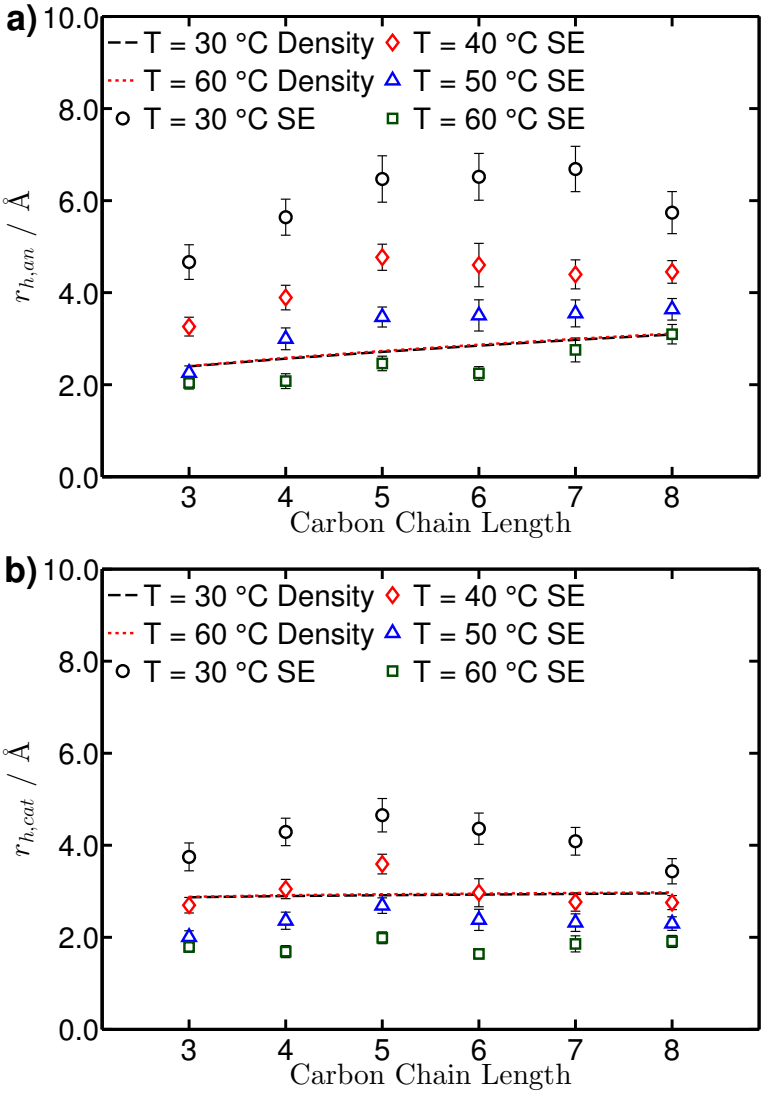

Figure 4.11: Hydrodynamic radii of **a)** the carboxylate anion and **b)** the $[DBNH]^+$ cation as a function of carbon chain length for six room-temperature DBN-based ILs. Points show radii calculated using diffusion data and the Stokes-Einstein equation (Equation 2.4). Lines show radii calculated using density data and Equation 2.5.

As with the diffusion, NMR relaxation and conductivity data, there is a peak

in $r_{h,i}$ as l increases. Interestingly, the peaks occur at different chain lengths for each ion, with the anion peaking between $l = 5$ and $l = 7$ depending on temperature (Figure 4.11a) and the cation peaking at $l = 5$ (Figure 4.11b). This is a striking result, as one would expect the ionic size to increase proportionally with the chain length, particularly with the anion radii; the departure from this trend suggests there is ionic pairing or aggregation, where the size of the aggregates depends on a balance between the size of the anion constituent and the disruption of any aggregate structure by long hydrophobic chains.

$r_{h,i}$ decreases as temperature increases for both anion and cation. This decrease is large and fairly uniform across the six ILs, consistent with the breakup of aggregated structures due to entropic forces. Comparing the radii derived from density data shows a distinction between the two ions. The 'diffusional' $r_{h,cat}$ are broadly in agreement with the 'density' values (Figure 4.11b). Whereas, the 'diffusional' $r_{h,an}$ are larger than the corresponding 'density' values for all temperatures below 60 °C (Figure 4.11a). Along with the higher values for $r_{h,an}$, this suggests that the anion is more involved in any aggregate formation than the cation, consistent with the anion-rich aggregates proposed by Hou et al. [145] and discussed in previous chapters.

Figure 4.12 shows the relation between the NMR relaxation times and the viscosity for [DBNH][Pr] and [DBNH][Oct]. These two ILs were chosen to highlight the maximum difference in behaviour through the IL series; the trends observed here emerge progressively as l increases.

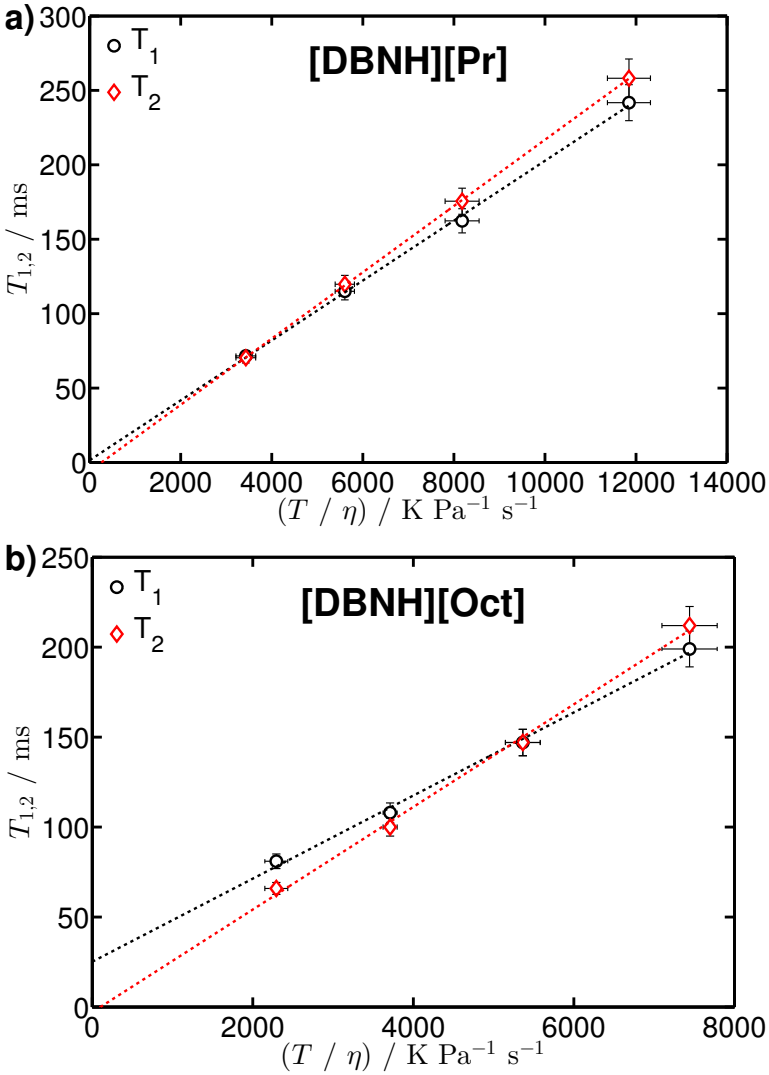

Figure 4.12: Plots showing the relationship between NMR relaxation data and the ratio of temperature and viscosity for **a)** [DBNH][Pr] and **b)** [DBNH][Oct], based on Equation 2.6. Lines show linear fits where the y-intercept was allowed to vary.

According to Equation 2.6, T_1 and T_2 should both show a linear relationship to T/η with an intercept of 0. The data for [DBNH][Pr] (Figure 4.12a) fit this trend near-perfectly, suggesting that [DBNH][Pr] behaves similarly to a molecular liquid on a microscopic scale. For [DBNH][Oct] (Figure 4.12b), the T_2 data also fits the theory well. However, the T_1 data for [DBNH][Oct] deviates from Equa-

tion 2.6. This suggests there are some low-frequency dynamics in [DBNH][Oct] that are not observed by T_1 measurements at 20 MHz; as discussed in Section 3.3.6, this originates from slow motions, either from the longer carbon chain or more substantial aggregate formation in [DBNH][Oct] compared to [DBNH][Pr]. A longer chain will lead to more molecular degrees of freedom, increasing the rotational mobility, and therefore T_1, while the translational mobility, and therefore η, decrease. It is worth noting that the deviation from Equation 2.6 shown by [DBNH][Oct] is substantially smaller than that shown by [C_2MIM][Oct] in Figure 3.11c; this confirms that this effect is principally due to aggregation in [C_2MIM][Oct], not just due to the anion tail. This aggregation will be discussed in more detail in subsequent sections.

Hydrodynamic radii can be calculated for all six room-temperature DBN ILs, using Equation 2.6 and the A values given in Table 4.1. There is insufficient resolution in the 20 MHz spectrometer to distinguish between the cation and anion, but the averaged r_h values for all six ILs fell in the range of 2 - 2.5 Å. These are in good agreement with the $r_{h,i}$ values from density data (Figure 4.11).

4.3.7 Nernst-Einstein Analysis

The Nernst-Einstein equation (Equation 2.10) can be used to calculate the molar conductivity from NMR-measured diffusion coefficients, denoted Λ_{NMR} here. This predicted conductivity can be compared to the conductivity measured by impedance measurements, Λ_{imp}. Therefore, the ratio of Λ_{NMR} to Λ_{imp} for an IL, sometimes known as the inverse-Haven ratio, indicates how well that IL obeys the Nernst-Einstein equation. Figure 4.13 shows the inverse-Haven ratio for the six ILs.

There is a huge discrepancy between the 'ideal' inverse-Haven ratio of 1 and the experimental data shown in Figure 4.13, reaching an order of magnitude at 60 °C. This shows that a picture of a pure ionic electrolytic system, assumed by the Nernst-Einstein equation, is a poor description of these ILs. This is similar to the case of the imidazolium-based ILs discussed in Section 3.3.7, except the DBN-based ILs show a much higher deviation from the ideal case. As with the

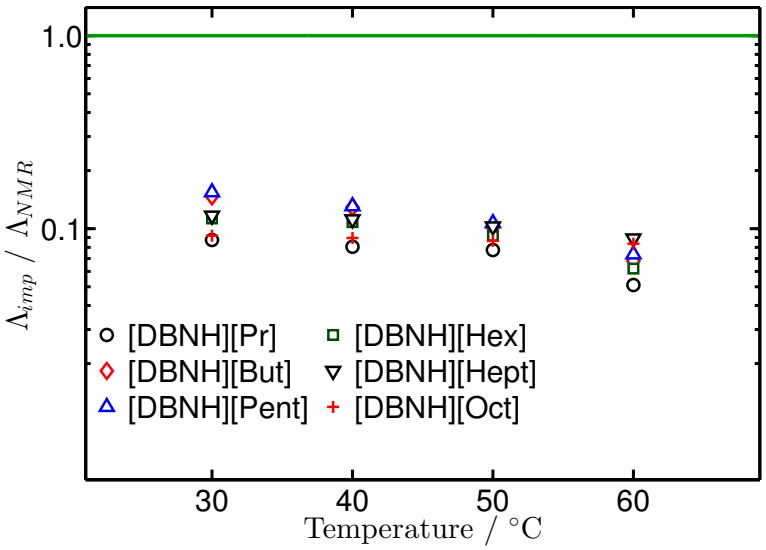

Figure 4.13: Ratio of molar conductivity calculated from impedance measurements (Equation 2.9) and molar conductivity calculated from NMR measurements of diffusion coefficients (Equation 2.10), for the six room-temperature DBN-based ILs as a function of temperature. Λ_{NMR} was calculated simply from D_{cat} and D_{an} values, partially shown in Figure 4.2. Solid line shows a ratio of 1, where the molar conductivity is the value predicted by the Nernst-Einstein equation.

imidazolium-based ILs, it is likely that the cause for this behaviour is ion pairing and aggregation.

Figure 4.14 shows a Walden plot for the six ILs. Walden plots relate the molar conductivity to the viscosity of a liquid, based on the Walden rule (Equation 2.12). The plot shows a line representing an ideal electrolytic solution. As with the inverse-Haven ratio, the data for these ILs falls far below the ideal case. Therefore, it is the molar conductivity that is lower-than-expected, as the inverse-Haven plot and the Walden plot relate Λ_{imp} to D and η data, respectively. This is consistent with conductivity data for DBU acetate by Miran et al. [175], which showed this IL to be a "poor ionic liquid".

There is significant evidence for aggregation in the DBN-based ILs, most notably in the conductivity data reported in this section and the diffusion coefficient ratios in Figure 4.4. However, when compared to some of the trends observed for the imidazolium-based ILs, there appear to be some differences in the nature of

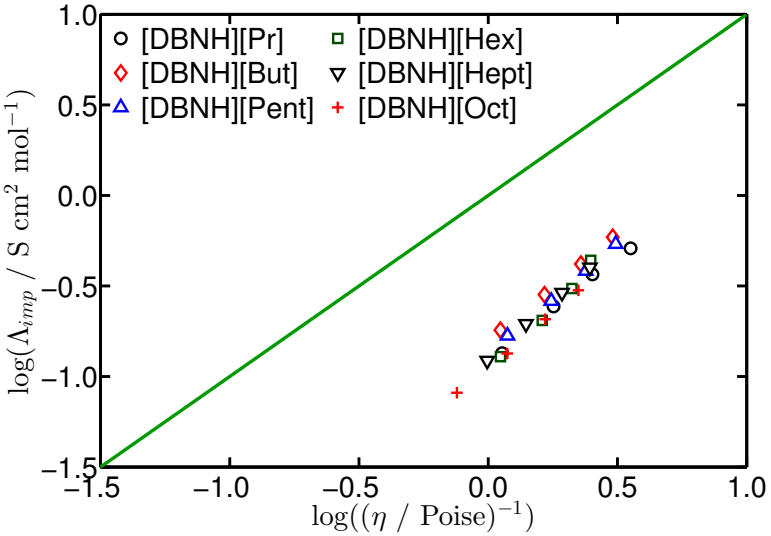

Figure 4.14: A Walden plot for the six room-temperature ILs at a range of temperatures. Molar conductivity is calculated using Equation 2.12, from the conductivity data shown in Figure 4.9. Solid line shows the data for an ideal electrolyte (aqueous KCl), with a gradient of 1.

the aggregate structures of the DBN-based ILs. In particular, Λ_{imp} is comparatively much lower for the DBN-based, suggesting a much lower population of charged ions or aggregates *i.e.* an increased amount of ion pairing.

4.4 Discussion

4.4.1 Pair Model and Aggregate Model

The physical properties of the DBN-based ILs studied here point to the existence of ion pairing and aggregation. In order to better understand the nature of this aggregation, three different models will be applied to the room-temperature DBN ILs: the ion pairing model, the charged aggregate model and a combined model of both pairs and aggregates. See Sections 2.3 and 3.4 for a more in-depth introduction to these models. Appendix C also contains the key equations for each model, as a quick reference.

The aim of this modelling is, once again, to accurately describe *i*) the inverse-Haven ratio *ii*) the Walden relation and *iii*) the ratio of the anion and cation diffusion coefficients, for the series of room-temperature DBN-based ILs.

As with the imidazolium-based ILs, the ratio of the anion and cation diffusion coefficients is moderately lower experimentally than expected from an isolated ions model. However, the discrepancy between molar conductivity experiments and diffusion/viscosity experiments is much more substantial for the DBN ILs than the imidazolium ILs. Therefore, it is expected that the nature of the ionic aggregation will differ between the two classes of IL.

Firstly, the ion pair model will be applied to the DBN data, as a depressed molar conductivity suggests a lack of charge carriers, such as when the ions form uncharged pairs. The model was applied and fitted quantitatively, as detailed in Section 3.4.3. The charged aggregate size, n, was set to 1 (as in the isolated ions case) and the fraction of paired ions, P, was the only fitting parameter.

The fitting parameters for each IL are shown in Table 4.2. As with many of the experimental data, there is no clear trend between chain length and the optimum degree of pairing. The higher P values at either end of the range ($l = 3$ and $l = 8$) suggest a competition between formation of pairs through hydrophilic/ionic bonding and pairing through hydrophobic bonding of the longer aliphatic chains; the more amphiphilic mid-length chains ($l = 4 - 7$) therefore form less pairs.

Dataset Fitted	P
[DBNH][Pr]	0.87
[DBNH][But]	0.79
[DBNH][Pent]	0.76
[DBNH][Hex]	0.82
[DBNH][Hept]	0.82
[DBNH][Oct]	0.85

Table 4.2: Fitting parameters for the ion pair model, applied to the six room-temperature DBN-based ILs. The fraction of paired ions, P, is shown for the optimised fits for each IL fitted separately.

Figure 4.15 shows the effects of the optimised ion pair model on the inverse-Haven ratio and Walden plot for the six DBN-based ILs. In both plots there is a huge improvement compared to those of the isolated ions model (Figures 4.13 and 4.14). In particular, the inverse-Haven ratio plot (Figure 4.15a) shows excellent agreement with the ideal result, accounting for temperature change effects. The individual fits for each IL mean all six ILs fall into similar trends with respect to temperature, with $\Lambda_{imp}/\Lambda_{NMR}$ decreasing substantially as temperature decreases.

The Walden plot of the six ILs (Figure 4.15b) shows a substantial improvement due to the pair model. Though, the majority of the data still falls below the ideal case, they are far closer than for the isolated ions model (Figure 4.14). [DBNH][Pr] shows a near-perfect agreement with the ideal case, using just the pair model. Combined with the improvement in the inverse-Haven ratio plot for this IL, this result hints that a simple pair model is a good approximation for the microstructure in [DBNH][Pr].

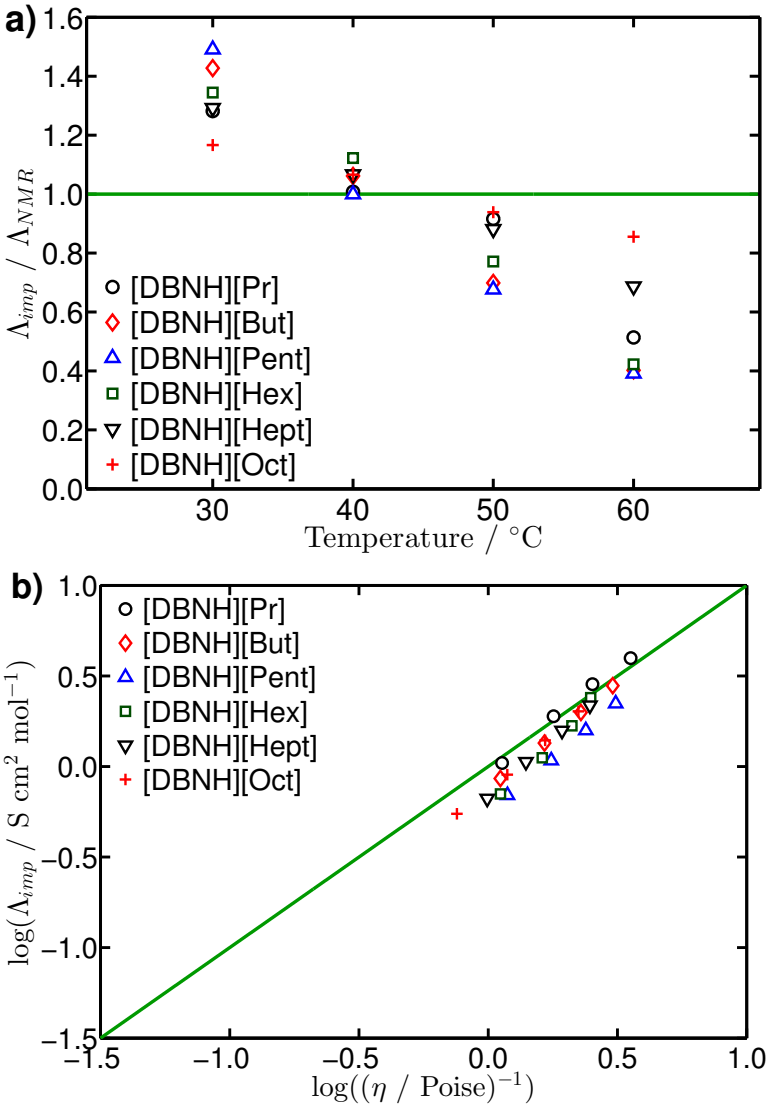

Figure 4.15: Effects of modelling ion pairs on the molar conductivity for the six room-temperature DBN-based ILs. Aggregation is limited to ion pairing (*i.e.* $n = 1$). Fraction of paired ions, P, was optimised for each IL individually. **a)** Ratio of molar conductivities from impedance and NMR measurements, as a function of temperature. **b)** Walden plot for these parameters, see Figure 4.14 for details.

The diffusion coefficient ratio is the third measure of model quality used here. However, the experimental values for D_{an}/D_{cat} in the six room-temperature DBN-based ILs all fall below 1. The pair model cannot produce modelled values significantly below 1 (see Section 3.4.1), and therefore, it is unable to produce a good agreement with the experimental data. This will be presented and discussed in more detail later in this section.

Next, the charged aggregate was applied to the DBN-based ILs, as a comparison to the ion pair model. The pairing fraction, P, was set to 0 and n used as the sole fitting parameter, according to the method described in Section 3.4.3. Here, n is used as the average aggregate size in a distribution of different aggregates, rather than as strict integer values representing the exact number of anions in an aggregate. The fitting parameters for each of these optimisations are shown in Table 4.3.

Dataset Fitted	n
[DBNH][Pr]	13.36
[DBNH][But]	8.59
[DBNH][Pent]	9.33
[DBNH][Hex]	7.96
[DBNH][Hept]	7.21
[DBNH][Oct]	7.51

Table 4.3: Fitting parameters for the charged aggregate model, applied to the six room-temperature DBN-based ILs. Size of charged aggregate, n, is shown for the optimised fits for each IL fitted separately.

The fitting parameters shown in Table 4.3 show a slight trend towards smaller aggregates as the chain length increases, with [DBNH][Pr] the only substantially different result. This suggests the longer chains disrupt the formation of larger aggregates. It is also worth noting that, as with the P values in Table 4.2, the n values for the DBN-based ILs are substantially higher than those of the imidazolium-based ILs in the previous chapter. This follows on from the low molar conductivities of the DBN-based ILs and shows a significant difference between the microscopic structuring in the two classes of ILs.

Figure 4.16 shows the inverse-Haven ratio plot and the Walden plot for the DBN-based ILs, using the optimised charged aggregate model. As with the ion

pair model, the charged aggregate model provides a much better description of the experimental data than the isolated ions model shown in Figures 4.13 and 4.14. Though, this model is less effective at describing the molar conductivity ratio (Figure 4.16a) than the ion pair model; the data for all six ILs is closer to the ideal value of $\Lambda_{imp}/\Lambda_{NMR} = 1$ than the isolated ions model but some of the larger ILs are still far from the ideal case.

The Walden plot shown in Figure 4.16b shows a good agreement between the charged aggregate model and ideal molar conductivities. Like the ion pair model, there is a near-perfect fit for some ILs but a noticeable discrepancy for others. This suggests the charged aggregate picture is somewhat accurate for these ILs. Close inspection of both the inverse-Haven ratio plot and the Walden plot shows that the ILs closer to the ideal case in one plot are those further from ideality in the other plot *e.g.* [DBNH][Oct] shows a poor fit in the inverse-Haven ratio plot but a good fit for the Walden plot. This suggests an antagonistic effect in the fitting procedure, as both these plots are modified similarly by a changing value of Λ_{imp}. Based on this result and the result for the ion pair model, it is likely that a more complex model is required to accurately describe these ILs.

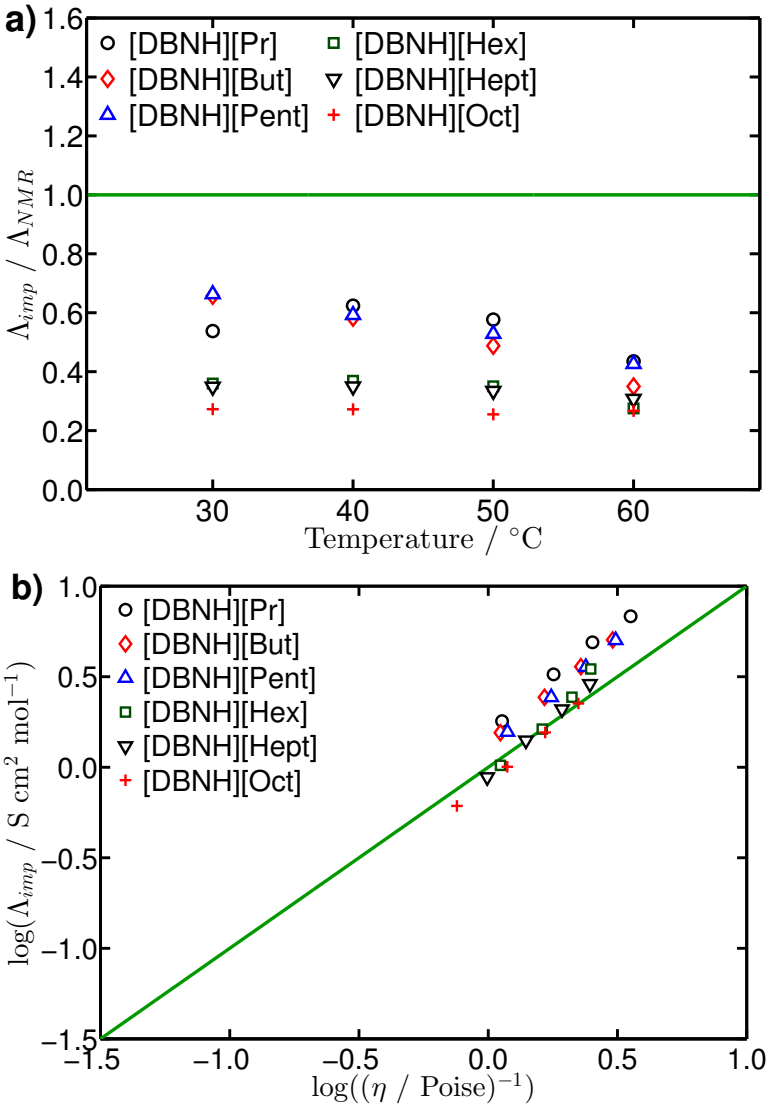

Figure 4.16: Effects of modelling ionic aggregation on the molar conductivity for the six room-temperature DBN-based ILs. Aggregation is limited to charged aggregates only (*i.e.* $P = 0$). Size of charged aggregates, n, was optimised for each IL individually. **a)** Ratio of molar conductivities from impedance and NMR measurements, as a function of temperature. **b)** Walden plot for these parameters.

Figure 4.17 shows the ratio of anion diffusion coefficient to cation diffusion coefficient as a function of anion chain length, optimised as part of the fittings described above. The diffusion ratio is shown for the isolated ions model, the ion pair model and the charged aggregate model.

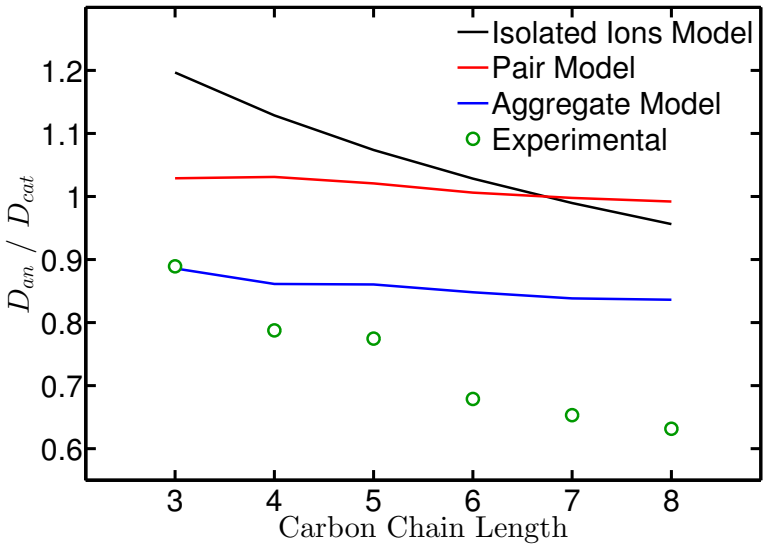

Figure 4.17: Effects of two separate models of ion pairing and aggregation on the ratio of anion diffusion coefficient to cation diffusion coefficient for the six room-temperature DBN-based ILs. The two models were applied separately to each IL, optimising either P or n and keeping the other parameter fixed. Experimental data at 40 °C are shown as points and modelled data are shown as solid lines.

As mentioned earlier, the pair model cannot give a value of D_{an}/D_{cat} much lower than 1. This can be seen graphically in Figure 4.17, where the diffusion ratio is close to 1 for all six ILs. While this is an improvement from the isolated ions model for $l = 3 - 6$, it is not a large improvement. In fact, for $l = 7 - 8$ the pair model actually gives a worse value for D_{an}/D_{cat} than the isolated ions model. In contrast to this, the aggregate model gives a much improved fit for the diffusion ratio, particularly for the shorter chain lengths. The modelling of the diffusion ratio is relatively insensitive to both the size of the aggregate and the size of the anion. Therefore, there is relatively little change in D_{an}/D_{cat} across the IL series. Despite this, the aggregate model provides a much improved description of the diffusion ratio than the ion pair model and the isolated ions

model in all cases.

The behaviour of the diffusion ratio would suggest the aggregate model is the more accurate model for the DBN-based ILs, as with the imidazolium ILs. Whereas, the inverse-Haven ratio plots suggest the ion pair model is more accurate for these ILs. This implies that neither model is complex enough to completely describe the structure of the DBN ILs. Therefore, the two models will be combined and optimised simultaneously in the next section.

4.4.2 Combined Model

The modelling presented in the previous section showed that neither the ion pair model nor the charged aggregate model could accurately describe the DBN-based ILs alone. Therefore, these two models were combined to form a single model with two fitting parameters, n and P, as set out in Section 2.3.4 and applied to the imidazolium-based ILs in Section 3.4.3. Using this combined model allows a greater depth in the fitting procedure and correspondingly, provides a greater insight into the nature of the system studied.

The combined model was applied to each IL individually and optimised by varying n and P simultaneously. The optimised fitting parameters for each IL are shown in Table 4.4. As in Section 3.4.3, n values are estimated as accurate to ± 0.2 and P values to ± 0.1.

Dataset Fitted	n	P
[DBNH][Pr]	6.20	0.21
[DBNH][But]	5.43	0.17
[DBNH][Pent]	6.13	0.14
[DBNH][Hex]	6.29	0.22
[DBNH][Hept]	5.79	0.23
[DBNH][Oct]	6.37	0.26

Table 4.4: Fitting parameters for the combined model, applied to the six room-temperature DBN-based ILs individually. Size of charged aggregate, n, and fraction of paired ions, P, are shown for the optimised fits for each IL.

The plots obtained from these parameters are shown in Figures 4.18 and 4.19. The inverse-Haven ratio and the Walden plot shown in Figure 4.18 both show huge

improvement over the isolated ions model and a good improvement over the ion pair model and charged aggregate model. Most importantly, these improvements have been made simultaneously, showing the combined model to be an effective fit for the DBN-based ILs.

The diffusion ratio fittings shown in Figure 4.19 are less impressive than those of the molar conductivity ratio and the Walden plot. Though, they are still a substantial improvement from the pair model and the isolated ions model, especially for the shorter chain lengths. As discussed in the previous section, the aggregate model can improve the fit of the diffusion ratio but only to an extent; also, addition of pairs on top of charged aggregates does worsen the fit very slightly. Therefore, the combined model struggles to accurately describe D_{an}/D_{cat} for the longer chain lengths, suggesting additional complexity that this model is unable to account for. This slight worsening of the diffusion ratio fit is far outweighed in the fitting procedure by the large improvements in the other two plots.

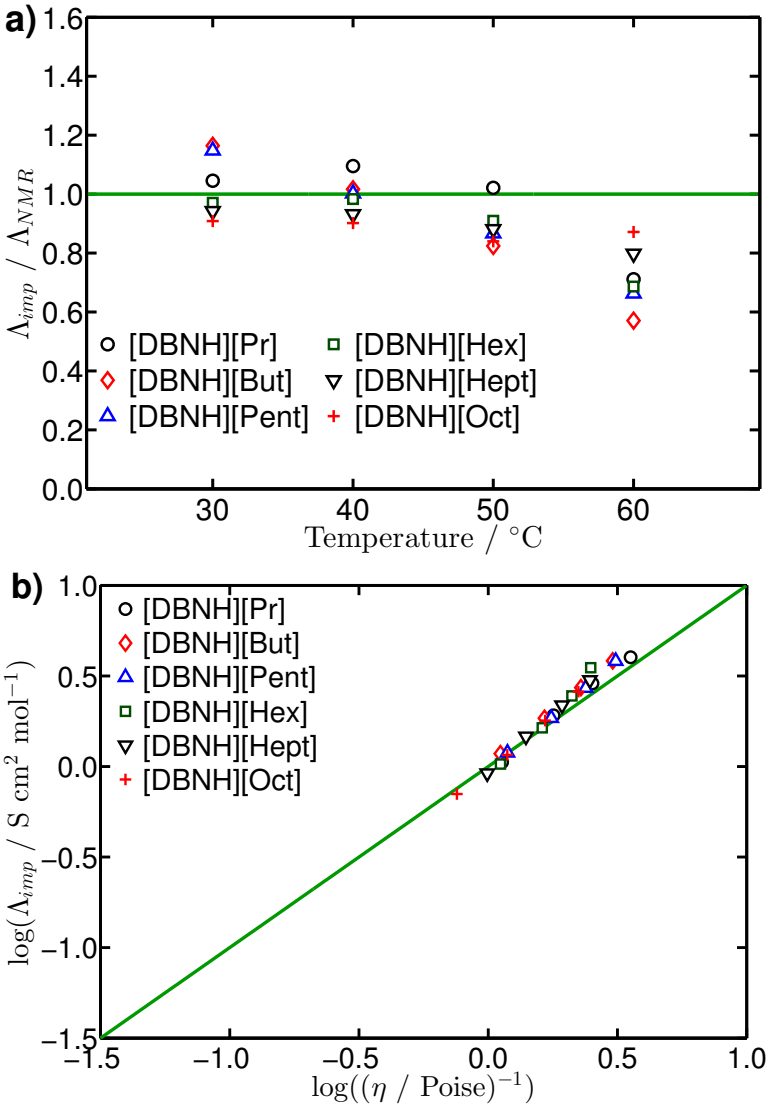

Figure 4.18: Effects of modelling both ion pairing and aggregation on the molar conductivity for the six room-temperature DBN-based ILs. Size of charged aggregates, n, and fraction of paired ions, P, were optimised simultaneously for each IL. **a)** Ratio of molar conductivities from impedance and NMR measurements, as a function of temperature. **b)** Walden plot for these parameters.

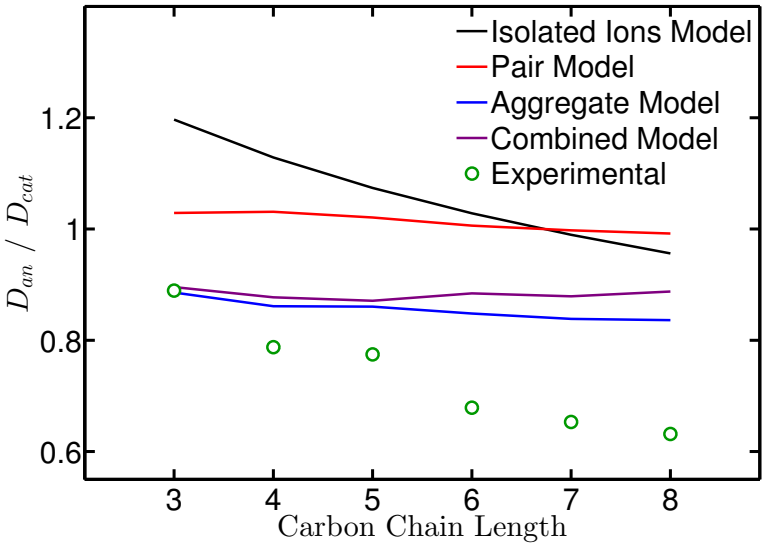

Figure 4.19: A comparison of the three models using the ratio of anion diffusion coefficient to cation diffusion for the six room-temperature DBN-based ILs. Size of charged aggregates, n, and fraction of paired ions, P, were optimised for each IL in each model. The models fitted P separately (pair model), n separately (aggregate model) and then both n and P simultaneously (combined model). Experimental data at 40 °C are shown as points and modelled data are shown as solid lines.

Figure 4.20 shows a comparison of the inverse-Haven ratio for the three models and the isolated ions case at 40 °C. The low Λ_{imp} for the isolated ions model leaves a large discrepancy to correct to obtain the ideal molar conductivity ratio. The aggregate model goes some way to fixing this disparity but not far enough, particularly for the longer anion chain lengths. In contrast to this, the pair model provides a very good description of the ideal case for all six ILs. This agreement is maintained in the combined model, despite the addition of fairly significant aggregation.

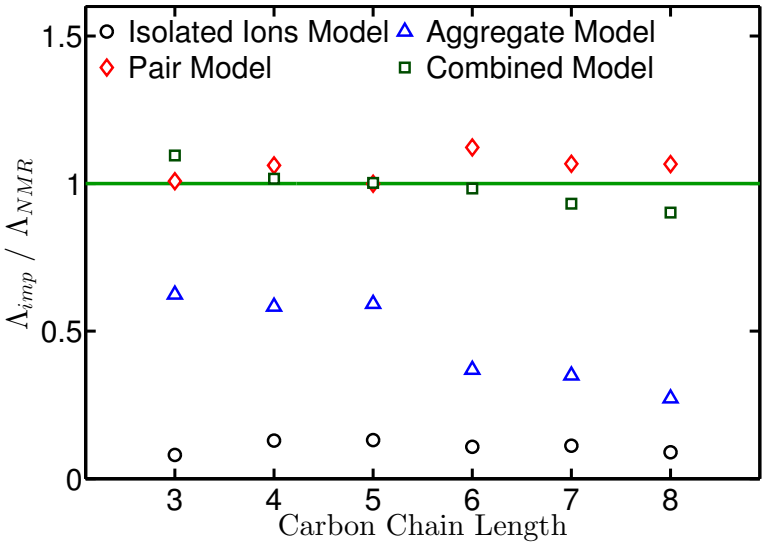

Figure 4.20: A comparison of the three models using the ratio of molar conductivities from impedance and NMR measurements for the six room-temperature DBN-based ILs at 40 °C. Size of charged aggregates, n, and fraction of paired ions, P, were optimised for each IL in each model. The models fitted P separately (pair model), n separately (aggregate model) and then both n and P simultaneously (combined model). Data from the models are shown as points and the solid line shows a ratio of 1, where the molar conductivity is the value predicted by the Nernst-Einstein equation.

Figure 4.21 shows a comparison of the Walden rule at 40 °C for all six ILs. As before, the low Λ_{imp} values for the isolated ions model are far from the ideal result of $\Lambda_{imp} \cdot \eta = 1$. However, unlike the inverse-Haven ratio, both the pair model and the aggregate model provide very good fits with the values for an ideal electrolyte; though the pair model slightly undershoots the ideal case, whereas the aggregate model slightly overshoots the ideal conductivity. The combined model takes both aspects from each model, giving an excellent fit to the ideal data.

The plots presented here indicate that the combined model is the best description for the six DBN-based ILs studied here. Therefore, the fitting parameters provide a useful insight into the true microscopic structuring in these ILs. The parameters in Table 4.4 show a number of interesting features. The n values are all much larger than 1 and the P values are all non-zero, unlike in the imidazolium ILs (Table 3.2). This is further evidence of significant differences in the

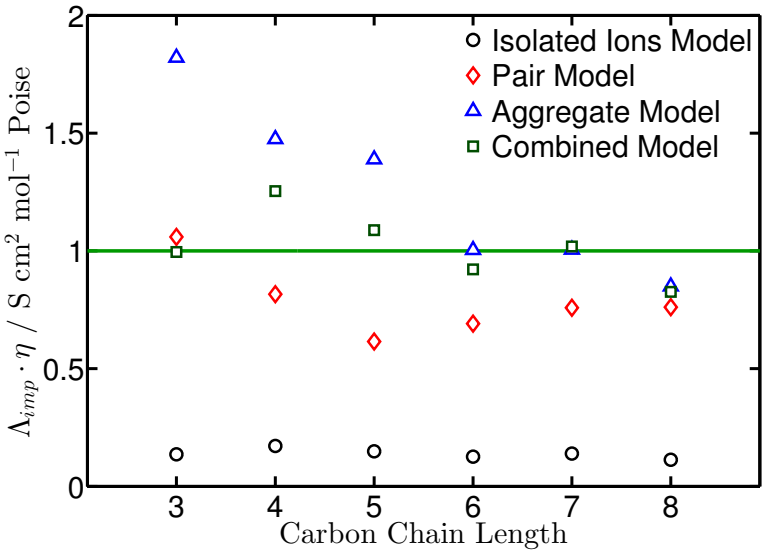

Figure 4.21: Effects of modelling ionic aggregation on the molar conductivity for the six room-temperature DBN-based ILs compared to the viscosity, at 40 °C. Aggregation includes both charged aggregates and ion pairs *i.e.* both P and n are varied. The Walden rule (Equation 2.12) is used to evaluate the model, where the solid line shows the expected data for an ideal electrolyte (aqueous KCl) and data from the models are shown as points. The modelled data were obtained from the parameters shown in Table 4.4.

microstructure between the two classes of ILs and in excellent agreement with the findings of Tsuzuki et al. which showed that protic ILs, such as the DBN-based ILs, have a stronger ion-ion attraction than those of aprotic ILs, such as the imidazolium-based ILs [174]. X-ray crystal structures for several PILs (including [DBNH][Ac]) also show a preference for these ILs to form ion pairs and even larger clusters such as ion pair 'dimers' [56, 58]. Mass spectrometry typically gives information on the gas phase and X-ray diffraction gives information on the solid phase. Therefore, if both methods show signs of ion pairing and aggregation, it is likely that this type of structuring also exists in the liquid phase.

There is a little variation in the n values as the chain length increases, centred around a value of $n = 6$. At first, this seems like quite a large figure for the average aggregate size, suggesting that some very large anion-rich aggregates are formed, balancing with single ions and smaller cation-rich aggregates not accounted for directly in this model. However, Kennedy et al. used electrospray ionisation

mass spectrometry to study PILs and found that clusters of eight cations and larger were formed [147]. It was even found that clusters of eight cations (corresponding to $l = 8$) were unexpectedly abundant in the positive mode, with a large spike in their relative population compared to smaller and larger aggregate sizes. The spike at eight cations was also fairly insensitive to cation side-chain length, consistent with the n values shown here. This is a direct contrast to the modelling shown for the aprotic imidazolium ILs in the previous chapter, which showed clusters of only 2 anions, in agreement with literature [146].

The P values in Table 4.4 show a dip as l increases, followed by an increase to a maximum at $l = 8$. This suggests a lower degree of pairing for [DBNH][But] and [DBNH][Pent], matching well with the elevated molar conductivity in these ILs (Figure 4.9). The degree of pairing and size of aggregates are both lower in the combined model than for the separate models; this is unsurprising, as the two aspects of the model are generally co-operative in their effects. One feature that becomes more apparent with the combined model is the larger sizes and higher degree of pairing in [DBNH][Oct] and [DBNH][Pr]; this suggests that the mid-size anions are striking a balance between increased ionic attraction from the shorter, more polar anions, compared to increased hydrophobic interactions in the longer chains.

4.4.3 Conclusion

A series of eight 1,5-diazabicyclo[4.3.0]non-5-enium ionic liquids with carboxylate anions were studied using a range of techniques. The anions were chosen to provide a systematic variation in carbon chain length, varying between the formate anion and the octanoate anion. A number of different experimental techniques were used to investigate both macroscopic and microscopic properties of the ILs. Three different models were applied to the six room-temperature DBN-based ILs, in order to provide an insight into the microstructure of these ILs.

Different properties had markedly different behaviour as anion chain length, l, was varied. Diffusion, NMR relaxometry and conductivity measurements showed peaks for $l = 3{-}4$. Whereas, density measurements showed a steady decrease with increasing l, in line with the increasing anion size, and viscosity measurements

were fairly insensitive to anion size in the range studied. This spread of behaviour indicates complex behaviour and structuring at the microscopic scale, with several competing factors affected by the change in anion size.

Stokes-Einstein and Nernst-Einstein analysis were used to compare the disparate datasets. Stokes-Einstein analysis provided evidence for anion-rich structuring; Nernst-Einstein analysis and the Walden rule provided evidence for ion pairing. Based on these observations, three simple models were applied sequentially; first, only neutral ion pairs were introduced, then only charged anion-rich aggregates, then the two models were combined to model both structures simultaneously. The two individual models provided some agreement with the experimental and ideal data for the six room-temperature DBN-based ILs, particularly the pair model. The combined model of pairs and aggregates then improved on the individual models, providing an excellent agreement with the ideal case. The nature of these fits allowed a number of inferences to be made about the microscopic behaviour of these ILs. Most notably, the combined model showed that a mixture of ion pairing and charged aggregate formation was the most effective description of all six ILs.

As with the previously discussed imidazolium-based ILs, the modelling method used here provided a good description of the DBN-based ILs and a useful insight into the true microstructure. A significant difference between the two classes of ILs was that the DBN ILs appeared to exhibit a much higher degree of structuring than the imidazolium ILs; the average charged aggregate size was much larger in the DBN ILs and they also showed a non-zero degree of pairing in the optimum fits. This was shown to be consistent with experimental studies on protic ILs [146, 147, 174]. These findings may be helpful in the future design and use of either class of IL.

Chapter 5

Dissolution of Glucose, Cellobiose and Cellulose in 1-Ethyl-3-methylimidazolium Octanoate

5.1 Introduction

Chapter 3 focused on the properties of pure imidazolium ionic liquids and the effects of changing anion chain lengths. As this class of ILs is commonly used for dissolving lignocellulosic materials, specifically using $[C_2MIM][Ac]$, the next step in this line of research is to investigate how changing the anion chain length can affect the dissolution of isolated carbohydrates. To this end $[C_2MIM][Oct]$ was chosen, as a sufficiently different IL to $[C_2MIM][Ac]$ whilst avoiding any of the viscosity problems encountered in $[C_2MIM][Ddc]$. A literature review will be presented, exploring the different aspects of carbohydrate dissolution in imidazolium-based ILs. This will be followed by an experimental investigation into solutions of $[C_2MIM][Oct]$ and three carbohydrates: glucose, cellobiose and cellulose. Finally, a detailed examination of the microscopic environment and properties of these solutions will be undertaken, as a comparison to the established picture in $[C_2MIM][Ac]$.

5.1.1 Carbohydrate Dissolution and the Cation Effect in Imidazolium-based Ionic Liquids

Imidazolium-based ILs have been used for cellulose dissolution since the first studies by Swatloski et al. [47, 49, 50, 52]. In particular, [C_2MIM][Ac] became the favoured IL for many academic studies and applications [57–61, 70, 74, 83, 84, 88, 138, 148, 184], due to its relatively low viscosity and melting point. A wide range of different techniques have been used to better understand the interactions between [C_2MIM][Ac] and cellulose, as well as the properties of their solutions.

Rheological investigations have shown that solutions of cellulose in [C_2MIM][Ac] behave like standard polymer solutions, exhibiting different behaviour in the dilute, semidilute and concentrated regimes [60, 84]. It was also shown that [C_2MIM][Ac] was close to a θ solvent for cellulose and that the thermodynamic quality of the IL solvent decreased as temperature increased [60]. Early NMR investigations by Remsing et al. indicated the solvation of cellulose to occur through one-to-one hydrogen-bonds between IL anions and cellulose hydroxyls, first in [C_4MIM]Cl [51] and then including [C_2MIM][Ac] [59]. This manner of interaction was similar to the previously studied cellulose solvent dimethylacetamide (DMAC) and LiCl [47] and was backed up by a number of computational studies [70, 74, 184, 185].

The exact role of the imidazolium cation in cellulose dissolution has remained more elusive, in contrast to the role of the anion. From the beginning, it was clear that the identity of the cation is vital in cellulose dissolution [47]. However, there was some debate about whether the cation had a direct effect, *e.g.* by bonding to the cellulose, or an indirect effect, through limiting viscosity or stabilising the anion while it bonds to cellulose hydroxyl groups.

NMR studies by Zhang et al. suggested that the imidazolium cation formed strong H-bonds with the cellulose dimer, cellobiose [186]. This claim was hotly contested by Remsing et al. who proposed the cation's role was entirely non-specific with respect to cellulose [187, 188]. A number of computational studies were undertaken separately, indicating weak hydrophobic bonding between the cation and cellulose [70, 71, 184, 185]. Experimental studies by the Sixta and Kilpeläinen groups have shown that the acidity of the cation plays a key role in

an IL's ability to dissolve cellulose [57, 58]. More specifically, they demonstrated that the difference between the cation acidity and the anion basicity was the key parameter, based on the Kamlet-Taft parameters of different ILs [57]. This provides further support to the concept that the cation does play some part in the solvation process but the interplay between the cation and the anion is more important than the cation identity alone [63].

5.1.2 Effects of Modifying the Carboxylate Anion

As mentioned previously in Section 3.1.2, one advantage of imidazolium-carboxylate ILs, such as $[C_2MIM][Ac]$, is that there are modifiable aliphatic carbon chains on both the cation and the anion. Systematic structural studies into carbohydrate dissolution have generally focused on changing the cation side-chain [47, 55, 71, 74, 88, 160]. For the most part, increasing cation chain length only affects the viscosity of the IL and the mobility of the ions, with a few exceptions. For example, Schubert et al. found evidence of an odd-even effect on cellulose solubility when changing the cation chain length [88, 160] and Rabideau et al. found that increasing cation chain length led to increased anion bridging when binding to cellulose hydroxyl groups [71].

Studies into modifying the carboxylate anion have generally focussed on short chain lengths [52, 56–58]. Zhao et al. performed an in-depth study on anion chain lengths in cellulose dissolution, ranging from formate (one carbon atom) to butyrate (four carbon atoms) and including several branched derivatives [54]. They found a peak in the solubility for $[C_2MIM]$ propionate, compared to $[C_2MIM][Ac]$, as well as an improvement in solubility from the disubstituted *iso*-butyrate compared to straight-chain *n*-butyrate. Their findings highlight the importance of both anion size and anion structure.

Xu and Wang et al. performed a series of studies on imidazolium-based ILs with a range of carboxylate anions [80, 155, 189]. They studied the 1-allyl-3-methylimidazolium cation [80] and the 1-butyl-3-methylimidazolium ($[C_4MIM]^+$) cation [155], systematically varying the length of the carboxylate anion from formate to butyrate. In both cases, the propionate anion was found to give the highest cellulose solubility; this was ascribed to an increased electron donating

power in the longer chains, compared to the acetate anion. However, their results were subject to a number of shortcomings, including short dissolution times and lack of atmospheric control, meaning kinetic factors could have significantly impacted the results. Additionally, computational work by King et al. showed the proton affinities, and therefore electron donating power, were very similar for the propionate and acetate anions [138].

At this point, it is worth drawing the distinction between cellulose and other carbohydrates studied in literature. Cellulose is the polymeric form of glucose (Figure 5.1a), where the repeat unit is two anhydroglucose units (AGUs) in opposing conformations, as shown in Figure 5.1c. The dimer unit (two AGU) is known as cellobiose and is shown in Figure 5.1b. The majority of publications use cellulose, as the most industrially relevant compound, but a number of publications have used glucose [59, 70, 148] and cellobiose [59, 148, 186] as simplified model systems of cellulose.

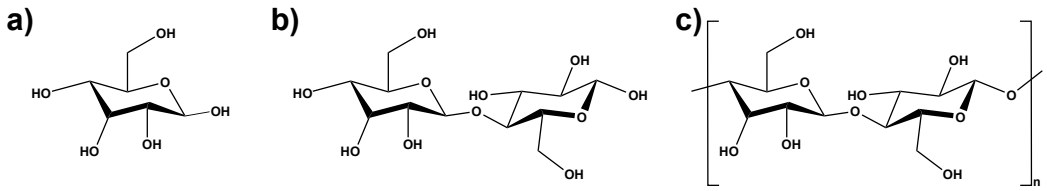

Figure 5.1: The three carbohydrates used in this study: **a)** glucose, **b)** cellobiose and **c)** cellulose.

5.1.3 The 5,4,3 Rule in 1-Ethyl-3-methylimidazolium Acetate

Previous work by the Ries and Budtova groups investigated the rheological and NMR properties of cellulose solutions in $[C_2MIM][Ac]$ and $[C_4MIM][Cl]$ [60, 61, 84]. Following on from these studies, Ries et al. used pulsed-field gradient NMR to investigate solutions of glucose, cellobiose and cellulose in $[C_2MIM][Ac]$, in order to elucidate the dissolution mechanism of these carbohydrates [148].

It was found that the self-diffusion coefficient, D, of both ions decreased as carbohydrate concentration increased, as expected. However, D decreased faster for glucose solutions, then cellobiose solutions, then cellulose, in contrast to what

would be expected based on viscosity in those systems. As discussed in previous sections, it was known from simulations that carbohydrate-IL interactions occurred principally through H-bonding between the anion and the carbohydrate hydroxyl groups. Glucose, cellobiose and cellulose possess a different number of hydroxyl groups per AGU: 5 for glucose, 4 for cellobiose and 3 for cellulose. Therefore, the associated fraction of hydroxyl groups, α, was introduced to replace the concentration by weight percentage, defined as the following [148],

$$\alpha = N \frac{M_{IL}}{M_{AGU}} \frac{\phi}{(100 - \phi)} \tag{5.1}$$

where N is the number of hydroxyl groups per AGU, M_{IL} is the molar mass of the IL, M_{AGU} is the molar mass of the 'repeat unit' (180, 171, and 162 g mol^{-1}, respectively, for glucose, cellobiose, and cellulose) and ϕ is the weight percentage of dissolved carbohydrate. Practically, α is a hydroxyl-weighted fractional molar concentration of carbohydrate to IL, and the three carbohydrates will have three different α values for any given weight percentage.

By rescaling diffusion data for α, a unified trend was obtained for all three carbohydrates. This provided strong experimental evidence for a one-to-one interaction between the acetate anion and carbohydrate hydroxyl groups. In the same paper, it was also shown that the chemical shift change, $\Delta\delta$, for [C_2MIM][Ac] solutions also correlated with α; later, the same was found for T_1 and T_2 relaxation data [190]. This correlation between physical properties and α will here be referred to as the "5,4,3 rule", after the respective number of hydroxyl groups on glucose, cellobiose and cellulose.

5.1.4 Carbohydrate Dissolution in 1-Ethyl-3-methylimidazolium Octanoate

The mechanism and solvation environment of [C_2MIM][Ac] have been extensively studied and there has been some investigation of other short carboxylate chain lengths, as discussed above. However, the effects of using a longer carboxylate chain for carbohydrate dissolution, such as the octanoate anion presented in Chapter 3, have remained unexplored. It has been demonstrated in previous

chapters that the anion chain length has noticeable effects on the physical properties of ILs, therefore, it would be expected that some of these changes will affect the dissolution of carbohydrates.

$[C_2MIM][Oct]$ was chosen as a suitable IL for this study; the octanoate chain is sufficiently long to affect the properties of the IL, compared to $[C_2MIM][Ac]$, but short enough to avoid the viscosity issues found in $[C_2MIM][Ddc]$. The work of Ries et al. [148] will be reproduced for $[C_2MIM][Oct]$, in order to compare and contrast the effects of changing the anion chain length. Figure 5.2 shows the structure of $[C_2MIM][Oct]$, including the assigned NMR proton resonances.

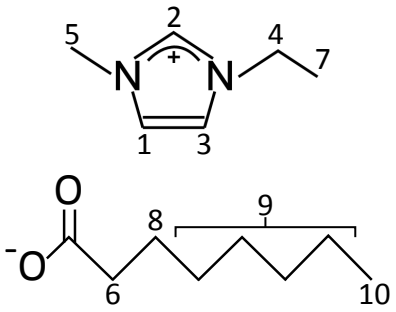

Figure 5.2: 1-ethyl-3-methylimazolium octanoate, the ionic liquid principally investigated in this study. ^{1}H NMR resonances are labelled according to previous publications [148].

5.2 Methods and Materials

5.2.1 Materials and Sample Preparation

$[C_2MIM][Oct]$ was obtained from IoLiTec GmbH, Germany, with a purity of $> 95\%$. Glucose, cellobiose and Avicel PH-101 microcrystalline cellulose (DP ≈ 180) were obtained from Sigma Aldrich. Prior to dissolution, all carbohydrates were dried under vacuum at 80 °C for a minimum of 12 hours. Water content in the pure $[C_2MIM][Oct]$ was measured by Karl-Fischer titration and found to be $< 0.2\%$.

IL-carbohydrate solutions for NMR samples were all prepared in a glove box, as detailed in Section 2.1.1. Samples for viscosity were sealed under a nitrogen

atmosphere during mixing. Glucose, cellobiose and cellulose were mixed with [C_2MIM][Oct] under constant stirring at 60 °C for 6 hours, followed by additional stirring at room temperature for 12 - 72 hours, as required. Solutions in the range of 0 - 15% glucose and cellobiose were prepared, by weight, and in the range of 0 - 10% for cellulose. Attempts were made to obtain solutions with a cellulose concentration $>$ 10% but the high viscosity of these solutions meant these concentrations were unobtainable on a reasonable timescale. The weight percentage was used for carbohydrate concentration, calculated as follows: wt% $= m_{solute}$ / $(m_{IL} + m_{solute})$, where m_{IL} and m_{solute} are the mass of the IL solvent and dissolved solute respectively.

Clough et al. have previously reported carbohydrate decomposition during dissolution in this type of IL above 100 °C, catalysed by the imidazolium cation [86]. Additional work was undertaken to ascertain the validity of our dissolution method and it was found that no measurable decomposition occurred under these conditions, see Appendix section B.1 for further details.

All [C_2MIM][Ac] data was obtained, with permission, from previous publications [61, 84, 148, 190].

5.2.2 Viscosity Method

Viscosity was measured using the equipment and techniques detailed in Section 2.1.3.

5.2.3 NMR Method

Self-diffusion coefficients and low-field relaxation times were measured using the equipment and pulse sequences detailed in Section 2.1.2. Diffusion coefficients for each ion were averaged over the relevant peaks for the imidazolium cation (peaks 1-5, 7) and the octanoate anion (6, 8-10) based on the spectral assignment of each peak, as shown in Figure 5.2.

Chemical shift values, δ, were measured for each proton resonance as part of PFG diffusion experiments. Proton resonance 5 was used as a reference point for chemical shift calibration, according to several publications that have shown δ for this resonance to be stable under a wide range of conditions [148, 157, 186]. The

δ values of each resonance in pure [C_2MIM][Oct] were then used to calculate the change in chemical shift, $\Delta\delta$, as carbohydrate concentration increased for each of the three carbohydrates.

5.3 Results

5.3.1 Viscosity

Figure 5.3 shows the temperature dependence of viscosity, η, for solutions of glucose, cellobiose and cellulose dissolved in [C_2MIM][Oct]. Viscosity was calculated from the Newtonian plateau in steady-state flow curves for each carbohydrate concentration and temperature.

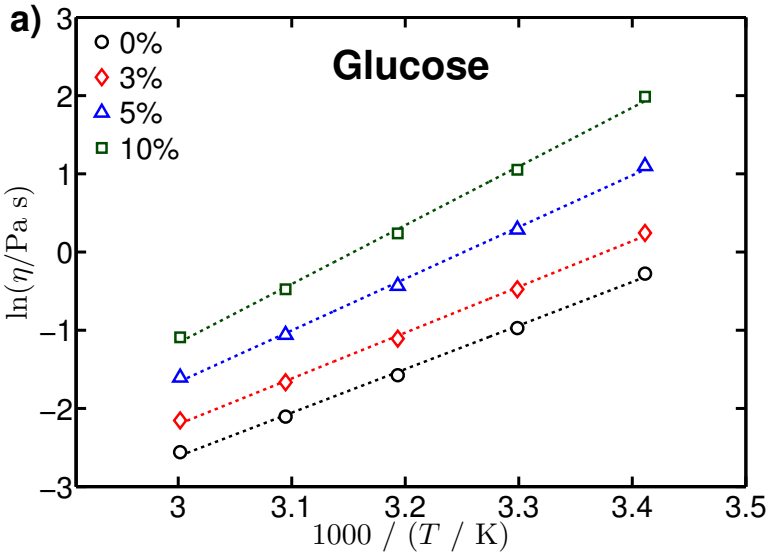

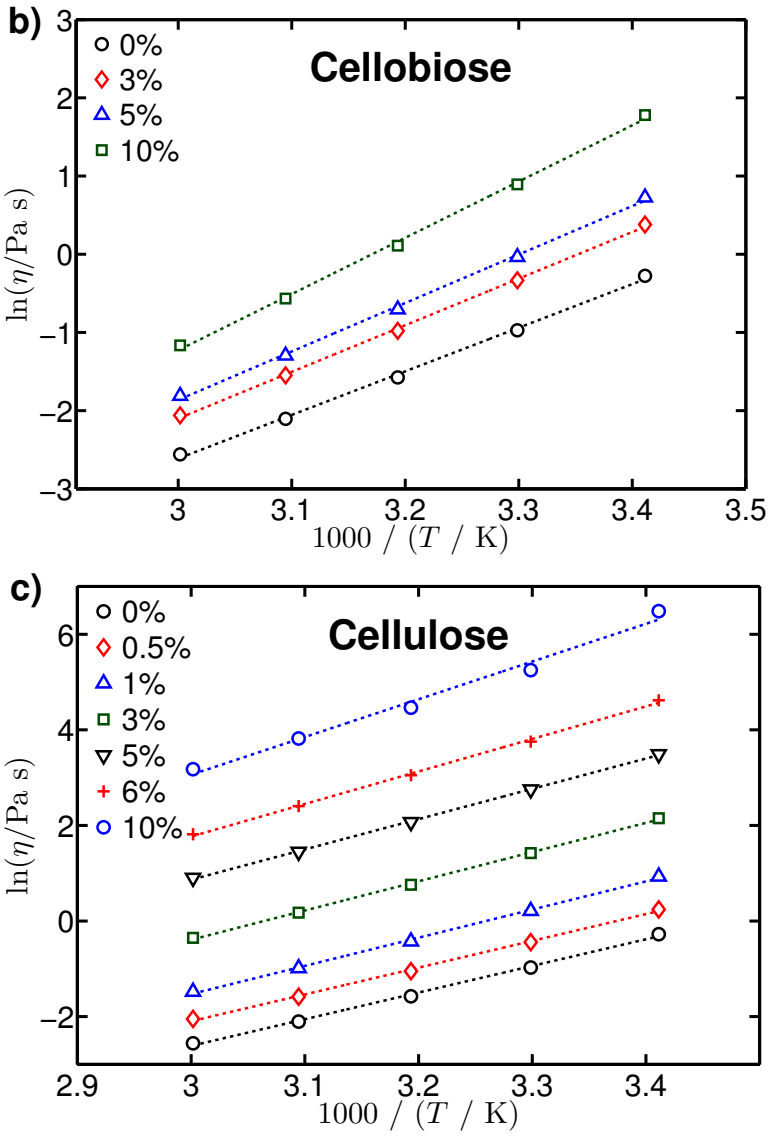

Figure 5.3: Arrhenius plots for viscosity in solutions of carbohydrates dissolved in $[C_2MIM][Oct]$. Plots show solutions of **a)** glucose, **b)** cellobiose and **c)** cellulose at a range of concentrations (in weight percentage). Error bars are approximately the size of data points . Straight lines show fits based on Equation 5.2.

The plots in Figure 5.3 show that increasing temperature and decreasing carbohydrate content lead to a decrease in viscosity in all three cases, as expected. Glucose and cellobiose (Figures 5.3a and 5.3b) give similar η values, indicating these simple sugars behave broadly the same in solution. In contrast, dissolving cellulose leads to markedly higher viscosities (Figure 5.3c), as expected from the polymeric nature of cellulose.

Figure 5.4 shows η as a function of carbohydrate concentration for solutions of glucose, cellobiose and cellulose in $[C_2MIM][Oct]$, at a temperature of 40 °C. Solutions of glucose, cellobiose and cellulose in $[C_2MIM][Ac]$ show near-identical trends but at a lower viscosity [190].

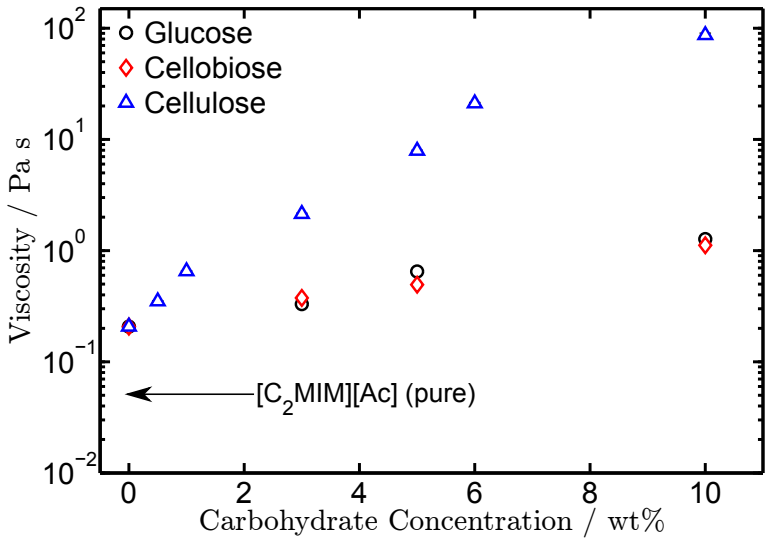

Figure 5.4: Newtonian viscosity as a function of carbohydrate concentration for solutions of glucose, cellobiose and cellulose in $[C_2MIM][Oct]$, at a temperature of 40 °C. Viscosity for pure $[C_2MIM][Ac]$ is marked for reference. Errors are approximately the size of the data points.

It is even clearer from this plot that, for both ILs, glucose and cellobiose have a much smaller effect on η than cellulose. It should be noted that the higher viscosity of $[C_2MIM][Oct]$ prevented the dissolution of $\geq 15\%$ cellulose in this IL on a reasonable timescale. Pure $[C_2MIM][Oct]$ has a higher viscosity than pure $[C_2MIM][Ac]$, as shown in Chapter 3; this feature is retained in carbohydrate solutions, with $[C_2MIM][Oct]$ solutions all exhibiting a viscosity roughly 4 times

that of the corresponding [C_2MIM][Ac] solutions. Figure 5.5 shows the relative viscosities, η_{rel}, for cellulose solutions in [C_2MIM][Oct] and [C_2MIM][Ac], at each cellulose concentration. η_{rel} is the ratio of the viscosity of the IL-cellulose solution and the viscosity of the pure IL.

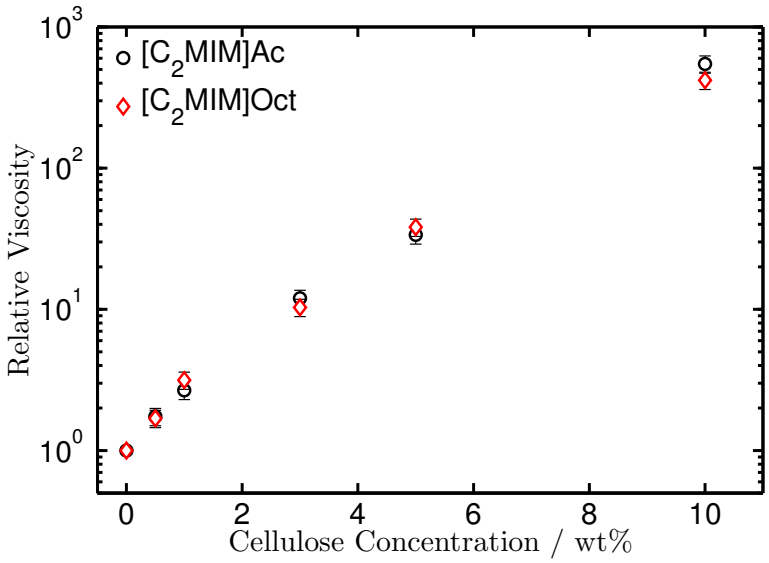

Figure 5.5: The relative viscosities of [C_2MIM][Oct] and [C_2MIM][Ac], as a function of cellulose concentration for solutions in both ILs, at a temperature of 40 °C.

The relative viscosity for [C_2MIM][Oct] and [C_2MIM][Ac] solutions are equal for all cellulose concentrations, within experimental error. In fact, considering the η values cover 3 orders of magnitude, the relative viscosities remain remarkably close. This provides a firm indication that for cellulose, the intrinsic viscosity, and therefore the solvent quality, of [C_2MIM][Oct] is the same as that of [C_2MIM][Ac]. Based on this, it is likely that the local interactions between cellulose and [C_2MIM][Oct] in solution will be similar to those of [C_2MIM][Ac] too.

The Arrhenius-type plots shown in Figure 5.3 exhibit linear dependences in all cases. Therefore, Arrhenius analysis is appropriate for these systems, using the following,

$$\ln\eta = \ln\eta_0 + \frac{E_{a,\eta}}{RT} \tag{5.2}$$

where η_0 is the viscosity at infinite temperature, $E_{a,\eta}$ is the activation energy of

viscous flow and R is the universal gas constant. Figure 5.6 shows the activation energies obtained from this analysis for all three carbohydrates dissolved in [C_2MIM][Oct].

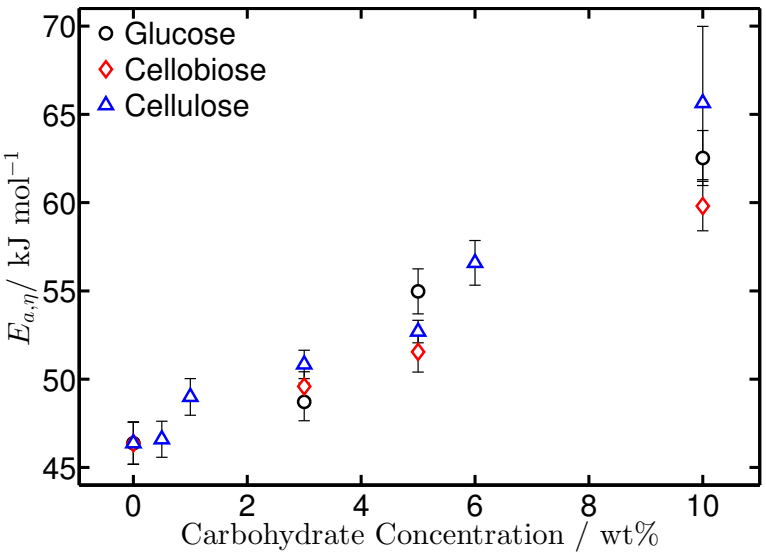

Figure 5.6: Activation energy of viscous flow as a function of carbohydrate concentration for solutions of glucose, cellobiose and cellulose in [C_2MIM][Oct], calculated from the plots shown in Figure 5.3.

In all cases, the activation energies increase linearly with increasing concentration. This indicates that the presence of a solute increases the energy barrier to flow, this is likely to be due to the multiple ions clustering around a single anhydroglucose unit as part of the solvation [148]. Additionally, the $E_{a,\eta}$ values are all broadly the same between the three carbohydrates, within experimental error. This is somewhat surprising for cellulose based on the viscosity values, because of the elevated viscosity of cellulose solutions. This indicates that the local microscopic interactions are the same for cellulose and glucose/cellobiose, suggesting some similarity in the IL-solute environment for all three carbohydrates. Therefore, despite a much larger η in cellulose solutions, the three carbohydrate solutions all possess a similar effective local friction coefficient. In fact, the higher η values for cellulose solutions are due to the larger pre-exponential factor η_0, which arises in part from the influence of the macroscopic polymer.

5.3.2 Diffusion

Figure 5.7 shows the temperature dependence of the self-diffusion coefficients, D_{cat}, of the $[C_2MIM]^+$ cation for solutions of glucose, cellobiose and cellulose in $[C_2MIM][Oct]$.

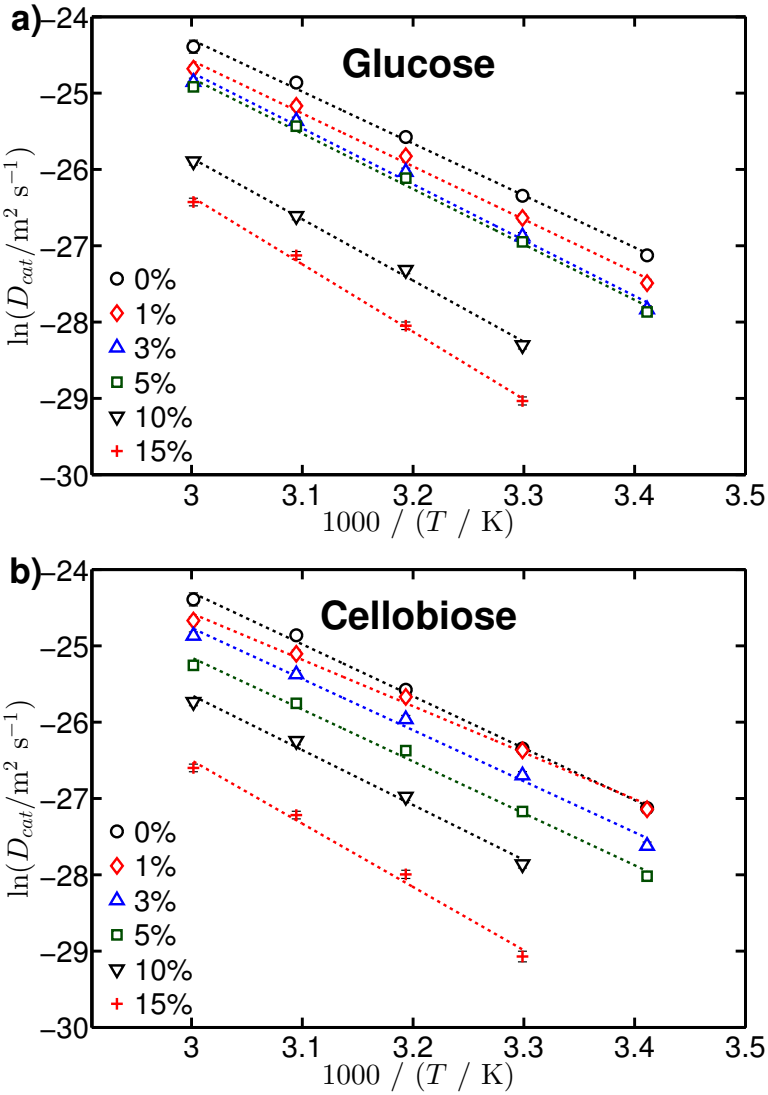

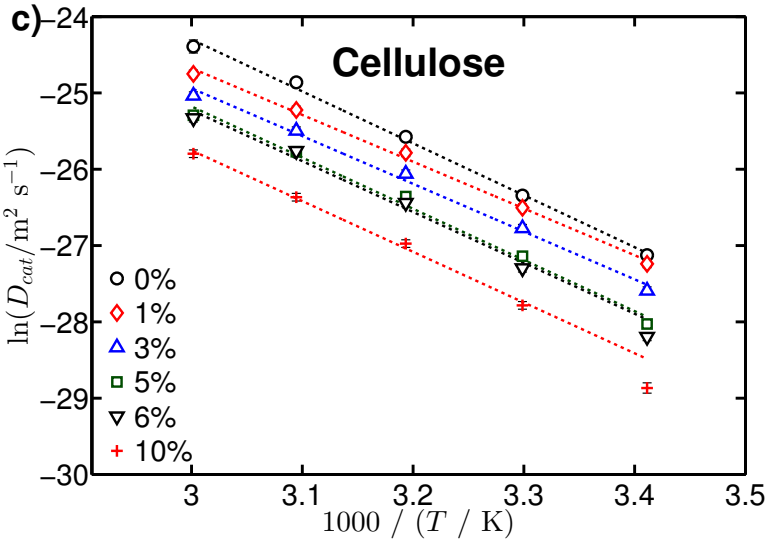

Figure 5.7: Arrhenius plots for self-diffusion coefficients of the imidazolium cation in solutions of carbohydrates dissolved in $[C_2MIM][Oct]$. Plots show solutions of **a)** glucose, **b)** cellobiose and **c)** cellulose at a range of concentrations (in weight percentage). Straight lines show fits based on Equation 3.1. Error bars are typically the size of data points.

As expected from viscosity, D_{cat} increases with increasing temperature and decreases with increasing carbohydrate concentration. However unlike viscosity, there is no substantial difference between D_{cat} values for each carbohydrate. This suggests there is some complex behaviour occurring to disrupt the relationship between the microscopic and macroscopic regimes, such as that in $[C_2MIM][Ac]$ [148].

The plots in Figure 5.7 show a decrease in D_{cat} as carbohydrate concentration increases, somewhat in agreement with the viscosity. However, the dependence of D_{cat} on the type of carbohydrate is markedly different than that of η. As with viscosity, D_{cat} is similar for glucose and cellobiose. Though, D_{cat} values for cellulose solutions are also roughly the same as glucose and cellobiose, in contrast to both $[C_2MIM][Oct]$ viscosity data and $[C_2MIM][Ac]$ diffusion data. In fact, D_{cat} exhibits very little dependence on the type of carbohydrate. This is shown later in the chapter (Figure 5.15a) and will be discussed in more detail in subsequent sections.

The ratio of anion diffusion coefficient to cation diffusion coefficient was calculated for all solutions and temperatures. However, D_{an}/D_{cat} showed no strong dependence on either temperature or carbohydrate concentration; D_{an}/D_{cat} values were close to those of pure [C_2MIM][Oct] (see Figure 3.3) at low concentrations and had high scatter at higher concentrations.

As with the viscosity data, the diffusion data has a linear, Arrhenius-type dependence on temperature, as shown in Figure 5.7. Therefore Arrhenius analysis can be used to extract activation energies of diffusion using Equation 3.1. The $E_{a,D}$ values for the imidazolium cation are shown in Figure 5.8 as a function of carbohydrate concentration.

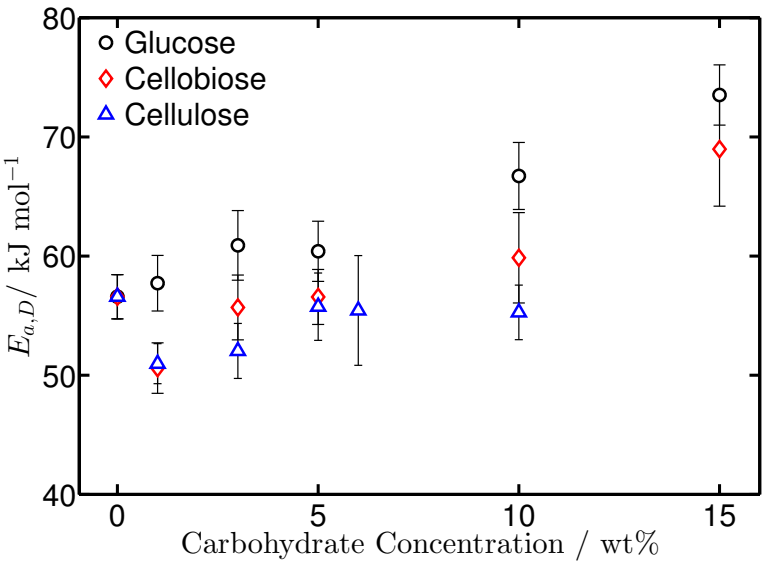

Figure 5.8: Activation energy of diffusion as a function of carbohydrate concentration for the cation in solutions of glucose, cellobiose and cellulose in [C_2MIM][Oct], calculated from the plots shown in Figure 5.7

The $E_{a,D}$ values exhibit more complex behaviour than the $E_{a,\eta}$ data shown in Figure 5.6. There is relatively little increase in $E_{a,D}$ up to 10%, in fact, there is even a slight drop for cation diffusion in cellobiose and cellulose solutions. This could be due to carbohydrate molecules disrupting the microscopic clustering found in [C_2MIM][Oct].

Additionally, unlike the viscosity activation energies, the cation diffusion values show differences between the different carbohydrate solutions, albeit only

small changes. In all cases, $E_{a,D}$ values for glucose solutions are higher than the other two carbohydrate solutions, followed by values for cellobiose and then cellulose solutions. Though, many of the $E_{a,D}$ values fall within error of the other carbohydrate solutions, particularly in cellobiose and cellulose solutions.

One thing in common with all $E_{a,D}$ data is that $E_{a,D} > E_{a,\eta}$ for all the corresponding concentrations and carbohydrates. This indicates additional microscopic factors are inhibiting the ionic self-diffusion compared to viscous flow, consistent with strong IL-carbohydrate bonding which would also increase as concentration increases. Taken together, there appear to be several competing factors affecting the diffusional processes in these solutions.

5.3.3 NMR Relaxometry

Figure 5.9 shows NMR relaxation data for $[C_2MIM][Oct]$ as a function of temperature, in a representative set of glucose, cellobiose and cellulose solutions. BPP fits of the relaxation data are also shown (dashed lines). As in previous chapters, the correlation time was modelled using an Arrhenius-type equation (Equation 3.2) and fitted to BPP theory (Equations 2.1 and 2.2) by varying A, $E_{a,\tau}$ and τ_0. These fitting parameters are shown in Tables A.1 and A.2 in Appendix section A.3.

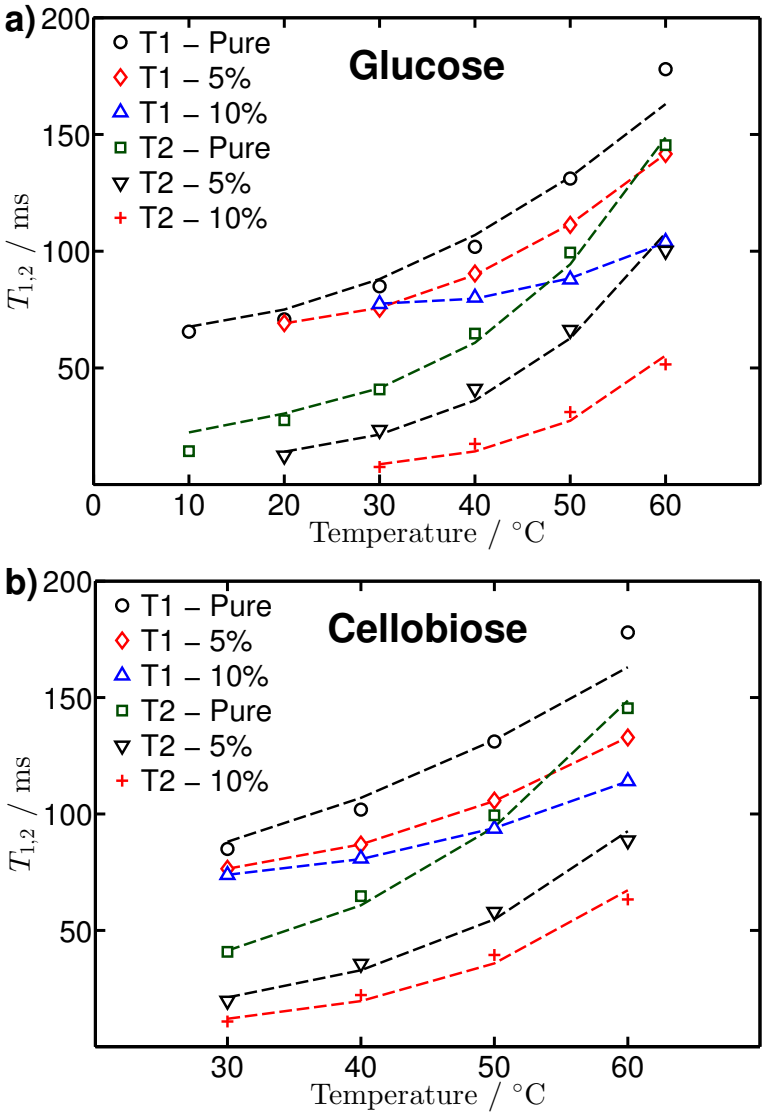
a)
Glucose
T1 – Pure
T1 – 5%
T1 – 10%
T2 – Pure
T2 – 5%
T2 – 10%
$T_{1,2}$ / ms
Temperature / °C
b)
Cellobiose
T1 – Pure
T1 – 5%
T1 – 10%
T2 – Pure
T2 – 5%
T2 – 10%
$T_{1,2}$ / ms
Temperature / °C

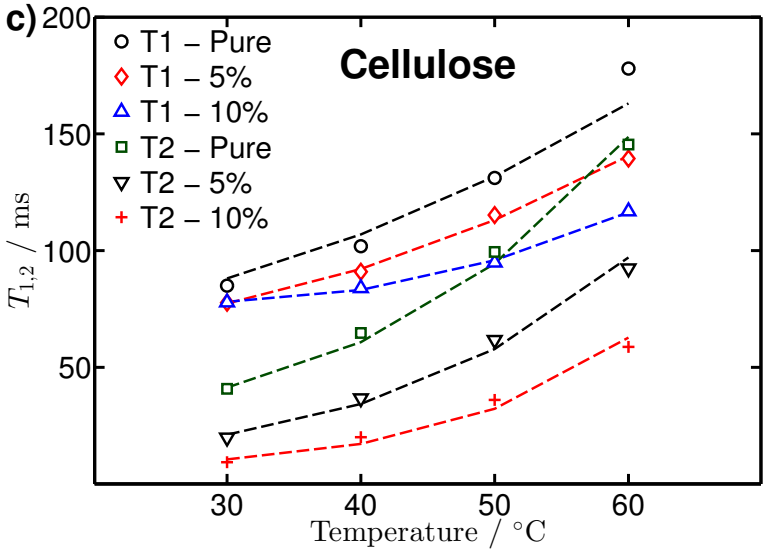

Figure 5.9: T_1 and T_2 relaxation data for $[C_2MIM][Oct]$ at 20 MHz as a function of temperature for carbohydrate solutions. Plots show solutions of **a)** glucose, **b)** cellobiose and **c)** cellulose at representative concentrations of 0% (pure IL), 5% and 10% (in weight percentage). Points show experimentally measured T_1 and T_2, dashed lines show fits obtained from Equations 2.1 and 2.2. Fitting parameters are shown in Tables A.1 and A.2 in Appendix section A.3. Error bars of 5% are omitted for clarity.

Figure 5.9 shows that T_1 and T_2 both increase as temperature increases, in all cases. This indicates that the solutions shown are not in the 'solid-like' regime *i.e.* the system correlation times are much shorter than the NMR timescale defined by the inverse of the Larmor frequency. The correlation times shown in Tables A.1 and A.2 support this observation. However, T_1 and T_2 values begin to level off at lower temperatures, consistent with approaching the 'transitional' regime where τ is close to the NMR timescale.

One notable aspect of all the datasets is the significant discrepancy between T_1 and T_2 data, with the former larger than the latter; Tables A.1 and A.2 show the two separate fittings required for T_1 and T_2, respectively. This is unexpected for the 'liquid-like', or high-temperature, regime that most of the relaxation data occupies. This is likely to be due to 'zero-frequency' dynamics arising from slow dynamical motions and affecting T_2, as discussed in Section 3.3.2. Though as temperature increases, the relative difference between T_1 and T_2 decreases *i.e.*

the system moves towards the high-temperature limit where $T_1 = T_2$.

The discrepancy between T_1 and T_2 remains for all carbohydrate concentrations, as shown in Figure 5.9. As previously observed, T_1 is higher than T_2 and increasing concentration leads to a decrease in relaxation times. The relaxation data also show very little dependence on the type of carbohydrate, in agreement with diffusion data (Figure 5.7) and in contrast to viscosity data (Figure 5.4). By comparison, the discrepancy between T_1 and T_2 is much lower for pure $[C_2MIM][Ac]$, as shown in Section 3.3.2, and this feature remains throughout the concentration range [190]. This indicates the slower dynamical motions that give rise to the lower T_2 in $[C_2MIM][Oct]$ are not present in $[C_2MIM][Ac]$. This is likely to be due to the extended carbon 'tail' on the octanoate anion, as discussed in Section 3.3.2. Further reasons for the differences between $[C_2MIM][Ac]$ and $[C_2MIM][Oct]$ will be discussed in more detail in following sections.

5.3.4 NMR Chemical Shift

Chemical shift data for $[C_2MIM][Oct]$ in all the carbohydrate solutions were obtained during PFG NMR diffusion measurements. By comparing the ^1H chemical shift data for each carbohydrate concentration to that of pure $[C_2MIM][Oct]$, another perspective can be gained of carbohydrate dissolution. Figure 5.10 shows the chemical shift change for each $[C_2MIM][Oct]$ proton resonance as a function of concentration for each glucose solution, relative to the chemical shifts of pure $[C_2MIM][Oct]$. The chemical shift changes were measured for each resonance peak in the spectrum, Figure 5.2 details the peak numbering used. See Figure A.2 for the spectrum of pure $[C_2MIM][Oct]$.

The $\Delta\delta$ values shown in Figure 5.10 depict a negative change for the ^1H resonances attached to carbon atoms in the imidazolium ring as glucose concentration increases; the remaining resonances, attached to aliphatic carbon atoms, exhibit small positive changes. This behaviour is mirrored in similar datasets obtained for cellobiose and cellulose solutions and is consistent with other studies of imidazolium-based ILs [61, 148, 186].

The chemical shift changes indicate the charged imidazolium-ring centre is affected most by the presence of dissolved carbohydrates, where the negative

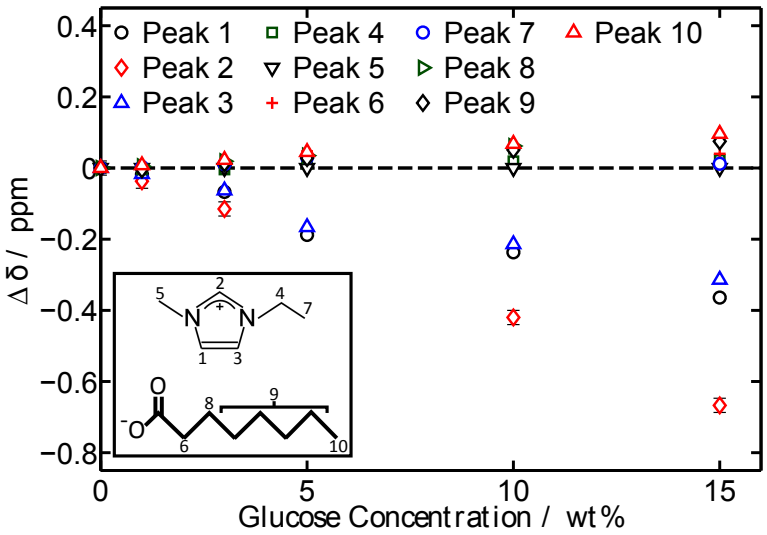

Figure 5.10: NMR chemical shift change, $\Delta\delta$, for $[C_2MIM][Oct]$ as a function of concentration for glucose solutions, relative to pure $[C_2MIM][Oct]$. All shifts were obtained at a temperature of 40 °C. Chemical shift changes are shown for each resonance, labelled according to Figure 5.2. Peak numbering is shown inset. Errors are shown for resonance 2 as representative values but are left off the remaining data for clarity.

change in chemical shift indicates an increase in electron density across the imidazolium ring. The H2 resonance exhibits a larger change than the H1 and H3 resonances due to its higher Brønsted acidity, as evidenced by its higher chemical shift. There is some debate whether these negative $\Delta\delta$ are purely a consequence of the carboxylate anion decreasing its interaction with the cation in favour of H-bonding with the dissolved carbohydrate [51, 59, 187] or whether the cation itself is involved in some specific interactions with the carbohydrates [55, 186, 188]. Regardless, the chemical shift decreases fairly uniformly for all three ring-hydrogens as glucose concentration increases. The positive changes are also consistent with those previously observed in $[C_2MIM][Ac]$ and other imidazolium-based ILs [61, 148, 186]. The magnitudes of $\Delta\delta$ are all larger for $[C_2MIM][Oct]$, compared to $[C_2MIM][Ac]$. This suggests that there is a larger difference in the relative strengths of interionic bonding in pure $[C_2MIM][Oct]$ and ion-solute bonding in carbohydrate solutions, as compared to the same situation in $[C_2MIM][Ac]$.

Figure 5.11 shows the chemical shift for three representative resonances in

[C_2MIM][Oct] as a function of carbohydrate concentration in glucose, cellobiose and cellulose solutions. These three resonances were chosen to represent three distinct positions: the positive shift of protons on aliphatic carbon atoms (10) and the negative shifts of two different positions on the imidazolium ring (2 and 3).

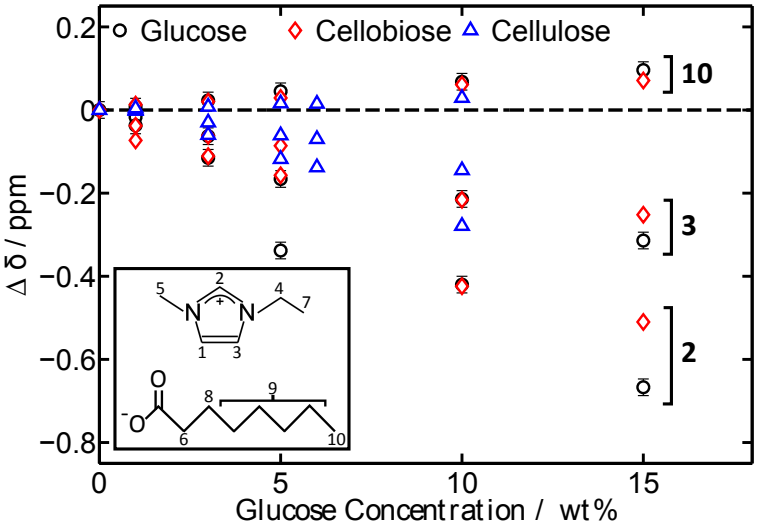

Figure 5.11: Comparison of chemical shift changes, $\Delta\delta$, for [C_2MIM][Oct] as a function of carbohydrate concentration for glucose, cellobiose and cellulose solutions, relative to pure [C_2MIM][Oct]. All shifts were obtained at a temperature of 40 °C. Shifts are shown for a representative selection of peaks, corresponding to resonances 10, 3 and 2 (top to bottom). Peak numbering is shown inset. Errors are shown for glucose as representative values but are left off the remaining data for clarity.

Though there is some scatter in the data, there are a few notable trends. As expected, the three solutions follow the same trends for all three resonances, confirming that the solvation process and environment is similar for glucose, cellobiose and cellulose. In general, the magnitude of the chemical shift change is slightly larger in glucose, then cellobiose and then cellulose in order. This is consistent with [C_2MIM][Ac], where $\Delta\delta$ correlates well with the number of dissolved hydroxyl groups [148]. This is an interesting contrast to some of the other datasets presented here and will be explored further in subsequent sections.

5.4 Discussion

Despite their chemical similarity, there are some differences between the behaviour of glucose, cellobiose and cellulose when dissolved in [C_2MIM][Oct], as demonstrated by the results in the previous section. There are also differences between the behaviour of these carbohydrate solutions in [C_2MIM][Oct], compared to [C_2MIM][Ac]. This section will address both these observations and provide a deeper insight into IL-carbohydrate solutions.

5.4.1 Summary of Results

The viscosity data for [C_2MIM][Oct] in Figure 5.4 show that the macroscopic environments of glucose and cellobiose are very similar, whereas, the macromolecular character of cellulose leads to a far more viscous environment. This is not unexpected for these types of solute, despite their chemical similarity. However, the activation energies of viscous flow (Figure 5.6) show a different picture: $E_{a,\eta}$ depends only on the carbohydrate concentration, not the type of carbohydrate. This means the local interactions, and therefore the microscopic environment, is roughly the same for all three carbohydrate-IL systems.

The dependence of D_{cat} on carbohydrate concentration was also broadly independent of the type of carbohydrate. This indicates that the relatively large length scales ($\sim$ 10 µm) and slow dynamical motions of diffusion depend on specific local features that are universal to all three types of [C_2MIM][Oct]-carbohydrate solution. The activation energies of diffusion (Figure 5.8) present an even more complex picture. Increasing the solute concentration will increase the amount of H-bonding between ions and solute molecules, which should then increase $E_{a,D}$ [148]; however, the activation energies for [C_2MIM][Oct] remain lower or the same up until concentrations of 10%. This suggests there is a competing effect decreasing $E_{a,D}$ on addition of carbohydrate, such as the disruption of aggregates or larger structures present in the pure IL.

Pure [C_2MIM][Oct] showed a discrepancy between T_1 and T_2, as well as clear differences in the theoretical modelling of both relaxation times (see Section 3.3.2). This feature remains for all solutions of glucose, cellobiose and cellulose in [C_2MIM][Oct], as shown in Figure 5.9. The difference in T_1 and T_2 was

attributed to the motion of the carbon 'tail' on the octanoate ion; this motion remains active throughout the full concentration.

The chemical shift changes in [C_2MIM][Oct] solutions (Figure 5.11) showed differences between the three carbohydrates. Broadly, glucose caused the greatest $\Delta\delta$, followed by cellobiose, then cellulose, very similar to the case in [C_2MIM][Ac] [148]. This adds to the complexity of the data presented here, not just between microscopic and macroscopic scales but between the relative timescales of the different factors.

5.4.2 Testing the 5,4,3 Rule in [C_2MIM][Oct]

The self-diffusion coefficients and other properties of carbohydrate solutions in [C_2MIM][Ac] were shown to scale with the concentration of hydroxyl groups, not simply the carbohydrate concentration [148], as discussed in Section 5.1.3. The D_{cat} data was initially used for this correlation, which was then found to extend to chemical shift change [148] and relaxometry data [190]. This means that D_{cat}, T_1, T_2 and $\Delta\delta$ can all be plotted against the associated fraction, α (Equation 5.1), for [C_2MIM][Ac], and the three carbohydrate datasets follow a single trend as a function of α.

Figure 5.12 shows plots of chemical shift change against carbohydrate concentration (in wt%) and α for peak 2 on the imidazolium cation in [C_2MIM][Oct].

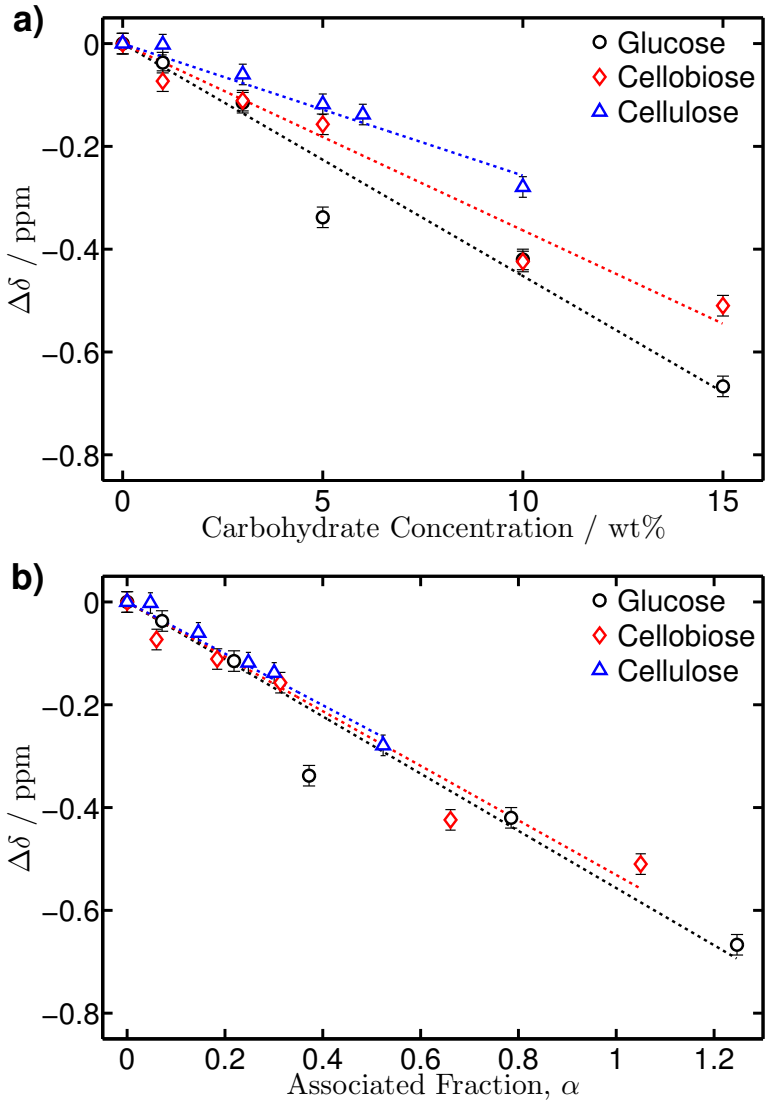

Figure 5.12: Chemical shift change, $\Delta\delta$, as a function of **a)** carbohydrate concentration and **b)** associated fraction for resonance 2 (see Figure 5.2) in solutions of glucose, cellobiose and cellulose dissolved in $[C_2MIM][Oct]$, at a temperature of 40 °C. Lines are simple linear fits, shown as a guide to the eye.

Figure 5.12a shows that the three carbohydrates exhibit slightly different trends when plotted against concentration. In contrast, Figure 5.12b shows a convergence of carbohydrate data when plotted against α, similar to the analagous data in $[C_2MIM][Ac]$ [148]. This indicates the 5,4,3 rule is obeyed for $\Delta\delta$ in $[C_2MIM][Oct]$.

The 5,4,3 relationship applies to T_1 and T_2 in [C_2MIM][Ac] [190]. Based on the chemical shift data shown in Figure 5.12, it would be expected that the relaxation data for [C_2MIM][Oct] would also follow the 5,4,3 rule. Figures 5.13 and 5.14 show T_1 and T_2 as a function of both carbohydrate concentration (in wt%) and α for [C_2MIM][Oct].

As expected, the T_1 data shown in 5.13 obeys the 5,4,3 rule; the three carbohydrate datasets are slightly divergent for concentration but fall into the same trend when plotted against α. However, the T_2 data exhibits a single trend for the three carbohydrates as a function of concentration (Figure 5.14a) and a slight divergence from this trend when plotted as a function of α (Figure 5.14b). This suggests that the 5,4,3 rule is not followed by T_2 in [C_2MIM][Oct]. T_2 is significantly different in magnitude to T_1 in [C_2MIM][Oct], as shown in Figure 5.9, due to slow dynamical motions that are picked up by T_2 but not T_1. These motions may also affect the 5,4,3 rule, so the difference in behaviour between the two datasets is not wholly surprising.

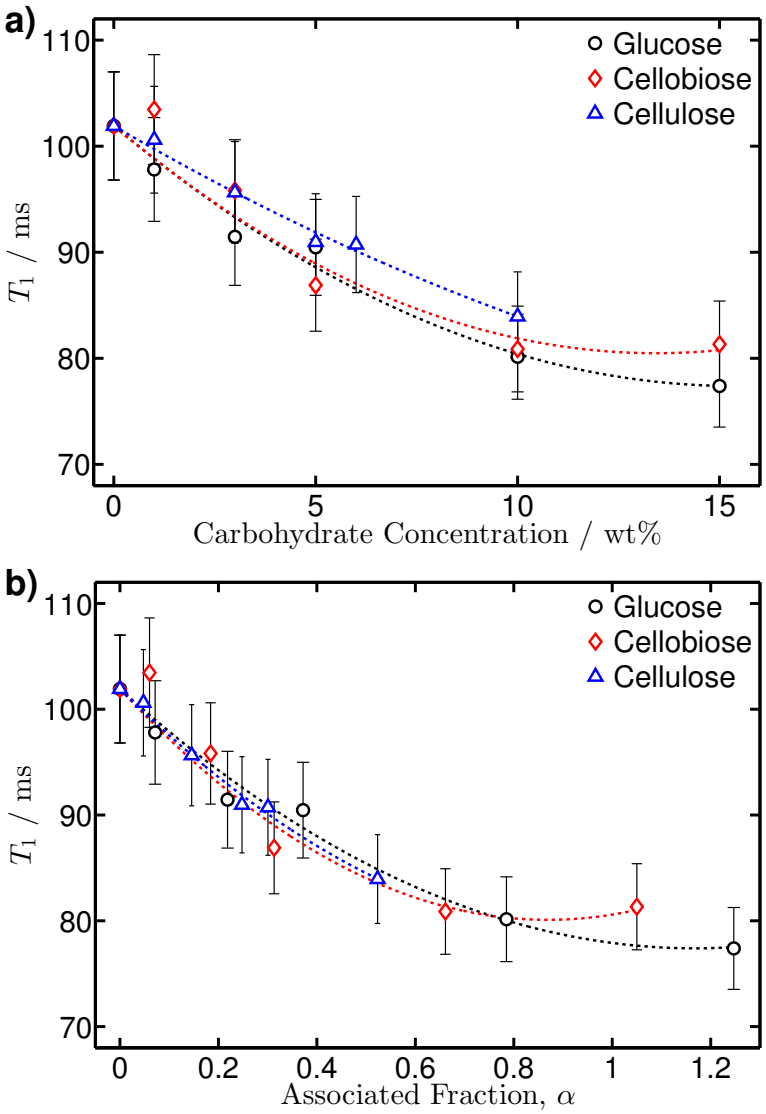

Figure 5.13: T_1 relaxation data as a function of **a)** carbohydrate concentration and **b)** associated fraction for solutions of glucose, cellobiose and cellulose dissolved in $[C_2MIM][Oct]$, at a temperature of 40 °C. Lines are arbitrary quadratic fits, as a guide to the eye.

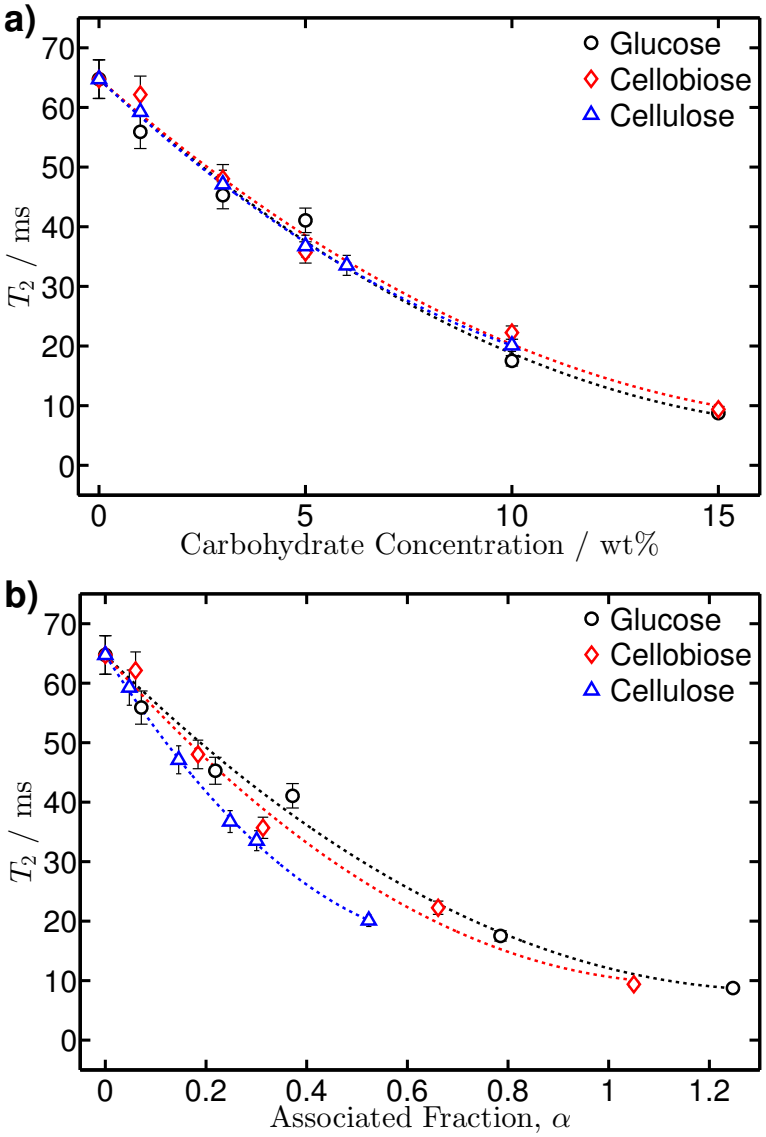

Figure 5.14: T_2 relaxation data as a function of **a)** carbohydrate concentration and **b)** associated fraction for solutions of glucose, cellobiose and cellulose dissolved in $[C_2MIM][Oct]$, at a temperature of 40 °C. Lines are arbitrary quadratic fits, as a guide to the eye.

Diffusion was shown to obey the 5,4,3 rule in [C_2MIM][Ac] [148]. However, self-diffusion is slow dynamical process, acting over a relatively large length scale compared to other NMR techniques. Therefore, it is likely that D_{cat} will disobey the 5,4,3 rule, in common with the T_2 data. Figure 5.15 shows a comparison of D_{cat} for [C_2MIM][Oct] solutions as a function of concentration and associated fraction. The first of these plots (Figure 5.15a) already draws a distinction between D_{cat} and $\Delta\delta$; here, D_{cat} is only a function of concentration and is not affected by the identity of the carbohydrate or the relative number of hydroxyl groups.

Figure 5.15b shows D_{cat} as a function of α for [C_2MIM][Oct]. Though the effect is relatively subtle, there is more of a difference between carbohydrate datasets when α is used, as compared to Figure 5.15a. Specifically, plotting D_{cat} as a function of α for [C_2MIM][Oct] does not substantially improve the agreement between the carbohydrates. This shows that the 5,4,3 rule is not followed by the self-diffusion of [C_2MIM][Oct] solutions, as expected.

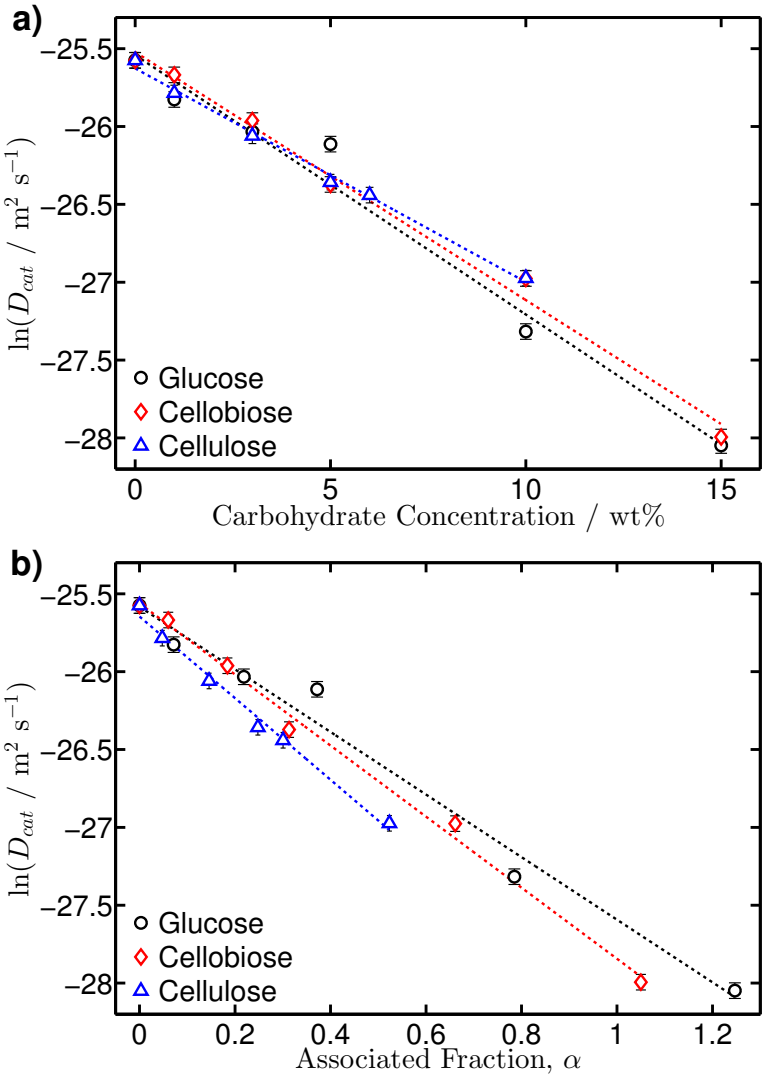

Figure 5.15: Self-diffusion coefficients of the imidazolium cation as a function of **a)** carbohydrate concentration and **b)** associated fraction for solutions of glucose, cellobiose and cellulose in $[C_2MIM][Oct]$, at a temperature of 40 °C. Lines are simple linear fits, used as guides to the eye.

Now, an interpretation of all the disparate NMR data will be attempted, in order to assess why the 5,4,3 rule is sometimes disobeyed in [C_2MIM][Oct]. First, the diffusion data will be considered; diffusion was found not to obey the 5,4,3 rule in [C_2MIM][Oct]. There are several potential reasons for this, including steric crowding around dissolved AGUs, unfavourable microstructure of [C_2MIM][Oct] ions or even a different bonding mechanism to the anion-carbohydrate H-bonding mechanism found in [C_2MIM][Ac].

A different bonding mechanism in [C_2MIM][Oct], such as substantial hydrophobic bonding between the aliphatic anion tail and the carbohydrate backbone, is unlikely; this mechanism would be substantially less effective in the more hydrophilic glucose compared to the amphiphilic cellulose. Additionally, carbohydrate dissolution in [C_2MIM][Oct] behaves similarly to [C_2MIM][Ac] on a chemical level, as evidenced by the similar $\Delta\delta$ values.

The microstructure of [C_2MIM][Oct] may restrict its ability to interact with carbohydrates, for example, anion-rich clusters will prevent those anions from bonding to carbohydrate hydroxyl groups. Though, the nature and effects of ion aggregation can have a number of effects; it is difficult to make any clear inference about these effects without a complete understanding of the microstructure.

Steric crowding around an AGU could be more significant for the larger octanoate ion in [C_2MIM][Oct] than for the smaller acetate anion in [C_2MIM][Ac]. Therefore, it may not be possible to fit 5 octanoate anions around a single glucose molecule, regardless of the bonding between anions and carbohydrate hydroxyl groups. In fact, for the higher concentrations of glucose and cellobiose, it is found that $\alpha > 1$ *i.e.* there is more than one carbohydrate hydroxyl group per IL anion. This effectively requires a single anion to bond to more than one hydroxyl group, requiring the anion to bridge multiple groups. This behaviour has been observed in computational studies [70, 71, 74]. It is also worth noting that diffusion measurements probe large length scales and therefore slow dynamics, as compared to other NMR techniques. If the carbohydrate bonding and ions' motion is limited by the sterics and dynamics of the octanoate chain, D_{cat} measurements will be dominated by these slower, longer range dynamics.

While chemical shift values can depend on a wide variety of factors, they provide chemical detail on a very short length scale ($\sim$ Å) and therefore short

timescales. Therefore, the 5,4,3 rule is followed for $\Delta\delta$ data, in agreement with T_1 data and consistent with previous observations. The interatomic length scale, and therefore short timescale, probed by chemical shift measurements is comparable to the length scale and lifetime of the one-to-one anion-hydroxyl bonding.

For T_1 and T_2 data, the discrepancy in magnitudes of the two relaxation constants (Figure 5.9) hints at a reason for the different correlation with α between T_1 and T_2. T_2 is shorter for $[C_2MIM][Oct]$ due to slow dynamical motions that are only observed by the 'zero frequency' component of T_2 relaxation (recall Equation 2.2). Therefore, these slow dynamical motions may be 'screening' the one-to-one interaction between anion and hydroxyl groups; the lifetime of the anion-hydroxyl bond is dictated by the slower motions of the octanoate ion, in agreement with steric restrictions proposed above for D_{cat}. In contrast, T_1 is only sensitive to short-lived motions, defined here by the NMR timescale of $\sim 1/(20\ \text{MHz})$. This timescale is likely to only include the anion-carbohydrate bonding and not the slower motions that cause the disruption of the 5,4,3 rule in T_2 and D_{cat}.

A simple fitting of different N values (Equation 5.1) was attempted for the diffusion data of $[C_2MIM][Oct]$, where N was allowed to vary from the intuitive values, representing the number of hydroxyl groups on each unit (5 for glucose, 4 for cellobiose, 3 for cellulose). Cellulose was defined as $N_{cel} = 3$ and values of $N_{gl} = 3.6$ and $N_{cb} = 3.2$ were obtained for glucose and cellobiose respectively, at 40 °C. These values show relatively little change from the case of $N_{gl} = N_{cb} = N_{cel}$, and little visible improvement to a plot of D_{cat} data. This indicates that the relationship between D_{cat} and concentration is broadly agreed for all three carbohydrates, with just a slight adherence to the 5,4,3 rule. $N_{cel} = 3$ was chosen somewhat arbitrarily, as there is no way of knowing from D data if cellulose is forming exactly three hydroxyl-anion bonds. A similar fitting can be carried out by setting N_{gl} to 5 and varying N_{cb} and N_{cel}. However, the optimum solution for this case requires $N_{cb} > 4$ and $N_{cel} > 3$. This would imply that single hydroxyl groups on cellobiose and cellulose are bonding to multiple anions, which seems unlikely due to the limited accessibility of the bonded hydroxyl groups. Based solely on the evidence here, it is not possible to say N_{cel} is exactly 3 but it can be assumed that $N_{cel} \leq 3$ and therefore, the hydroxyl groups on cellobiose and glucose are not bonding to their full capacity on a longer timescale.

5.4.3 Conclusion

The carbohydrates glucose, cellobiose and cellulose were dissolved in the imidazolium-based ionic liquid, $[C_2MIM][Oct]$, and the resultant solutions were studied using a range of rheological and NMR techniques. Previous studies had investigated these types of solutions using the similar IL, $[C_2MIM][Ac]$ [148, 190], but to the best of the author's knowledge, no such study had been undertaken on $[C_2MIM][Oct]$ previously. The different size of the carboxylate anion in $[C_2MIM][Oct]$ compared to $[C_2MIM][Ac]$ leads to subtle differences in their respective carbohydrate solutions. NMR data from several experimental techniques were compared in order to understand the origin of these differences.

Viscosity measurements showed a marked difference between the small-molecule glucose and cellobiose, as compared to the polymeric cellulose. However, the viscosity activation energies showed the three carbohydrate solutions to have a very similar local ($\sim$ µm) environment. Diffusion data mirrored this similarity, showing a comparable relationship between D_{cat} and carbohydrate concentration (in wt%) for the three different carbohydrates, in contrast to $[C_2MIM][Ac]$ diffusion data. The diffusion activation energies showed a complex dependence on concentration for each carbohydrate, hinting at a number of competing factors controlling the diffusion process. Relaxometry data added another dimension to the data, indicating that slow dynamical motions were prevalent in the full concentration range of all three carbohydrate solutions. In contrast to the other datasets, chemical shift data showed little difference between $[C_2MIM][Oct]$ and $[C_2MIM][Ac]$.

A more detailed examination of the NMR data was undertaken. Specifically, the 5,4,3 rule found for interaction between glucose, cellobiose and cellulose when dissolved in $[C_2MIM][Ac]$ [148] was investigated in $[C_2MIM][Oct]$. The 5,4,3 rule was obeyed in $[C_2MIM][Oct]$ chemical shift data but disobeyed in diffusion data. A similar picture was found for relaxation data, where T_1 followed the 5,4,3 rule but T_2 did not. The correlation between the two regimes was one of relative time and length scales; techniques investigating a short timescale/small length scale ($\sim$ Å), namely T_1 and chemical shift, exhibited the 5,4,3 rule, whereas, the techniques that probed slower motions/larger length scales ($\sim$ µm), namely

diffusion and T_2, did not. It was proposed that the slower motions related to the long octanoate-anion tail were controlling the diffusion and T_2 relaxation, smearing out the one-to-one interaction between anion and carbohydrate hydroxyl group that causes the 5,4,3 rule.

Two distinct pictures emerge from the data presented here: *i*) a short-lived, very localised anion-carbohydrate bonding regime, shown by T_1 and $\Delta\delta$, where the 5,4,3 rule is obeyed and *ii*) a longer timescale, shown by D_{cat} and T_2, where anion-carbohydrate bonding is controlled and restricted by slower dynamical processes and length scales involving the hydrophobic tail on the octanoate ion. This suggests that [C_2MIM][Oct] interacts with carbohydrates in the same way as [C_2MIM][Ac] on a chemical level but the additional dynamical features hinder IL-carbohydrate interactions.

Chapter 6

Conclusions and Outcomes

The work presented here demonstrates an investigation into a number of ionic liquids, with a view to understanding and improving the dissolution of cellulose in ionic liquids. NMR, rheology and conductivity measurements were used on pure ILs with two different cations and a range of carboxylate anions. A novel method of modelling ion pairing and aggregation was introduced, tested and applied in order to determine the microscopic differences, and similarities, between the ILs. The model was successful in correlating experimental data and theory, and indicated that ionic pairing and aggregation had a small dependence on anion size but a significant dependence on the identity and nature of the cation; imidazolium-based ILs showed a much lower degree of pairing and aggregation than DBN-based ILs. Following this, $[C_2MIM][Oct]$ was used as a solvent for three carbohydrates, including cellulose, in order to understand the influence of anion size. The solvation environment in this IL was compared with analogous work on carbohydrates dissolved in $[C_2MIM][Ac]$. The findings indicated that $[C_2MIM][Oct]$ dissolved the carbohydrates in a similar fashion to $[C_2MIM][Ac]$ but certain microscopic features, such as ion self-diffusion, were limited by the size and motion of the octanoate anion.

This understanding of the microscopic aggregation and structuring in ILs can shed an important light on their macroscopic properties. This is vital in designing new task-specific ILs. A simple, easily-applicable model can provide an important link between these different properties, such as diffusion, viscosity

and conductivity. Combined with systematic studies on cation/anion roles, this information can help with the application of ILs to many different situations.

6.1 Research Outcomes

Imidazolium-based ILs

Firstly, four imidazolium-based ILs were investigated with a range of carboxylate anions: [C_2MIM][Ac], [C_2MIM][But], [C_2MIM][Oct] and [C_2MIM][Ddc]. The aim was to understand the impact of increasing the anion size on microscopic and macroscopic properties. NMR, rheology, conductivity and density were used to investigate both macroscopic and microscopic properties. Macroscopic techniques, such as viscosity and density, showed a relatively simple dependence on anion size. Some microscopic properties, such as NMR relaxometry, indicated more complex effects of changing anion chain length. Correlation of macroscopic and microscopic properties indicated the same discrepancies between the two scales, with distinct differences between 'shorter' chain ILs ([C_2MIM][Ac] and [C_2MIM][But]) compared to 'longer' chain ILs ([C_2MIM][Oct] and [C_2MIM][Ddc]).

Three simple models of ion pairing and aggregation were applied to the NMR, conductivity and viscosity data for the four imidazolium-based ILs. The ion pair model showed some agreement between the modelled data and ideal theoretical data. The charged aggregate model showed further improvement in describing the IL properties accurately. The combined model was used to provide a quantitative fitting of the data to the ideal theoretical case. These quantitative fits were found to be the most successful, providing legitimacy to this combined model. A low degree of ion pairing and relatively small average aggregate size was found for the imidazolium-based ILs, in agreement with some literature results using very different techniques [144, 146].

DBN-based ILs

The next study used the same techniques and methodology to investigate a series of 1,5-diazabicyclo[4.3.0]non-5-enium (DBN) based protic ILs, in order to compare this class to the imidazolium-based ILs. A similar series of aliphatic

carboxylate anions were used, with chain lengths between 1 and 8 carbon atoms (formate to octanoate). The different experimental techniques showed different trends as anion chain length varied. For example some techniques, such as conductivity, showed a peak for mid-ranged chain lengths, whereas other techniques, such as density, showed more uniform trends across the different chain lengths. This suggests that the effects of changing anion chain length depend on an interplay of several microscopic features.

The three models were then applied to the six room-temperature DBN-based ILs (chain lengths 3 to 8). The ion pair model gave a good agreement with experimental data and the charged aggregate model gave a reasonable agreement. The combined model gave a much improved fit to the theoretical data than either individual model, indicating both pairing and charged aggregate formation are important in these ILs. This draws a contrast to the aprotic imidazolium-based ILs, which showed very little ion pairing. The aggregate sizes were also larger for the DBN-based ILs, consistent with literature comparisons of protic and aprotic ILs [146, 147].

Carbohydrate Dissolution

The final study revisited the imidazolium-based ILs, this time as carbohydrate solvents; $[C_2MIM][Oct]$ was used as a solvent for glucose, cellobiose and cellulose, then compared to literature studies on the same solutions in $[C_2MIM][Ac]$. The three carbohydrates are the polymer cellulose, and it's constituent monomer (glucose) and dimer (cellobiose) units. $[C_2MIM][Oct]$ was an efficient solvent for the carbohydrates, producing solutions of high viscosity and low ion diffusivity. Viscosity was highly affected by cellulose, compared to glucose and cellobiose, whereas, diffusion was equally affected by the three carbohydrates.

Previous studies showed that in $[C_2MIM][Ac]$, ion diffusivity was controlled by the relative number of carbohydrate hydroxyl groups dissolved, not simply the concentration of dissolved carbohydrate [148, 190]; this was referred to as the 5,4,3 rule (corresponding to the number of hydroxyl groups on glucose, cellobiose and cellulose) and was also found in a number of other properties of

[C_2MIM][Ac] solutions. For [C_2MIM][Oct] solutions, chemical shift and T_1 relaxation data obeyed the 5,4,3 rule, initially suggesting that [C_2MIM][Oct] had exactly the same carbohydrate dissolution mechanism as [C_2MIM][Ac]. However, T_2 relaxation and cation diffusion data disobeyed the 5,4,3 rule, indicating differences between [C_2MIM][Ac] and [C_2MIM][Oct] solutions. These differences were attributed to the different time and length scales each process acts over. This indicated that [C_2MIM][Oct] dissolves cellulose with the same mechanism as [C_2MIM][Ac], but the larger octanoate anion imposes additional restrictions on the IL-carbohydrate interactions. This work provides an insight into the complex process of carbohydrate dissolution in ILs, highlighting some of the competing factors that dictate the solvation environment.

6.2 Future Directions

The results and discussions presented here suggest a number of future research directions, either continuing in an academic vein, or as the next steps towards utilising these types of ILs in an industrial context. The customisable nature of ILs means there are a vast number of distinct cation/anion combinations that the techniques presented here could be applied to. The ion pair, charged aggregate and combined models were tested on two different cations but could easily be applied to a different class of anion, such as branched carboxylates, halides or dimethylphosphate. Addition of co-solvents disrupts microscopic structuring, this could be tested using the three models. These models should also be equally applicable to ILs used for applications other than cellulose dissolution. The difference between aprotic and protic ILs could be examined in detail by using mixtures of different cations while keeping the anion unchanged, for example, by studying a series of mixtures of [C_2MIM][Ac] and [DBNH][Ac].

There are a number of unexplained phenomena in the pure ILs that could be studied in more detail with additional experimental work. An in-depth DSC study of the imidazolium-based ILs could provide some insight into the differences between [C_2MIM][Ac] and [C_2MIM][Oct], as observed in the high-field relaxometry data. While limited DSC has been conducted on the DBN-based series, a more thorough examination is required to fully understand the phase behaviour

of these ILs, particularly [DBNH][Form] and [DBNH][Ac]. NMR measurements of [DBNH][Ac] at 70 °C or higher, well above the melting point, would also assist in understanding the variation in diffusion coefficients with anion size and the effects of supercooling. X-ray measurements are an important tool in understanding microscopic structure. A systematic study of either, or both, IL series could be undertaken in both the solid or liquid phases and correlated to the findings of the aggregation models. A systematic study using computer simulation could also be correlated with the basic modelling presented here, using methods such as molecular dynamics or even more coarse-grained methods.

The modelling techniques used here provide no direct insight into the nature of the structures forming. A more complex model could be derived to consider different types of aggregation, such as micellar phases or liquid crystalline phases. The complexity required in these models would likely require additional data, such as X-ray structures or simulations. A simpler addition to the model would be to automate the fitting procedure, perhaps even forming a basic software package for distribution to other researchers.

Many academic studies have used co-solvents for cellulose dissolution in ILs, with dimethyl sulfoxide (DMSO) a commonly used example [149, 191, 192]. These co-solvents are highly useful in industry, decreasing the solution viscosity and decreasing the amount of expensive IL needed. Co-solvents will undoubtedly have an affect on the aggregation behaviour in ILs. The modelling techniques used here could be adapted for the presence of co-solvents, in order to elucidate the microscopic structure of co-solvent-IL mixtures.

A clear direction would be a combination of two studies; DBN-based ILs are highly effective at dissolving cellulose but it is unknown if changing to this cation might affect the 5,4,3 rule. It would also be interesting to see if the techniques shown in Chapter 5 would detect any significant difference in the dissolution of glucose, cellobiose and cellulose in DBN-based ILs, and whether this could be related to the differences in pairing and aggregation shown by these ILs. The 5,4,3 rule could also be tested on other anion chain lengths, using either the [C_2MIM] or DBN cations.

Further cellulose dissolution work could be undertaken with imidazolium-based ILs. In order to move closer towards industrial application, the next process

to study is the regeneration of cellulose in an anti-solvent. Water is typically used and [C_2MIM][Ac] has been studied extensively, but different anion chain lengths could also be investigated. Cellulose is typically regenerated to form fibres or films. Both the coagulation kinetics and the properties of these fibres, such as morphology and mechanical strength, may be affected by a change in anion size. The addition of smaller amounts of water to IL-cellulose solutions could provide a valuable insight into the resistance of IL solutions to water contamination. This is an important property for industrial applications and the changing hydrophobicity of different anion chain lengths may have significant effects.

Appendix A

Additional Data

A.1 NMR Spectra

Imidazolium-based ILs

Chapter 3 studied four imidazolium-based ILs. The spectra for these ILs are given below, obtained on a Bruker Avance II 400 MHz spectrometer, as detailed in Section 2.1.2.

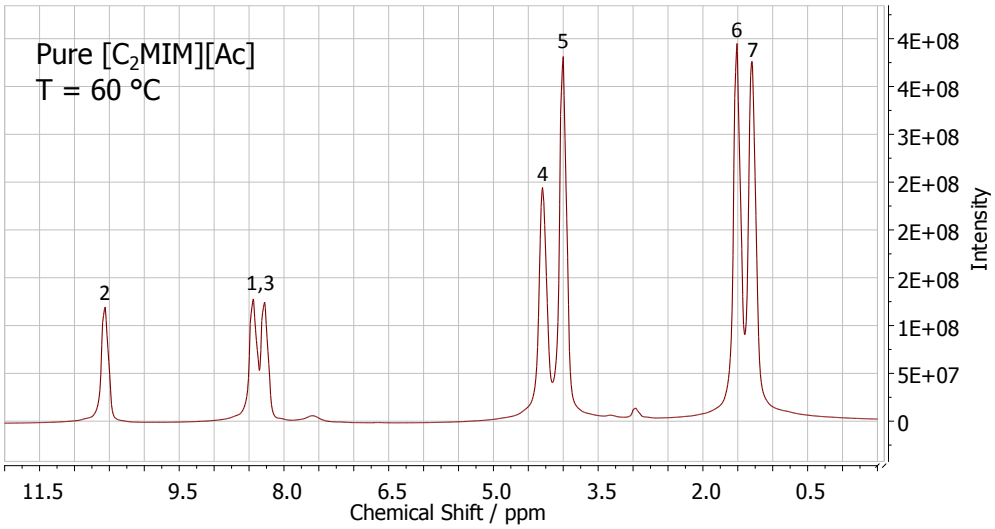

Figure A.1: ^{1}H NMR spectrum for [C_2MIM][Ac], as used in Chapter 3 and shown in Figure 3.1.

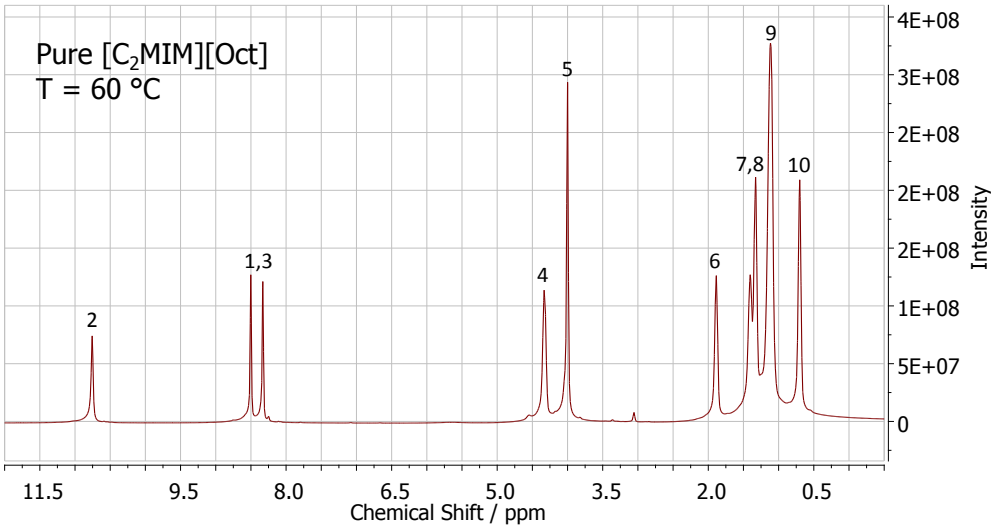

Figure A.2: ^{1}H NMR spectrum for [C_2MIM][Oct], as used in Chapters 3 and 5 and shown in Figures 3.1 and 5.2.

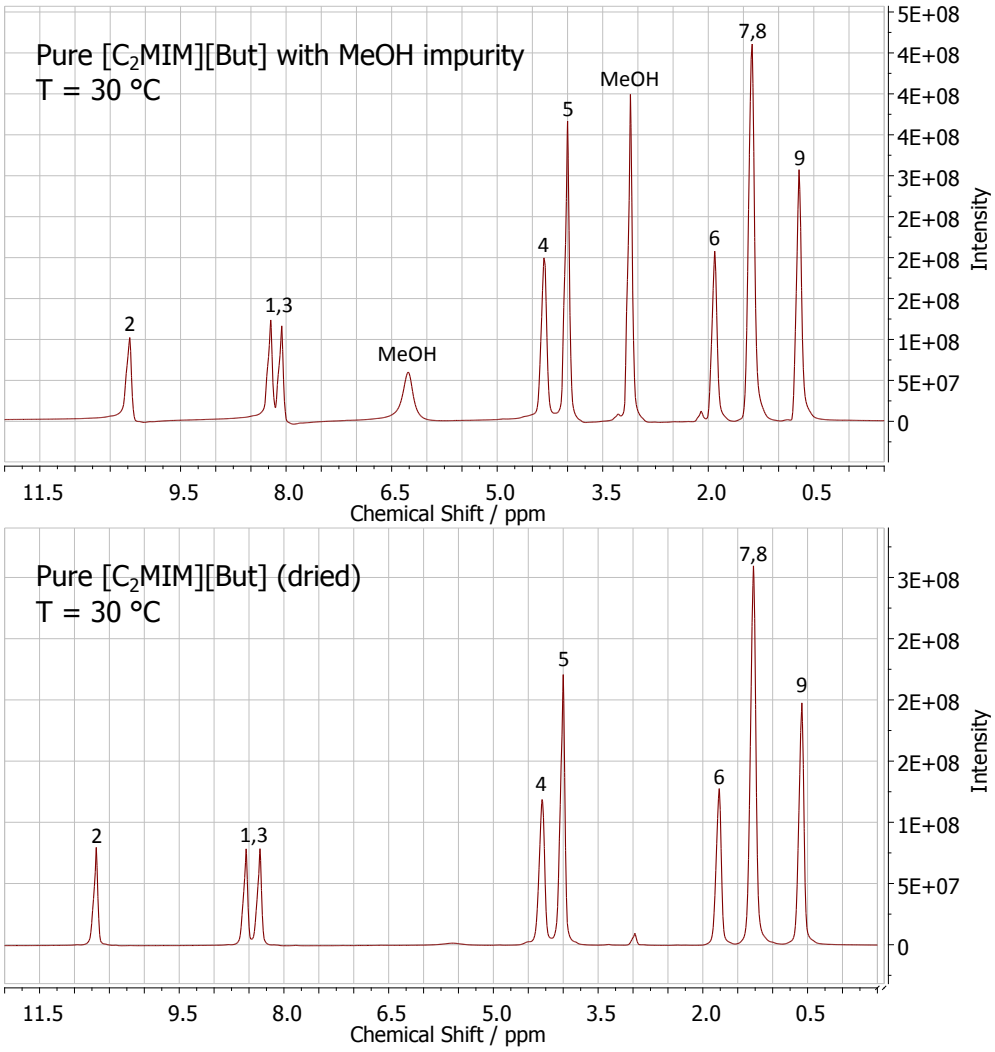

Figure A.3: ^{1}H NMR spectra for [C_2MIM][But], as used in Chapters 3 and shown in Figure 3.1. Spectra show sample contaminated with methanol from the manufacturer, followed by a sample that has had the residual methanol removed.

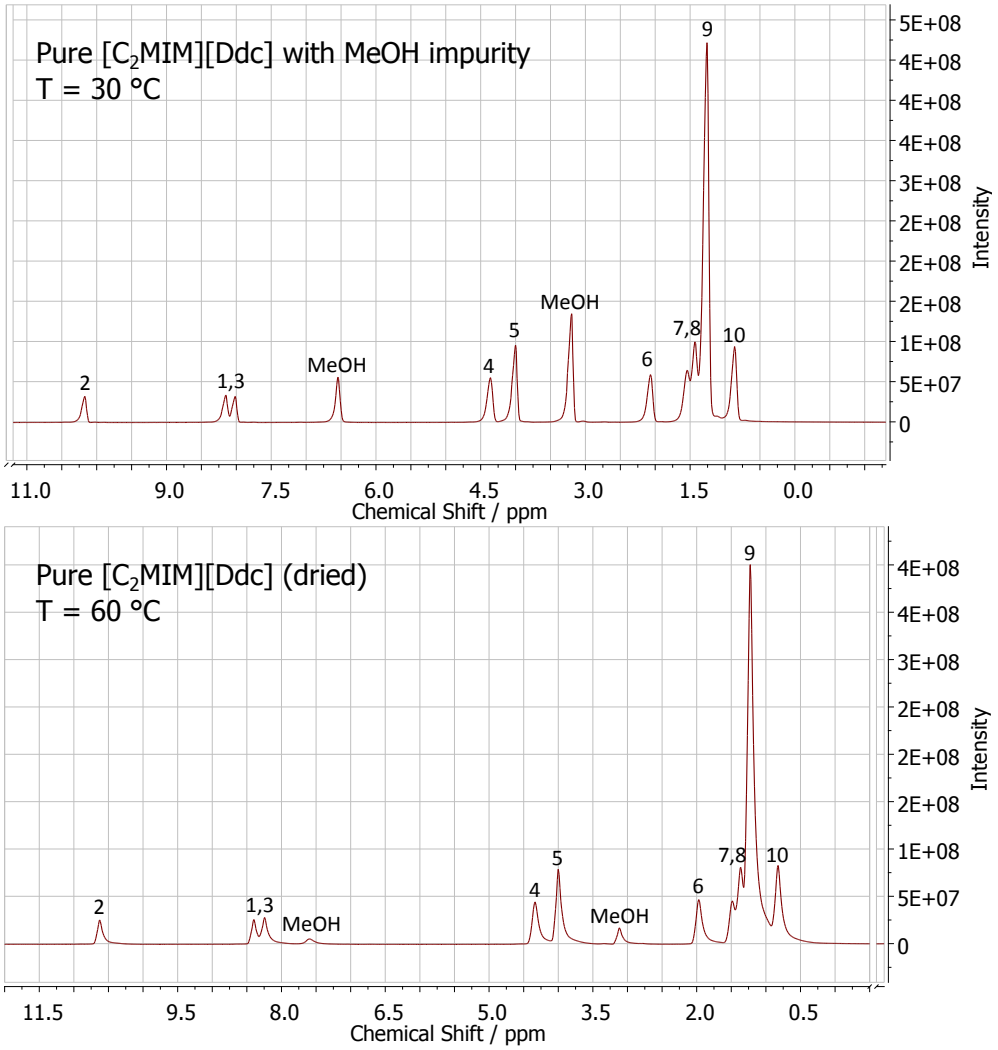

Figure A.4: ^{1}H NMR spectra for [C_2MIM][Ddc], as used in Chapter 3 and shown in Figure 3.1. Spectra show sample contaminated with methanol from the manufacturer, followed by a sample that has had as much residual methanol removed as possible.

DBN-based ILs

Chapter 4 studied eight DBN-based ILs. The spectra for these ILs are given below, obtained on a Bruker Avance II 400 MHz spectrometer, as detailed in Section 2.1.2.

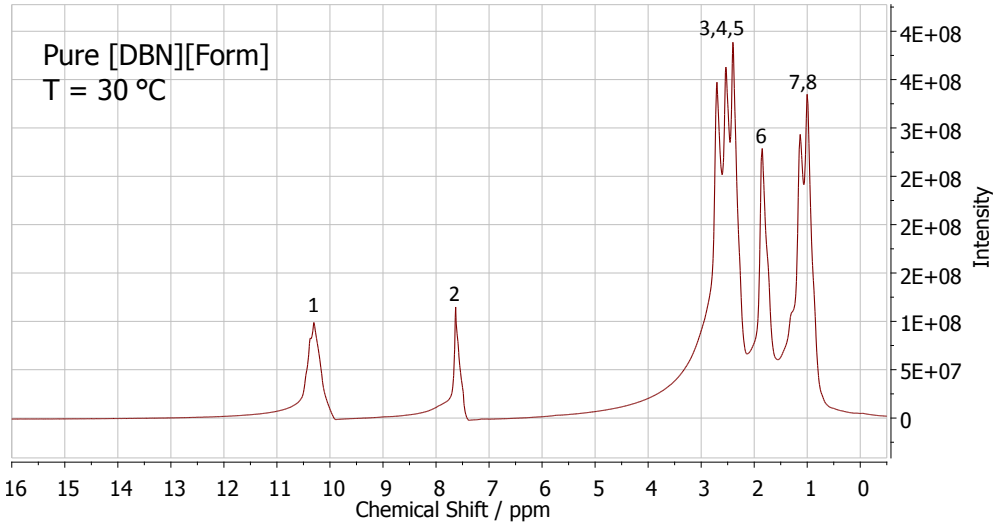

Figure A.5: ^{1}H NMR spectrum for [DBNH][Form], as used in Chapter 4 and shown in Figure 4.1. The sample shown here is in a supercooled state.

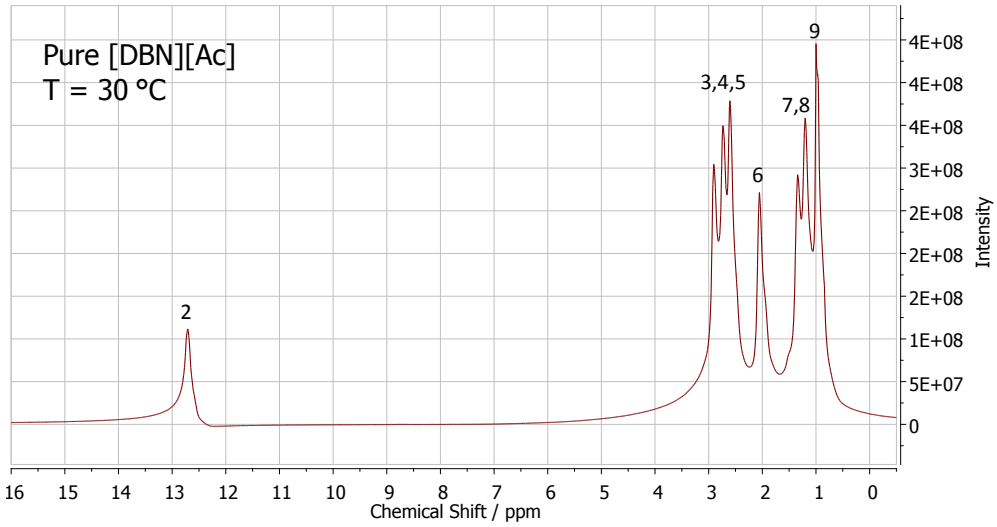

Figure A.6: ^{1}H NMR spectrum for [DBNH][Ac], as used in Chapter 4 and shown in Figure 4.1. The sample shown here is in a supercooled state.

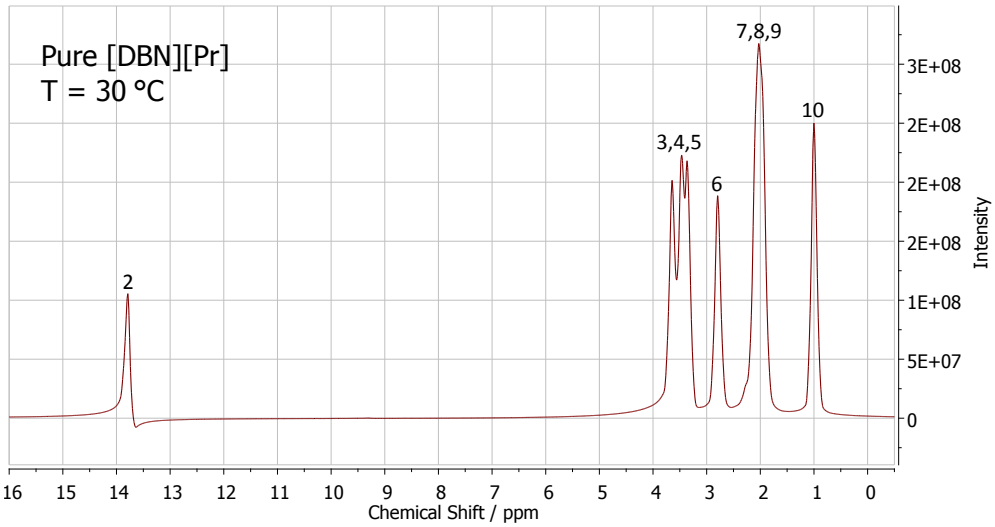

Figure A.7: ^{1}H NMR spectrum for [DBNH][Pr], as used in Chapter 4 and shown in Figure 4.1.

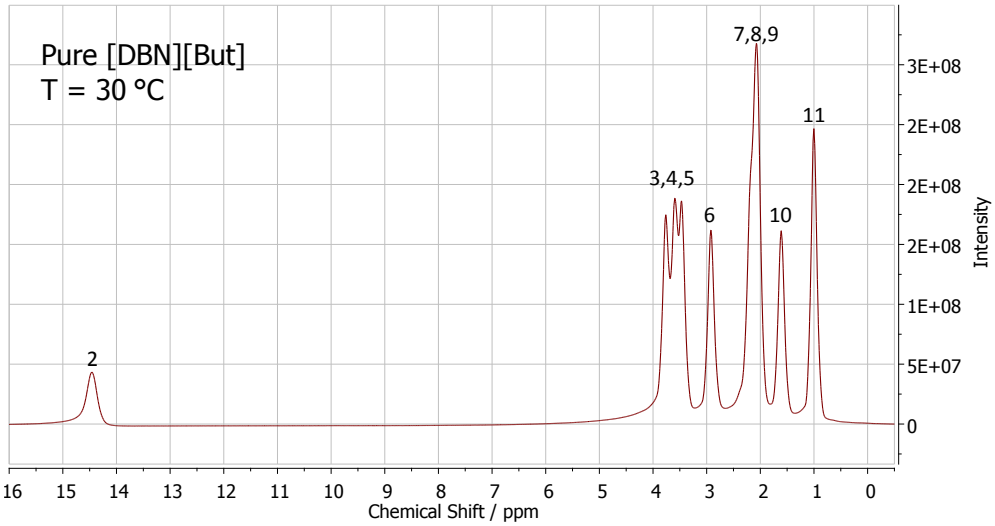

Figure A.8: ^{1}H NMR spectrum for [DBNH][But], as used in Chapter 4 and shown in Figure 4.1.

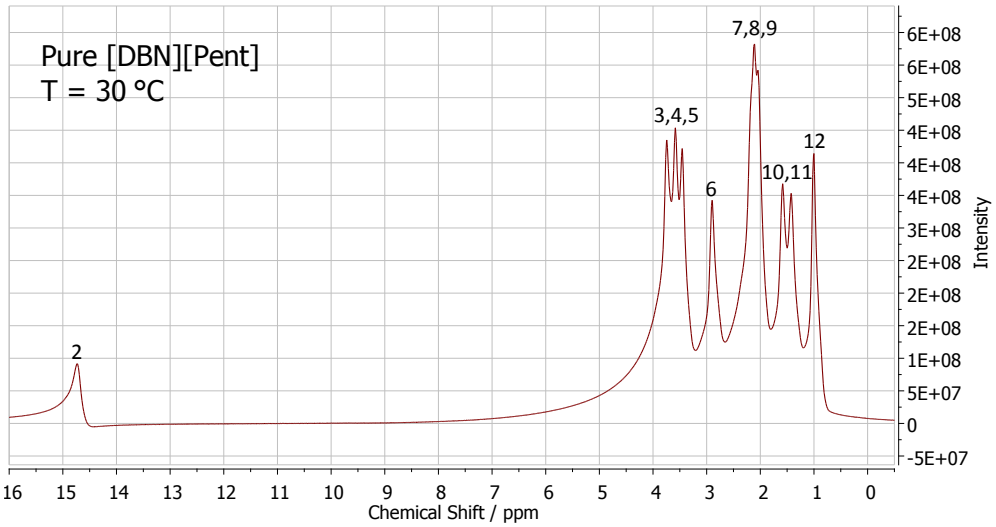

Figure A.9: ^{1}H NMR spectrum for [DBNH][Pent], as used in Chapter 4 and shown in Figure 4.1.

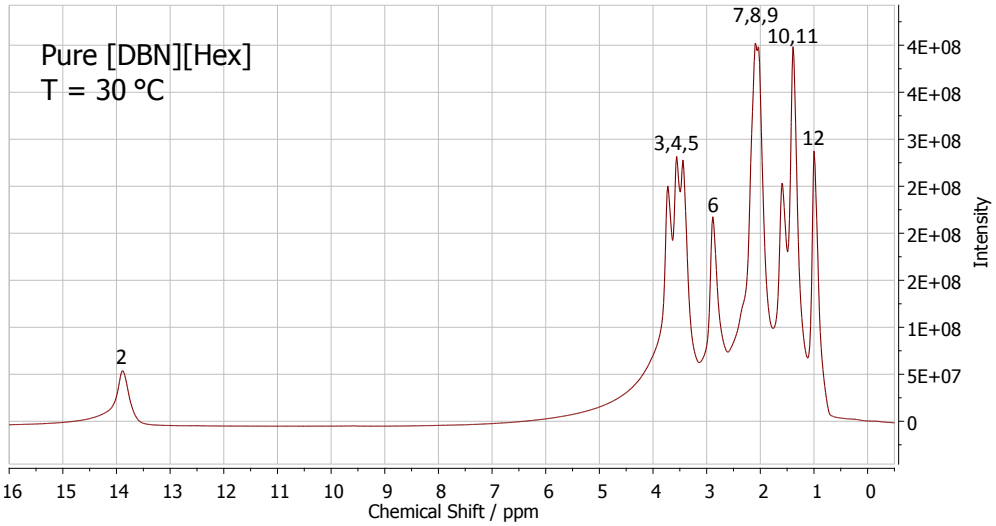

Figure A.10: ^{1}H NMR spectrum for [DBNH][Hex], as used in Chapter 4 and shown in Figure 4.1.

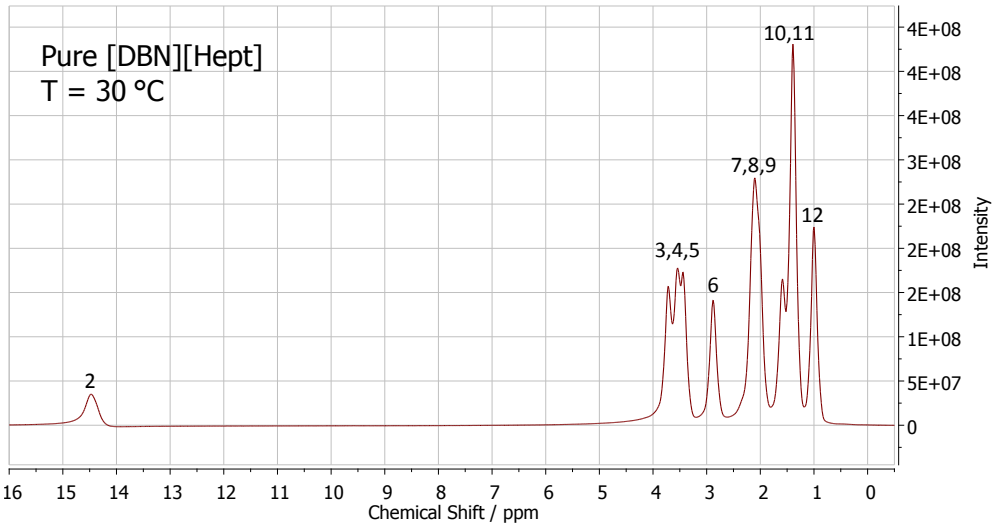

Figure A.11: ^{1}H NMR spectrum for [DBNH][Hept], as used in Chapter 4 and shown in Figure 4.1.

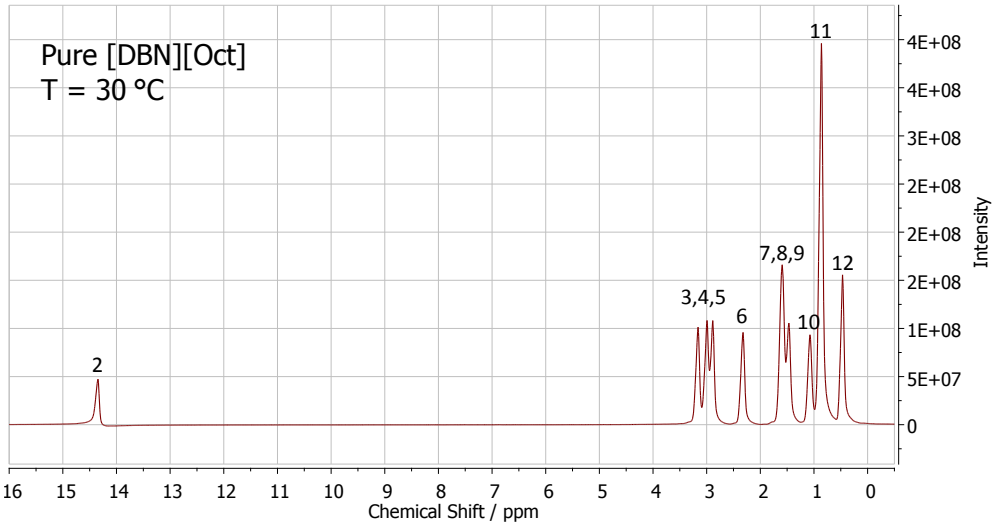

Figure A.12: ^{1}H NMR spectrum for [DBNH][Oct], as used in Chapter 4 and shown in Figure 4.1.

A.2 DSC Data

Differential Scanning Calorimetry (DSC) was measured for several DBN-based ILs on a TA Q2000 Differential Scanning Calorimeter, with a liquid nitrogen cooling system for temperature control. The temperature and heat flow of the system were calibrated using standard samples of indium and adamantane. Samples were placed in aluminium hermetically sealed pans and measured at a rate of 10 K min^{-1} from -90 °C to 90 °C. Figures A.13 to A.16 show the traces obtained for [DBNH][Form], [DBNH][Ac], [DBNH][Pr] and [DBNH][But].

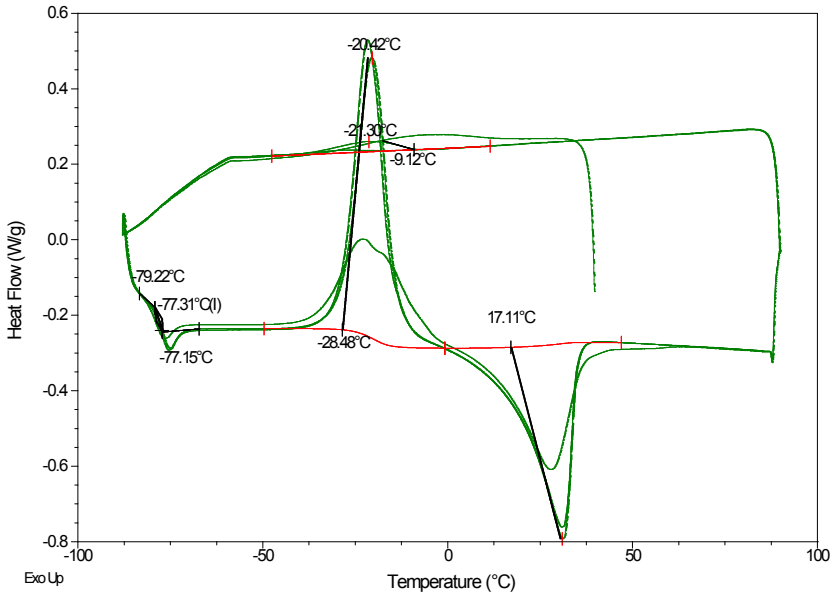

Figure A.13: DSC trace for [DBNH][Form], as used in Chapter 4 and shown in Figure 4.1. Temperatures associated with the glass transition and melting are labelled.

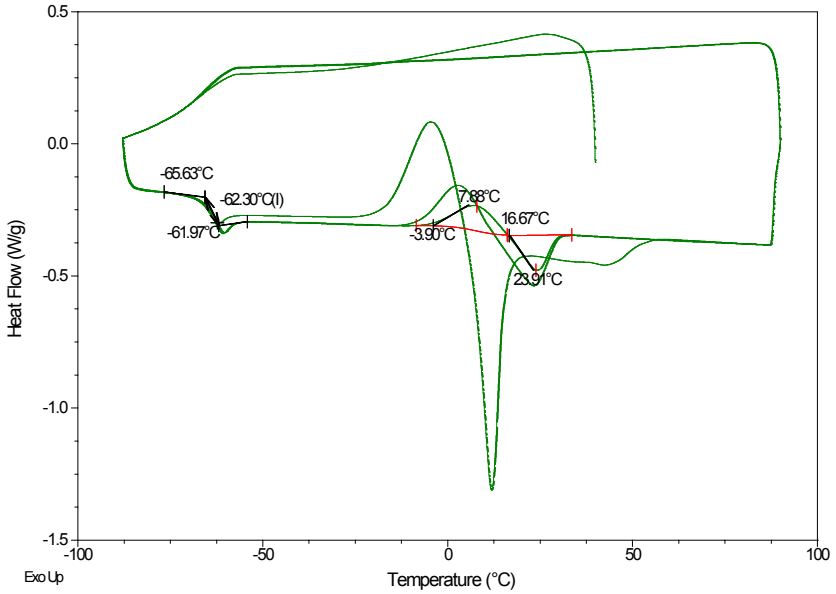

Figure A.14: DSC trace for [DBNH][Ac], as used in Chapter 4 and shown in Figure 4.1. Temperatures associated with the glass transition and melting are labelled.

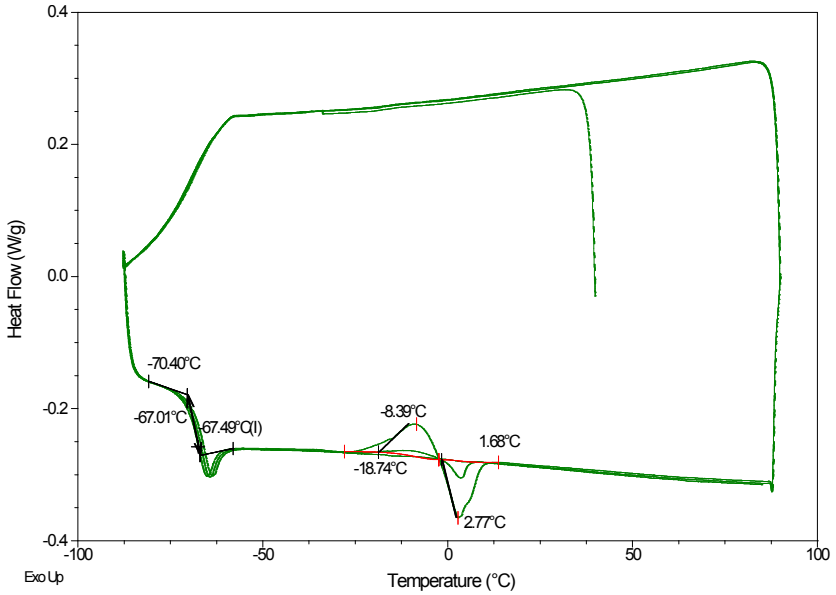

Figure A.15: DSC trace for [DBNH][Pr], as used in Chapter 4 and shown in Figure 4.1. Temperatures associated with the glass transition and melting are labelled.

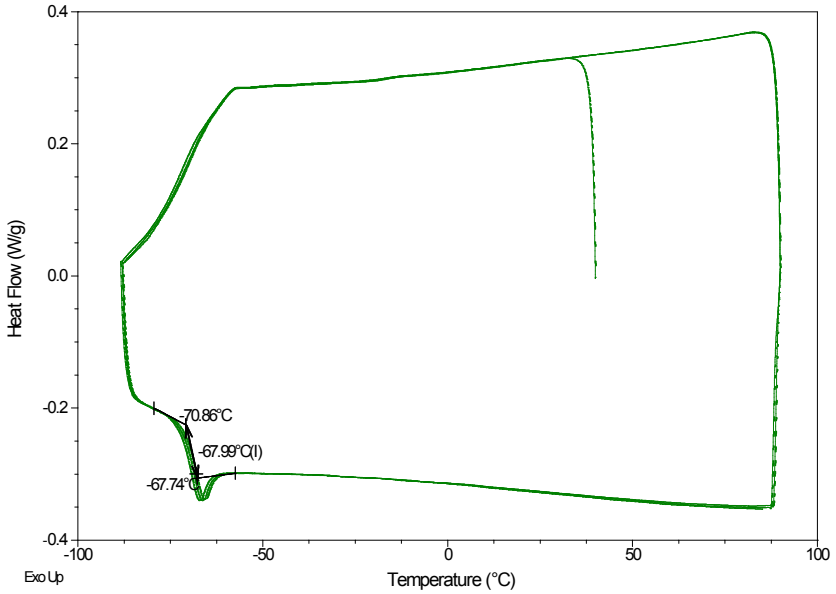

Figure A.16: DSC trace for [DBNH][But], as used in Chapter 4 and shown in Figure 4.1. Temperatures associated with the glass transition are labelled.

[DBNH][Form] and [DBNH][Ac] both exhibit strong melting points between 0 and 50 °C. Unfortunately, these phase transitions are somewhat inconsistent, both with literature data [58, 93] and with expected results. By comparison, [DBNH][Pr] has no sign of melting/freezing point above 20 °C and [DBNH][But] exhibits no melting point. All four ILs show a glass transition at around -70 °C.

These data support the claim that all ILs with chain lengths above $l = 3$ ([DBNH][Pr] to [DBNH][Oct]) are room-temperature ILs. In contrast, [DBNH][Form] and [DBNH][Ac] have a more complex phase behaviour at room-temperature and are susceptible to freezing or forming a supercooled liquid.

A.3 NMR Fitting Parameters

T_1 / ms				
Glucose Conc. (wt %)	A / 10^8 s^{-2}	$E_{a,\tau}$ / kJ mol^{-1}	τ_0 / 10^{-13} s	τ / 10^{-10} s (at 40 °C)
0	6.69	21.6	3.94	15.8
1	6.61	26.5	0.67	17.8
3	6.31	26.7	0.74	21.2
5	6.43	26.0	0.99	21.4
10	5.69	25.9	1.81	37.6
15	5.69	28.8	0.76	48.9
Cellobiose Conc. (wt %)	A / 10^8 s^{-2}	$E_{a,\tau}$ / kJ mol^{-1}	τ_0 / 10^{-13} s	τ / 10^{-10} s (at 40 °C)
0	6.69	21.6	3.94	15.8
1	7.64	25.4	0.81	13.9
3	7.08	24.2	1.60	17.2
5	5.96	27.2	0.75	26.0
10	6.03	25.5	1.69	30.0
15	5.41	25.3	2.71	45.5
Cellulose Conc. (wt %)	A / 10^8 s^{-2}	$E_{a,\tau}$ / kJ mol^{-1}	τ_0 / 10^{-13} s	τ / 10^{-10} s (at 40 °C)
0	6.69	21.6	3.94	15.8
1	6.44	27.0	0.56	17.9
3	6.76	24.3	1.59	17.8
5	6.7	23.3	2.56	19.4
6	6.27	23.1	3.07	21.6
10	5.65	27.0	1.03	33.0

Table A.1: Fitting parameters for low-field (20 MHz) T_1 relaxation data in solutions of glucose, cellobiose and cellulose in [C_2MIM][Oct], shown partially in Figure 5.9, based on Equations 2.1 and 2.2.

T_2 / ms

Glucose Conc. (wt %)	A / 10^8 s^{-2}	$E_{a,\tau}$ / kJ mol^{-1}	τ_0 / s	τ / 10^{-10} s (at 40 °C)
0	6.69	43.5	1.56×10^{-16}	28.0
1	16.1	50.1	6.01×10^{-18}	13.9
3	24.2	52.6	1.91×10^{-18}	11.5
5	16.7	49.6	9.24×10^{-18}	17.6
10	24.3	66.1	3.29×10^{-20}	34.5
15	43.0	79.7	2.06×10^{-22}	40.5
Cellobiose Conc. (wt %)	**A / 10^8 s^{-2}**	**$E_{a,\tau}$ / kJ mol^{-1}**	**τ_0 / s**	**τ / 10^{-10} s (at 40 °C)**
0	6.7	43.5	1.56×10^{-16}	28.0
1	11.0	35.6	1.73×10^{-15}	15.1
3	14.7	41.4	1.96×10^{-16}	15.5
5	12.7	49.6	1.45×10^{-17}	27.1
10	20.0	58.9	4.41×10^{-19}	29.3
15	44.3	78.0	3.46×10^{-22}	35.6
Cellulose Conc. (wt %)	**A / 10^8 s^{-2}**	**$E_{a,\tau}$ / kJ mol^{-1}**	**τ_0 / s**	**τ / 10^{-10} s (at 40 °C)**
0	6.69	43.5	1.56×10^{-16}	28.0
1	12.0	39.2	4.51×10^{-16}	15.4
3	13.0	43.1	1.18×10^{-16}	18.4
5	15.9	47.7	2.13×10^{-17}	19.6
6	16.0	49.8	1.05×10^{-17}	21.7
10	21.4	62.4	1.23×10^{-19}	31.8

Table A.2: Fitting parameters for low-field (20 MHz) T_2 relaxation data in solutions of glucose, cellobiose and cellulose in [C_2MIM][Oct], shown partially in Figure 5.9, based on Equations 2.1 and 2.2.

Appendix B

Testing Dissolution Conditions

B.1 IL Reactivity During Carbohydrate Dissolution

Chapter 5 details an investigation into using [C_2MIM][Oct] as a solvent for glucose, cellobiose and cellulose; [C_2MIM][Ac] has also been used extensively as a solvent for cellulose. Cellulose solvents such as these are often referred to as 'non-derivatising' solvents, meaning neither the cellulose nor the solvent undergo a chemical change during dissolution. However, a number of studies have questioned this assumption. In particular, Clough et al. studied a range of ILs dissolving glucose at elevated temperatures, including [C_2MIM][Ac] [86]. It was found that the C2 atom on the imidazolium ring (see Figure 3.1) reacted with glucose in a substitution reaction. The substituted glucose then decomposed sequentially to leave a single hydroxylated alkyl group attached to the C2 atom on the imidazolium ring. This final byproduct is identifiable by an NMR peak at a chemical shift of 4.79 ppm.

The conditions used in Chapter 5 involved a dissolution temperature of 60 °C, compared to the temperatures of 120 °C used by Clough et al. [86]. A short experiment was carried out to assess the extent of degradation under the conditions used here. Concentrated solutions of glucose were prepared in [C_2MIM][Ac] and [C_2MIM][Oct] at room temperature. Glucose was chosen as the most reactive analogue of cellulose [86] and the easiest to dissolve. The solutions were then

held in an oil bath at 60 °C for 6 hours, to simulate the dissolution process used in Chapter 5. NMR spectra were obtained for these solutions using the equipment and methods described in Section 2.1.2. Figures B.1a and B.2a show the spectra obtained after 6 hours at 60 °C. The same solutions were then held at 100 °C for an additional 6 hours. NMR spectra were obtained again and are shown in Figures B.1b and B.2b.

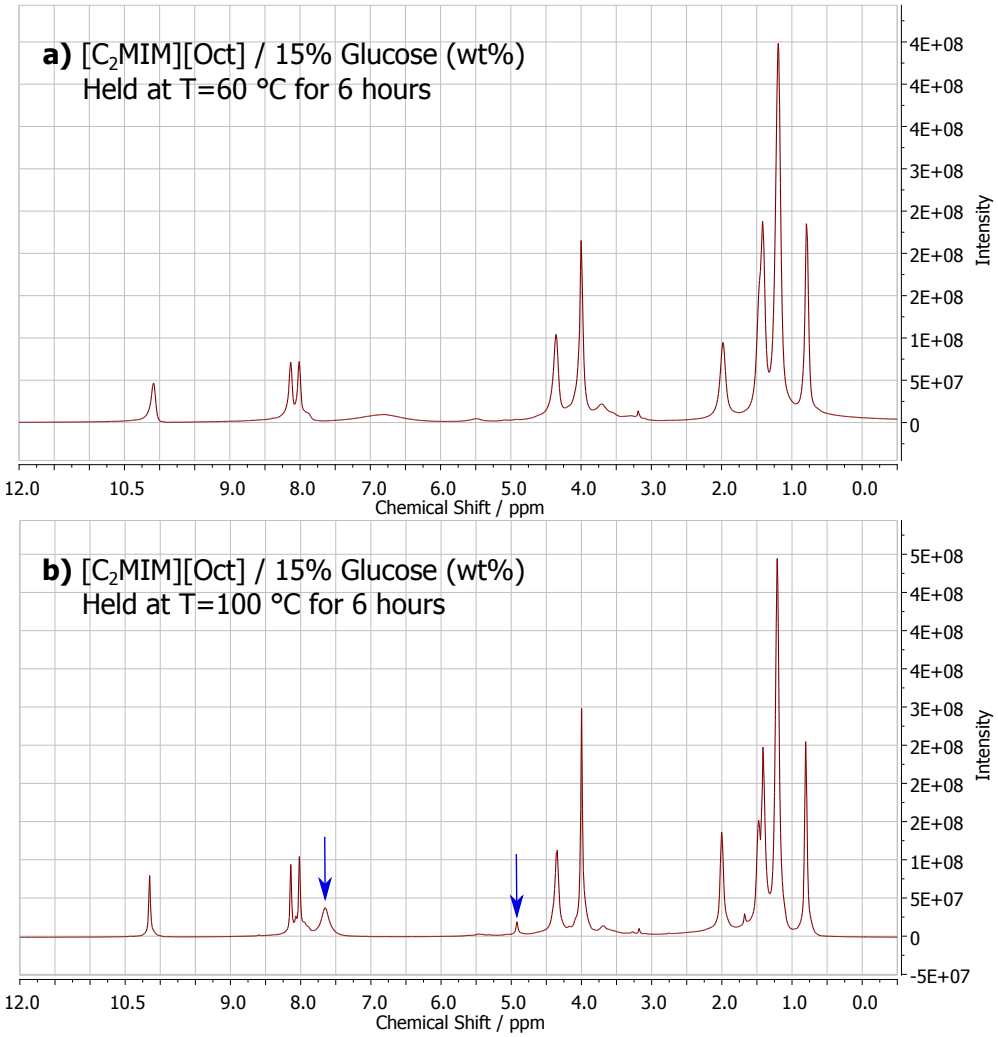

Figure B.1: ^{1}H NMR spectrum for glucose dissolved in [C_2MIM][Oct], as used in Chapter 5. The two spectra show solutions held at two different temperatures of **a)** 60 °C and **b)** 100 °C. The sample shown in **b)** shows additional peaks, marked by the blue arrows.

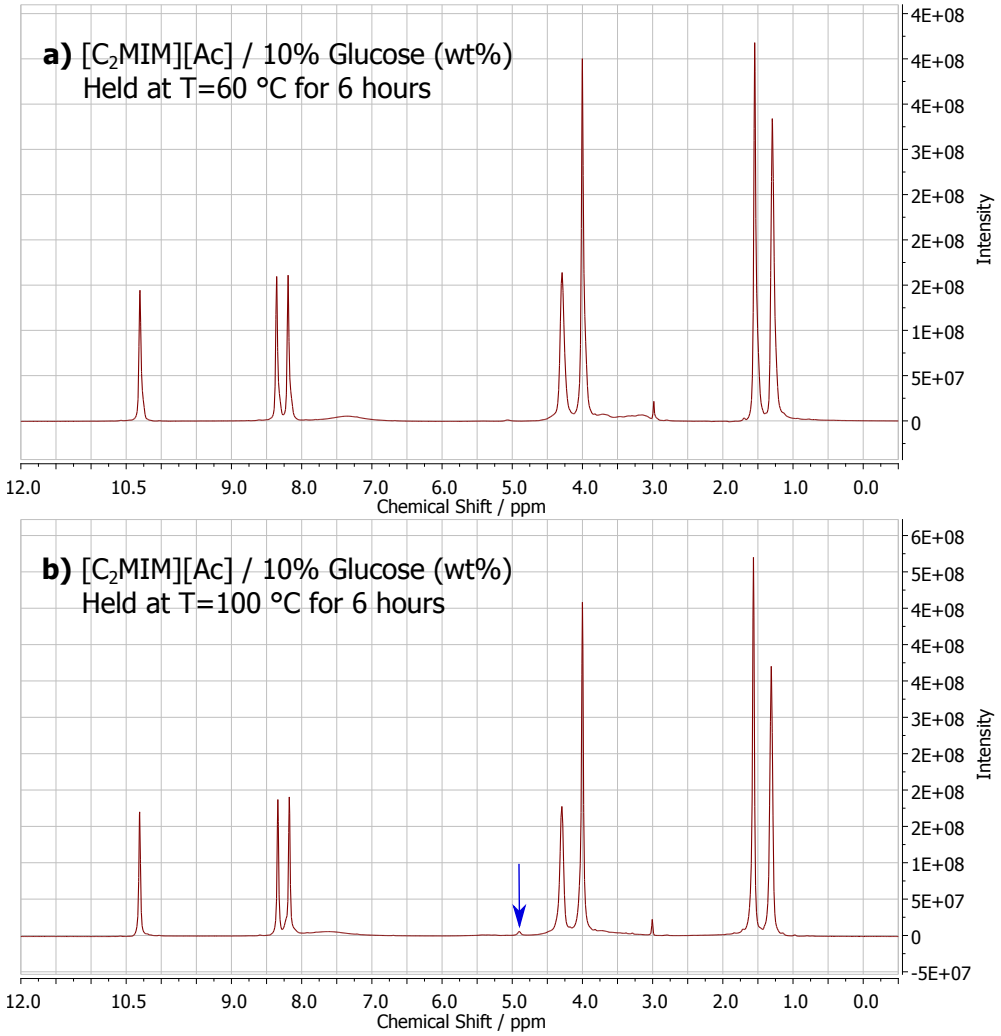

Figure B.2: ^{1}H NMR spectrum for glucose dissolved in [C_2MIM][Ac], as a comparison to [C_2MIM][Oct]. The two spectra show solutions held at two different temperatures of **a)** 60 °C and **b)** 100 °C. The sample shown in **b)** shows an additional peak, marked by the blue arrow.

For the samples held at 60 °C, there are no signs of any peak at ≈4.8 ppm. This indicates that the degradation of glucose in these ILs is minimal, under the conditions used in Chapter 5. As glucose is more reactive than cellobiose or cellulose [86], it is safe to assume that all the solutions prepared in Chapter 5 have not degraded to any significant degree. In contrast to this, the samples held at 100 °C both show additional peaks formed at ≈4.8 ppm. This is in

agreement with the work of Clough et al. [86]. The extent of degradation appears to be much higher in $[C_2MIM][Oct]$ (Figure B.1) than $[C_2MIM][Ac]$ (Figure B.2). This is an interesting result, perhaps suggesting that the anion plays a role in the carbohydrate degradation process. Though, this could be due to the higher glucose content used in the $[C_2MIM][Oct]$ sample. It is also worth noting that for both ILs, the colour of the solution changed from pale yellow to a dark brown colour after being held at 100 °C. This is consistent with the glucose 'caramelising' and degrading at the higher temperature.

Appendix C

Equation Reference Tables

C.1 Theory

Stokes-Einstein	$D_i = \frac{k_B T}{6 f \pi \eta r_{h,i}}$	Equation 2.4
Stokes-Einstein-Debye	$\tau_r = \frac{4}{3}\pi r_h^3 \frac{\eta}{k_B T}$	Equation 2.6
Nernst-Einstein	$\Lambda = \frac{N_A e^2}{k_B T}(v_+ z_+^2 D_{pos} + v_- z_-^2 D_{neg})$	Equation 2.10
BPP Theory	$\frac{1}{T_1} = 2A\left(\frac{\tau}{1+\omega^2\tau^2} + \frac{4\tau}{1+4\omega^2\tau^2}\right)$	Equation 2.1
	$\frac{1}{T_2} = A\left(3\tau + \frac{5\tau}{1+\omega^2\tau^2} + \frac{2\tau}{1+4\omega^2\tau^2}\right)$	Equation 2.2
Hydrodynamic Radius	$r_{h,i} \approx \frac{1}{2}\left(\frac{M_i}{\rho N_A}\right)^{\frac{1}{3}}$	Equation 2.5
Walden Rule	$\Lambda\eta = constant$	Equation 2.12

C.2 Modelling

Equations describe models defined in Section 2.3 and used in Sections 3.4 and 4.4. Experimentally measured quantities are D_{an}, D_{cat}, η, ρ and σ. Molar masses M_{IL}, M_+, M_-, M_p and M_{agg} are derived from chemical formulae. Parameters n, P and R are fitting parameters, where R is simply related to P (see below).

C.2.1 Isolated Ions Model

Molar Conductivity	$\Lambda_{imp} = \frac{\sigma}{c} = \frac{\sigma M_{IL}}{\rho}$	Equation 2.13
	$\Lambda_{NMR} = \frac{N_A e^2}{k_B T}(D_{cat} + D_{an})$	Equation 2.15
Diffusion Ratio	$\frac{D_{an}}{D_{cat}} = \left(\frac{M_+}{M_-}\right)^{\frac{1}{3}}$	Equation 2.14

C.2.2 Pair Model

Molar Conductivity	$\Lambda_{imp} = \frac{\sigma M_{IL}}{\rho(1-P)}$	Equation 2.20
	$\Lambda_{NMR} = \frac{N_A e^2}{k_B T}(D_{cat} + D_{an} - 2PD_p)$	Equation 2.19
Diffusion Ratio	$\frac{D_{an}}{D_{cat}} = \frac{PM_p^{-\frac{1}{3}} + (1-P)M_-^{-\frac{1}{3}}}{PM_p^{-\frac{1}{3}} + (1-P)M_+^{-\frac{1}{3}}}$	Equation 2.18

C.2.3 Aggregate Model

Molar Conductivity	$\Lambda_{imp} = \frac{\sigma M_{eff}}{\rho} = \frac{n\sigma M_{IL}}{\rho}$	Equation 2.30
	$\Lambda_{NMR} = \frac{N_A e^2}{k_B T}(nD_{cat} - (n-2)D_{an})$	Equation 2.28
Diffusion Ratio	$\frac{D_{an}}{D_{cat}} = \frac{nM_{agg}^{-\frac{1}{3}}}{M_+^{-\frac{1}{3}} + (n-1)M_{agg}^{-\frac{1}{3}}}$	Equation 2.29

C.2.4 Combined Model

R	$P = \frac{R}{n+R}$	Equation 2.31
Molar Conductivity	$\Lambda_{imp} = \frac{\sigma M_{eff}}{\rho} = \frac{(n+R)\sigma M_{IL}}{\rho}$	Equation 2.44
	$\Lambda_{NMR} = \frac{N_A e^2 (n+R)}{k_B T(1+R)}\left(D_{cat} + \left(\frac{2}{n} - 1\right) D_{an} - \frac{2RD_p}{n(n+R)}\right)$	Equation 2.41
Diffusion Ratio	$\frac{D_{an}}{D_{cat}} = \frac{nM_{agg}^{-\frac{1}{3}} + RM_p^{-\frac{1}{3}}}{M_+^{-\frac{1}{3}} + (n-1)M_{agg}^{-\frac{1}{3}} + RM_p^{-\frac{1}{3}}}$	Equation 2.36

References

[1] D. Klemm, B. Heublein, H.-P. Fink, and A. Bohn, "Cellulose: fascinating biopolymer and sustainable raw material.," *Angewandte Chemie (International ed. in English)*, vol. 44, pp. 3358–93, May 2005. 1, 2, 3, 4, 5

[2] H. G. Wiedemann and G. Bayer, "Papyrus: The paper of ancient Egypt," *Analytical Chemistry*, vol. 55, no. 12, pp. 1220–1230, 1983. 2

[3] A. Payen, "Mémoire sur la composition du tissu propre des plantes et du ligneux," *Comptes Rendus*, vol. 7, pp. 1052–1056, 1838. 2

[4] "Innovia films - innovation timeline." http://www.innoviafilms.com/innovation-centre/Innovation-Timeline.aspx accessed 12th May 2017. 2

[5] G. B. Kauffman, "Rayon: The first semi-synthetic fiber product," *Journal of Chemical Education*, vol. 70, no. 11, p. 887, 1993. 2

[6] H. Staudinger, "Über polymerisation," *European Journal of Inorganic Chemistry*, vol. 53, no. 6, pp. 1073–1085, 1920. 2

[7] P. T. Anastas and M. M. Kirchhoff, "Origins, current status, and future challenges of green chemistry," *Accounts of Chemical Research*, vol. 35, pp. 686–694, sep 2002. 3, 7

[8] R. H. Atalla and D. L. VanderHart, "Native Cellulose: A Composite of Two Distinct Crystalline Forms," *Science*, vol. 223, no. 4633, pp. 283–285, 1984. 4

[9] Y. Nishiyama, G. P. Johnson, A. D. French, V. T. Forsyth, and P. Langan, "Neutron Crystallography, Molecular Dynamics, and Quantum Mechanics Studies of the Nature of Hydrogen Bonding in Cellulose I," *Biomacromolecules*, vol. 9, pp. 3133–3140, 2008. 4

[10] A. S. Gross and J.-W. Chu, "On the molecular origins of biomass recalcitrance: the interaction network and solvation structures of cellulose microfibrils.," *The Journal of Physical Chemistry B*, vol. 114, pp. 13333–41, Oct 2010. 4

[11] W. G. Glasser, R. H. Atalla, J. Blackwell, R. Malcolm Brown, W. Burchard, A. D. French, D. O. Klemm, and Y. Nishiyama, "About the structure of cellulose: debating the Lindman hypothesis," *Cellulose*, vol. 19, pp. 589–598, Mar 2012. 4

[12] Y. Nishiyama, G. P. Johnson, and A. D. French, "Diffraction from nonperiodic models of cellulose crystals," *Cellulose*, vol. 19, no. 2, pp. 319–336, 2012. 4

[13] B. Lindman, G. Karlström, and L. Stigsson, "On the mechanism of dissolution of cellulose," *Journal of Molecular Liquids*, vol. 156, pp. 76–81, Sep 2010. 4, 10

[14] B. Medronho, A. Romano, M. G. Miguel, L. Stigsson, and B. Lindman, "Rationalizing cellulose (in)solubility: reviewing basic physicochemical aspects and role of hydrophobic interactions," *Cellulose*, vol. 19, pp. 581–587, Jan 2012. 4, 10

[15] C. Roy, T. Budtova, and P. Navard, "Rheological properties and gelation of aqueous cellulose-NaOH solutions.," *Biomacromolecules*, vol. 4, pp. 259–264, 2003. 5

[16] R. D. Rogers and K. R. Seddon, "Ionic Liquids - Solvents of the Future?," *Science*, vol. 302, no. 5646, pp. 792–793, 2003. 5

[17] N. V. Plechkova and K. R. Seddon, "Applications of ionic liquids in the chemical industry," *Chemical Society Reviews*, vol. 37, pp. 123–150, 2008. 5, 6, 8

[18] H. Niedermeyer, J. P. Hallett, I. J. Villar-Garcia, P. A. Hunt, and T. Welton, "Mixtures of ionic liquids.," *Chemical Society Reviews*, vol. 41, pp. 7780–802, Dec 2012. 5

[19] G. Chatel, J. F. B. Pereira, V. Debbeti, H. Wang, and R. D. Rogers, "Mixing ionic liquids - simple mixtures or double salts?," *Green Chemistry*, vol. 16, pp. 2051–2083, 2014. 5

[20] H. Tokuda, K. Ishii, M. A. B. H. Susan, S. Tsuzuki, K. Hayamizu, and M. Watanabe, "Physicochemical Properties and Structures of Room-Temperature Ionic Liquids. 3. Variation of Cationic Structures," *Journal of Physical Chemistry B*, vol. 110, no. 6, pp. 2833–2839, 2006. 6, 30, 39

[21] J. G. Huddleston, A. E. Visser, W. M. Reichert, H. D. Willauer, G. A. Broker, and R. D. Rogers, "Characterization and comparison of hydrophilic and hydrophobic room temperature ionic liquids incorporating the imidazolium cation," *Green Chemistry*, vol. 3, pp. 156–164, 2001. 6, 7, 38

[22] H. Tokuda, K. Hayamizu, K. Ishii, M. A. B. H. Susan, and M. Watanabe, "Physicochemical Properties and Structures of Room Temperature Ionic Liquids. 1. Variation of Anionic Species," *J. Phys. Chem. B*, vol. 108, no. 42, pp. 16593–16600, 2004. 21, 27, 30, 39

[23] W. Liu, L. Cheng, Y. Zhang, H. Wang, and M. Yu, "The physical properties of aqueous solution of room-temperature ionic liquids based on imidazolium: Database and evaluation," *Journal of Molecular Liquids*, vol. 140, pp. 68–72, Apr 2008. 6

[24] H. Tokuda, K. Hayamizu, K. Ishii, M. A. B. H. Susan, and M. Watanabe, "Physicochemical Properties and Structures of Room Temperature Ionic Liquid . 2. Variation of Alkyl Chain Length in Imidazolium Cation," *J. Phys. Chem. B*, vol. 109, no. 13, pp. 6103–6110, 2005. 6, 38, 39, 54, 57

[25] S. Zhang, N. Sun, X. He, X. Lu, and X. Zhang, "Physical properties of ionic liquids: Database and evaluation," *Journal of Physical and Chemical Reference Data*, vol. 35, no. 4, pp. 1475–1517, 2006. 6

[26] I. López-Martin, E. Burello, P. N. Davey, K. R. Seddon, and G. Rothenberg, "Anion and cation effects on imidazolium salt melting points: A descriptor modelling study," *ChemPhysChem*, vol. 8, no. 5, pp. 690–695, 2007. 6

[27] J. N. A. Canongia Lopes and A. A. H. Pádua, "Nanostructural organization in ionic liquids," *Journal of Physical Chemistry B*, vol. 110, no. 7, pp. 3330–3335, 2006. 6, 39, 84

[28] Y. Wang and G. A. Voth, "Tail aggregation and domain diffusion in ionic liquids," *Journal of Physical Chemistry B*, vol. 110, no. 37, pp. 18601–18608, 2006. 6, 39, 84

[29] D. T. Bowron, C. D'Agostino, L. F. Gladden, C. Hardacre, J. D. Holbrey, M. C. Lagunas, J. McGregor, M. D. Mantle, C. L. Mullan, and T. G. A. Youngs, "Structure and Dynamics of 1-Ethyl-3-methylimidazolium Acetate via Molecular Dynamics and Neutron Diffraction," *Journal of Physical Chemistry B*, vol. 114, no. 23, pp. 7760–7768, 2010. 6, 39

[30] O. Russina, F. Lo Celso, N. V. Plechkova, and A. Triolo, "Emerging Evidences of Mesoscopic-Scale Complexity in Neat Ionic Liquids and Their Mixtures," *Journal of Physical Chemistry Letters*, vol. 8, no. 6, pp. 1197–1204, 2017. 6

[31] M. Amde, J.-F. Liu, and L. Pang, "Environmental Application, Fate, Effects, and Concerns of Ionic Liquids: A Review," *Environmental Science and Technology*, vol. 49, no. 21, pp. 12611–12627, 2015. 7

[32] S.-K. Ruokonen, C. Sanwald, M. Sundvik, S. Polnick, K. Vyavaharkar, F. Duša, A. J. Holding, A. W. T. King, I. Kilpeläinen, M. Lämmerhofer, P. Panula, and S. K. Wiedmer, "Effect of Ionic Liquids on Zebrafish (Danio rerio) Viability, Behavior, and Histology; Correlation between Toxicity and Ionic Liquid Aggregation," *Environmental Science & Technology*, vol. 50, pp. 7116–7125, 2016. 7

[33] M. J. Earle, J. M. S. S. Esperança, M. A. Gilea, J. N. C. Lopes, L. P. N. Rebelo, J. W. Magee, K. R. Seddon, and J. A. Widegren, "The distillation and volatility of ionic liquids.," *Nature*, vol. 439, pp. 831–834, 2006. 7, 26, 84, 85

[34] K. R. Seddon, A. Stark, and M.-J. Torres, "Influence of chloride, water, and organic solvents on the physical properties of ionic liquids," *Pure Appl. Chem.*, vol. 72, no. 12, pp. 2275–2287, 2000. 7, 15

[35] C. A. Hall, K. A. Le, C. Rudaz, A. Radhi, C. S. Lovell, R. A. Damion, T. Budtova, and M. E. Ries, "Macroscopic and Microscopic Study of 1-Ethyl-3-Methyl-Imidazolium Acetate - Water Mixtures," *The Journal of Physical Chemistry B*, vol. 116, pp. 12810–12818, 2012. 7, 21, 22, 42, 57

[36] K. A. Le, R. Sescousse, and T. Budtova, "Influence of water on cellulose-EMIMAc solution properties: a viscometric study," *Cellulose*, vol. 19, pp. 45–54, Nov 2011. 7

[37] A. Menjoge, J. Dixon, J. F. Brennecke, E. J. Maginn, and S. Vasenkov, "Influence of water on diffusion in imidazolium-based ionic liquids: a pulsed field gradient NMR study.," *The Journal of Physical Chemistry B*, vol. 113, pp. 6353–9, May 2009. 7

[38] P. Walden, "Molecular weights and electrical conductivity of several fused salts," *Bull. Acad. Imper. Sci.(St. Petersburg)*, vol. 8, pp. 405–422, 1914. 7

[39] C. A. Angell, N. Byrne, and J. P. Belieres, "Parallel developments in aprotic and protic ionic liquids: Physical chemistry and applications," *Accounts of Chemical Research*, vol. 40, pp. 1228–1236, Nov 2007. 7, 23, 24, 63, 84

[40] M. Olkiewicz, M. P. Caporgno, J. Font, J. Legrand, O. Lepine, N. V. Plechkova, J. Pruvost, K. R. Seddon, and C. Bengoa, "A novel recovery process for lipids from microalgæ for biodiesel production using a hydrated phosphonium ionic liquid," *Green Chemistry*, vol. 17, pp. 2813–2824, 2015. 8

[41] H. Xie, X. Yu, Y. Yang, and Z. K. Zhao, "Capturing CO2 for cellulose dissolution," *Green Chemistry*, vol. 16, p. 2422, 2014. 8, 85

[42] J. Sakuda, M. Yoshio, T. Ichikawa, H. Ohno, and T. Kato, "2D assemblies of ionic liquid crystals based on imidazolium moieties: formation of ion-conductive layers," *New J. Chem.*, vol. 39, pp. 4471–4477, 2015. 8

[43] S. Fister, S. Fuchs, P. Mester, I. Kilpeläinen, M. Wagner, and P. Rossmanith, "The use of ionic liquids for cracking viruses for isolation of nucleic acids," *Separation and Purification Technology*, vol. 155, 2014. 8

[44] M. Shadid, G. Gurau, J. L. Shamshina, B.-C. Chuang, S. Hailu, E. Guan, S. K. Chowdhury, J.-T. Wu, S. A. A. Rizvi, R. J. Griffin, and R. D. Rogers, "Sulfasalazine in ionic liquid form with improved solubility and exposure," *Med. Chem. Commun.*, vol. 6, pp. 1837–1841, 2015.

[45] S.-K. Ruokonen, F. Duša, J. Lokajová, I. Kilpeläinen, A. W. King, and S. K. Wiedmer, "Effect of ionic liquids on the interaction between liposomes and common wastewater pollutants investigated by capillary electrophoresis," *Journal of Chromatography A*, vol. 1405, pp. 178–187, 2015. 8

[46] C. Graenacher, "Cellulose solution," Jan. 9 1934. US Patent 1,943,176. 8

[47] R. P. Swatloski, S. K. Spear, J. D. Holbrey, and R. D. Rogers, "Dissolution of Cellulose with Ionic Liquids," *Journal of the American Chemical Society*, vol. 124, pp. 4974–4975, May 2002. 8, 9, 10, 11, 38, 124, 125

[48] R. Swatloski, R. Rogers, and J. Holbrey, "Dissolution and processing of cellulose using ionic liquids," Aug. 21 2003. US Patent App. 10/256,521. 8

[49] H. Zhang, J. Wu, J. Zhang, and J. He, "1-Allyl-3-methylimidazolium Chloride Room Temperature Ionic Liquid: A New and Powerful Nonderivatizing Solvent for Cellulose," *Macromolecules*, vol. 38, pp. 8272–8277, Oct 2005. 8, 124

[50] J. S. Moulthrop, R. P. Swatloski, G. Moyna, and R. D. Rogers, "High-resolution 13C NMR studies of cellulose and cellulose oligomers in ionic liquid solutions.," *Chemical Communications*, pp. 1557–9, Mar 2005. 124

[51] R. C. Remsing, R. P. Swatloski, R. D. Rogers, and G. Moyna, "Mechanism of cellulose dissolution in the ionic liquid 1-n-butyl-3-methylimidazolium chloride: a 13C and 35/37Cl NMR relaxation study on model systems.," *Chemical Communications*, pp. 1271–3, Mar 2006. 8, 10, 124, 142

[52] Y. Fukaya, A. Sugimoto, and H. Ohno, "Superior solubility of polysaccharides in low viscosity, polar, and halogen-free 1,3-dialkylimidazolium formates.," *Biomacromolecules*, vol. 7, pp. 3295–7, Dec 2006. 8, 9, 38, 39, 124, 125

[53] A. Pinkert, K. N. Marsh, S. Pang, and M. P. Staiger, "Ionic liquids and their interaction with cellulose.," *Chemical Reviews*, vol. 109, pp. 6712–28, Dec 2009. 8, 9

[54] B. Zhao, L. Greiner, and W. Leitner, "Cellulose solubilities in carboxylate-based ionic liquids," *RSC Advances*, vol. 2, pp. 2476–79, 2012. 9, 10, 11, 125

[55] B. Lu, A. Xu, and J. Wang, "Cation does matter: how cationic structure affects the dissolution of cellulose in ionic liquids," *Green Chemistry*, vol. 16, pp. 1326–1335, 2014. 8, 125, 142

[56] A. W. T. King, J. Asikkala, I. Mutikainen, P. Järvi, and I. Kilpeläinen, "Distillable Acid-Base Conjugate Ionic Liquids for Cellulose Dissolution and Processing," *Angewandte Chemie*, vol. 123, pp. 6425–6429, Jul 2011. 8, 39, 84, 85, 120, 125

[57] L. K. J. Hauru, M. Hummel, A. W. T. King, I. Kilpeläinen, and H. Sixta, "Role of solvent parameters in the regeneration of cellulose from ionic liquid solutions.," *Biomacromolecules*, vol. 13, pp. 2896–905, Sep 2012. 9, 85, 124, 125

[58] A. Parviainen, A. W. T. King, I. Mutikainen, M. Hummel, C. Selg, L. K. J. Hauru, H. Sixta, and I. Kilpeläinen, "Predicting cellulose solvating capabilities of acid-base conjugate ionic liquids," *ChemSusChem*, vol. 6, no. 11, pp. 2161–2169, 2013. 8, 39, 85, 86, 88, 90, 99, 120, 125, 172

[59] R. C. Remsing, G. Hernandez, R. P. Swatloski, W. W. Massefski, R. D. Rogers, and G. Moyna, "Solvation of carbohydrates in n,n'-dialkylimidazolium ionic liquids: a multinuclear NMR spectroscopy study.," *The Journal of Physical Chemistry B*, vol. 112, pp. 11071–8, Sep 2008. 10, 38, 47, 124, 126, 142

[60] M. Gericke, K. Schlufter, T. Liebert, T. Heinze, and T. Budtova, "Rheological properties of cellulose/ionic liquid solutions: from dilute to concentrated states.," *Biomacromolecules*, vol. 10, pp. 1188–94, May 2009. 9, 10, 124, 126

[61] C. S. Lovell, A. Walker, R. A. Damion, A. Radhi, S. F. Tanner, T. Budtova, and M. E. Ries, "Influence of Cellulose on Ion Diffusivity in 1-Ethyl-3-Methyl-Imidazolium Acetate Cellulose Solutions.," *Biomacromolecules*, vol. 11, pp. 2927–2935, Oct 2010. 9, 16, 42, 88, 124, 126, 129, 141, 142

[62] Y. Fukaya, K. Hayashi, M. Wada, and H. Ohno, "Cellulose dissolution with polar ionic liquids under mild conditions: required factors for anions," *Green Chemistry*, vol. 10, pp. 44–46, 2008. 9, 38

[63] A. Pinkert, K. N. Marsh, and S. Pang, "Reflections on the Solubility of Cellulose," *Industrial and Engineering Chemistry Research*, vol. 49, no. 22, pp. 11121–11130, 2010. 9, 125

[64] "Web of science service for uk education." http://wok.mimas.ac.uk/ accessed 18th May 2017. 9

[65] J. Sundberg, G. Toriz, and P. Gatenholm, "Moisture induced plasticity of amorphous cellulose films from ionic liquid," *Polymer*, vol. 54, pp. 6555–6560, Nov 2013. 9

[66] I. Kilpeläinen, H. Xie, A. King, M. Granstrom, S. Heikkinen, and D. S. Argyropoulos, "Dissolution of wood in ionic liquids," *Journal of Agricultural and Food Chemistry*, vol. 55, no. 22, pp. 9142–9148, 2007. 9, 11

[67] D. A. Fort, R. C. Remsing, R. P. Swatloski, P. Moyna, G. Moyna, and R. D. Rogers, "Can ionic liquids dissolve wood? Processing and analysis of lignocellulosic materials with 1-n-butyl-3-methylimidazolium chloride," *Green Chemistry*, vol. 9, no. 1, pp. 63–69, 2007.

[68] M. Zavrel, D. Bross, M. Funke, J. Büchs, and A. C. Spiess, "High-throughput screening for ionic liquids dissolving (ligno-)cellulose.," *Bioresource Technology*, vol. 100, pp. 2580–7, May 2009. 9, 11

[69] T. G. A. Youngs, C. Hardacre, and J. D. Holbrey, "Glucose solvation by the ionic liquid 1,3-dimethylimidazolium chloride: a simulation study.," *Journal of Physical Chemistry B*, vol. 111, pp. 13765–74, Dec 2007. 9, 10

[70] T. G. A. Youngs, J. D. Holbrey, C. L. Mullan, S. E. Norman, M. C. Lagunas, C. D'Agostino, M. D. Mantle, L. F. Gladden, T. Bowron, and C. Hardacre, "Neutron diffraction, NMR and molecular dynamics study of glucose dissolved in the ionic liquid 1-ethyl-3-methylimidazolium acetate," *Chemical Science*, vol. 2, no. 8, p. 1594, 2011. 124, 126, 152

[71] B. D. Rabideau, A. Agarwal, and A. E. Ismail, "The role of the cation in the solvation of cellulose by imidazolium-based ionic liquids.," *The Journal of Physical Chemistry B*, vol. 118, pp. 1621–9, Feb 2014. 124, 125, 152

[72] S. Velioglu, X. Yao, J. Devemy, M. Goktug Ahunbay, S. Birgul Tantekin-Ersolmaz, A. Dequidt, M. F. Costa Gomes, and A. Padua, "Solvation of a Cellulose Microfibril in Imidazolium Acetate Ionic Liquids: Effect of a Cosolvent," *Journal of Physical Chemistry B*, vol. 118, pp. 14860–14869, 2014.

[73] Y. Li, X. Liu, S. Zhang, Y. Yao, X. Yao, J. Xu, and X. Lu, "Dissolving process of a cellulose bunch in ionic liquids: a molecular dynamics study.," *Physical Chemistry Chemical Physics*, vol. 17, no. 27, pp. 17894–905, 2015.

[74] B. D. Rabideau and A. E. Ismail, "Mechanisms of hydrogen bond formation between ionic liquids and cellulose and the influence of water content," *Physical Chemistry Chemical Physics*, vol. 17, pp. 5767–5775, 2015. 9, 124, 125, 152

[75] M. Deetlefs, M. Fanselow, and K. R. Seddon, "Ionic liquids: the view from Mount Improbable," *RSC Advances*, vol. 6, pp. 4280–4288, 2016. 9

[76] H. Ohno and Y. Fukaya, "Task Specific Ionic Liquids for Cellulose Technology," *Chemistry Letters*, vol. 38, no. 1, pp. 2–7, 2009. 9

[77] H. Wang, G. Gurau, and R. D. Rogers, "Ionic liquid processing of cellulose.," *Chemical Society Reviews*, vol. 41, pp. 1519–37, Mar 2012.

[78] K. C. Badgujar and B. M. Bhanage, "Factors governing dissolution process of lignocellulosic biomass in ionic liquid: Current status, overview and challenges," *Bioresource Technology*, vol. 178, pp. 2–18, 2015. 9

[79] A. S. Gross, A. T. Bell, and J.-W. Chu, "Entropy of cellulose dissolution in water and in the ionic liquid 1-butyl-3-methylimidazolim chloride," *Physical Chemistry Chemical Physics*, vol. 14, pp. 8425–8430, 2012. 10

[80] Y. Zhang, A. Xu, B. Lu, Z. Li, and J. Wang, "Dissolution of cellulose in 1-allyl-3-methylimizodalium carboxylates at room temperature: A structure-property relationship study.," *Carbohydrate Polymers*, vol. 117, pp. 666–72, 2015. 10, 125

[81] D. L. Minnick, R. A. Flores, M. R. DeStefano, and A. M. Scurto, "Cellulose Solubility in Ionic Liquid Mixtures: Temperature, Cosolvent and Antisolvent Effects," *The Journal of Physical Chemistry B*, vol. 120, pp. 7906–7919, 2016. 10

[82] H. Parviainen, A. Parviainen, T. Virtanen, I. Kilpeläinen, P. Ahvenainen, R. Serimaa, S. Grönqvist, T. Maloney, and S. L. Maunu, "Dissolution enthalpies of cellulose in ionic liquids.," *Carbohydrate Polymers*, vol. 113, pp. 67–76, Nov 2014. 10

[83] J.-M. Andanson, A. A. Padua, and M. C. Gomes, "Thermodynamics of Cellulose Dissolution in an Imidazolium Acetate Ionic Liquid," *Chemical Communications*, vol. 51, p. 4485, 2015. 10, 124

[84] R. Sescousse, K. A. Le, M. E. Ries, and T. Budtova, "Viscosity of cellulose-imidazolium-based ionic liquid solutions.," *The Journal of Physical Chemistry B*, vol. 114, pp. 7222–8, Jun 2010. 10, 17, 42, 53, 56, 124, 126, 129

[85] A. Michud, M. Hummel, S. Haward, and H. Sixta, "Monitoring of cellulose depolymerization in 1-ethyl-3-methylimidazolium acetate by shear and elongational rheology," *Carbohydrate Polymers*, vol. 117, pp. 355–363, 2015. 10

[86] M. T. Clough, K. Geyer, P. A. Hunt, S. Son, U. Vagt, and T. Welton, "Ionic liquids: not always innocent solvents for cellulose," *Green Chemistry*, vol. 17, pp. 231–243, 2015. 10, 129, 175, 177, 178

[87] M. Mazza, D.-A. Catana, C. Vaca-Garcia, and C. Cecutti, "Influence of water on the dissolution of cellulose in selected ionic liquids," *Cellulose*, vol. 16, pp. 207–215, Oct 2008. 11

[88] J. Vitz, T. Erdmenger, C. Haensch, and U. S. Schubert, "Extended dissolution studies of cellulose in imidazolium based ionic liquids," *Green Chemistry*, vol. 11, no. 3, p. 417, 2009. 11, 124, 125

[89] H. Sixta, A. Michud, L. Hauru, S. Asaadi, Y. Ma, A. W. T. King, I. Kilpeläinen, and M. Hummel, "Ioncell-F : A High-strength regenerated cellulose fibre," *Nordic Pulp & Paper Research Journal*, vol. 30, pp. 43–57, 2015. 11, 85

[90] A. Parviainen, R. Wahlström, U. Liimatainen, T. Liitiä, S. Rovio, J. K. J. Helminen, U. Hyväkkö, A. W. T. King, A. Suurnäkki, and I. Kilpeläinen, "Sustainability of cellulose dissolution and regeneration in 1,5-diazabicyclo[4.3.0]non-5-enium acetate: a batch simulation of the IONCELL-F process," *RSC Advances*, vol. 5, no. 85, pp. 69728–69737, 2015.

[91] W. Ahmad, A. Ostonen, K. Jakobsson, P. Uusi-Kyyny, V. Alopaeus, U. Hyväkkö, and A. W. T. King, "Feasibility of thermal separation in

recycling of the distillable ionic liquid [DBNH][OAc] in cellulose fiber production," *Chemical Engineering Research and Design*, vol. 114, pp. 287–298, 2016.

[92] A. Michud, M. Hummel, and H. Sixta, "Influence of process parameters on the structure formation of man-made cellulosic fibers from ionic liquid solution," *Journal of Applied Polymer Science*, vol. 133, no. 30, p. 43718, 2016.

[93] A. Ostonen, J. Bervas, P. Uusi-Kyyny, V. Alopaeus, D. H. Zaitsau, V. N. Emel'Yanenko, C. Schick, A. W. T. King, J. Helminen, I. Kilpelainen, A. A. Khachatrian, M. A. Varfolomeev, and S. P. Verevkin, "Experimental and Theoretical Thermodynamic Study of Distillable Ionic Liquid 1,5-Diazabicyclo[4.3.0]non-5-enium Acetate," *Industrial and Engineering Chemistry Research*, vol. 55, no. 39, pp. 10445–10454, 2016. 85, 88, 172

[94] A. M. Stepan, A. Michud, S. Hellstén, M. Hummel, and H. Sixta, "IONCELL-P&F: Pulp Fractionation and Fiber Spinning with Ionic Liquids," *Industrial & Engineering Chemistry Research*, vol. 55, pp. 8225–8233, 2016. 11, 86

[95] H. Abushammala, I. Krossing, and M. P. Laborie, "Ionic liquid-mediated technology to produce cellulose nanocrystals directly from wood," *Carbohydrate Polymers*, vol. 134, pp. 609–616, 2015. 11

[96] H. Abushammala, R. Goldsztayn, A. Leao, and M. P. Laborie, "Combining steam explosion with 1-ethyl-3-methylimidazlium acetate treatment of wood yields lignin-coated cellulose nanocrystals of high aspect ratio," *Cellulose*, vol. 23, no. 3, pp. 1813–1823, 2016. 11

[97] J. Mao, A. Osorio-Madrazo, and M. P. Laborie, "Preparation of cellulose I nanowhiskers with a mildly acidic aqueous ionic liquid: Reaction efficiency and whiskers attributes," *Cellulose*, vol. 20, no. 4, pp. 1829–1840, 2013. 11

[98] Q. Zhao, R. C. M. Yam, B. Zhang, Y. Yang, X. Cheng, and R. K. Y. Li, "Novel all-cellulose ecocomposites prepared in ionic liquids," *Cellulose*, vol. 16, no. 2, pp. 217–226, 2009. 11

[99] B. J. C. Duchemin, A. P. Mathew, and K. Oksman, "All-cellulose composites by partial dissolution in the ionic liquid 1-butyl-3-methylimidazolium chloride," *Composites Part A: Applied Science and Manufacturing*, vol. 40, no. 12, pp. 2031–2037, 2009.

[100] W. Gindl-Altmutter, J. Keckes, J. Plackner, F. Liebner, K. Englund, and M. P. Laborie, "All-cellulose composites prepared from flax and lyocell fibres compared to epoxy-matrix composites," *Composites Science and Technology*, vol. 72, no. 11, pp. 1304–1309, 2012. 11

[101] R. Sescousse, R. Gavillon, and T. Budtova, "Aerocellulose from cellulose-ionic liquid solutions: Preparation, properties and comparison with cellulose-NaOH and cellulose-NMMO routes," *Carbohydrate Polymers*, vol. 83, pp. 1766–1774, Feb 2011. 11, 38

[102] C. Rudaz and T. Budtova, "Rheological and hydrodynamic properties of cellulose acetate/ionic liquid solutions.," *Carbohydrate Polymers*, vol. 92, pp. 1966–71, Feb 2013. 11

[103] O. Gordobil, I. Egüés, I. Urruzola, and J. Labidi, "Xylan-cellulose films: Improvement of hydrophobicity, thermal and mechanical properties," *Carbohydrate Polymers*, vol. 112, pp. 56–62, 2014. 11

[104] S. Bylin, C. Olsson, G. Westman, and H. Theliander, "Solvation behavior of cellulose and xylan in the MIM/EMIMAc ionic liquid solvent system parameters for small scale solvation," *BioResources*, vol. 9, no. 1, pp. 1038–1054, 2014. 11

[105] W. Liu and T. Budtova, "Ionic liquid: A powerful solvent for homogeneous starch-cellulose mixing and making films with tuned morphology," *Polymer*, vol. 53, pp. 5779–5787, Nov 2012. 11

[106] W. Liu and T. Budtova, "Dissolution of unmodified waxy starch in ionic liquid and solution rheological properties.," *Carbohydrate Polymers*, vol. 93, pp. 199–206, Mar 2013.

[107] B. Zhang, L. Chen, F. Xie, X. Li, R. W. Truss, P. J. Halley, J. L. Shamshina, R. D. Rogers, and T. McNally, "Understanding the structural disorganization of starch in water-ionic liquid solutions.," *Physical Chemistry Chemical Physics*, vol. 17, pp. 13860–71, 2015.

[108] B. Zhang, F. Xie, T. Zhang, L. Chen, X. Li, R. W. Truss, P. J. Halley, J. L. Shamshina, T. McNally, and R. D. Rogers, "Different characteristic effects of ageing on starch-based films plasticised by 1-ethyl-3-methylimidazolium acetate and by glycerol," *Carbohydrate Polymers*, vol. 146, pp. 67–79, 2016. 11

[109] C. Rudaz, R. Courson, L. Bonnet, S. Calas-Etienne, H. Sallee, and T. Budtova, "Aeropectin: Fully Biomass-Based Mechanically Strong and Thermal Superinsulating Aerogel," *Biomacromolecules*, vol. 15, pp. 2188–2195, 2014. 11

[110] A. Takegawa, M.-A. Murakami, Y. Kaneko, and J.-I. Kadokawa, "Preparation of chitin/cellulose composite gels and films with ionic liquids," *Carbohydrate Polymers*, vol. 79, pp. 85–90, Jan 2010. 11

[111] O. Kuzmina, T. Heinze, and D. Wawro, "Blending of Cellulose and Chitosan in Alkyl Imidazolium Ionic Liquids," *ISRN Polymer Science*, vol. 2012, pp. 1–9, 2012. 38

[112] P. S. Barber, C. S. Griggs, G. Gurau, Z. Liu, S. Li, Z. Li, X. Lu, S. Zhang, and R. D. Rogers, "Coagulation of chitin and cellulose from 1-ethyl-3-methylimidazolium acetate ionic-liquid solutions using carbon dioxide.," *Angewandte Chemie (International ed. in English)*, vol. 52, pp. 12350–3, Nov 2013. 38

[113] X. Shen, J. L. Shamshina, P. Berton, J. Bandomir, H. Wang, G. Gurau, and R. D. Rogers, "Comparison of Hydrogels Prepared with Ionic-Liquid-Isolated vs Commercial Chitin and Cellulose," *ACS Sustainable Chemistry and Engineering*, vol. 4, no. 2, pp. 471–480, 2016. 11

[114] L. Kyllönen, A. Parviainen, S. Deb, M. Lawoko, M. Gorlov, I. Kilpeläinen, and A. W. T. King, "On the solubility of wood in non-derivatising ionic liquids," *Green Chemistry*, vol. 15, p. 2374, 2013. 11

[115] I. Anugwom, V. Eta, P. Virtanen, P. Mäki-Arvela, M. Hedenström, M. Yibo, M. Hummel, H. Sixta, and J.-P. Mikkola, "Towards optimal selective fractionation for Nordic woody biomass using novel amineorganic superbase derived switchable ionic liquids (SILs)," *Biomass and Bioenergy*, vol. 70, pp. 373–381, 2014. 11

[116] A. Abragam, *Principles of Nuclear Magnetism*. Clarendon Press, Oxford, 1961. 15

[117] P. T. Callaghan, *Principles of Nuclear Magnetic Resonance Microscopy*. Oxford science publications, Clarendon Press, 1993.

[118] M. Levitt, *Spin Dynamics: Basics of Nuclear Magnetic Resonance*. Wiley, 2001. 15

[119] G. Annat, D. R. Macfarlane, and M. Forsyth, "Transport properties in ionic liquids and ionic liquid mixtures: the challenges of NMR pulsed field gradient diffusion measurements.," *The Journal of Physical Chemistry B*, vol. 111, pp. 9018–24, Aug 2007. 16

[120] E. O. Stejskal and J. E. Tanner, "Spin diffusion measurements: spin echoes in the presence of a time-dependant field gradient," *The Journal of Chemical Physics*, vol. 42, no. 1, pp. 288–292, 1965. 16

[121] H. Y. Carr and E. M. Purcell, "Effects of diffusion on free precession in nuclear magnetic resonance experiments," *Physical Review*, vol. 94, no. 3, pp. 630–638, 1954. 17

[122] S. Meiboom and D. Gill, "Modified spin-echo method for measuring nuclear relaxation times," *Review of Scientific Instruments*, vol. 29, no. 8, pp. 688–691, 1958. 17

[123] N. Bloembergen, E. M. Purcell, and R. V. Pound, "Relaxation effects in nuclear magnetic resonance absorption," *Physical Review*, vol. 73, no. 7, pp. 679–712, 1948. 19, 50

[124] B. Blicharska, H. Peemoeller, and M. Witek, "Hydration water dynamics in biopolymers from NMR relaxation in the rotating frame.," *Journal of Magnetic Resonance*, vol. 207, pp. 287–93, Dec 2010. 19

[125] R. E. Powell, W. E. Roseveare, and H. Eyring, "Diffusion, Thermal Conductivity, and Viscous Flow of Liquids," *Industrial & Engineering Chemistry*, vol. 33, no. 4, pp. 430–435, 1941. 20, 21

[126] J. C. M. Li and P. Chang, "Self-Diffusion Coefficient and Viscosity in Liquids," *The Journal of Chemical Physics*, vol. 23, no. 3, p. 518, 1955. 21

[127] D. J. Gisser and M. D. Ediger, "Modification of Solvent Rotational Dynamics by the Addition of Small Molecules or Polymers," *Journal of Physical Chemistry*, vol. 97, no. 41, pp. 10818–10823, 1993. 21

[128] H. Antony, A. Dölle, D. Mertens, P. Wasserscheid, W. R. Carper, and P. G. Wahlbeck, "NMR Relaxation Rates in the Ionic Liquid 1-Methyl-3-nonylimidazolium Hexafluorophosphate," *J. Phys. Chem. A*, vol. 109, pp. 6676–6682, 2005. 20, 21, 47

[129] E. McLaughlin, "Viscosity and Self-Diffusion in Liquids," *Transactions of the Faraday Society*, vol. 55, p. 28, 1958. 20, 21

[130] R. Schiller, "The Stokes-Einstein law by macroscopic arguments," *International Journal of Radiation Applications and Instrumentation. Part C. Radiation Physics and Chemistry*, vol. 37, no. 3, pp. 549–550, 1991. 21

[131] T. Köddermann, R. Ludwig, and D. Paschek, "On the validity of Stokes-Einstein and Stokes-Einstein-Debye relations in ionic liquids and ionic-liquid mixtures," *ChemPhysChem*, vol. 9, pp. 1851–1858, 2008. 21

[132] W. R. Carper, G. J. Mains, B. J. Piersma, S. L. Mansfield, and C. K. Larive, "13 C NMR Relaxation and 1 H Diffusion (DOSY) Studies of an Acidic Chloroaluminate Melt," *The Journal of Physical Chemistry*, vol. 100, no. 12, pp. 4724–4728, 1996. 22, 47

[133] P. Atkins and J. De Paula, *Physical Chemistry*. W. H. Freeman, 2009. 22

[134] K. R. Harris, "Relations between the Fractional Stokes-Einstein and Nernst-Einstein Equations and Velocity Correlation Coefficients in Ionic Liquids and Molten Salts," *J. Phys. Chem B*, vol. 114, pp. 9572–9577, 2010. 23

[135] J. Bockris and A. Reddy, *Modern Electrochemistry: An Introduction to an Interdisciplinary Area*. Modern Electrochemistry: An Introduction to an Interdisciplinary Area, Plenum Pub. Corp., 1973. 23

[136] M. Yoshizawa, W. Xu, and C. A. Angell, "Ionic Liquids by Proton Transfer: Vapor Pressure, Conductivity, and the Relevance of pKa from Aqueous Solutions," *Journal of the American Chemical Society*, vol. 125, no. 50, pp. 15411–15419, 2003. 23, 24, 63, 84, 85

[137] J. P. Leal, J. M. S. S. Esperança, M. E. M. Da Piedade, J. N. C. Lopes, L. P. N. Rebelo, and K. R. Seddon, "The nature of ionic liquids in the gas phase," *Journal of Physical Chemistry A*, vol. 111, no. 28, pp. 6176–6182, 2007. 26, 84, 85

[138] A. W. T. King, A. Parviainen, P. Karhunen, J. Matikainen, L. K. J. Hauru, H. Sixta, and I. Kilpeläinen, "Relative and inherent reactivities of imidazolium-based ionic liquids: the implications for lignocellulose processing applications," *RSC Advances*, vol. 2, no. 21, p. 8020, 2012. 26, 124, 126

[139] D. R. MacFarlane, M. Forsyth, E. I. Izgorodina, A. P. Abbott, G. Annat, and K. Fraser, "On the concept of ionicity in ionic liquids," *Physical Chemistry Chemical Physics*, vol. 11, pp. 4962–7, 2009. 26, 27, 39, 63, 84

[140] G. L. Burrell, I. M. Burgar, Q. Gong, N. F. Dunlop, and F. Separovic, "NMR Relaxation and Self-Diffusion Study at High and Low Magnetic Fields of Ionic Association in Protic Ionic Liquids.," *The Journal of Physical Chemistry B*, vol. 114, pp. 11436–11443, 2010. 26, 84

[141] H. Kataoka and Y. Saito, "New approached for determining the degree of dissociation of a salt by measurements of dynamic properties of lithium ion electrolytes," *Journal of Physical Chemistry B*, vol. 106, no. 50, pp. 13064–13068, 2002. 27

[142] A. Noda, K. Hayamizu, and M. Watanabe, "Pulsed-Gradient Spin-Echo 1H and 19F NMR Ionic Diffusion Coefficient, Viscosity, and Ionic Conductivity of Non-Chloroaluminate Room-Temperature Ionic Liquids," *Journal of Physical Chemistry B*, vol. 105, no. 20, pp. 4603–4610, 2001. 28, 56, 63

[143] J. Dupont, "On the solid, liquid and solution structural organization of imidazolium ionic liquids," *Journal of the Brazilian Chemical Society*, vol. 15, no. 3, pp. 341–350, 2004. 30, 39

[144] F. C. Gozzo, L. S. Santos, R. Augusti, C. S. Consorti, J. Dupont, and M. N. Eberlin, "Gaseous supramolecules of imidazolium ionic liquids: "Magic" numbers and intrinsic strengths of hydrogen bonds," *Chemistry - A European Journal*, vol. 10, no. 23, pp. 6187–6193, 2004. 28, 30, 63, 81, 82, 84, 157

[145] J. Hou, Z. Zhang, and L. A. Madsen, "Cation/Anion Associations in Ionic Liquids Modulated by Hydration and Ionic Medium," *Journal of Physical Chemistry B*, vol. 115, pp. 4576–4582, 2011. 28, 30, 39, 45, 59, 63, 65, 71, 93, 103

[146] P. J. Dyson, I. Khalaila, S. Luettgen, J. S. McIndoe, and D. Zhao, "Direct probe electrospray (and nanospray) ionization mass spectrometry of neat ionic liquids," *Chemical Communications*, pp. 2204–2205, 2004. 30, 81, 82, 121, 122, 157, 158

[147] D. F. Kennedy and C. J. Drummond, "Large aggregated ions found in some protic ionic liquids," *Journal of Physical Chemistry B*, vol. 113, no. 17, pp. 5690–5693, 2009. 30, 81, 82, 84, 121, 122, 158

[148] M. E. Ries, A. Radhi, A. S. Keating, O. Parker, and T. Budtova, "Diffusion of 1-Ethyl-3-methyl-imidazolium Acetate in Glucose, Cellobiose, and Cellulose Solutions.," *Biomacromolecules*, vol. 15, pp. 609–17, Feb 2014. 38, 42, 124, 126, 127, 128, 129, 134, 136, 141, 142, 143, 144, 145, 146, 150, 154, 158

[149] A. Radhi, K. A. Le, M. E. Ries, and T. Budtova, "Macroscopic and microscopic study of 1-ethyl-3-methyl-imidazolium acetate-DMSO mixtures," *Journal of Physical Chemistry B*, vol. 119, no. 4, pp. 1633–1640, 2015. 38, 160

[150] G. Gurau, H. Wang, Y. Qiao, X. Lu, S. Zhang, and R. D. Rogers, "Chlorine-free alternatives to the synthesis of ionic liquids for biomass processing," *Pure and Applied Chemistry*, vol. 84, pp. 745–754, Jan 2012. 38

[151] P. Bonhôte, A.-P. Dias, N. Papageorgiou, K. Kalyanasundaram, and M. Grätzel, "Hydrophobic, Highly Conductive Ambient-Temperature Molten Salts.," *Inorganic Chemistry*, vol. 35, no. 5, pp. 1168—-1178, 1996. 38, 56

[152] M. Tariq, P. J. Carvalho, J. A. P. Coutinho, I. M. Marrucho, J. N. C. Lopes, and L. P. N. Rebelo, "Viscosity of (C2-C14) 1-alkyl-3-methylimidazolium bis(trifluoromethylsulfonyl)amide ionic liquids in an extended temperature range," *Fluid Phase Equilibria*, vol. 301, pp. 22–32, 2011. 38

[153] S. Fendt, S. Padmanabhan, H. W. Blanch, and J. M. Prausnitz, "Viscosities of Acetate or Chloride-Based Ionic Liquids and Some of Their Mixtures with Water or Other Common Solvents," *Journal of Chemical and Engineering Data*, vol. 56, pp. 31–34, 2011. 38

[154] A. Xu, J. Wang, Y. Zhang, and Q. Chen, "Effect of alkyl chain length in anions on thermodynamic and surface properties of 1-butyl-3-methylimidazolium carboxylate ionic liquids," *Industrial and Engineering Chemistry Research*, vol. 51, pp. 3458–3465, Feb 2012. 39

[155] A. Xu, Y. Zhang, W. Lu, K. Yao, and H. Xu, "Effect of alkyl chain length in anion on dissolution of cellulose in 1-butyl-3-methylimidazolium carboxylate ionic liquids," *Journal of Molecular Liquids*, vol. 197, pp. 211–214, 2014. 39, 125

[156] Y. Wang and G. A. Voth, "Unique spatial heterogeneity in ionic liquids," *Journal of the American Chemical Society*, vol. 127, no. 35, pp. 12192–12193, 2005. 39

[157] Y. Zhao, S. Gao, J. Wang, and J. Tang, "Aggregation of ionic liquids [C(n)mim]Br (n = 4, 6, 8, 10, 12) in D2O: a NMR study.," *J. Phys. Chem. B*, vol. 112, no. 7, pp. 2031–2039, 2008. 40, 129

[158] M. Blesic, M. H. Marques, N. V. Plechkova, K. R. Seddon, L. P. N. Rebelo, and A. Lopes, "Self-aggregation of ionic liquids: micelle formation in aqueous solution," *Green Chemistry*, vol. 9, pp. 481–490, 2007. 40

[159] M. G. Freire, C. Neves, J. N. Canongia Lopes, I. M. Marrucho, J. A. P. Coutinho, and L. P. N. Rebelo, "Impact of Self-Aggregation on the formation of ionic-liquid-based aqueous biphasic systems," *Journal of Physical Chemistry B*, vol. 116, pp. 7660–7668, 2012. 40

[160] T. Erdmenger, C. Haensch, R. Hoogenboom, and U. S. Schubert, "Homogeneous tritylation of cellulose in 1-butyl-3-methylimidazolium chloride," *Macromolecular Bioscience*, vol. 7, pp. 440–445, 2007. 40, 125

[161] M. A. A. Rocha, C. M. S. S. Neves, M. G. Freire, O. Russina, A. Triolo, J. A. P. Coutinho, and L. M. N. B. F. Santos, "Alkylimidazolium based ionic liquids: Impact of cation symmetry on their nanoscale structural organization," *Journal of Physical Chemistry B*, vol. 117, pp. 10889–10897, 2013.

[162] A. A. Niazi, B. D. Rabideau, and A. E. Ismail, "Effects of water concentration on the structural and diffusion properties of imidazolium-based ionic liquid-water mixtures," *Journal of Physical Chemistry B*, vol. 117, pp. 1378–1388, 2013.

[163] L. Xue, E. Gurung, G. Tamas, Y. P. Koh, M. Shadeck, S. L. Simon, M. Maroncelli, and E. L. Quitevis, "Effect of Alkyl Chain Branching on Physicochemical Properties of Imidazolium-Based Ionic Liquids," *Journal of Chemical & Engineering Data*, vol. 61, pp. 1078–1091, 2016. 40

[164] A. Menjoge and S. Vasenkov, "Suppression of the Anomalous Relationship between Diffusivities of Cations and Anions by Water in Imidazolium-Based Ionic liquids," *Diffusion Fundamentals*, vol. 9, pp. 3.1 – 3.7, 2008. 43, 45, 93

[165] N. E. Heimer, R. E. Del Sesto, and W. R. Carper, "Evidence for spin diffusion in a H,H-NOESY study of imidazolium tetrafluoroborate ionic liquids," *Magnetic Resonance in Chemistry*, vol. 42, pp. 71–75, 2004. 51

[166] D. M. Rein, R. Khalfin, N. Szekely, and Y. Cohen, "True molecular solutions of natural cellulose in the binary ionic liquid-containing solvent mixtures.," *Carbohydrate Polymers*, vol. 112, pp. 125–33, Nov 2014. 54

[167] A. Filippov, M. Taher, F. U. Shah, S. Glavatskih, and O. N. Antzutkin, "The effect of the cation alkyl chain length on density and diffusion in dialkylpyrrolidinium bis(mandelato)borate ionic liquids," *Physical Chemistry Chemical Physics*, vol. 16, no. 48, pp. 26798–26805, 2014. 57

[168] K. Ueno, H. Tokuda, and M. Watanabe, "Ionicity in ionic liquids: correlation with ionic structure and physicochemical properties," *Physical Chemistry Chemical Physics*, vol. 12, no. 8, pp. 1649–1658, 2010. 84

[169] R. Atkin and G. G. Warr, "The smallest amphiphiles: Nanostructure in protic room-temperature ionic liquids with short alkyl groups," *Journal of Physical Chemistry B*, vol. 112, no. 14, pp. 4164–4166, 2008. 84

[170] A. M. Moschovi and V. Dracopoulos, "Structure of protic (HCnImNTf2, n=0-12) and aprotic (C1CnImNTf2, n=1-12) imidazolium ionic liquids: A vibrational spectroscopic study," *Journal of Molecular Liquids*, vol. 210, pp. 189–199, 2015. 84

[171] A. G. Avent, P. A. Chaloner, M. P. Day, K. R. Seddon, and T. Welton, "Evidence for hydrogen bonding in solutions of 1-ethyl-3-methylimidazolium halides, and its implications for room-temperature halogenoaluminate(III) ionic liquids," *Journal of the Chemical Society, Dalton Transactions*, p. 3405, 1994. 84

[172] J. L. E. Campbell, K. E. Johnson, and J. R. Torkelson, "Infrared and Variable-Temperature 1H-NMR Investigations of Ambient-Temperature Ionic Liquids Prepared by Reaction of HCl with 1-Ethyl-3-methyl-1H-imidazolium Chloride," *Inorganic Chemistry*, vol. 33, no. 15, pp. 3340–3345, 1994.

[173] K. Dong, S. Zhang, D. Wang, and X. Yao, "Hydrogen bonds in imidazolium ionic liquids.," *The Journal of Physical Chemistry A*, vol. 110, pp. 9775–82, Aug 2006. 84

[174] S. Tsuzuki, W. Shinoda, M. S. Miran, H. Kinoshita, T. Yasuda, and M. Watanabe, "Interactions in ion pairs of protic ionic liquids: Comparison with aprotic ionic liquids," *Journal of Chemical Physics*, vol. 139, no. 17, p. 174504, 2013. 84, 120, 122

[175] M. S. Miran, H. Kinoshita, T. Yasuda, M. A. B. H. Susan, and M. Watanabe, "Physicochemical properties determined by ΔpKa for protic ionic liquids based on an organic super-strong base with various Brønsted acids.," *Physical Chemistry Chemical Physics*, vol. 14, pp. 5178–86, Apr 2012. 85, 106

[176] K. C. Lethesh, S. N. Shah, and M. A. Mutalib, "Synthesis, Characterization, and Thermophysical Properties of 1,8- Diazobicyclo[5.4.0]undec-7-ene Based Thiocyanate Ionic Liquids," *Journal of Chemical & Engineering Data*, vol. 59, p. 17881795, 2014. 85

[177] Y. Yang, H. Xie, and E. Liu, "Acylation of cellulose in reversible ionic liquids," *Green Chemistry*, vol. 16, no. 6, p. 3018, 2014. 85

[178] A.-G. Ying, L. Liu, G.-F. Wu, G. Chen, X.-Z. Chen, and W.-D. Ye, "Aza-Michael addition of aliphatic or aromatic amines to alpha,beta-unsaturated compounds catalyzed by a DBU-derived ionic liquid under solvent-free conditions," *Tetrahedron Letters*, vol. 50, pp. 1653–1657, 2009. 85

[179] J. Nowicki, M. Muszyński, and S. Gryglewicz, "Novel basic ionic liquids from cyclic guanidines and amidines - new catalysts for transesterification of oleochemicals," *Journal of Chemical Technology & Biotechnology*, vol. 89, pp. 48–55, Jan 2014.

[180] L. Wu, J. Song, B. Zhang, B. Zhou, H. Zhou, H. Fan, Y. Yang, and B. Han, "Very efficient conversion of glucose to 5-hydroxymethylfurfural in DBU-based ionic liquids with benzenesulfonate anion," *Green Chemistry*, vol. 16, p. 3935, Jun 2014. 85

[181] Y. Ma, M. Hummel, M. Määttänen, A. Särkilahti, A. Harlin, and H. Sixta, "Upcycling of waste paper and cardboard to textiles," *Green Chemistry*, vol. 18, pp. 858–866, 2016. 86

[182] A. Stepan, A. Monshizadeh, M. Hummel, A. Roselli, and H. Sixta, "Cellulose Fractionation with IONCELL-P," *Carbohydrate Polymers*, vol. 150, pp. 99–106, 2016. 86

[183] M. D. Lingwood, Z. Zhang, B. E. Kidd, K. B. McCreary, J. Hou, and L. A. Madsen, "Unraveling the local energetics of transport in a polymer ion conductor Electronic Supplementary Information," *Chemical Communications*, vol. 49, no. 39, pp. 4283–5, 2013. 93

[184] H. Liu, K. L. Sale, B. M. Holmes, B. A. Simmons, and S. Singh, "Understanding the interactions of cellulose with ionic liquids: a molecular dynamics study.," *The Journal of Physical Chemistry B*, vol. 114, pp. 4293–301, Apr 2010. 124

[185] H. M. Cho, A. S. Gross, and J.-W. Chu, "Dissecting force interactions in cellulose deconstruction reveals the required solvent versatility for overcoming biomass recalcitrance.," *Journal of the American Chemical Society*, vol. 133, pp. 14033–41, Sep 2011. 124

[186] J. Zhang, H. Zhang, J. Wu, J. Zhang, J. He, and J. Xiang, "NMR spectroscopic studies of cellobiose solvation in EmimAc aimed to understand the dissolution mechanism of cellulose in ionic liquids," *Physical Chemistry Chemical Physics*, vol. 12, pp. 1941–1947, Feb 2010. 124, 126, 129, 141, 142

[187] R. C. Remsing, I. D. Petrik, Z. Liu, and G. Moyna, "Comment on "NMR spectroscopic studies of cellobiose solvation in EmimAc aimed to understand the dissolution mechanism of cellulose in ionic liquids" by J. Zhang, H. Zhang, J. Wu, J. Zhang, J. He and J. Xiang, Phys. Chem. Chem. Phys., 2010, 12, 1941.," *Physical Chemistry Chemical Physics*, vol. 12, pp. 14827–8; discussion 14829–30, Nov 2010. 124, 142

[188] J. Zhang, H. Zhang, J. Wu, J. Zhang, J. He, and J. Xiang, "Reply to Comment on NMR spectroscopic studies of cellobiose solvation in EmimAc aimed to understand the dissolution mechanism of cellulose in ionic liquids"' by R . C . Remsing , I . D . Petrik , Z . Liu and Moyna, G," *Physical Chemistry Chemical Physics*, vol. 12, pp. 14827–8, Nov 2010. 124, 142

[189] A. Xu, J. Wang, and H. Wang, "Effects of anionic structure and lithium salts addition on the dissolution of cellulose in 1-butyl-3-methylimidazolium-based ionic liquid solvent systems," *Green Chemistry*, vol. 12, pp. 268–275, 2010. 125

[190] A. Radhi, *NMR Studies of Cellulose Dissolution in Ionic Liquids*. PhD thesis, University of Leeds, 2014. 127, 129, 132, 141, 145, 147, 154, 158

[191] K. A. Le, C. Rudaz, and T. Budtova, "Phase diagram, solubility limit and hydrodynamic properties of cellulose in binary solvents with ionic liquid," *Carbohydrate Polymers*, vol. 105, pp. 237–243, May 2014. 160

[192] J.-M. Andanson, E. Bordes, J. Devémy, F. Leroux, A. A. H. Pádua, and M. F. C. Gomes, "Understanding the role of co-solvents in the dissolution of cellulose in ionic liquids," *Green Chemistry*, vol. 16, p. 2528, 2014. 160